

UNCLASSIFIED

|   |
|---|
|   |
|   |
|   |
| AD NUMBER   |
| AD856560  |
| NEW LIMITATION CHANGE   |
| TO<br>Approved for public release, distribution unlimited   |
| FROM<br>Distribution authorized to U.S. Gov't. agencies and their contractors; Administrative/Operational Use; MAY 1969. Other requests shall be referred to Rome Air Development Center, Attn: EMASS, Griffiss AFB, NY 13441-5700. |
| AUTHORITY   |
| RADC, per DTIC form 55  |

THIS PAGE IS UNCLASSIFIED

AD856560

RADC-TR-68-340, Vol III  
Final Technical Report  
May 1969



INVESTIGATION OF SCATTERING PRINCIPLES  
Volume III - Analytical Investigation

R. A. Ross  
Prepared by Cornell Aeronautical Laboratory, Inc.  
for the Fort Worth Division of General Dynamics  
Under Subcontract P. O. No. 287502  
(Prime F30602-67-C-0074)

This document is subject to special export controls and each transmittal to foreign governments, foreign nationals, or representatives thereto may be made only with prior approval of RADC (EMASS), GAFB, NY 13440.

AUG 19 1969

Rome Air Development Center  
Air Force Systems Command  
Griffiss Air Force Base, New York

When US Government drawings, specifications, or other data are used for any purpose other than a definitely related government procurement operation, the government thereby incurs no responsibility nor any obligation whatsoever; and the fact that the government may have formulated, furnished, or in any way supplied the said drawings, specifications, or other data is not to be regarded, by implication or otherwise, as in any manner licensing the holder or any other person or corporation, or conveying any rights or permission to manufacture, use, or sell any patented invention that may in any way be related thereto.

|                      |                                     |
|----------------------|-------------------------------------|
| PERMISSION TO        |                                     |
| WHITE SECTION        | <input checked="" type="checkbox"/> |
| BLUE SECTION         | <input type="checkbox"/>            |
| REMARKS              |                                     |
| DATE                 |                                     |
| BY                   |                                     |
| OR - AUTHORITY CODES |                                     |
| P.O.                 | ACQ. NO. OR SYMBOL                  |
| 2                    |                                     |

Do not return this copy. Retain or destroy.

**INVESTIGATION OF SCATTERING PRINCIPLES  
Volume III - Analytical Investigation**

**R. A. Ross  
Prepared by Cornell Aeronautical Laboratory, Inc.  
for the Fort Worth Division of General Dynamics  
Under Subcontract P. O. No. 287502  
(Prime F30602-67-C-0074)**

**This document is subject to special export controls and each transmittal to foreign governments, foreign nationals or representatives thereto may be made only with prior approval of RADC (EMASS), GAFB, NY 13440.**

## FOREWORD

This document comprises the Final Technical Report specified under Subcontract P.O. No. 287502, "Investigation of Scattering Principles," which is the analytical phase of scattering investigations performed for Rome Air Development Center under Prime Contract F30602-67-C-0074 assigned to the Fort Worth Division of General Dynamics, Fort Worth TX 76101. This sub-contract was performed by Cornell Aeronautical Laboratories (CAL) and this document was prepared by R. A. Ross of CAL. This document is Volume III of four volumes produced under the prime contract. (Reference 22, 23, 24) It contains applications of Keller's geometrical theory of diffraction to seven distinct shapes: cylinder, frustum, cone, frustum-cylinder, cylinder-flare, cone-cylinder, and hemisphere-cylinder.

Study of scattering by geometrical diffraction theory was initiated at CAL in 1965 under Project DISTRACT, Contract No. AF 30(602)-3289, an ARPA funded program monitored by Rome Air Development Center. That effort yielded nonspecular solutions for the cylinder and for the right conical frustum, for both monostatic and bistatic radar geometry. This and the investigation of scattering by a cone were continued under the present contract to General Dynamics/Fort Worth and Contract No. F33612-67-C-1713 from Wright-Patterson Air Force Base.

This investigation was performed under the direction of Dr. C. C. Freeny, Dr. G. W. Gruver, and W. P. Cahill of the Fort Worth Division of General Dynamics. The author wishes to thank these personnel for their full cooperation throughout this program. He is also pleased to acknowledge valuable discussions with D. B. Larson of the CAL Computer Services Department.

The RADC project number is 6512, task 651207. Distribution of this report is limited by the Mutual Security Acts of 1949.

This document has been reviewed and is approved.

## ABSTRACT

Among the most powerful techniques for the calculation of radar scattering from bodies more than several wavelengths in size are those based upon one form or another of asymptotic analysis. By far the most practical of the asymptotic techniques advanced to date is the geometrical theory of diffraction developed principally by J. B. Keller at New York University. The work reported here examined the utility of geometrical diffraction theory for predicting the aspect-dependent scattering matrix of cylinders, frustums, cones, and their derivable shapes. These analytical results were evaluated in comparison with measurement data obtained at General Dynamics/Fort Worth.

This final report outlines the application of unmodified geometrical diffraction theory to seven axially-symmetric targets. As part of the analytical task, basic theory has been modified to predict scattering 1) at and near aspects which give rise to specular scattering, and 2) at and near the nose-on aspect for a cone. Resultant analytical formulations were programmed for the IBM-360 digital computer. Comparison of predictions with scattering matrix measurements shows that theory is accurate for the following shapes: cylinder, frustum, frustum-cylinder, cylinder-flare, and hemisphere-cylinder. Further, bistatic predictions are at least as accurate as corresponding monostatic calculations. Additional modification of geometrical diffraction theory will be required to achieve similar capability in the case of a cone and a cone-cylinder.

A direction for future investigations of scattering by a cone has been outlined within the context of geometrical diffraction theory. In addition, more detailed study of the phase of the scattering interaction, both predicted and measured, is advocated.

## CONTENTS

| <u>Section</u>   | <u>Page</u> |
|--|-------------|
| 1 INTRODUCTION .....   | 1           |
| 2 BACKGROUND .....   | 5           |
| 2.1 Polarization Scattering Matrix .....                     | 5           |
| 2.2 Scattering Center Concept .....                          | 7           |
| 2.3 Geometrical Diffraction Theory .....                     | 10          |
| 3 OUTLINE OF TECHNICAL PROGRAM .....                         | 13          |
| 3.1 Scope of Investigation .....                             | 13          |
| 3.2 Data Comparison Procedure .....                          | 15          |
| 3.2.1 Radar Cross Section Data .....                         | 16          |
| 3.2.2 Scattering Phase Data .....                            | 16          |
| 3.2.3 Discussion of Magnetic Tapes .....                     | 20          |
| 4 ANALYTICAL RESULTS AND COMPARISON<br>WITH EXPERIMENT ..... | 22          |
| 4.1 Cylinder .....   | 23          |
| 4.1.1 Analytical Formulation .....                           | 23          |
| 4.1.2 Results .....  | 28          |
| 4.1.3 Remarks .....  | 31          |
| 4.2 Frustum .....  | 60          |
| 4.2.1 Analytical Formulation .....                           | 60          |
| 4.2.2 Results .....  | 64          |
| 4.2.3 Remarks .....  | 66          |
| 4.3 Cone .....   | 95          |
| 4.3.1 Analytical Formulation .....                           | 95          |
| 4.3.2 Preliminary Results .....                              | 98          |
| 4.3.3 Remarks .....  | 99          |
| 4.4 Frustum-Cylinder .....                                   | 112         |
| 4.4.1 Analytical Formulation .....                           | 112         |
| 4.4.2 Results .....  | 116         |
| 4.4.3 Remarks .....  | 117         |

## CONTENTS (Cont.)

| <u>Section</u>                               | <u>Page</u> |
|--|-------------|
| 4.5 Cylinder-Flare .....                     | 130         |
| 4.5.1 Analytical Formulation .....           | 130         |
| 4.5.2 Results .....                          | 134         |
| 4.5.3 Remarks .....                          | 135         |
| 4.6 Cone-Cylinder .....                      | 144         |
| 4.6.1 Analytical Formulation .....           | 144         |
| 4.6.2 Results .....                          | 148         |
| 4.6.3 Remarks .....                          | 149         |
| 4.7 Hemisphere-Cylinder .....                | 162         |
| 4.7.1 Analytical Formulation .....           | 162         |
| 4.7.2 Results .....                          | 164         |
| 4.7.3 Remarks .....                          | 165         |
| 5 SUMMARY AND CONCLUSIONS .....              | 170         |
| REFERENCES .....                             | 171         |
| <br><b>Appendix</b>                          |             |
| A SCATTERING BY A CYLINDER .....             | A-1         |
| B SCATTERING BY A FRUSTUM .....              | B-1         |
| C SCATTERING BY A CONE .....                 | C-1         |
| D GENERAL EDGE DIFFRACTION COEFFICIENT ..... | D-1         |



## ILLUSTRATIONS

| <u>Figure</u> |  | <u>Page</u> |
|---------------|--|-------------|
| 1             | Target Phase Reference — Center of Rotation Geometry . .                           | 19          |
| 2             | Scattering Centers on a Cylinder . . . . .   | 24          |
| 3             | Vertical Polarization Radar Cross Section.<br>Cylinder CY3, Monostatic . . . . .   | 32          |
| 4             | Horizontal Polarization Radar Cross Section.<br>Cylinder CY3, Monostatic . . . . . | 33          |
| 5             | Vertical Polarization Scattering Phase.<br>Cylinder CY3, Monostatic . . . . .      | 34          |
| 6             | Horizontal Polarization Scattering Phase.<br>Cylinder CY3, Monostatic . . . . .    | 35          |
| 7             | Vertical Polarization Radar Cross Section.<br>Cylinder CY5, Monostatic . . . . .   | 36          |
| 8             | Horizontal Polarization Radar Cross Section.<br>Cylinder CY5, Monostatic . . . . . | 37          |
| 9             | Vertical Polarization Scattering Phase.<br>Cylinder CY5, Monostatic . . . . .      | 38          |
| 10            | Horizontal Polarization Scattering Phase.<br>Cylinder CY5, Monostatic . . . . .    | 39          |
| 11            | Vertical Polarization Radar Cross Section.<br>Cylinder CY5, Bistatic . . . . .     | 40          |
| 12            | Horizontal Polarization Radar Cross Section.<br>Cylinder CY5, Bistatic . . . . .   | 41          |
| 13            | Vertical Polarization Scattering Phase.<br>Cylinder CY5, Bistatic . . . . .        | 42          |
| 14            | Horizontal Polarization Scattering Phase.<br>Cylinder CY5, Bistatic . . . . .      | 43          |
| 15            | Vertical Polarization Radar Cross Section.<br>Cylinder CY5, Bistatic . . . . .     | 44          |
| 16            | Horizontal Polarization Radar Cross Section.<br>Cylinder CY5, Bistatic . . . . .   | 45          |

# ILLUSTRATIONS (Cont.)

| <u>Figure</u> |  | <u>Page</u> |
|---------------|--|-------------|
| 17            | Vertical Polarization Scattering Phase.<br>Cylinder CY5, Bistatic . . . . .        | 46          |
| 18            | Horizontal Polarization Scattering Phase.<br>Cylinder CY5, Bistatic . . . . .      | 47          |
| 19            | Vertical Polarization Radar Cross Section.<br>Cylinder CY6, Monostatic . . . . .   | 48          |
| 20            | Horizontal Polarization Radar Cross Section.<br>Cylinder CY6, Monostatic . . . . . | 49          |
| 21            | Vertical Polarization Scattering Phase.<br>Cylinder CY6, Monostatic . . . . .      | 50          |
| 22            | Horizontal Polarization Scattering Phase.<br>Cylinder CY6, Monostatic . . . . .    | 51          |
| 23            | Vertical Polarization Radar Cross Section.<br>Cylinder CY6, Bistatic . . . . .     | 52          |
| 24            | Horizontal Polarization Radar Cross Section.<br>Cylinder CY6, Bistatic . . . . .   | 53          |
| 25            | Vertical Polarization Scattering Phase.<br>Cylinder CY6, Bistatic . . . . .        | 54          |
| 26            | Horizontal Polarization Scattering Phase.<br>Cylinder CY6, Bistatic . . . . .      | 55          |
| 27            | Vertical Polarization Radar Cross Section.<br>Cylinder CY6, Bistatic . . . . .     | 56          |
| 28            | Horizontal Polarization Radar Cross Section.<br>Cylinder CY6, Bistatic . . . . .   | 57          |
| 29            | Vertical Polarization Scattering Phase.<br>Cylinder CY6, Bistatic . . . . .        | 58          |
| 30            | Horizontal Polarization Scattering Phase.<br>Cylinder CY6, Bistatic . . . . .      | 59          |
| 31            | Scattering Centers on Frustum . . . . .  | 61          |
| 32            | Vertical Polarization Radar Cross Section.<br>Frustum F3, Monostatic . . . . .     | 67          |

# ILLUSTRATIONS (Cont.)

| <u>Figure</u> |  | <u>Page</u> |
|---------------|--|-------------|
| 33            | Horizontal Polarization Radar Cross Section.<br>Frustum F3, Monostatic ..... | 68          |
| 34            | Vertical Polarization Scattering Phase.<br>Frustum F3, Monostatic .....      | 69          |
| 35            | Horizontal Polarization Scattering Phase.<br>Frustum F3, Monostatic .....    | 70          |
| 36            | Vertical Polarization Radar Cross Section.<br>Frustum F4, Monostatic .....   | 71          |
| 37            | Horizontal Polarization Radar Cross Section.<br>Frustum F4, Monostatic ..... | 72          |
| 38            | Vertical Polarization Scattering Phase.<br>Frustum F4, Monostatic .....      | 73          |
| 39            | Horizontal Polarization Scattering Phase.<br>Frustum F4, Monostatic .....    | 74          |
| 40            | Vertical Polarization Radar Cross Section.<br>Frustum F4, Bistatic .....     | 75          |
| 41            | Horizontal Polarization Radar Cross Section.<br>Frustum F4, Bistatic .....   | 76          |
| 42            | Vertical Polarization Scattering Phase.<br>Frustum F4, Bistatic .....        | 77          |
| 43            | Horizontal Polarization Scattering Phase.<br>Frustum F4, Bistatic .....      | 78          |
| 44            | Vertical Polarization Radar Cross Section.<br>Frustum F4, Bistatic .....     | 79          |
| 45            | Horizontal Polarization Radar Cross Section.<br>Frustum F4, Bistatic .....   | 80          |
| 46            | Vertical Polarization Scattering Phase.<br>Frustum F4, Bistatic .....        | 81          |
| 47            | Horizontal Polarization Scattering Phase.<br>Frustum F4, Bistatic .....      | 82          |

# ILLUSTRATIONS (Cont.)

| <u>Figure</u> |  | <u>Page</u> |
|---------------|--|-------------|
| 48            | Vertical Polarization Radar Cross Section.<br>Frustum F5, Monostatic .....   | 83          |
| 49            | Horizontal Polarization Radar Cross Section.<br>Frustum F5, Monostatic ..... | 84          |
| 50            | Vertical Polarization Scattering Phase.<br>Frustum F5, Monostatic .....      | 85          |
| 51            | Horizontal Polarization Scattering Phase.<br>Frustum F5, Monostatic .....    | 86          |
| 52            | Vertical Polarization Radar Cross Section.<br>Frustum F5, Bistatic .....     | 87          |
| 53            | Horizontal Polarization Radar Cross Section.<br>Frustum F5, Bistatic .....   | 88          |
| 54            | Vertical Polarization Scattering Phase.<br>Frustum F5, Bistatic .....        | 89          |
| 55            | Horizontal Polarization Scattering Phase.<br>Frustum F5, Bistatic .....      | 90          |
| 56            | Vertical Polarization Radar Cross Section.<br>Frustum F5, Bistatic .....     | 91          |
| 57            | Horizontal Polarization Radar Cross Section.<br>Frustum F5, Bistatic .....   | 92          |
| 58            | Vertical Polarization Scattering Phase.<br>Frustum F5, Bistatic .....        | 93          |
| 59            | Horizontal Polarization Scattering Phase.<br>Frustum F5, Bistatic .....      | 94          |
| 60            | Scattering Centers on Cone .....   | 95          |
| 61            | Vertical Polarization Radar Cross Section.<br>Cone C1, Monostatic .....      | 100         |
| 62            | Horizontal Polarization Radar Cross Section.<br>Cone C1, Monostatic .....    | 101         |
| 63            | Vertical Polarization Scattering Phase.<br>Cone C1, Monostatic .....         | 102         |

## ILLUSTRATIONS (Cont.)

| <u>Figure</u> |  | <u>Page</u> |
|---------------|--|-------------|
| 64            | Horizontal Polarization Scattering Phase.<br>Cone C1, Monostatic .....                   | 103         |
| 65            | Vertical Polarization Radar Cross Section.<br>Cone C2, Monostatic .....                  | 104         |
| 66            | Horizontal Polarization Radar Cross Section.<br>Cone C2, Monostatic .....                | 105         |
| 67            | Vertical Polarization Scattering Phase.<br>Cone C2, Monostatic .....                     | 106         |
| 68            | Horizontal Polarization Scattering Phase.<br>Cone C2, Monostatic .....                   | 107         |
| 69            | Vertical Polarization Radar Cross Section.<br>Cone C4, Monostatic .....                  | 108         |
| 70            | Horizontal Polarization Radar Cross Section.<br>Cone C4, Monostatic .....                | 109         |
| 71            | Vertical Polarization Scattering Phase.<br>Cone C4, Monostatic .....                     | 110         |
| 72            | Horizontal Polarization Scattering Phase.<br>Cone C4, Monostatic .....                   | 111         |
| 73            | Scattering Centers on a Frustum-Cylinder .....   | 112         |
| 74            | Vertical Polarization Radar Cross Section.<br>Frustum-Cylinder F4CY3, Monostatic .....   | 118         |
| 75            | Horizontal Polarization Radar Cross Section.<br>Frustum-Cylinder F4CY3, Monostatic ..... | 119         |
| 76            | Vertical Polarization Scattering Phase.<br>Frustum-Cylinder F4CY3, Monostatic .....      | 120         |
| 77            | Horizontal Polarization Scattering Phase.<br>Frustum-Cylinder F4CY3, Monostatic .....    | 121         |
| 78            | Vertical Polarization Radar Cross Section.<br>Frustum-Cylinder F5CY5, Bistatic .....     | 122         |
| 79            | Horizontal Polarization Radar Cross Section.<br>Frustum-Cylinder F5CY5, Bistatic .....   | 123         |

# ILLUSTRATIONS (Cont.)

| <u>Figure</u> |  | <u>Page</u> |
|---------------|--|-------------|
| 80            | Vertical Polarization Scattering Phase.<br>Frustum-Cylinder F5CY5, Bistatic .....      | 124         |
| 81            | Horizontal Polarization Scattering Phase.<br>Frustum-Cylinder F5CY5, Bistatic .....    | 125         |
| 82            | Vertical Polarization Radar Cross Section.<br>Frustum-Cylinder F5CY5, Bistatic .....   | 126         |
| 83            | Horizontal Polarization Radar Cross Section.<br>Frustum-Cylinder F5CY5, Bistatic ..... | 127         |
| 84            | Horizontal Polarization Scattering Phase.<br>Frustum-Cylinder F5CY5, Bistatic .....    | 128         |
| 85            | Vertical Polarization Scattering Phase.<br>Frustum-Cylinder F5CY5, Bistatic .....      | 129         |
| 86            | Scattering Centers on a Cylinder-Flare .....   | 130         |
| 87            | Vertical Polarization Radar Cross Section.<br>Cylinder-Flare CY4F4, Bistatic .....     | 136         |
| 88            | Horizontal Polarization Radar Cross Section.<br>Cylinder-Flare CY4F4, Bistatic .....   | 137         |
| 89            | Vertical Polarization Scattering Phase.<br>Cylinder-Flare CY4F4, Bistatic .....        | 138         |
| 90            | Horizontal Polarization Scattering Phase.<br>Cylinder-Flare CY4F4, Bistatic .....      | 139         |
| 91            | Vertical Polarization Radar Cross Section.<br>Cylinder-Flare CY4F4, Bistatic .....     | 140         |
| 92            | Horizontal Polarization Radar Cross Section.<br>Cylinder-Flare CY4F4, Bistatic .....   | 141         |
| 93            | Vertical Polarization Scattering Phase.<br>Cylinder-Flare CY4F4, Bistatic .....        | 142         |
| 94            | Horizontal Polarization Scattering Phase.<br>Cylinder-Flare CY4F4, Bistatic .....      | 143         |
| 95            | Scattering Centers on a Cone-Cylinder .....  | 144         |

## ILLUSTRATIONS (Cont.)

| <u>Figure</u> |   | <u>Page</u> |
|---------------|---|-------------|
| 96            | Vertical Polarization Radar Cross Section.<br>Cone-Cylinder C1CY3, Monostatic .....         | 150         |
| 97            | Horizontal Polarization Radar Cross Section.<br>Cone-Cylinder C1CY3, Monostatic .....       | 151         |
| 98            | Vertical Polarization Scattering Phase.<br>Cone-Cylinder C1CY3, Monostatic .....            | 152         |
| 99            | Horizontal Polarization Scattering Phase.<br>Cone-Cylinder C1CY3, Monostatic .....          | 153         |
| 100           | Vertical Polarization Radar Cross Section.<br>Cone-Cylinder C2CY3, Monostatic .....         | 154         |
| 101           | Horizontal Polarization Radar Cross Section.<br>Cone-Cylinder C2CY3, Monostatic .....       | 155         |
| 102           | Vertical Polarization Scattering Phase.<br>Cone-Cylinder C2CY3, Monostatic .....            | 156         |
| 103           | Horizontal Polarization Scattering Phase.<br>Cone-Cylinder C2CY3, Monostatic .....          | 157         |
| 104           | Vertical Polarization Radar Cross Section.<br>Cone-Cylinder C4CY5, Monostatic .....         | 158         |
| 105           | Horizontal Polarization Radar Cross Section.<br>Cone-Cylinder C4CY5, Monostatic .....       | 159         |
| 106           | Vertical Polarization Scattering Phase.<br>Cone-Cylinder C4CY5, Monostatic .....            | 160         |
| 107           | Horizontal Polarization Scattering Phase.<br>Cone-Cylinder C4CY5, Monostatic .....          | 161         |
| 108           | Scattering Centers on a Hemisphere-Cylinder .....   | 162         |
| 109           | Vertical Polarization Radar Cross Section.<br>Hemisphere-Cylinder H3CY3, Monostatic .....   | 166         |
| 110           | Horizontal Polarization Radar Cross Section.<br>Hemisphere-Cylinder H3CY3, Monostatic ..... | 167         |

## ILLUSTRATIONS (Cont.)

| <u>Figure</u> |  | <u>Page</u> |
|---------------|--|-------------|
| 111           | Vertical Polarization Scattering Phase.<br>Hemisphere-Cylinder H3CY3, Monostatic .....   | 168         |
| 112           | Horizontal Polarization Scattering Phase.<br>Hemisphere-Cylinder H3CY3, Monostatic ..... | 169         |
| A-1           | Diffraction at a Point on the Edge of a Two-Dimensional<br>Wedge .....                   | A-5         |
| A-2           | Angular Relationships .....  | A-7         |
| A-3           | Angular Transformation: Two-Dimensional<br>Rectangular Cylinder .....                    | A-9         |
| A-4           | Angular Relations for Right-Circular Cylinder .....                                      | A-12        |
| A-5           | Phase Angle Geometry: Unrestricted Orientation<br>of Bistatic Array .....                | A-15        |
| A-6           | Spherical Geometry: View Along Line OC .....   | A-18        |
| B-1           | Scattering Centers on Frustum .....  | B-2         |
| B-2           | Broadside Specular: Unmodified Geometrical<br>Diffraction Theory .....                   | B-10        |
| C-1           | Longitudinal Section of a Pointed, Right-Circular Cone ..                                | C-2         |
| C-2           | Radar Cross Section of Pointed Cone, Vertical<br>Polarization .....                      | C-13        |
| C-3           | Radar Cross Section of Pointed Cone, Horizontal<br>Polarization .....                    | C-14        |
| C-4           | Short Pulse Target .....   | C-18        |
| C-5           | Sphere-Tipped Cone Used for Short Pulse Measurements ,                                   | C-19        |
| C-6           | Location and Magnitude of Major Scattering Center<br>on Cone .....                       | C-20        |



## ILLUSTRATIONS (Cont.)

| <u>Figure</u> |  | <u>Page</u> |
|---------------|--|-------------|
| D-1           | Diffraction at the Edge of a Two-Dimensional Wedge . . . . .                       | D-3         |
| D-2           | Local Interpretation of Ring Discontinuity in Terms<br>of Infinite Wedge . . . . . | D-4         |
| D-3           | Angular Relations as a Function of Position on the<br>Ring Discontinuity . . . . . | D-5         |
| D-4           | Polarization Transformation . . . . .  | D-6         |

## TABLES

| <u>Table</u>  | <u>Page</u> |
|---|-------------|
| 1    Technical Tasks .....                          | 14          |
| 2    Dimensions of Generic Shapes .....             | 15          |
| 3    Parameters Defining Phase Residuals .....      | 20          |
| 4    Parameters for Cylinder Study .....            | 29          |
| 5    Parameters for Frustum Study .....             | 64          |
| 6    Parameters for Cone Study .....                | 97          |
| 7    Parameters for Frustum-Cylinder Study .....    | 116         |
| 8    Parameters for Cylinder-Flare Study .....      | 134         |
| 9    Parameters for Cone-Cylinder Study .....       | 148         |
| 10   Parameters for Hemisphere-Cylinder Study ..... | 164         |
| C-1   C-band Short Pulse Data .....                 | C-17        |

## 1. INTRODUCTION

The objective of the effort reported here is to develop analytical expressions which accurately describe electromagnetic scattering from conducting bodies having the following basic generic surfaces and their derivable shapes: finite, right-circular cylinders, frustums, and cones. Bodies of interest are those whose overall dimensions are at least several wavelengths in extent. It is required that the analysis treat the scattering matrix of each target, and the theory be applicable to bistatic as well as monostatic situations. The analytical results are evaluated by comparing quantitative theoretical predictions generated at Cornell Aeronautical Laboratory (CAL) with scattering matrix measurements performed at the Fort Worth Division of General Dynamics (GD/FW).

Study of the scattering of electromagnetic waves from obstacles of complex shape is a broad and comprehensive subject. The fundamental problem is the determination of the total field in amplitude, phase, and polarization in terms of the geometrical and material constants characteristic of a given configuration of source and obstacle. In practice, accurate calculation of the radar scattering properties of any body is difficult at best.

Of course, the most satisfactory solution is an exact one. Here the major mathematical methods are separation of variables and the integral-equation formulation. The method of separation of variables has allowed treatment of particularly simple shapes,\* the best known of which are the perfectly reflecting half-plane or wedge, the sphere, and the two-dimensional elliptic cylinder. While the wedge solution has a direct bearing on analyses applied in Section 3, it is not possible to obtain an exact solution for any of the finite targets of interest to this program via separation of variables. Until recently, attempts to reduce the scattering problem to integral equations had proved fruitful in providing a useful viewpoint on the mechanism of scattering, but little use was made for practical solutions of particular problems.

---

\* Because there is a small number of separable coordinate systems, eleven in all, the method of separation of variables is severely restricted.

With the advent of high-speed digital computers, numerical procedures for evaluating integral equations have evolved and the approach now offers exciting possibilities. Firstly, results may be obtained to any specified accuracy.\* Secondly, the integral-equation formulation applies for obstacles of arbitrary shape; this has greatly enlarged the class of scattering problems for which numerical results may be obtained. Thirdly, the method accounts for all parametric dependencies observable by a radar. Results obtained by Oshiro,<sup>1</sup> Andreason,<sup>2</sup> and Harrington<sup>3</sup> indicate the power of the method. The one great disadvantage of the integral-equation approach is experienced when the obstacle is large compared to a wavelength. Both the required computer-storage capability and the cost of computations become prohibitive. For these reasons, application of the "unmodified" integral-equation formulation is limited to obstacles lying in the Rayleigh and low resonance regions (maximum dimension of the target less than several wavelengths). Since targets of interest on this program have minimum dimension at least several wavelengths in extent, the integral-equation approach is not applicable.

An important aspect of research in scattering theory is concerned with the derivation of approximate formulas that are useful in restricted ranges of the variables or parameters which characterize the particular problem. Due to the nature of radar scattering problems, we limit the following discussion to techniques based upon high frequency approximations. The two earliest approximate theories had their historical origin in the study of optics. They are Geometric Optics, which is treated by the method of rays, and Physical Optics, which involves primarily the theory of waves. In general, geometric optics is used whenever possible because of its comparative simplicity. However, this approximate theory is valid only in the limit of

---

\*In practice, boundary conditions are not imposed at every point on the obstacle, but rather at a finite number of points in a mesh covering the body. By reducing mesh-point separation, accuracy is improved. It is this characteristic which suggests discussion of this integral equation approach with exact solutions.

\*\*References 4 and 5 examine suitable means for modifying the integral-equation approach to handle targets large compared to a wavelength. However, no satisfactory technique has yet evolved.

vanishing wavelength, i. e., exceptionally large targets where diffraction effects may be ignored. Because most targets of interest are viewed at wavelengths which are an appreciable fraction of target dimensions, physical optics, a more difficult technique, has enjoyed wider application. For specular scattering from doubly curved surfaces many wavelengths in extent, the physical optics result is the same as the geometric optics result and both are very accurate, the accuracy tending to increase as the radii of curvature of the surface increases. For a singly curved or flat surface with surface normal parallel to the radar line of sight, the geometric optics prediction is infinite; here, physical optics permits a finite (and accurate) result to be obtained. Thus, specular scattering from flat plates, cylinders, frustums, cones, etc., can be found accurately (generally within one dB) for surfaces more than one or two wavelengths in extent.

Certain fundamental limitations are inherent in the physical-optics method. First, physical optics when applied to bistatic situations (transmitter and receiver in different locations) yields results that do not satisfy reciprocity and are thus patently invalid. A second limitation of physical optics, when applied to the backscattering case, is that the scattered wave is always found to have the same polarization as the incident wave; no depolarization effects can be predicted, and the cross-polarization radar cross section predicted by physical optics always vanishes.\* A third limitation is the assumption of a sharp geometric shadow boundary, which introduces a false discontinuity in the derivatives (especially higher-order derivatives) of the electromagnetic field vectors at this assumed boundary with consequent false predictions of scattering from the boundary. Still another limitation is the inability of physical optics to account for effects occurring in the geometrical-shadow region. In summary, it is apparent that geometric and physical optics are poorly suited to the present investigation of polarization-dependent and bistatic scatter, at least at nonspecular aspects.

The increased activity in scattering theory since World War II has generated a new approximate theory called the geometrical theory of diffraction. The method has been developed principally by J. B. Keller<sup>6</sup> at New York University and is largely dependent upon an extension of Fermat's principle that takes into account diffracted, as well as reflected (geometric optics), rays.

---

\* At best, physical optics seems to give a rough average of the horizontal- and vertical polarization radar cross sections.

As pointed out by Kline and Kay,<sup>7</sup> Keller's method is as yet without rigorous mathematical foundation. However, the geometrical theory of diffraction retains polarization dependence and satisfies reciprocity in bistatic situations. Further, the most significant statement one can make about the theory is that it produces remarkably good results for many bodies. Results obtained by Bechtel and Ross<sup>8</sup> and Kouyoumjian<sup>9</sup> are representative in illustrating the utility of Keller's theory; they, and the preceding comments form the basis of our choice of geometrical diffraction theory as the basis of analyses contained in this report.

Section 2 presents the formalism of the polarization scattering matrix. Simplification of the matrix for axially symmetric targets is noted. The scattering center concept is discussed prior to presentation of the scattering matrix in scattering center notation. Then the geometrical theory of diffraction is reviewed and the limitations attendant upon a single-diffraction analysis are discussed.

Section 3 details the scope of the present investigation and notes general comments pertaining to evaluation of analytical data. In Section 4, we compare results of theory and measurement. Section 5 contains conclusions based upon investigations performed as part of this study. The bulk of the detailed analysis is contained in Appendices A through D. In Appendix A, we present a detailed analysis of scattering by a cylinder. Appendix B outlines the corresponding treatment of a frustum. Results of analyses of scattering by a cone are reported in Appendices C and D.

## 2. BACKGROUND

Before detailed discussion of the investigations which are the main subject of this report, it may be helpful to review three technical concepts on which this work has been based. These concepts are:

1. The Polarization Scattering Matrix
2. The Scattering Center Concept
3. Geometric Diffraction Theory

Each will be discussed in turn.

### 2.1 POLARIZATION SCATTERING MATRIX

Although it is common to speak of "the" radar cross section of an object, it is well known that radar cross section depends upon the target shape and material, the angle (or angles, in the case of a bistatic system) at which the target is viewed, radar frequency, and polarization of the radar transmitting and receiving antennas. In particular, if a target is viewed at a specific aspect angle with a single frequency, the radar cross section depends upon the radar polarization. The polarization scattering matrix is introduced in order to express target reradiation independent of radar polarization. In the following discussion we show the relationship between the scattering matrix of a rotationally symmetric target and the principal polarization radar cross sections and scattering phases: a detailed treatment of the scattering matrix may be found in Reference 10.

Scattering is expressed as an explicit function of radar polarization when matrices are defined which describe the polarization properties of antennas and target. Consider a transmitting antenna; this antenna can be represented by the expression

$$\hat{q}_t = \begin{bmatrix} \cos \gamma_t \\ \sin \gamma_t e^{j\delta_t} \end{bmatrix} \quad (1)$$

where  $\hat{q}_t$  is a unit column matrix defining the polarization of the transmitted wave;  $\gamma_t$  is an angle ( $0 \leq \gamma_t \leq \frac{\pi}{2}$ ) which denotes the orientation of the linear polarization that results if  $\delta_t$  is zero, referred to the horizontal plane;  $\delta_t$  is a phase angle which can vary from 0 to  $2\pi$ . Any wave

polarization is thus specified when  $\gamma$ ,  $\delta$ , and the direction of propagation are known. Next consider a receiving antenna represented by a row matrix  $\hat{p}$ :

$$\hat{p} = [\cos \gamma_r \quad \sin \gamma_r e^{j\delta_r}] \quad (2)$$

It is assumed that "polarization" of a receiving antenna means the polarization of that antenna when it is used as a transmitting antenna. The cross section of a target  $\sigma_{\hat{q}\hat{p}}$  for transmitting antenna polarization  $\hat{q}$  and receiving antenna polarization  $\hat{p}$  is given by

$$\sigma_{\hat{q}\hat{p}} = |\hat{p} S \hat{q}|^2 \quad (3)$$

where  $S$  denotes the complex scattering matrix used to represent the polarization properties of the target. The assumptions in this formulation are:

- The distance between receiver and body is large compared to the wavelength and to the dimensions of the scattering body, and
- The material of the scatterer and intervening medium are such that there are linear relationships between field quantities at every point, whatever the incident field.

The scattering matrix of an arbitrary target may be expressed as a  $2 \times 2$  matrix of the form

$$S = \begin{bmatrix} \sqrt{\sigma_{HH}} e^{j\rho_{HH}} & \sqrt{\sigma_{HV}} e^{j\rho_{HV}} \\ \sqrt{\sigma_{VH}} e^{j\rho_{VH}} & \sqrt{\sigma_{VV}} e^{j\rho_{VV}} \end{bmatrix} e^{j\phi_r} \quad (4)$$

Here  $\sqrt{\sigma_{mn}}$  represents the real part of magnitude of the scattering matrix elements,  $\rho_{mn}$  denotes the associated phase, and  $\phi_r$  is a phase angle which may be ignored in the present discussion since it is a function of the separation between the radar and the target. The scattering matrix is symmetrical ( $\sqrt{\sigma_{HV}} = \sqrt{\sigma_{VH}}$  ;  $\rho_{HV} = \rho_{VH}$ ) in at least two important cases:

- Bistatic scattering when the scattering body is a perfect conductor, and
- Backscattering from an arbitrary body, consistent with the two assumptions stated previously.



Furthermore, a great simplification obtains when the target is a body of revolution. It is then possible to orient the target to present a horizontal plane of symmetry containing the line of sight, and the scattering matrix is diagonalized:  $\sqrt{\sigma_{HV}} = 0$ . Thus, for the targets considered in this report, which are bodies of revolution, we may write

$$\sigma_{\hat{t}\hat{r}} = \left[ \cos \gamma_r \quad \sin \gamma_r e^{j\beta_r} \right] \begin{bmatrix} \sqrt{\sigma_{HH}} e^{j\beta_{HH}} & 0 \\ 0 & \sqrt{\sigma_{VV}} e^{j\beta_{VV}} \end{bmatrix} \begin{bmatrix} \cos \gamma_t \\ \sin \gamma_t e^{j\beta_t} \end{bmatrix}^2 \quad (5)$$

It is evident in Equation 5 that  $\sqrt{\sigma_{HH}} e^{j\beta_{HH}}$  is the complex contribution to the radar cross section when transmitting and receiving antennas are linearly polarized with horizontal orientation (i. e.,  $\gamma_t = \gamma_r = 0$ ,  $\beta_t = \beta_r = 0$ ). Similarly,  $\sqrt{\sigma_{VV}} e^{j\beta_{VV}}$  is the corresponding quantity for the vertical polarization case. It is common practice to refer to  $\sigma_{HH}$  and  $\sigma_{VV}$  as the principal polarization radar cross sections;  $\beta_{HH}$  and  $\beta_{VV}$  are called the principal polarization scattering phases.

In the remainder of this report we work with the principal polarization radar cross sections and scattering phases. Scattering for arbitrary combinations of transmitting- and receiving-antenna polarizations may be determined from these four quantities according to Equation 5.

## 2.2 SCATTERING CENTER CONCEPT

One of the most important concepts that has been applied in recent investigations of short wavelength scattering is that the scattered fields appear to have localized sources (scattering centers) on the target. In terms of formal electromagnetic theory, each scattering center is identified with a mathematical discontinuity in the Chu-Stratton radiation integral — that is to say, with a corresponding physical location on the target at the place where the discontinuity occurs. Simplification of the scattering interaction in terms of scattering centers rests largely upon the cancellation properties of an integral with oscillating integrand and upon preservation of mathematical continuity except at the recognized geometric discontinuities. Thus, although

a surface remote from a discontinuity is assumed to produce a net contribution of zero to the total scattered field, truncation of the surface could introduce a pronounced discontinuity, and, so, generate a new scattering center. A smooth surface, then, plays a very important, although largely hidden, role in the description of the scattering interaction.

According to the scattering center concept, the field reradiated from each center on the target depends primarily upon the local dimensions and the surface conditions of the target. Secondary effects involve interactions between the various centers on the target. The first step in the analysis is to take a body of complex shape and find its individual scattering centers. Next, an analytical theory which accounts for aspect, frequency, polarization, and bistatic dependence is used to estimate the total field (primary and secondary contributions) reradiated from individual scattering centers. Finally, the vector and phasor sum of these contributions allows estimation of radar observables.

To illustrate the nature of the localization of scattering centers, let us consider monostatic scattering by a finite, right-circular cylinder. At aspect angles which exclude specular contributions, the important scattering centers are formed by the three illuminated edges. Then target scattering appears to arise from those three unshadowed points common to the extremities of the cylinder and the plane containing the axis of symmetry of the target and the radar line of sight.\* Such edge scattering centers behave in an extremely localized manner: for example, the phase associated with each scattering center behaves as if the contribution arises at a point. For aspects at which specular scattering occurs, reradiating area which is associated with the scattering center spreads laterally — because of the surface orientation relative to radar line of sight — while preserving its localization along the line of sight. Then the smooth surface which joins adjacent edge scattering centers becomes important due to reduction (and eventually disappearance, at the specular point) of the phase cancellation in the integrand of the radiation integral. Thus, for scattering by a cylinder at the broadside aspect, the singly-curved smooth cylindrical surface supports a scattering line the full length of the cylinder. Finally, lateral localization is minimal in the case

---

\* A fourth point, which is in the shadowed region of the target, also exists. It is usually much weaker than the other three.

of specular scattering by a cylinder at the axial aspects; here each point on the planar surface contributes equally to the scattered field.

According to the scattering center concept, the radar cross section of the target is given by the square of the absolute value of the complex scattering coefficient  $\sqrt{\sigma} e^{j\rho}$  which in turn is given by:

$$\sqrt{\sigma} e^{j\rho} = \sum_{i=1}^N \sqrt{\sigma_i} e^{j\rho_i} \quad (6)$$

where  $\sqrt{\sigma_i} e^{j\rho_i}$  is the complex contribution from the  $i$ th scattering center, and where there are  $N$  important scattering centers on the target. The radar cross section  $\sigma$  is given by

$$\sigma = \left| \sum_{i=1}^N \sqrt{\sigma_i} e^{j\rho_i} \right|^2 \quad (7)$$

and the scattering phase  $\rho$  is given by

$$\rho = \tan^{-1} \left\{ \frac{\sum_{i=1}^N \sqrt{\sigma_i} \sin \rho_i}{\sum_{i=1}^N \sqrt{\sigma_i} \cos \rho_i} \right\} \quad (8)$$

As demonstrated in the previous subsection, the scattering matrix of a body of revolution is known when we solve for the principal polarization values of  $\sigma$  and  $\rho$ .

The major simplification attendant upon applications of the scattering center concept is apparent in Equations 6 through 8; by treating only a small number of localized regions on the body (the discontinuities), target scattering can be estimated. Thus, the difficulty of the computation of high frequency

scattering is unrelated to the actual size of the target and depends only upon the number of important scattering centers  $N$ . Although large smooth surfaces on the target cannot be ignored when they support specular scattering, appropriate modification of scattering center formulations in these instances does not appreciably complicate the computations.

The scattering center concept is inherent in the geometrical theory of diffraction, which will be discussed in subsection 2.3. It has also proved useful as a guide to analysis: for example, Kell<sup>11</sup> was led to a proof of a bistatic-monostatic equivalence theorem based upon rigorous electromagnetic theory rather than upon physical optics as was an earlier more approximate relationship that has been frequently cited.<sup>12</sup>

The scattering center concept incorporates a powerful tool for synthesis: successful treatment of one type of center allows prediction of reradiation from similar centers located on targets of quite different shapes. Furthermore, unrelated analytical techniques may be combined to produce the optimum descriptor of scattering by a particular target.

Finally, it should be noted that the scattering center concept is not just a convenient mathematical fiction and that scattering actually does arise at the scattering centers. Returns from scattering centers are observable and coincide in position and magnitude with analytical predictions when the target is examined by a radar which transmits very short pulses.

### 2.3 GEOMETRICAL DIFFRACTION THEORY

By far the most practical of the asymptotic techniques formulated so far is the geometrical theory of diffraction developed by J. B. Keller and his associates of New York University. It has been described in a long series of papers treating various theoretical aspects of the method, the best general introduction being Keller.<sup>6</sup> Helstrom<sup>13</sup> has added an important rederivation of geometrical diffraction theory based upon Green's formulas. As stated earlier, the theory is not yet related in any precise manner to the exact asymptotic solution of Maxwell's equations, although it nevertheless gives very good results for many practical targets. Keller's approach provides the logical tool for the study of scattering centers at high frequencies.

In particular, geometrical diffraction theory provides estimates of the principal polarization values of scattering center contributions  $\sqrt{\sigma_i} e^{j\beta_i}$  introduced in the previous subsection.

Starting with geometrical optics, Keller introduced an extension of Fermat's principle that takes into account diffracted, as well as reflected, rays. The theory assumes localization of the scattering interaction at points defined by stationary phase arguments or by abrupt geometric discontinuities. It further assumes that the current distribution in the neighborhood of a scattering center is obtainable from that of a known (or solvable) case of similar geometry. A diffraction coefficient is assigned to each center based upon a known solution to a similar two-dimensional problem, and this coefficient is weighted by a divergence factor to allow treatment of three-dimensional problems. Having thus assigned a magnitude to diffracted rays, a phasor is introduced which is proportional to the distance along a ray projected from the scattering center to the radar. Incident rays which are diffracted in the direction of the receiver are termed "singly diffracted." Interaction between scattering centers is described by the mechanism of doubly and higher-order (multiply) diffracted rays. Once the complex vector fields reradiated from important scattering centers on the target are formulated, the calculation of scattering follows directly. The accuracy of results increases as the ratio of body size to wavelength increases, but they are often useful for wavelengths as large as the body.\*

The literature on geometrical diffraction theory is devoted almost entirely to analyses of scattering problems; experimental investigation of its validity has not been extensive. For right-circular cones, Keller has provided the formulation for backscattering<sup>14</sup> and has compared the results with measurement for axial incidence.<sup>15</sup> Of great interest is the ability of the theory to predict the angular dependence of an objects radar cross section. Bechtel<sup>16</sup> has compared cone results with measurements over a wide range of aspect angles and has found good agreement, except for a range of aspect

---

\*The present investigation is limited to use of the single-diffraction case. Then scattering centers should be separated by at least a few wavelengths.

angles around nose-on for vertical polarization, for which case further work has been done on this contract. Ross<sup>17</sup> has applied the method to rectangular flat plates and has shown the results to be in very good agreement with measurement data for all aspects except those within 10 degrees of grazing incidence. Ross<sup>18</sup> has investigated nonspecular scattering by a finite right-circular cylinder and has reported very good agreement between theory and monostatic measurements against aspect angle for four linear polarization combinations.

This report extends the earlier analysis of scattering by cylinders. Nonspecular scattering by cylinders, frustums, cones, and combinatorial shapes is treated using unmodified geometrical diffraction theory. In all cases, the edge scattering centers are analyzed using the diffraction coefficient obtained from the asymptotic expansion of the exact solution for the two-dimensional wedge. Modifications to geometrical diffraction theory are introduced to extend capability for specular scattering and for scattering by ring discontinuities at and near axial aspects. Formulas based upon unmodified and modified theory are derived in Appendices A through C.

### 3. OUTLINE OF TECHNICAL PROGRAM

In this section we detail the scope of the present investigation and note general comments pertaining to evaluation of analytical data.

#### 3.1 SCOPE OF INVESTIGATION

The technical program involved investigation of scattering from the following basic generic surfaces and their derivable shapes: finite, right-circular cylinders, frustums, and cones. Specific shapes, size conditions, and the desired range of calculations are listed in Table 1 along with the measured data supplied to CAL by GD/FW. The technical tasks listed in Table 1 include monostatic scattering, bistatic scattering, short pulse diagnostics, and measurements.

As part of the monostatic and bistatic scattering tasks we have developed analytical expressions which describe scattering from all shapes except the cone-cylinder-flare. These analytical expressions are used to predict principal polarization radar cross sections and scattering phases. Computer programs have been written for each of the shapes for which expressions have been developed and, excluding the hemisphere-cylinder, are such that computations are made every 0.1 degree over 360 degrees of aspect angle. In cases where bistatic predictions are required, the basic monostatic formulations have been appropriately extended.

Under short pulse diagnostics, short pulse measurement data supplied by GD/FW have been analyzed in an effort to determine secondary phenomena associated with scattering by a finite cone.

Under measurements, conventional scattering data were supplied to CAL by GD/FW. These data comprised principal polarization radar cross sections and scattering phases as functions of aspect angle for the various shapes and conditions noted in Table 1. All data were contained on magnetic tape in a format compatible with our computer requirements, and were plotted at CAL using a CALCOMP plotter.

**Table 1**  
**TECHNICAL TASKS**

| TYPE STUDY                 | SHAPES                                     | NO. OF CONDITIONS<br>SUCH AS $K_a$ , $K_h$ AND<br>CORE ANGLE                 |      |        | CALCULATIONS   |
|----------------------------|--|--|------|--------|--|
| MONOSTATIC<br>SCATTERING   | CYLINDER                                   | 3  |      |        | COMPUTATION EVERY 0.1<br>DEGREES OF ROTATION,<br>COMPUTATIONS INCLUDE<br>CR' 3 SECTION AND PHASE<br>FOR BOTH VERTICAL AND<br>HORIZONTAL POLARIZATIONS. |
|                            | CONE                                       | 3  |      |        |  |
|                            | FRUSTRUM                                   | 3  |      |        |  |
|                            | CONE-CYLINDER                              | 3  |      |        |  |
|                            | FRUSTRUM-<br>CYLINDER                      | 3  |      |        |  |
|                            | CONE-CYLINDER-<br>FLARE                    | 3  |      |        |  |
|                            | HEMISPHERE-<br>CYLINDER                    | 3  |      |        |  |
| BISTATIC<br>SCATTERING     | CYLINDER<br>FRUSTRUM<br>CYLINDER-<br>FLARE | BISTATIC ANGLES  |      | VALUES | COMPUTATIONS EVERY 0.1<br>DEGREES FOR 360 DEGREES OF<br>ROTATION. COMPUTATIONS<br>INCLUDE CROSS SECTION AND<br>PHASE FOR BOTH POLARIZATIONS.           |
|                            |  | 10.25  | 30.0 | 2      |  |
|                            |  | 10.25  | 30.0 | 2      |  |
|                            |  | 10.25  | 30.0 | 2      |  |
| SHORT PULSE<br>DIAGNOSTICS | CONE                                       | A MINIMUM OF 5<br>MEASUREMENTS MADE BY<br>GD/FW AND DATA<br>SUPPLIED TO CAL. |      |        | MEASURED DATA USED TO AID. IN<br>DEVELOPMENT OF SCATTERING<br>CENTER EXPRESSIONS.  |
| MEASUREMENTS               | ALL OF THE<br>ABOVE SHAPES                 | MEASUREMENTS MADE BY<br>GD/FW AND DATA<br>SUPPLIED TO CAL.                   |      |        | DATA USED AS AN AID IN<br>DEVELOPING ANALYTICAL<br>EXPRESSIONS AND USED TO<br>COMPARE WITH ANALYTICAL<br>RESULTS.                                      |



Values of radar cross section and scattering phase calculated from the analytical expressions derived at CAL were compared with scattering matrix measurements obtained at GD/FW. Designations and dimensions of each of the basic generic shapes examined in this study are given in Table 2. The nominal operating frequency was 6 GHz, which means that the minimum dimension of any target was about 1.5 wavelengths. Scattering by the simple shapes described in Table 2, and by various combinations of these shapes, is examined in Section 4.

**Table 2**  
**DIMENSIONS OF GENERIC SHAPES**

| MODEL TYPE | DESIGNATION | MAX. DIA.<br>(INCHES) | MIN. DIA.<br>(INCHES) | LENGTH<br>MAX.<br>(INCHES) | LENGTH<br>MIN.<br>(INCHES) |
|------------|-------------|-----------------------|-----------------------|----------------------------|----------------------------|
| CYLINDER   | Cy3         | 6.320                 | -                     | 10.513                     | -                          |
|            | Cy4         | 4.892                 | -                     | 8.000                      | -                          |
|            | Cy5         | 7.500                 | -                     | 17.260                     | -                          |
|            | Cy6         | 15.736                | -                     | 44.320                     | -                          |
| CONE       | C1          | 6.320                 | 0                     | 11.783                     | -                          |
|            | C2          | 6.320                 | 0                     | 15.814                     | -                          |
|            | C4          | 7.500                 | 0                     | 13.983                     | -                          |
| FRUSTRUM   | F3          | 7.500                 | 6.320                 | 3.358                      | -                          |
|            | F4          | 6.320                 | 4.892                 | 4.063                      | -                          |
|            | F5          | 7.500                 | 4.892                 | 7.421                      | -                          |
| HEMISPHERE | H3          | 6.320                 | -                     | 3.160                      | -                          |

### 3.2 DATA COMPARISON PROCEDURE

Prior to comparing theory and measurement, it is instructive to comment upon certain characteristics which are common to evaluation studies. These comments are noted below in separate discussions of plots of radar cross section and scattering phase. Problems encountered in plotting measurement data from magnetic tapes are discussed at the end of this subsection.

### 3.2.1 Radar Cross Section Data

Comparison of theoretical and experimental radar cross section data is straightforward: all plots present radar cross section (dBsm) versus aspect angle (degrees). The method of selecting the measurement data for comparison with theory may be illustrated by the case of a cylinder target. Theory predicts identical dependence of a cylinder's radar cross section in the aspect intervals  $0 \leq \phi \leq 90$ ,  $0 \leq \phi \leq -90$  degrees, where  $\phi = 0$  denotes axial incidence. Similar data obtained experimentally exhibit a high degree of correspondence but do not completely agree due to measurement errors. We have plotted measurement data for both aspect intervals and have utilized that section of the experimental results which compares most favorably with theory. Since the comparison plots show theory superimposed directly upon computer plots of measured data, the particular choice of aspect interval made in each case is apparent. Notice that agreement between theoretical and measured depths of nulls may be influenced by measurement capability: The minimum value of experimental results obtained from GD/FW is approximately -40 dBsm.

### 3.2.2 Scattering Phase Data

Although scattering phase is calculated and measured modulo  $2\pi$ , it was decided that plots of the cumulative value of scattering phase were more desirable. The advantages of the latter format are clear representation of the phenomenon and the ability to correct for that component of measured phase associated with the separation between radar and target.\* Towards this end, subroutines have been developed for accumulating scattering phase, both from the theoretical calculations and from the measured data. The resultant phase plots show the cumulative scattering phase (radians) versus aspect angle (degrees). Since the absolute value of scattering phase is unimportant, and since it determines the level of the phase progression with aspect angle, theory and measurement are compared by appropriate shifting of levels. As in the case of radar cross section plots, that section of the

---

\*This is the component phase  $\phi_r$  extracted from the scattering matrix in Equation 4 of subsection 2.1.

aspect angle plot of measured phase which agrees most favorably with theory has been chosen for purposes of comparison.

Comparison of theoretical and experimental scattering phase data is not straightforward due to two complications. One complication is associated with the basic scattering mechanism: it is a characteristic of scattering phenomena that the major changes in scattering phase occur simultaneous with minima in the level of the scattered signal (i. e., when nulls occur in the radar cross section record). Such behavior can be expected to perturb experimental estimates of scattered phase, especially for the horizontal polarization case where extremely deep cross section nulls are observed. However, theoretical predictions appear to be sensitive to the same characteristic. Mr. John C. Cleary of RADC has employed our formulation to predict cylinder's scattering phase using 0.01 degree increments in aspect angle. When his values of scattering phase were compared with corresponding results obtained at CAL (here using 0.1 degree increments in aspect angle), he observed that the direction of accumulation of the horizontal polarization scattering phase is opposed in at least one aspect region! Investigation of this behavior lay outside the scope of the present investigation.

The association of rapid phase change -- generally by either  $\pm \pi$  or 0 radians -- with passage through a null in the radar cross section pattern also stresses the importance of otherwise negligible gradients in electromagnetic field along the line of sight of the radar used for measurement. The null arises by virtue of the more-or-less exact balance between two oppositely phased field contributions from interfering scattering centers; the phase of each center is changing smoothly and continuously as the aspect angle changes, and the rates of phase change for the two centers are different. Whether there will be an abrupt change by  $\pi$  radians or an abrupt change but returning to the previous mean phase curve will depend solely upon which of the two nearly equal centers is the stronger. Therefore, a small local anomaly in field intensity can alter this phase progression very markedly.

An estimate of this effect can readily be made by observing that the depth of null is an index of the relative strength of centers. Thus, a -40 dB null is produced by two centers which differ by only 1/6 dB; a -30 dB null

represents two centers differing by 1/2 dB; and a -20 dB null represents two centers differing by 1.8 dB. If there are small differences — due to background scattering, or even simply 1/R field gradients — of 1/2 dB or more over the test region occupied by the target, we may expect experimental phase errors when 30 dB nulls occur.

A second complication in the comparison of predicted and measured scattering phases is related to the accuracy to which the phase reference chosen for measurement is positioned with respect to the center of rotation of the target. Figure 1 illustrates the problem. The center of mass of the cylinder has been chosen as the reference for phase measurements (Point B). This phase reference is shown displaced a distance  $R$  from the center of rotation of the target (Point A), and the line AB makes an angle  $\xi$  with the aspect angle corresponding to -180 degrees. If  $R$  is not zero, the phase progressions measured in the aspect intervals  $0 \leq \phi \leq -180$ ,  $0 \leq \phi \leq 180$  will not match except at the end points.\* The two sets of phase data will follow different slopes, with the true value of the scattering phase being the arithmetic mean between corresponding values in each set. Mr. W.P. Cahill of GD/FW has supplied estimates of the two-way electrical path length ( $2kR$ ) in degrees and the initial angular parameter  $\xi$  in degrees for each target examined in this report. His data are tabulated in Table 3. No attempt to remove the bias from phase measurements has been performed. We simply note that large values of  $2kR$  will result in cumulative displacement between theoretical and measured values of scattering phase.

---

\*Also, if  $R$  is not zero and  $\xi$  is not 0 or 180 degrees, there will exist a sinusoidal discrepancy between cylinder's aspect angle and the aspect registry assigned according to turntable rotation. However, this effect is believed to be negligible for the  $R$  values associated with present measurement data.

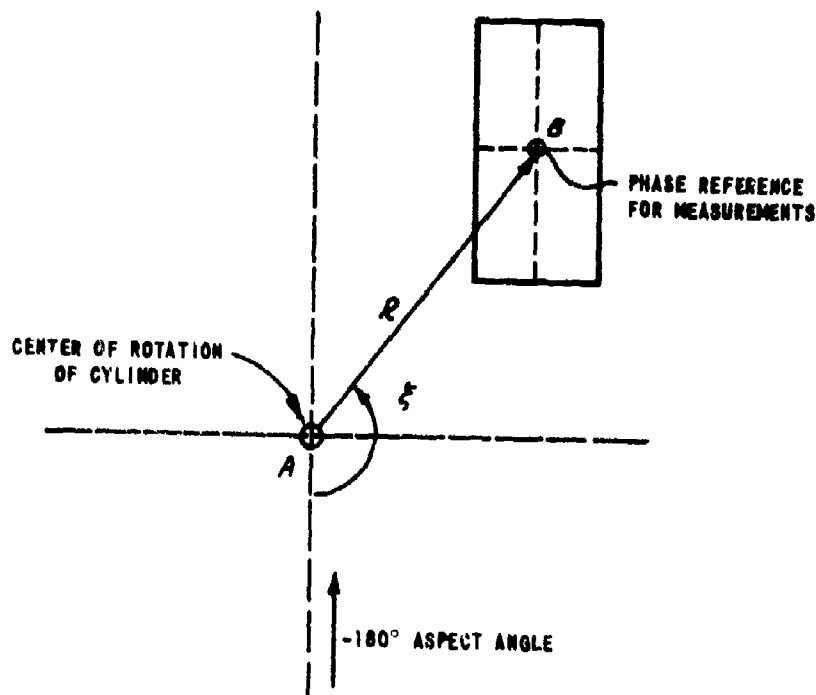


Figure 1 TARGET PHASE REFERENCE -- CENTER OF ROTATION GEOMETRY

Finally, in view of the complications attendant upon the comparison of phase data, we apply the following criterion. Theoretical and measured values of vertical polarization phase are considered to agree if the fine structures of phase variations correspond, and if the curves overlay to within a slope factor consistent with offset errors indicated by parameters introduced in Table 3. The horizontal polarization case is more critical; here we consider theory to be accurate if it agrees with measurements after vertical displacements between the two sets of phase data have been ignored.

**Table 3**  
**PARAMETERS DEFINING PHASE RESIDUALS**

| DESIGNATION | FREQUENCY<br>(GHz) | PISTATIC<br>ANGLE<br>(DEGREES) | $\xi$<br>(DEGREES) | $2kR$<br>(DEGREES) |
|-------------|--------------------|--------------------------------|--------------------|--------------------|
| CY3         | 5.975              | 0                              | 138.5              | 75                 |
| CY5         | 6.0                | 0                              | 234.5              | 248                |
|             | 5.885              | 10.25                          | 97.8               | 81                 |
|             | 6.050              | 30                             | 245.3              | 7                  |
|             | 6.0                | 0                              | 339.4              | 242                |
| CY6         | 5.885              | 10.25                          | 182.5              | 81                 |
|             | 6.050              | 30                             | 76.9               | 137                |
|             | 6.0                | 0                              | 214.4              | 295                |
| C1          | 6.0                | 0                              | 2.4                | 593                |
| C2          | 6.0                | 0                              | 177.4              | 839                |
| C4          | 5.975              | 0                              | 116.5              | 185                |
| F3          | 6.0                | 0                              | 31.4               | 330                |
|             | 5.885              | 10.25                          | 37.0               | 67                 |
|             | 6.050              | 30                             | 65.1               | 66                 |
|             | 6.0                | 0                              | 20.3               | 336                |
| F5          | 5.885              | 10.25                          | 163.9              | 175                |
|             | 6.050              | 30                             | 216.4              | 18                 |
|             | 6.0                | 0                              | 97.3               | 83                 |
| F4CY3       | 5.975              | 0                              | 0                  | 483                |
| CY4F4       | 5.885              | 10.25                          | 180                | 7                  |
|             | 6.050              | 30                             | 37.8               | 125                |
| C2CY3       | 5.975              | 0                              | 225.8              | 209                |
| C4CY5       | 6.0                | 0                              | 90.0               | 90                 |
| H3CY3       | 5.975              | 0                              |                    |                    |

### 3.2.3 Discussion of Magnetic Tapes

We note two limitations to the program specified in Table 1 due to problems with tapes containing measurement data. Altogether, eight magnetic tapes were received at CAL under this program. The designations of these tapes are 062566, 062563, 062680, 064216, 064389, 065501, 065979, and 965979. Of these eight tapes, three were of no use. Tapes 062563 and 065979 were recalled due to errors in measurement data. Much of the data on tape 062563 was repeated and made available in other tapes. Tape 965979 was sent to replace tape 065979. However, the CAL computer system would not allow extraction of measurement data from tape 965979 in the conventional manner, and plots of data were not obtained in this case.

Because of the recall of tape 062563, monostatic theory and measurement can only be compared for one frustum-cylinder instead of three (see Table 1 under monostatic study). However, bistatic measurement data were available, and these additional data were examined in the comparison of frustum-cylinder theory with experiment (see Table 7 of subsection 4.4.2). The bistatic study of the cylinder-flare calls for investigations of two models. However, measurement data were received for only one. Further, study of monostatic scattering by the hemisphere-cylinder calls for measurement data taken on three models; again, experimental results were received for one target.

A second problem with magnetic tapes was encountered when plots of these data were constructed. In a few isolated instances, the plotting program generated an error message which indicated that measurement data were not stored on the tape in the proper format. In these instances, we simply present theoretical estimates of scattering matrix parameters.

Certain difficulties can be expected in any program which includes experimental results. The overall consistency of measurement data received from GD/FW by CAL is considered exceptional, and we feel that the problems discussed above do not limit the goal of the present program.

#### 4. ANALYTICAL RESULTS AND COMPARISON WITH EXPERIMENT

This section contains the comparison of theory and measurement for cylinders, frustums, cones, frustum-cylinders, cylinder-flares, cone-cylinders, and the hemisphere-cylinder. The number of targets examined in each case is as specified in Table 1, subject to limitations noted in subsection 3.1 and 3.2.3. All targets are constructed from the simple shapes having designations and dimensions given in Table 2 of subsection 3.1.

For each of the above targets we present analytical formulations, compare predicted and measured values of principal polarization radar cross sections and cumulative scattering phases, and comment on the agreement obtained. To avoid repetition, we explain the polarization convention and the angular limits on scattering center contributions in the discussion of the cylinder only; these same observations apply for all other targets examined in this section.



## 4.1 CYLINDER

### 4.1.1 Analytical Formulation

According to theoretical considerations discussed in Section 2, the radar cross section  $\sigma$  and the scattering phase  $\rho$  of a finite, right-circular cylinder are given by

$$\sigma = \left| \sum_{i=1}^4 \sqrt{\sigma_i} e^{j\rho_i} \right|^2 \quad (9)$$

and

$$\rho = \tan^{-1} \left\{ \frac{\sum_{i=1}^4 \sqrt{\sigma_i} \sin \rho_i}{\sum_{i=1}^4 \sqrt{\sigma_i} \cos \rho_i} \right\} \quad (10)$$

where  $\sqrt{\sigma_i} e^{j\rho_i}$  is the complex contribution from the  $i^{\text{th}}$  scattering center on the target, and there can be four important scattering centers on a cylinder. Appendix A contains the detailed derivation of fields reradiated from the four scattering centers (edges) on a cylinder based upon the single-diffraction version of geometrical diffraction theory. These expressions exhibit dependence upon cylinder's dimensions and aspect angle, and radar's frequency, polarization and bistatic configuration. Thus, they are suited to prediction of the bistatic scattering matrix of a cylinder.

Figure 2 shows the location of scattering centers  $S_1$  through  $S_4$ , cylinder geometry, the aspect angle  $\phi$ , and the azimuth component of the bistatic angle  $\beta_a$ . Target symmetry permits restricting treatment of aspect dependent scattering to the limited angular interval  $0 \leq \phi \leq \frac{\pi}{2}$ . Summarizing the analysis of nonspecular scattering presented in subsections A.1 through A.4 of Appendix A, we obtain scattering center amplitudes:

$$\sqrt{\sigma_i} = \frac{2}{3} \sin\left(\frac{2\pi}{3}\right) \sqrt{\frac{a}{k \cos \beta_a \sin \phi}} \left[ \left\{ \cos\left(\frac{2\pi}{3}\right) - \cos\left(\frac{\pi + 2\phi}{3/2}\right) \right\}^{-1} \left\{ \cos\left(\frac{2\pi}{3}\right) - \cos\left(\frac{2\beta_a}{3}\right) \right\}^{-1} \right] \quad (11)$$

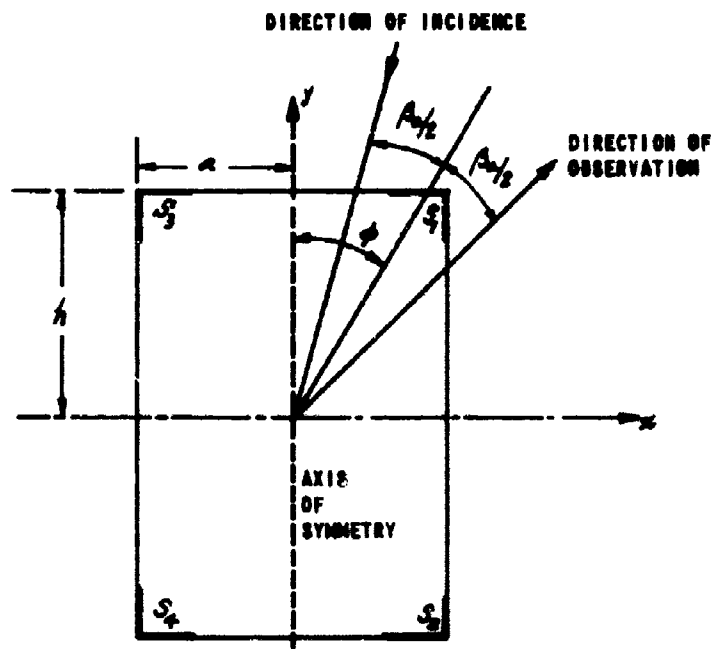


Figure 2 SCATTERING CENTERS ON A CYLINDER

$$\sqrt{\sigma_2} = \frac{2}{3} \sin\left(\frac{2\pi}{3}\right) \sqrt{\frac{a}{k \cos \beta_{0/2} \sin \phi}} \left[ \left\{ \cos\left(\frac{2\pi}{3}\right) - \cos\left(\frac{4\phi}{3}\right) \right\}^{-1} \mp \left\{ \cos\left(\frac{2\pi}{3}\right) - \cos\left(\frac{2\beta_0}{3}\right) \right\}^{-1} \right] \quad (12)$$

$$= 0; \phi < \beta_0/2$$

$$\phi \geq \beta_0/2$$

$$\sqrt{\sigma_3} = \frac{2}{3} \sin\left(\frac{2\pi}{3}\right) \sqrt{\frac{a}{k \cos \beta_{0/2} \sin \phi}} \left[ \left\{ \cos\left(\frac{2\pi}{3}\right) - \cos\left(\frac{\pi-2\phi}{3/2}\right) \right\}^{-1} \mp \left\{ \cos\left(\frac{2\pi}{3}\right) - \cos\left(\frac{2\beta_0}{3}\right) \right\}^{-1} \right] \quad (13)$$

$$= 0; \phi > \frac{\pi}{2} - \frac{\beta_0}{2}$$

$$\phi \leq \frac{\pi}{2} - \frac{\beta_0}{2}$$

$$\sqrt{\sigma_4} = \frac{2}{3} \sin\left(\frac{2\pi}{3}\right) \sqrt{\frac{a}{k \cos \beta_{0/2} \sin \phi}} \left[ \left\{ \cos\left(\frac{2\pi}{3}\right) - \cos\left(\frac{\pi+2\phi}{3/2}\right) \right\}^{-1} \mp \left\{ \cos\left(\frac{2\pi}{3}\right) - \cos\left(\frac{4\pi}{3} - \frac{2\beta_0}{3}\right) \right\}^{-1} \right] \quad (14)$$

$$= 0; \frac{\beta_0}{2} < \phi < \frac{\pi}{2} - \frac{\beta_0}{2}$$

$$\frac{\pi}{2} - \frac{\beta_0}{2} \leq \phi \leq \frac{\beta_0}{2}$$

and scattering center phases:

$$\rho_1 = \frac{\pi}{4} - 2(k \cos \beta/2) [a \sin \phi + h \cos \phi] \quad (15)$$

$$\rho_2 = \frac{\pi}{4} - 2(k \cos \beta/2) [a \sin \phi - h \cos \phi] \quad (16)$$

$$\rho_3 = -\frac{\pi}{4} + 2(k \cos \beta/2) [a \sin \phi - h \cos \phi] \quad (17)$$

$$\rho_4 = -\frac{\pi}{4} + 2(k \cos \beta/2) [a \sin \phi + h \cos \phi] \quad (18)$$

where

$a$  is the radius of the cylinder

$h$  is the half-height of the cylinder

$\phi$  is an equivalent azimuth aspect angle defined to be the angle between the axis of symmetry of the cylinder and the bistatic angle  $\beta$

$\beta$  is the bistatic angle between transmitting and receiving directions

$\beta_a$  is the projection of  $\beta$  in the plane containing the axis of symmetry of the target and the direction of the angle  $\phi$

and

$k$  is the wave number ( $= 2\pi/\lambda$ ).

Numerical subscripts used in Equations 11 through 18 refer to scattering centers illustrated in Figure 2. Dependence upon polarization is contained in the choice of signs in Equations 11 through 14. The upper signs are used for vertical polarization ( $E$  vectors associated with corresponding incident and scattered fields lie perpendicular to the azimuth ( $x-y$ ) plane), and the lower signs are used for horizontal polarization ( $E$  vectors lie in the azimuth plane). The angular restrictions on Equations 12 through 14 are a consequence of a single-diffraction analysis:

individual scattering centers contribute to the total (singly-diffracted) scattered field only when they are directly illuminated by the transmitter and directly observed by the receiver.

Notice the presence of singularities in Equations 11 through 14 at aspect angles which produce specular scattering ( $\phi = 0, \pi/2$ ) and in the forward scattering bistatic case ( $\beta = \beta_s = \pi$ ). Modification of geometrical diffraction theory has been effected for specular scattering. These analyses are detailed in subsection A.5 of Appendix A; only the results are given below.

At and near axial aspects, the polarization-independent contribution from scattering centers  $S_1$  and  $S_3$  accounts for the specular return. We denote this component by the expression  $(\sqrt{\sigma_1} e^{jP_1} + \sqrt{\sigma_3} e^{jP_3})_{pol}$ . According to the small angle analysis performed in subsection A.5.3 of Appendix A, we have

$$(\sqrt{\sigma_1} e^{jP_1} + \sqrt{\sigma_3} e^{jP_3})_{pol} = 2\sqrt{\pi} k \cos \beta/2 a^2 \frac{J_1(2ka \cos \beta/2 \sin \phi)}{(2ka \cos \beta/2 \sin \phi)} e^{-j\pi/2 - j2kh \cos \beta/2 \cos \phi} \quad (19)$$

where  $J_1$  is the first order Bessel function. Equation 19 has  $J_1(x)/x$  dependence, as does the physical optics result. Further, evaluation of the specular contribution at the axial aspect ( $\phi = 0$ ) gives

$$\sigma(\phi=0) = \frac{4\pi a^4}{\lambda^2} \cos^2 \beta/2 \quad (20)$$

and the monostatic form of Equation 20 agrees with the physical optics formula for scattering by a circular disc.<sup>19</sup> Thus, use of Equation 19 to describe the specular contribution from centers  $S_1$  and  $S_3$  at and near axial aspects eliminates two singularities contained in the scattering center description of reradiation. We remove the remaining singularities in Equations 11 through 17 by introducing the following constraint

$$\csc \phi \leq ka \cos \beta/2 \quad (21)$$

This constraint insures that the total contribution from scattering center  $S_2$  and the polarization-dependent contributions from centers  $S_1$  and  $S_3$  are finite. It also results in a formulation that predicts polarization-dependent scattering at the axial aspect, which behavior is known to be incorrect. However, the inclusion of polarization-dependent terms is necessary to achieve continuity in scattering predictions. The fact that the proper polarization dependence is not incorporated in the formulation is of little practical consequence; the specular contribution of Equation 19 is the major scattering contribution at and near axial aspects and it completely masks the secondary effects associated with polarization-dependent terms. It remains to determine the range of aspects in which the modification to the theory represented by Equation 19 is to be applied. Estimates of scattering by cylinders are found to be continuous in aspect angle when we use Equation 19 in the angular interval  $0 \leq \phi \leq \phi_{ca}$ , where  $\phi_{ca}$  denotes the axial "crossover" aspect angle given by the relation

$$2ka \sin \phi_{ca} = 2.44 \quad (22)$$

For  $\phi > \phi_{ca}$  we employ the scattering center description based upon unmodified geometrical diffraction theory (Equations 11 through 18).

At and near the broadside aspect, the polarization-independent contribution from scattering centers  $S_1$  and  $S_2$  should account for the specular return. We denote this component by the expression  $(\sqrt{\sigma_1} e^{j\rho_1} + \sqrt{\sigma_2} e^{j\rho_2})_{poli}$ . According to small angle analyses performed in subsection A.5.2 of Appendix A, we have

$$(\sqrt{\sigma_1} e^{j\rho_1} + \sqrt{\sigma_2} e^{j\rho_2})_{poli} = -\sqrt{2k \cos \beta/2} \cdot 2h \frac{\sin(2kh \cos \beta/2 \cos \phi)}{(2kh \cos \beta/2 \cos \phi)} \times e^{+j\frac{3\pi}{4} - j2ka \cos \beta/2 \sin \phi} \quad (23)$$

Again the  $\sin \alpha/2$  dependence in Equation 23 is common with the physical optics solution of the corresponding problem. At the broadside aspect ( $\phi = \pi/2$ ), radar cross section predicted by Equation 23 is

$$\sigma(\phi = \pi/2) = ka (2h)^2 \cos \beta/2 \quad (24)$$

Setting  $\beta = 0$  in Equation 24 we duplicate the well-known monostatic result based upon physical optics.<sup>19</sup> Modification of geometrical diffraction theory for the specular contribution alone is sufficient at and near broadside aspects. Estimates of scattering are found to be continuous with aspect angle when we employ Equation 23 in the aspect interval  $\phi_{cb} \leq \phi \leq \pi/2$ . Here  $\phi_{cb}$  is the broadside "crossover" aspect angle given by the relation

$$2kh \cos \phi_{cb} = 2.25 \quad (25)$$

In summary, Equations 11 through 18 describe cylinder's scattering according to the single diffraction representation of unmodified geometrical diffraction theory. They apply in the limited aspect interval  $\phi_{ca} < \phi < \phi_{cb}$  where the crossover aspects are defined by Equations 22 and 25. For scattering at and near the axial aspect ( $0 \leq \phi \leq \phi_{ca}$ ) we modify the theory according to the specular formulation of Equation 19 and introduce the constraint of Equation 21. Similarly, for scattering at and near the broadside aspect ( $\phi_{cb} \leq \phi \leq \pi/2$ ) we modify the theory according to Equation 23. The resultant description of cylinder's scattering was programmed for the IBM 360 and GE 635 digital computers. Computations were performed in the aspect interval  $0 \leq \phi \leq \pi/2$  at 0.1 degree increments in aspect angle.

We next compare the analytical formulation with measurement data.

#### 4.1.2 Results

Table 4 lists the designations of three cylinders used in the evaluation of cylinder theory. The table includes the dimensions of each target, the operating frequency, and the bistatic angle. The number of individual targets and bistatic situations listed are as specified in Table 1.

**Table 4**  
**PARAMETERS FOR CYLINDER STUDY**

| MODEL<br>DESIGNATION | DIMENSIONS (INCHES) |             | FREQUENCY<br>(GHz) | BISTATIC ANGLE $\phi_a$<br>(DEGREES) |
|----------------------|---------------------|-------------|--------------------|--------------------------------------|
|                      | DIAMETER (2a)       | LENGTH (2h) |                    |                                      |
| CY3                  | 6.320               | 10.513      | 5.975              | 0                                    |
| CY5                  | 7.500               | 17.260      | 6.000              | 0                                    |
|                      |                     |             | 5.885              | 10.25                                |
|                      |                     |             | 6.050              | 30.0                                 |
| CY6                  | 15.736              | 44.320      | 6.000              | 0                                    |
|                      |                     |             | 5.885              | 10.25                                |
|                      |                     |             | 6.050              | 30.0                                 |

A comprehensive discussion of results obtained for cylinder CY3 follows; This is intended to serve as background for limited discussion of other targets, where only major points are noted.

Figures 3 through 6 compare theoretical predictions with experimental estimates of parameters which describe the scattering matrix of cylinder CY3. Figure 3 shows the variation of radar cross section with aspect angle when the transmitting- and receiving-antennas are vertically polarized. The predicted lobe structure (dashed curve) faithfully duplicates experimental results (solid curve). Although some disagreement in the patterns is observed at intermediate aspect angles ( $40 < \phi < 55$  degrees), it is known that vertical polarization measurement data are most sensitive in the same aspect interval.\* Specular lobes are reasonably well predicted both in magnitude and angular width. In general, measured nulls are deeper than theoretical nulls, and measured peaks are somewhat lower than

---

\*When vertical polarization measurement data obtained in the equivalent aspect regions  $0 \leq \phi \leq -\pi/2$ ,  $0 \leq \phi \leq \pi/2$  are compared for consistency, observed discrepancies are greatest at intermediate aspects.

predictions. Figure 4 shows corresponding data for the horizontal polarization case. Better agreement between theory and measurement is observed. Notice that theoretical nulls may extend below the lowest measurable radar cross section (approximately -42 dBsm). The three solid vertical lines which terminate at the top of Figure 4 at aspect angles  $\phi \approx 68, 73$ , and  $74$  degrees correspond to measurement errors. Such errors usually are associated with measurements obtained at low signal level. Figure 5 compares predicted and measured estimates of the cumulative value of scattering phase. Agreement is good out to  $\phi = 73$  degrees, at which aspect the experimental curve is abruptly displaced by about 5 radians. This discontinuity illustrates the effect of a bad data point upon the logic employed in accumulating phase data. In such instances, one should ignore the displacement and compare the shapes of ensuing phase progressions. With this provision, agreement is good over all aspects. Figure 6 compares corresponding data for the horizontal polarization case. Analysis and experiment are in close agreement except at the isolated aspect angle  $\phi \approx 69$  degrees, where the directions of phase accumulation are opposed. As stated in subsection 3.2.2, either measurement or theoretical calculation could be correct, since the difference between them is  $2\pi$  radians, and both methods report data modulo  $2\pi$ . If one ignores the displacement between theoretical and measured scattering phases for  $\phi = 69$  degrees, close correspondence of aspect dependence is observed. The very rapid phase change occurring near  $\phi = 69$  degrees need to be followed more closely to resolve this ambiguity.

Monostatic results for cylinder CY5 are presented in Figures 7 through 10. In general, theoretical estimates of the principal polarization radar cross section tend to be higher than corresponding measurement data (see Figures 7 and 8).<sup>\*</sup> Vertical polarization phase

<sup>\*</sup>The accuracy of geometrical diffraction theory should increase with an increase in the size of the target in wavelengths, so that better agreement should be obtained for CY5 than for CY3. Since this is not the case, we compared monostatic and bistatic measurements of the radar cross section of CY5 (see Figures 11, 12, 15, and 16 for these latter data). The major effect of bistatic operation should be a shift in lobe position, the lobe amplitudes remaining essentially constant. In the case of CY5, comparison of measurements suggests that the monostatic experimental data are low in the region of intermediate aspect angles.



data show good correspondence and, neglecting displacements, the same is true for horizontal polarization phase data. Bistatic results for CY5 are given in Figures 11 through 14 for  $\beta_a = 10.25$  degrees. It is seen that theory provides very good estimates of parameters describing the scattering matrix. The disagreement between predicted and measured phase slopes for vertical polarization is probably due to the center-of-rotation offset error discussed in subsection 3.2.2. Figures 15 through 18 represent corresponding data for CY5 with  $\beta_a = 30.0$  degrees. Again, theory and measurement are in very close agreement.

Monostatic results for cylinder CY6 are shown in Figures 19 through 22. Due to the complexity of radar cross section patterns for this large a target, the comparison procedure for radar cross section is changed in favor of a vertical displacement format. Measured data constitute the upper curve, with theoretical data presented below. We employ a uniform shift of 20 dB in all cases. The resulting comparison of radar cross sections indicates gross agreement is good. Vertical polarization phases agree except for a slope factor related to center-of-rotation offset error. The disagreement between horizontal polarization phases reflects the complexity of the phase behavior; however, the basic shapes of each pattern, when compared segment by segment, show considerable similarity. Bistatic results for CY6 with  $\beta_a = 10.25$  degrees are given in Figures 23 through 26. Good agreement between theory and measurement is evidenced. Corresponding data for  $\beta_a = 30.0$  degrees are given in Figures 27 through 30. Here predicted and measured radar cross sections are in excellent agreement based upon independent overlay of results. Vertical polarization phase data suggest the presence of offset error. Horizontal polarization phase data agree very well for  $0 < \phi < 40$  degrees, at which aspect displacement is observed.

#### 4.1.3 Remarks

Results presented in Figures 3 through 30 establish confidence in geometrical diffraction theory for predicting the bistatic scattering matrix of a finite, right-circular cylinder. Modifications to the theory for specular scattering have been performed satisfactorily, and the assigned values of cross-over aspect angles appear to have general application. The very rapid phase changes associated with horizontal polarization data need to be followed more closely to resolve ambiguities between theory and measurement.

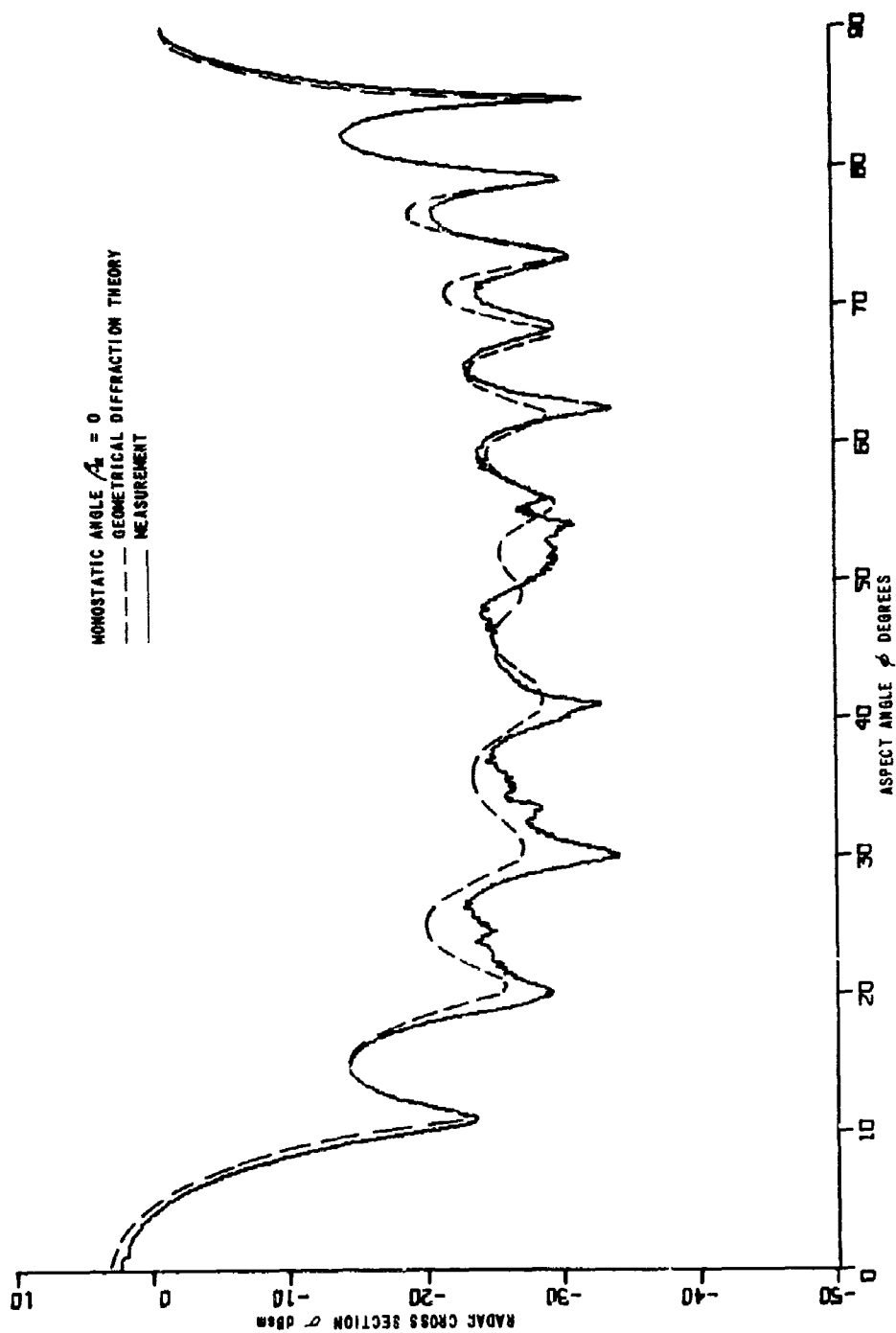


Figure 3 VERTICAL POLARIZATION RADAR CROSS SECTION. CYLINDER CYS, MONOSTATIC

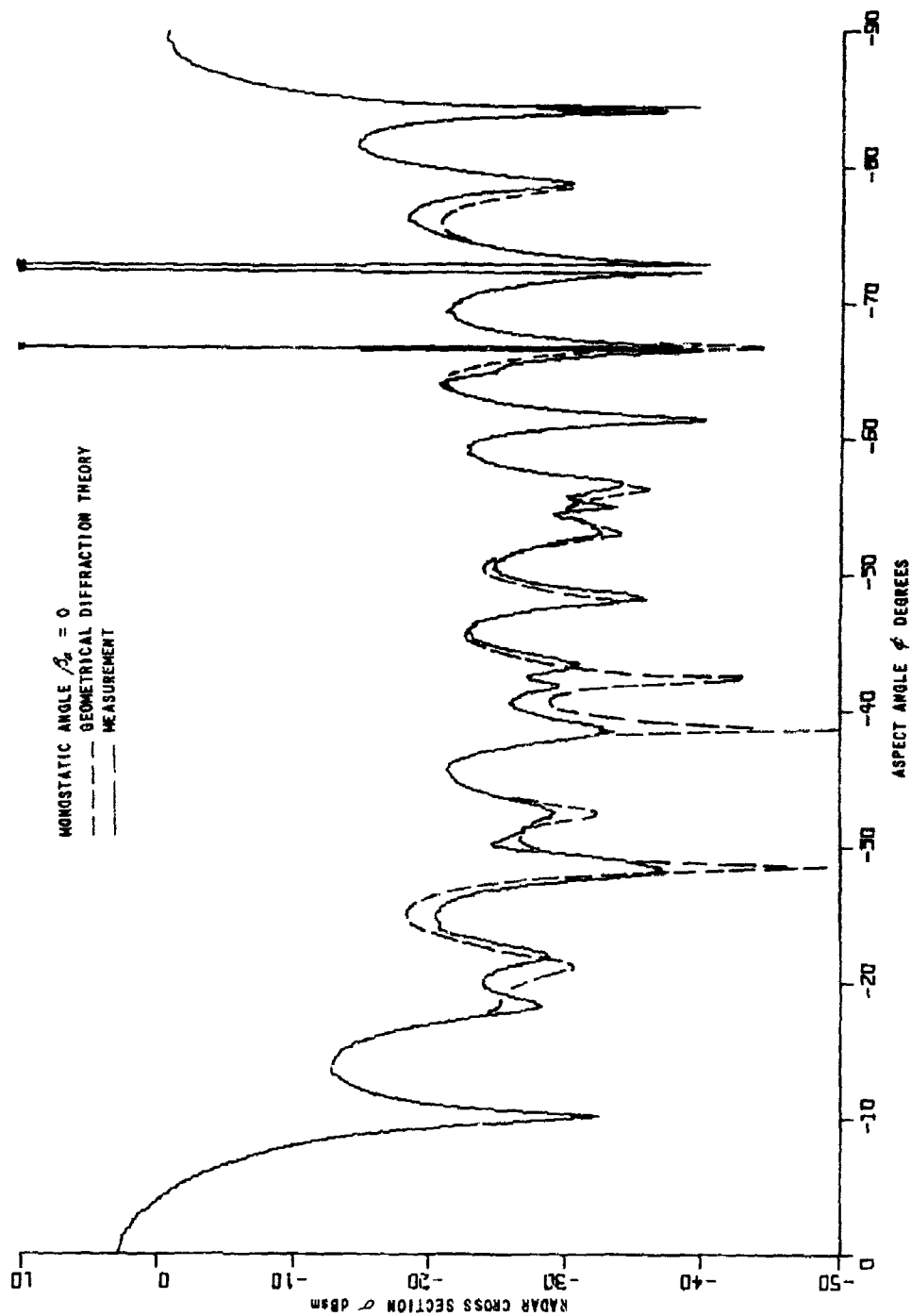


Figure 4 HORIZONTAL POLARIZATION RADAR CROSS SECTION. CYLINDER CV3, MONOSTATIC

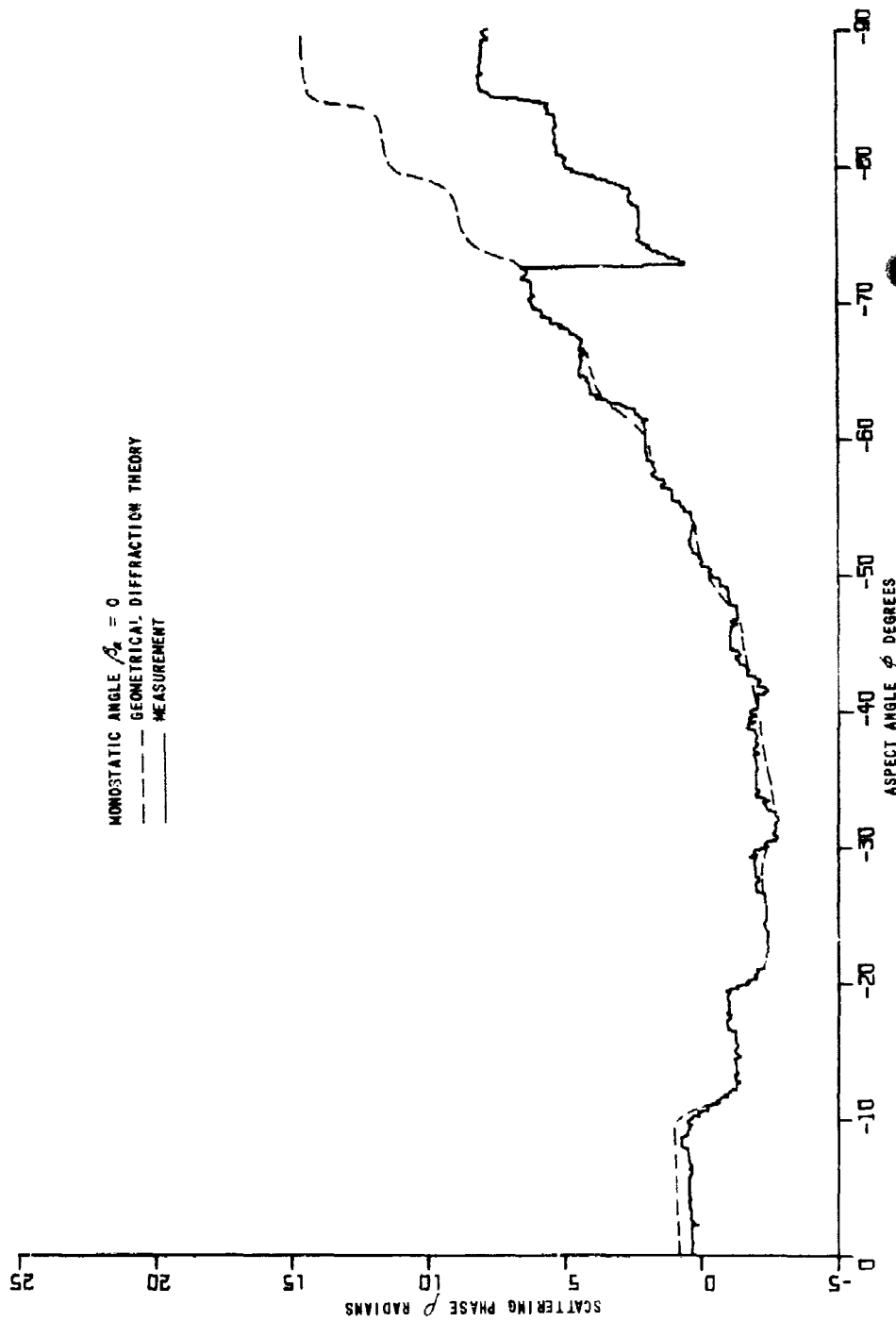


Figure 5 VERTICAL POLARIZATION SCATTERING PHASE. CYLINDER CY3, MONOSTATIC

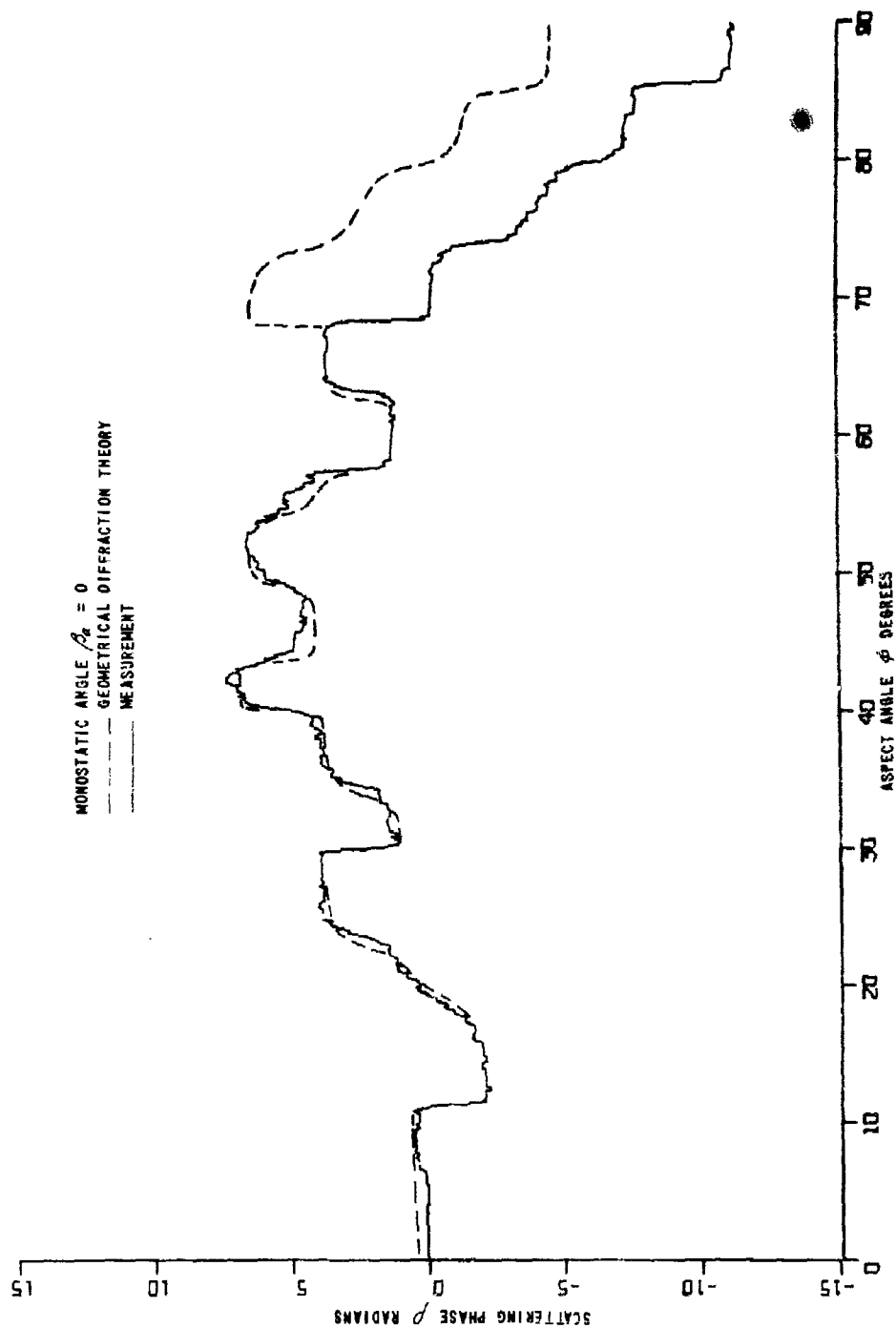


Figure 6 HORIZONTAL POLARIZATION SCATTERING PHASE. CYLINDER CY3, MONOSTATIC

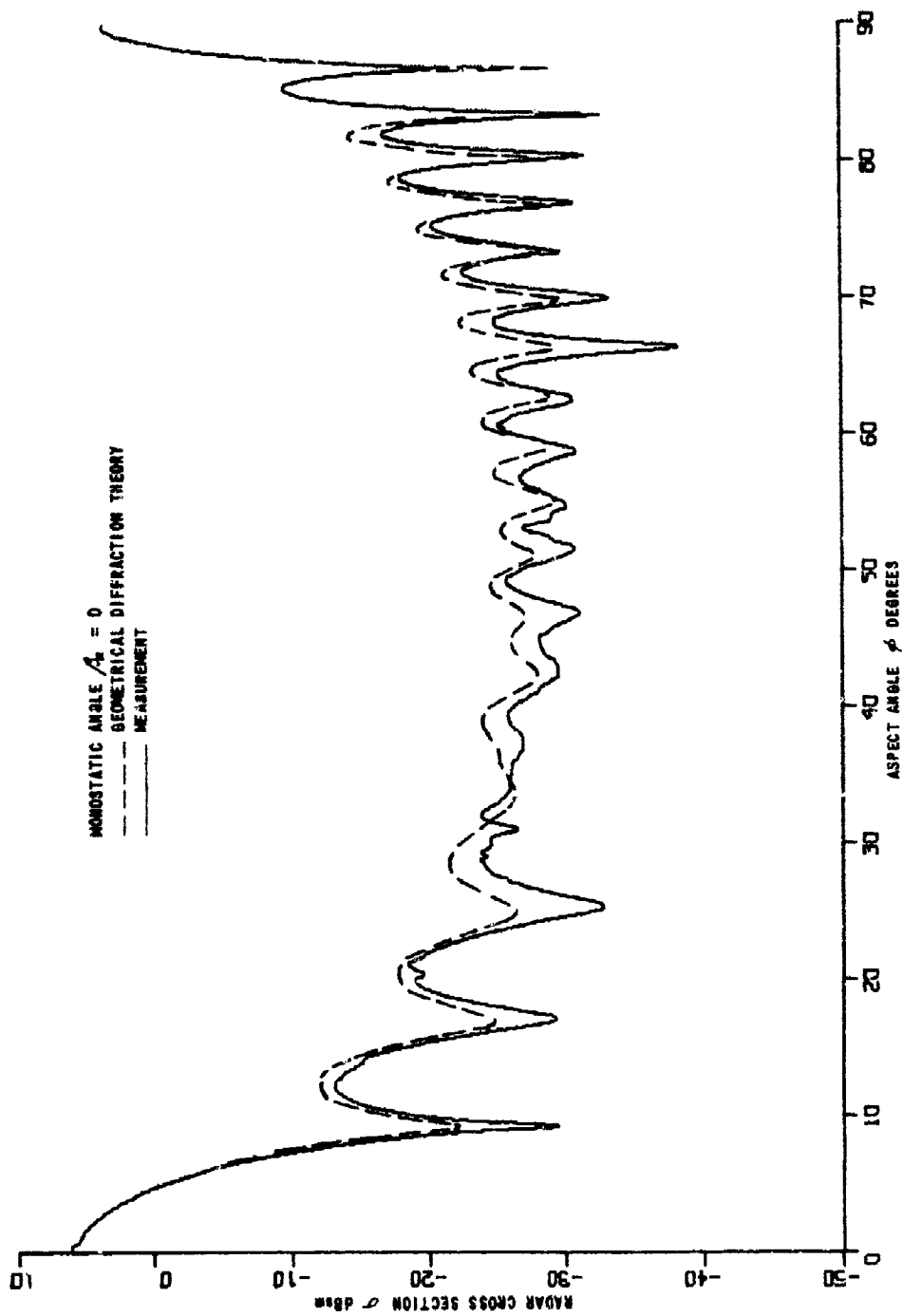


Figure 7 VERTICAL POLARIZATION RADAR CROSS SECTION. CYLINDER CYS. MONOSTATIC

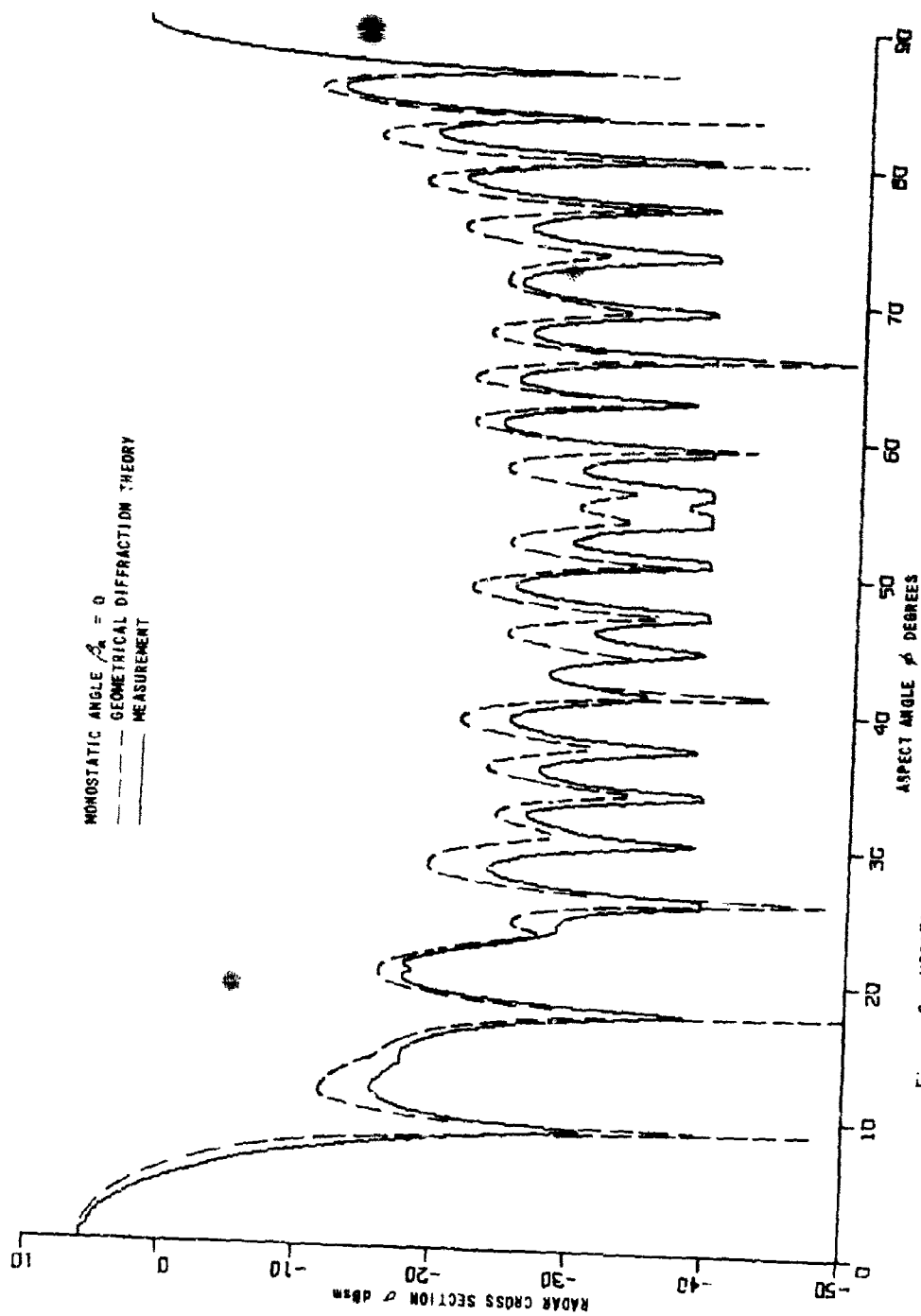


Figure 8 HORIZONTAL POLARIZATION RADAR CROSS SECTION. CYLINDER CYS, MONOSTATIC

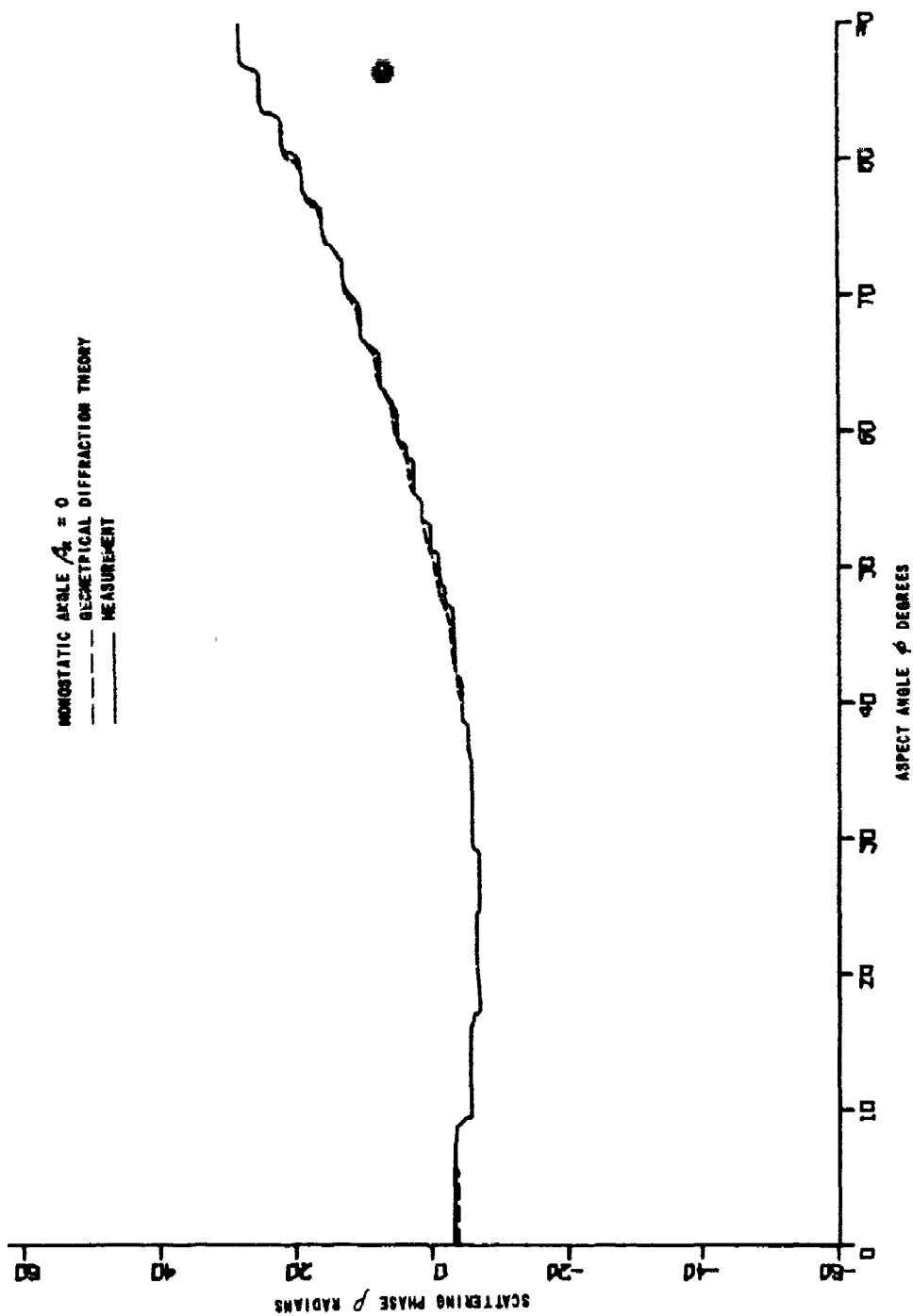


Figure 9 VERTICAL POLARIZATION SCATTERING PHASE. CYLINDER CYS, NONOSTATIC



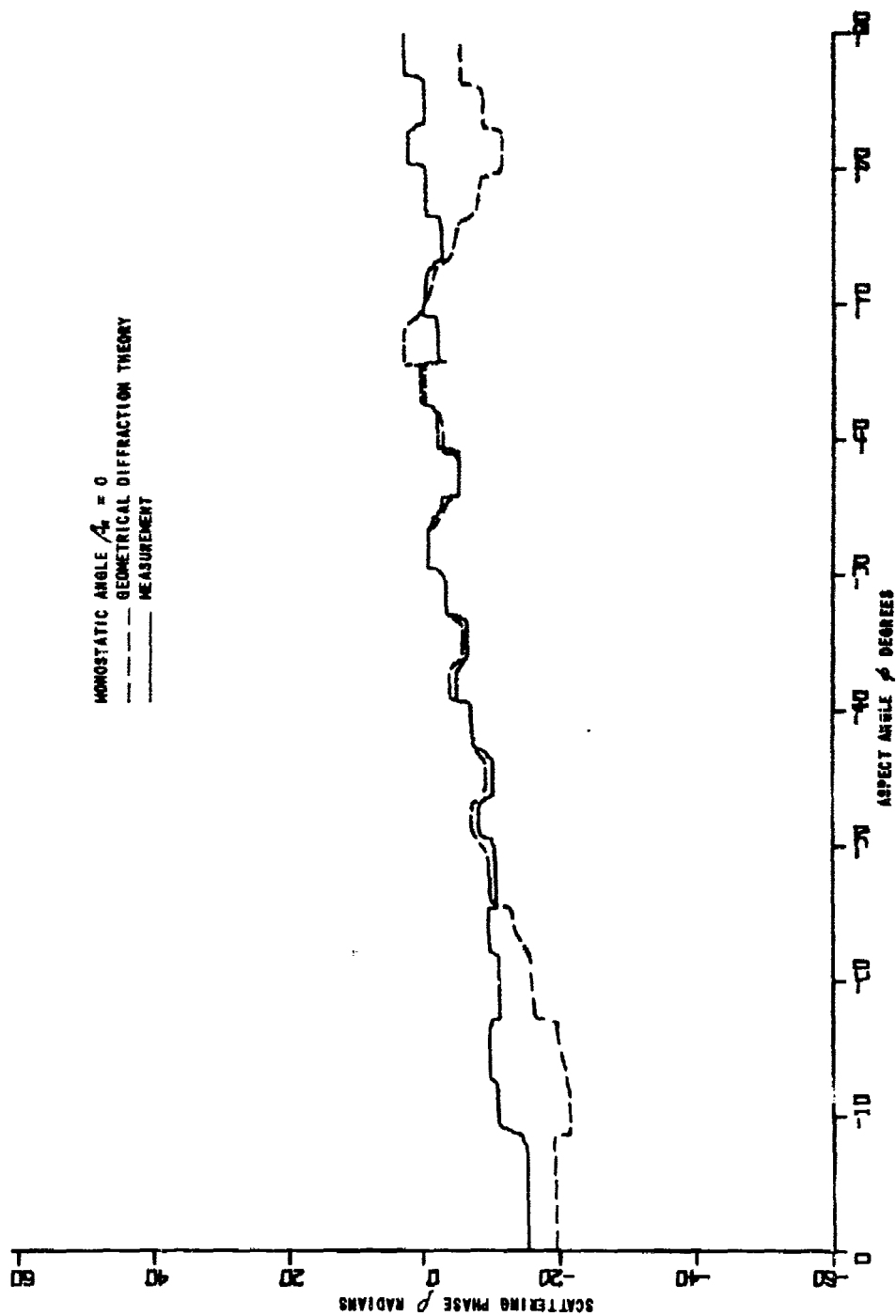


Figure 10 HORIZONTAL POLARIZATION SCATTERING PHASE. CYLINDER CYS, MONOSTATIC

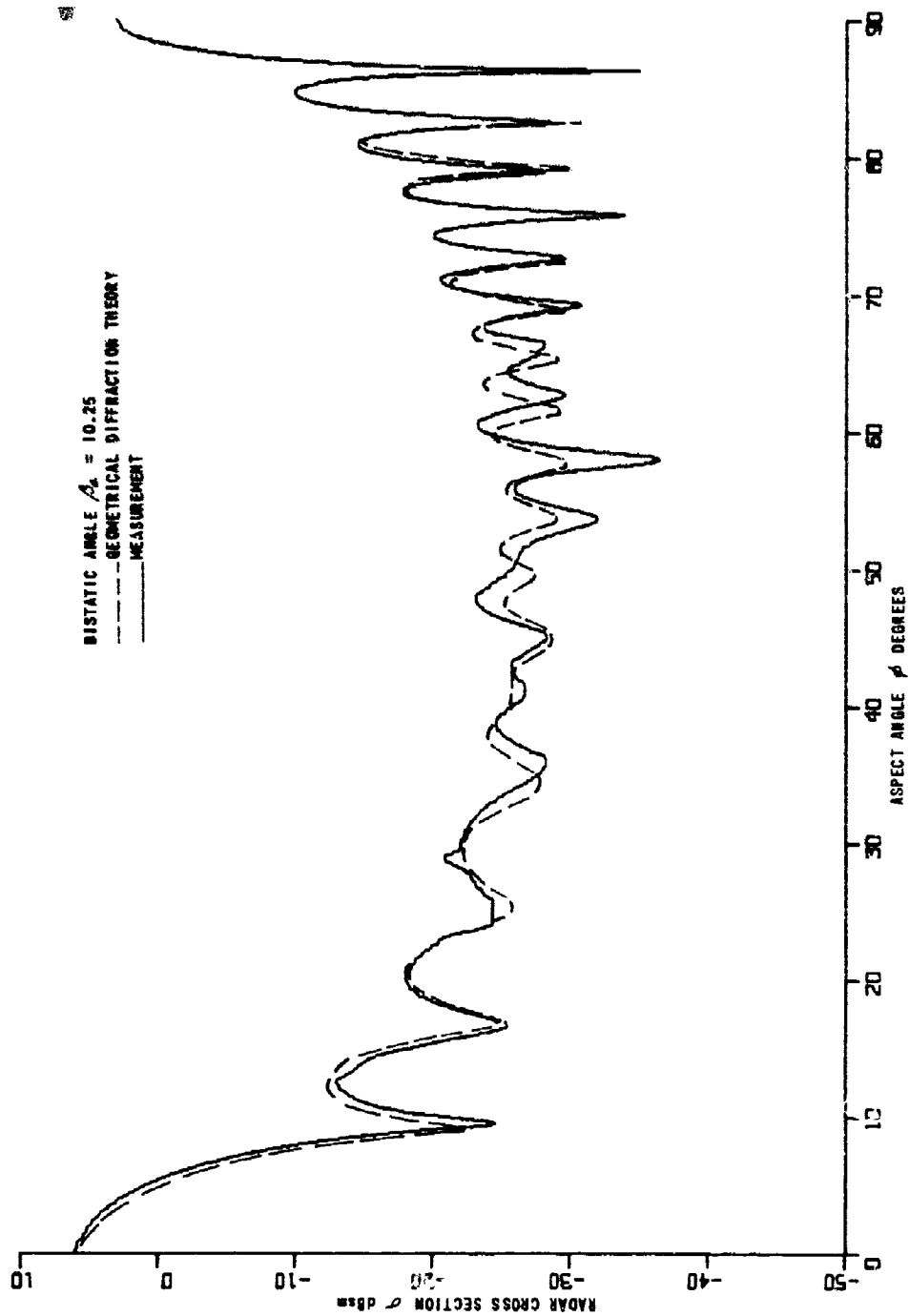


Figure 11 VERTICAL POLARIZATION RADAR CROSS SECTION. CYLINDER CYS. BISTATIC

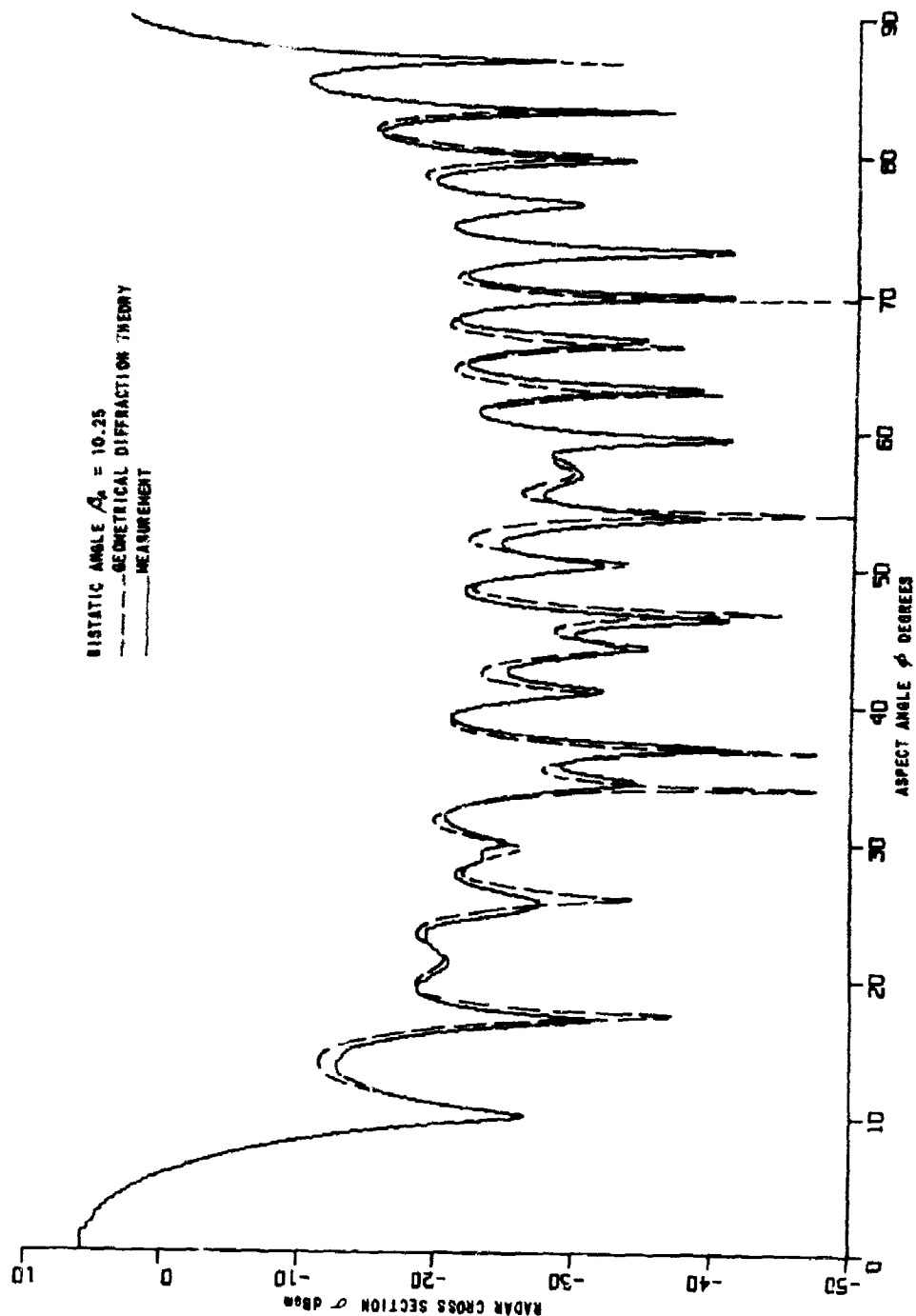


Figure 12 HORIZONTAL POLARIZATION RADAR CROSS SECTION. CYLINDER CTS, BISTATIC

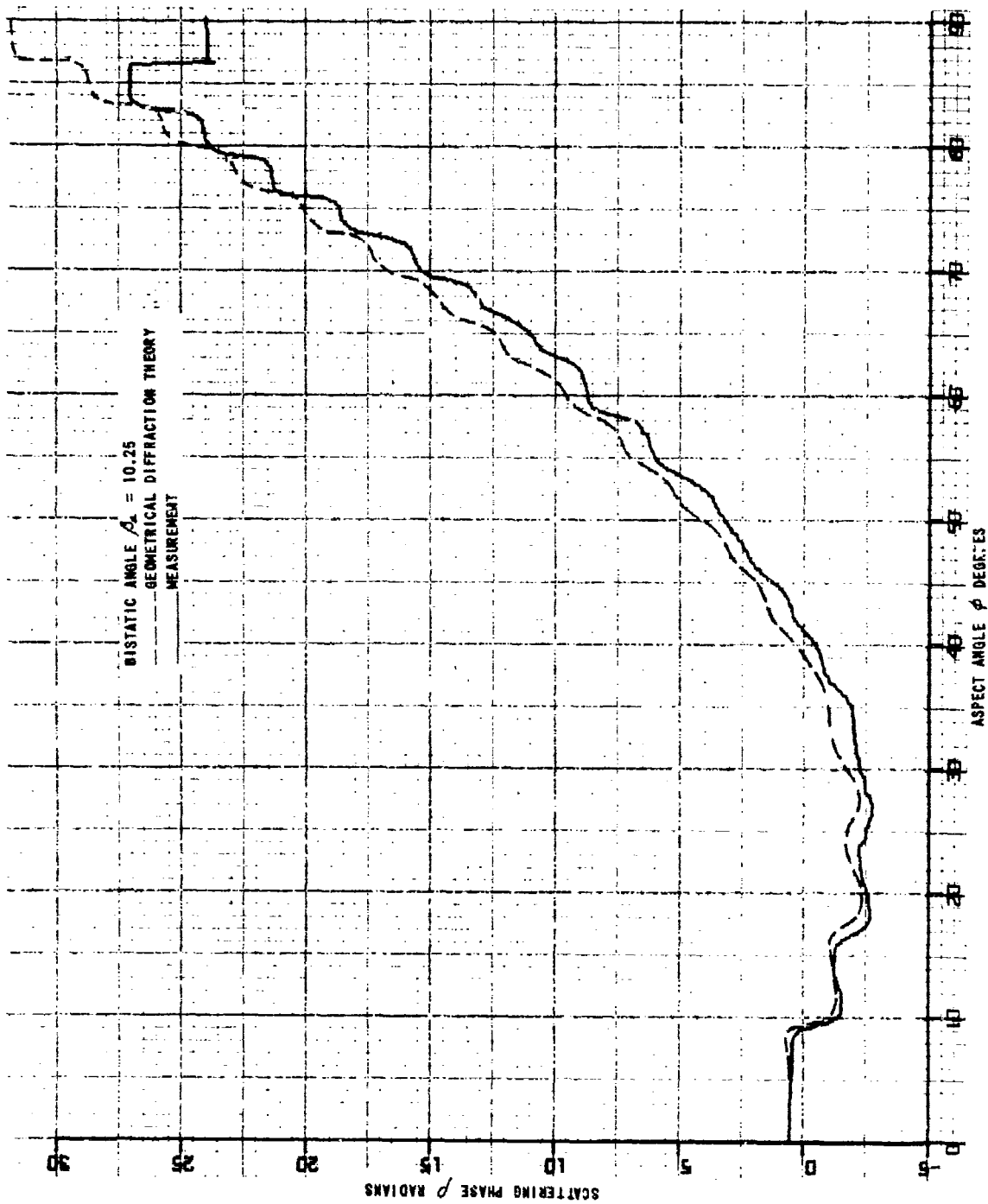


Figure 13 VERTICAL POLARIZATION SCATTERING PHASE. CYLINDER CY5, BISTATIC

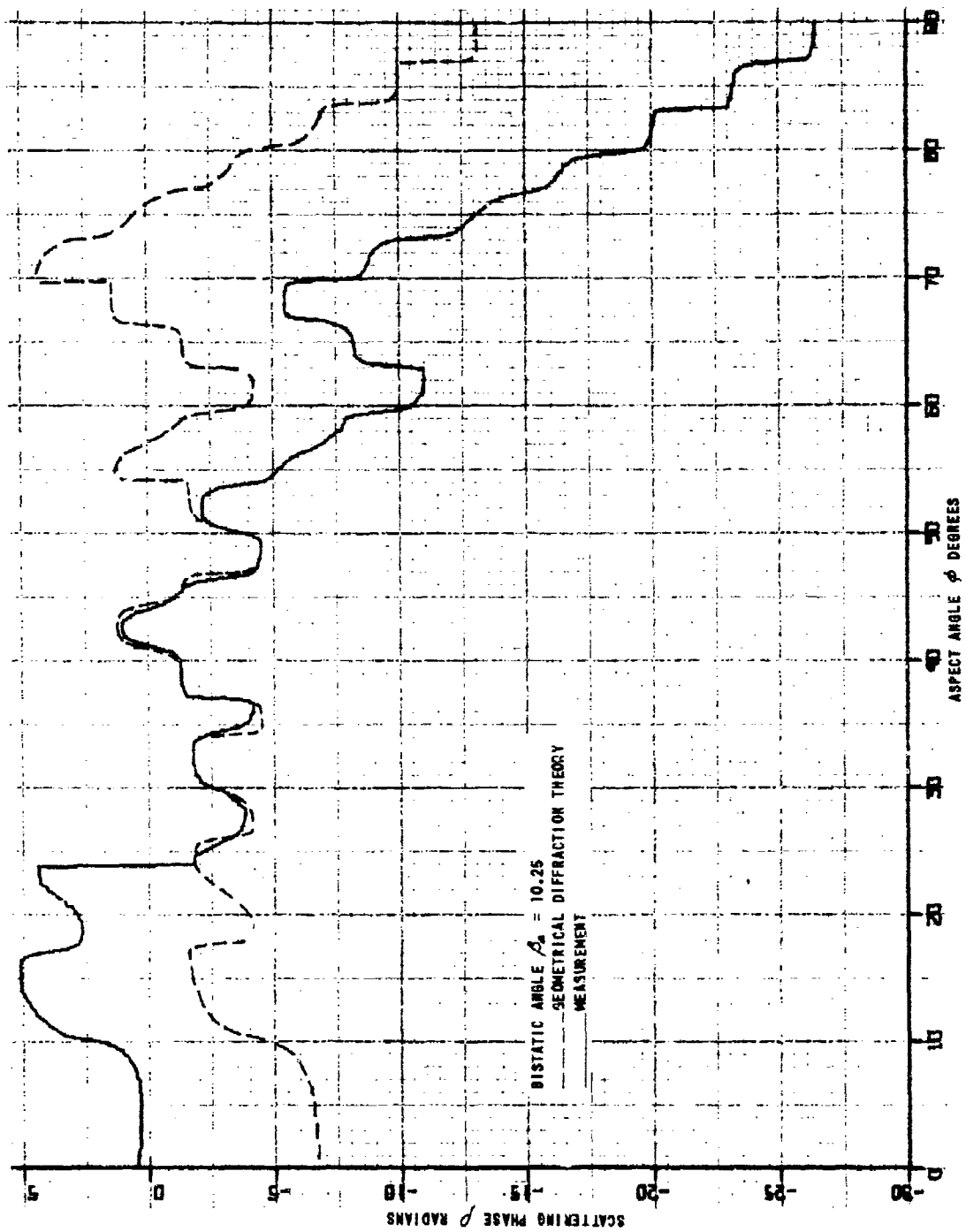


Figure 14 HORIZONTAL POLARIZATION SCATTERING PHASE. CYLINDER CV5, BISTATIC

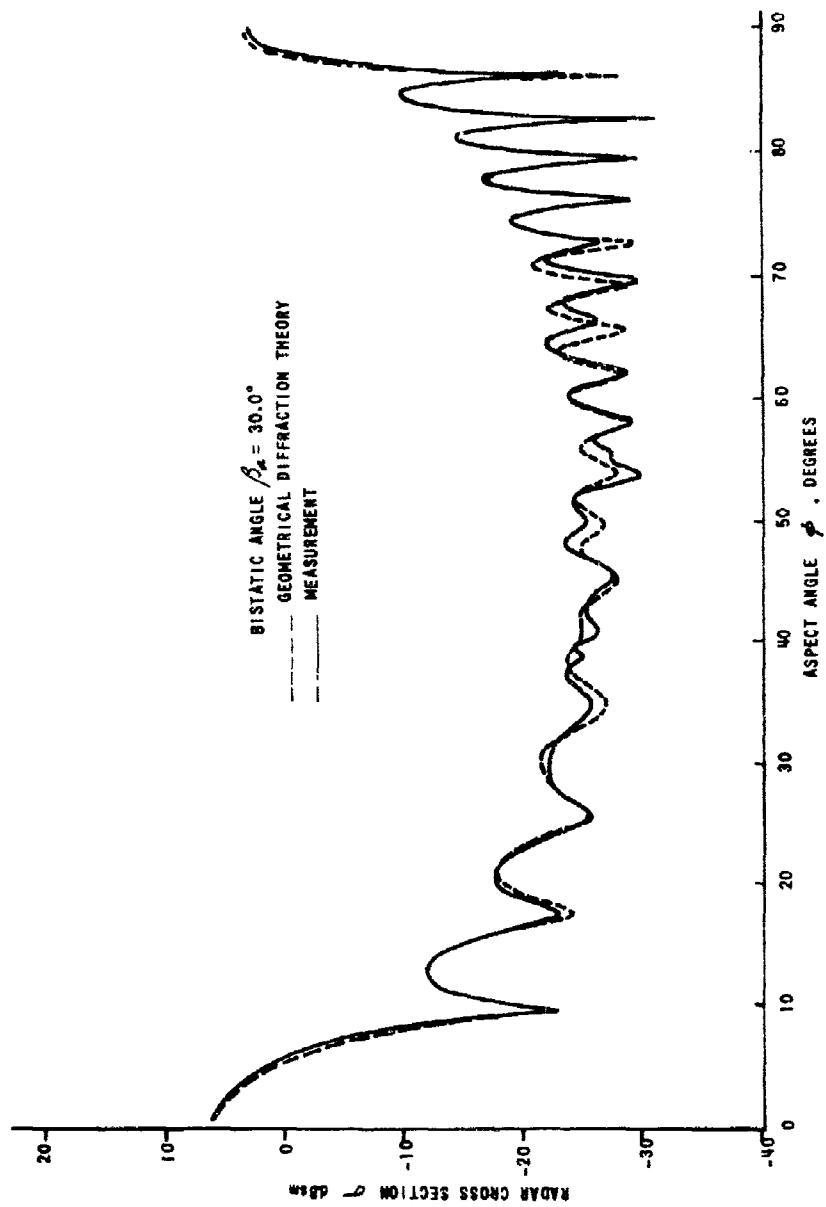


Figure 15 VERTICAL POLARIZATION RADAR CROSS SECTION. CYLINDER CYS, BISTATIC

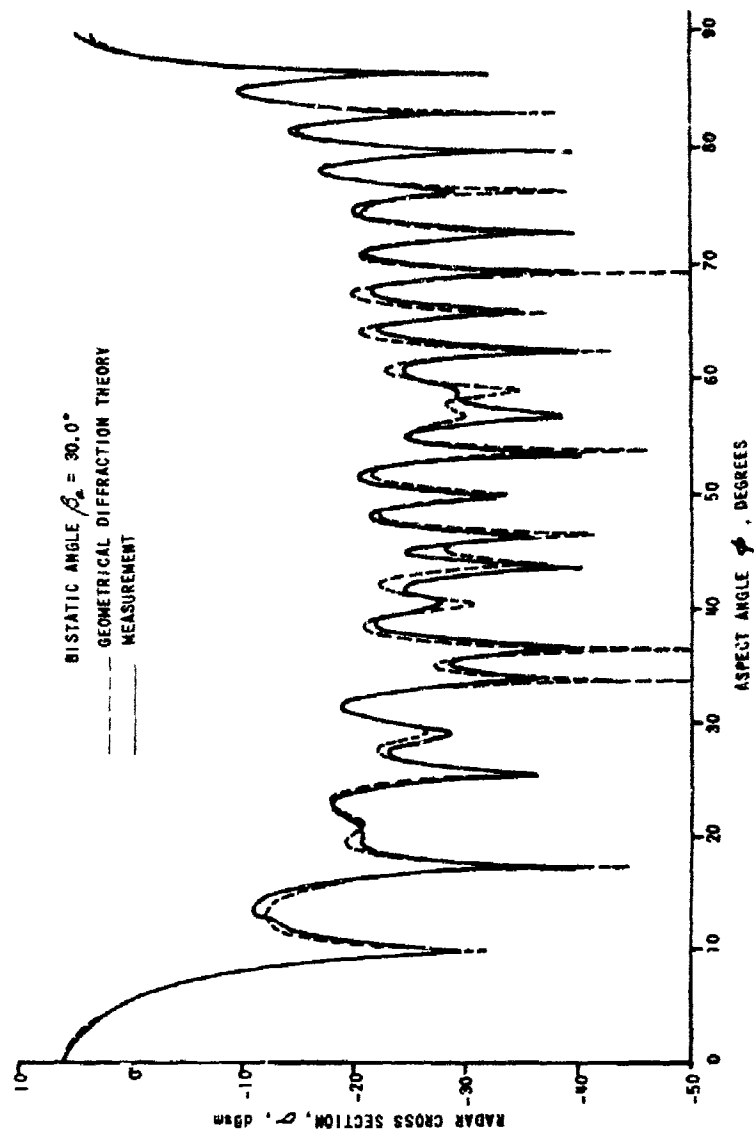


Figure 16 HORIZONTAL POLARIZATION RADAR CROSS SECTION. CYLINDER CY5, BISTATIC

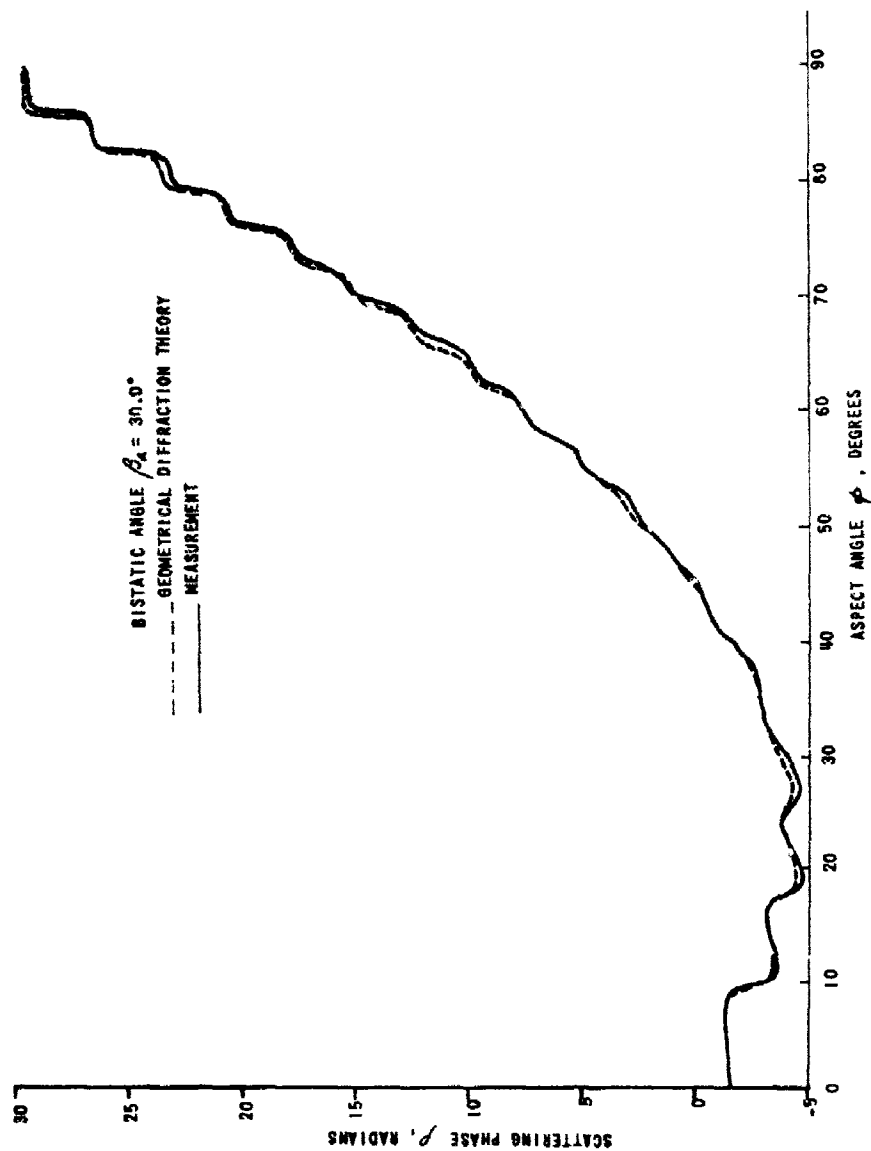


Figure 17 VERTICAL POLARIZATION RADAR CROSS SECTION. CYLINDER CY5. BISTATIC



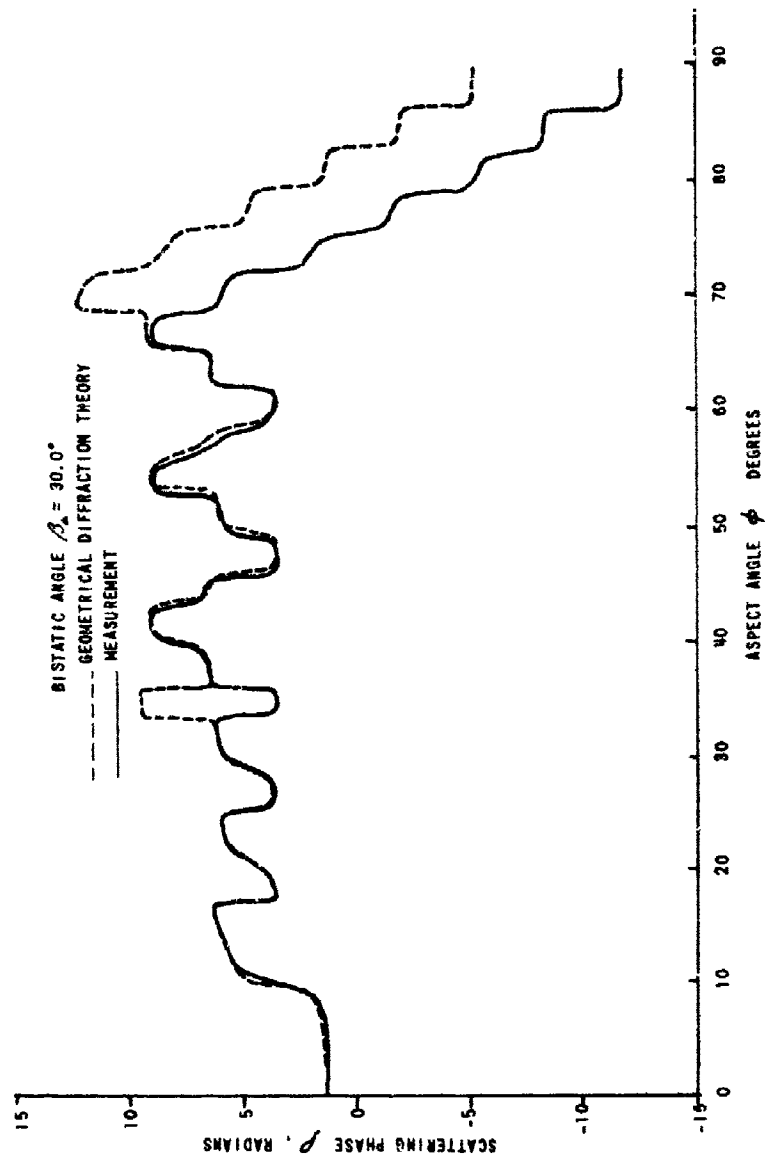


Figure 18 HORIZONTAL POLARIZATION RADAR CROSS SECTION, CYLINDER CYS, BISTATIC

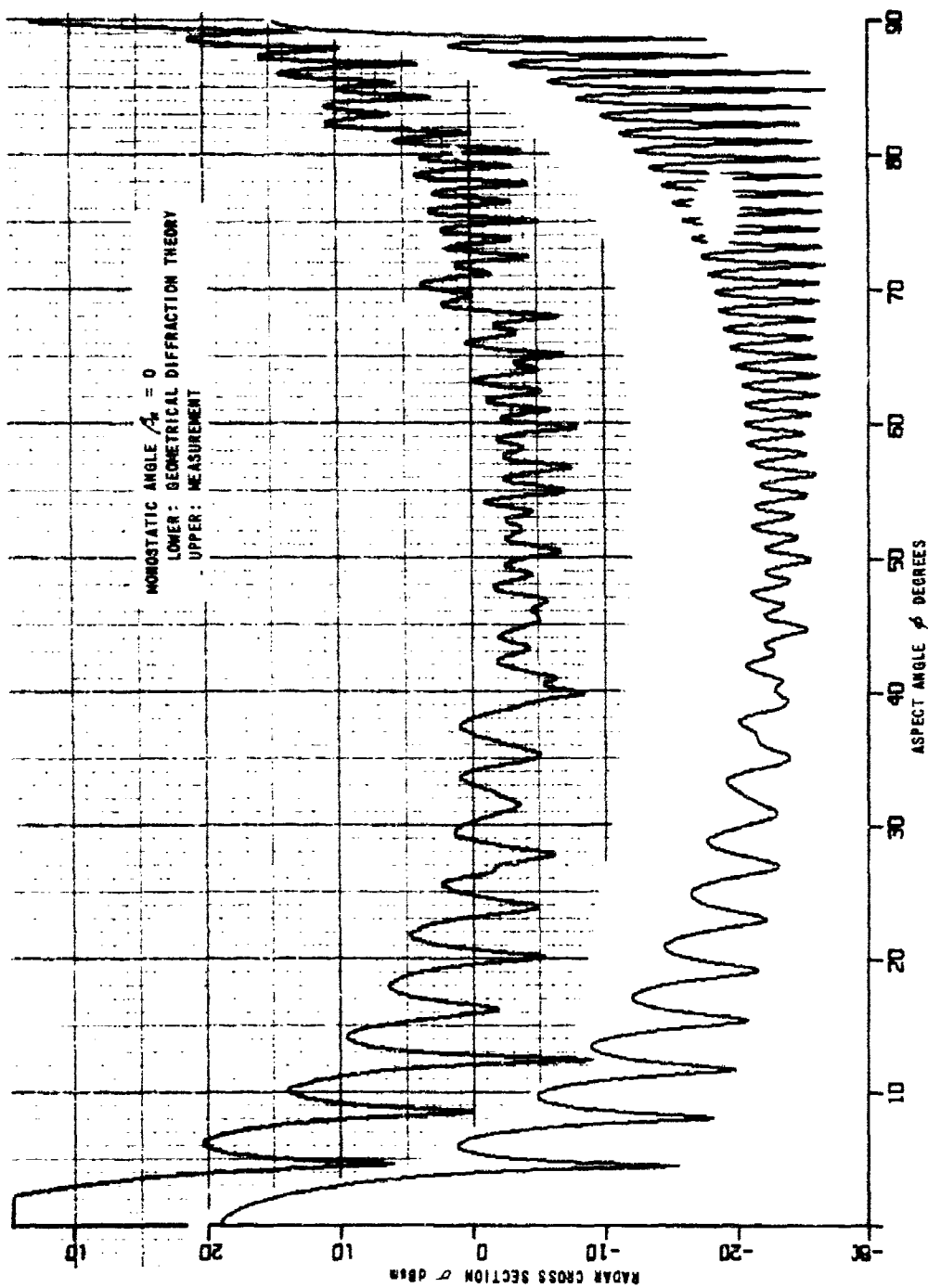


Figure 19 VERTICAL POLARIZATION RADAR CROSS SECTION. CYLINDER CY6, MONOSTATIC

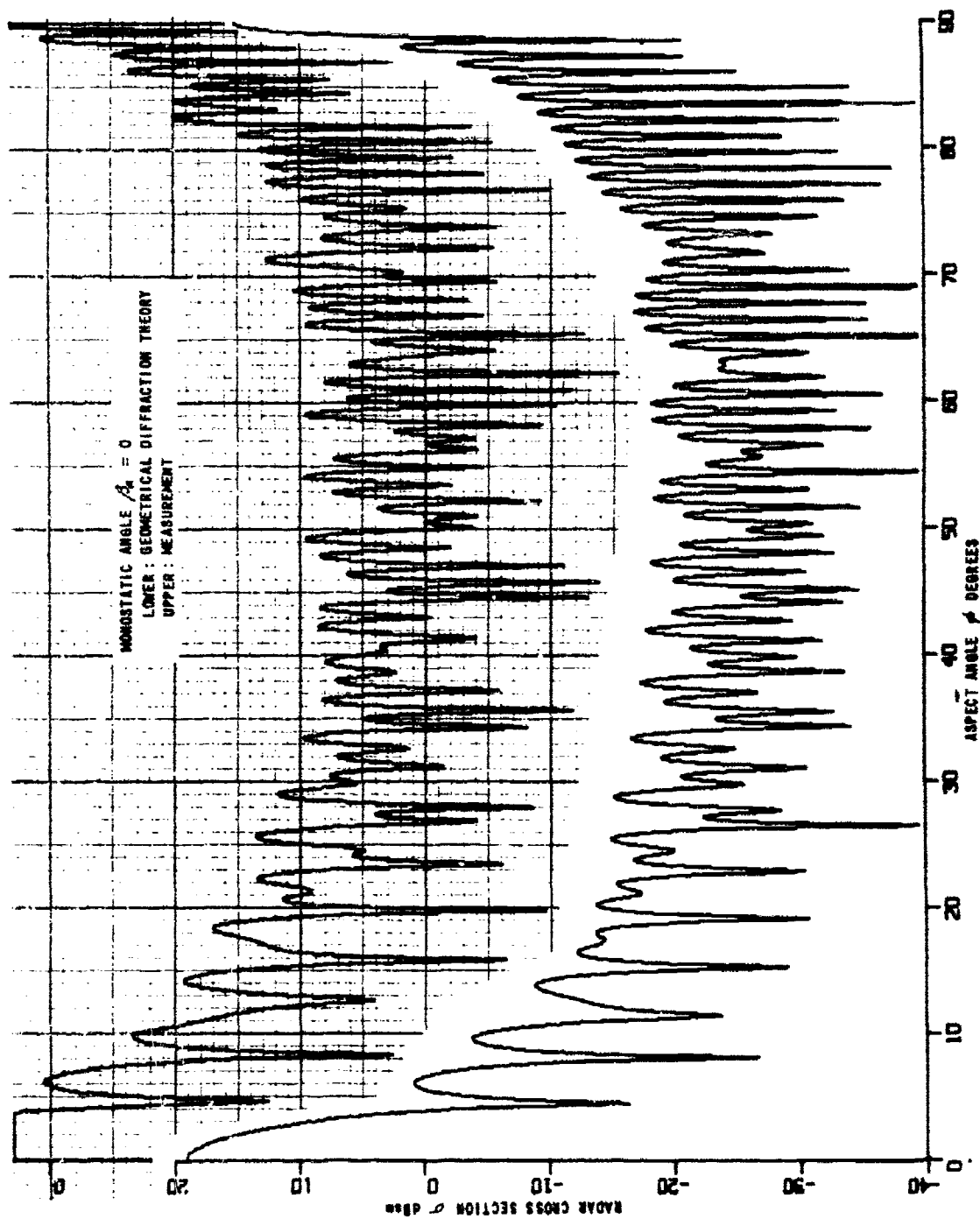


Figure 20 HORIZONTAL POLARIZATION RADAR CROSS SECTION. CYLINDER C76, NONSTATIC

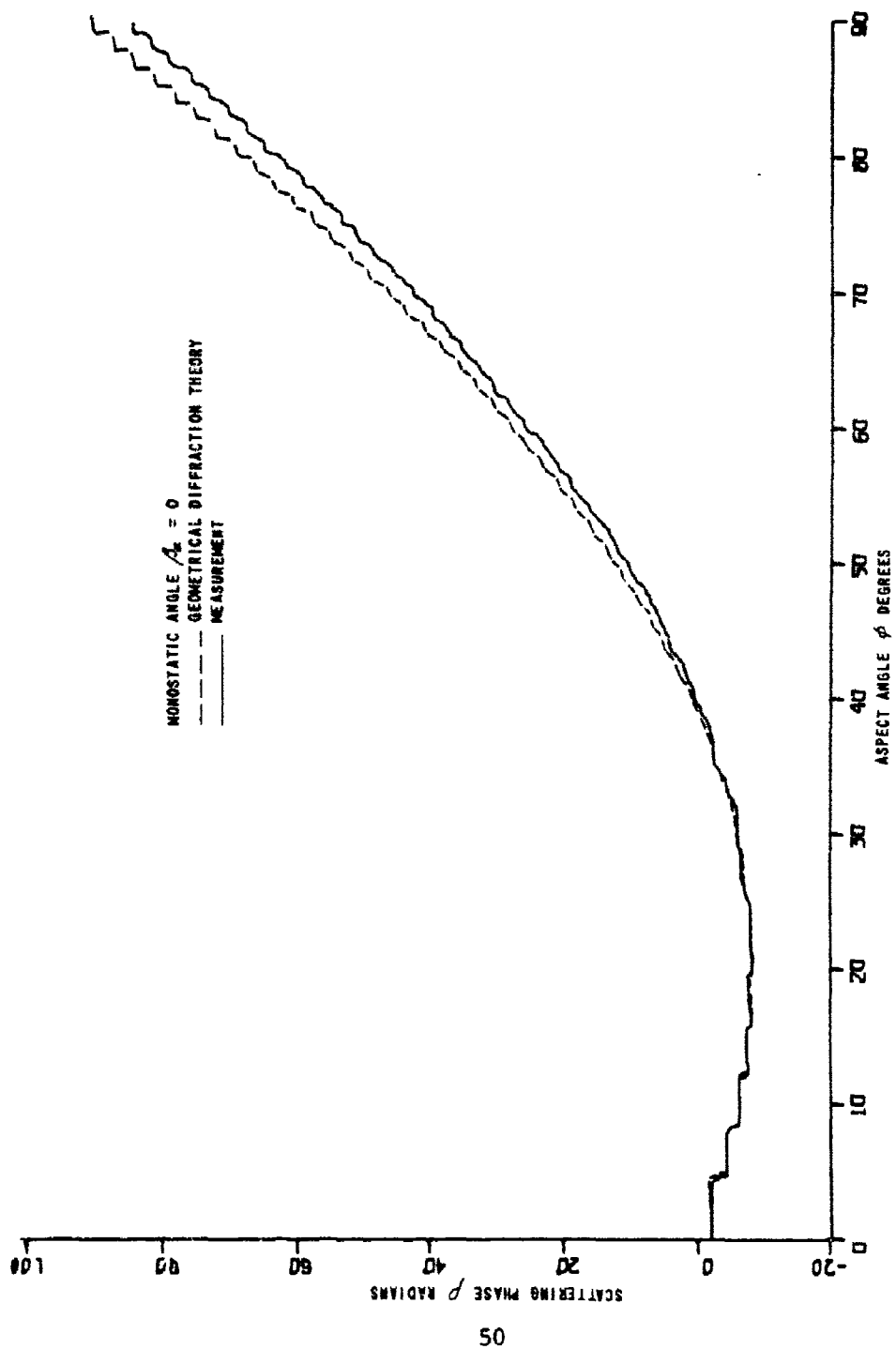


Figure 21 VERTICAL POLARIZATION SCATTERING PHASE. CYLINDER CY6, MONOSTATIC

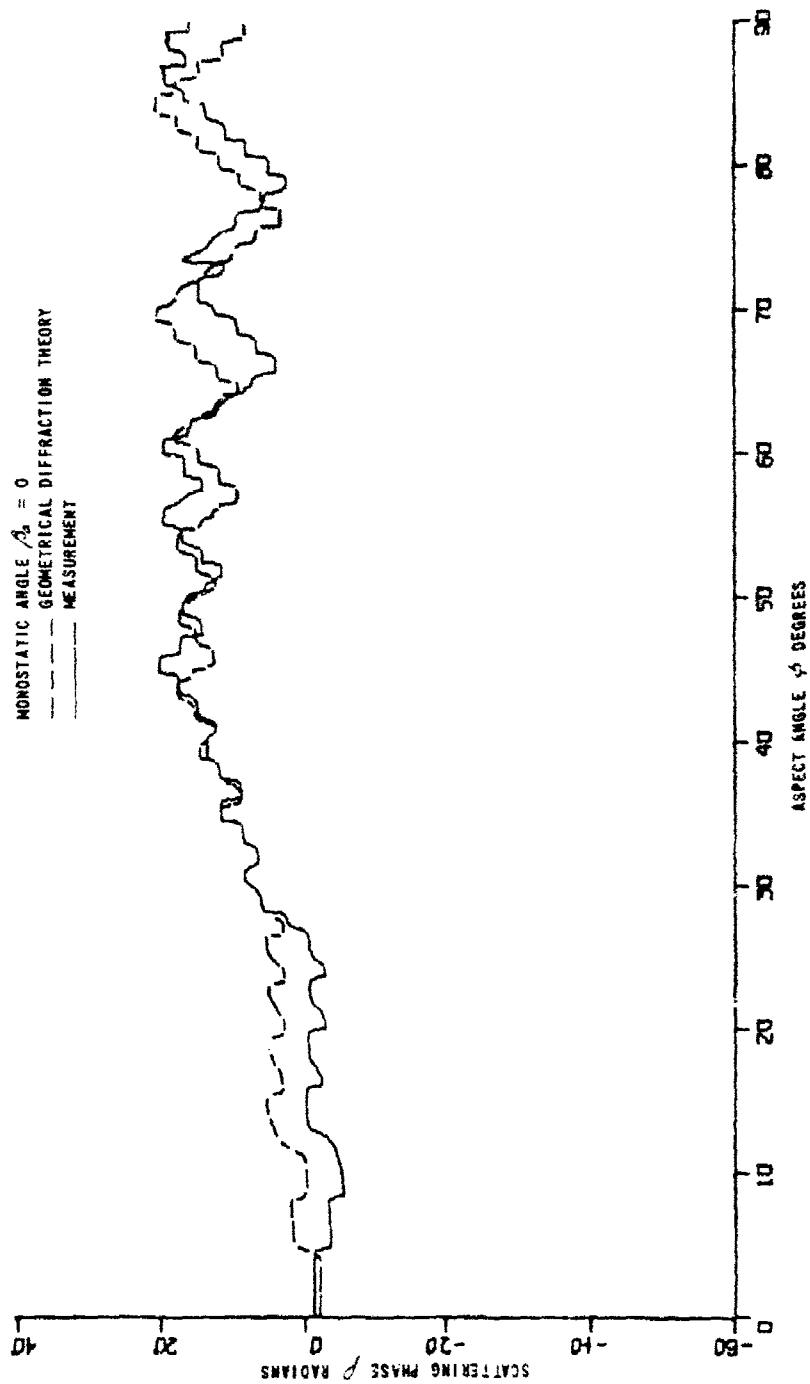


Figure 22 HORIZONTAL POLARIZATION SCATTERING PHASE. CYLINDER CY6, MONOSTATIC

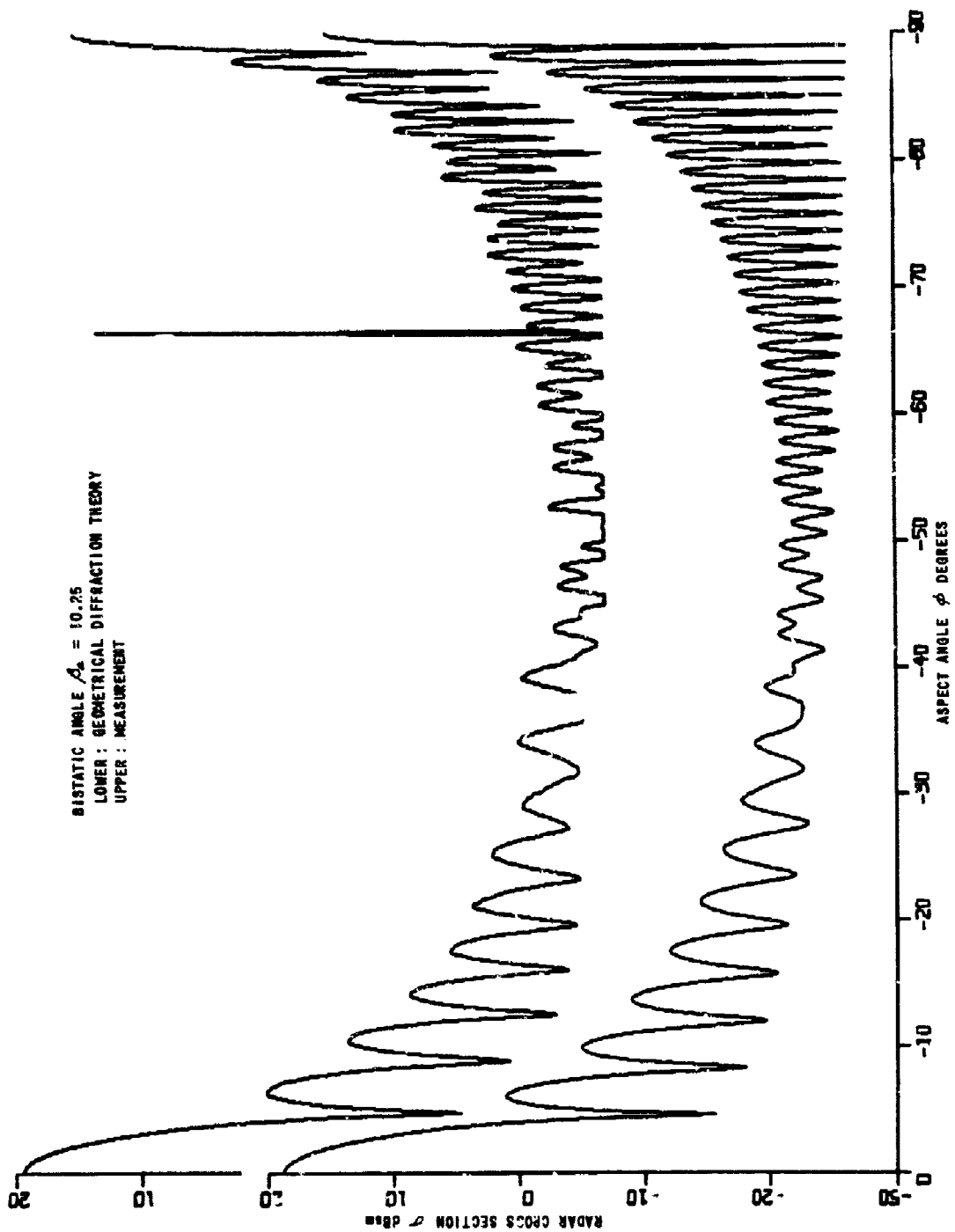


Figure 23 VERTICAL POLARIZATION RADAR CROSS SECTION. CYLINDER CY6, BISTATIC

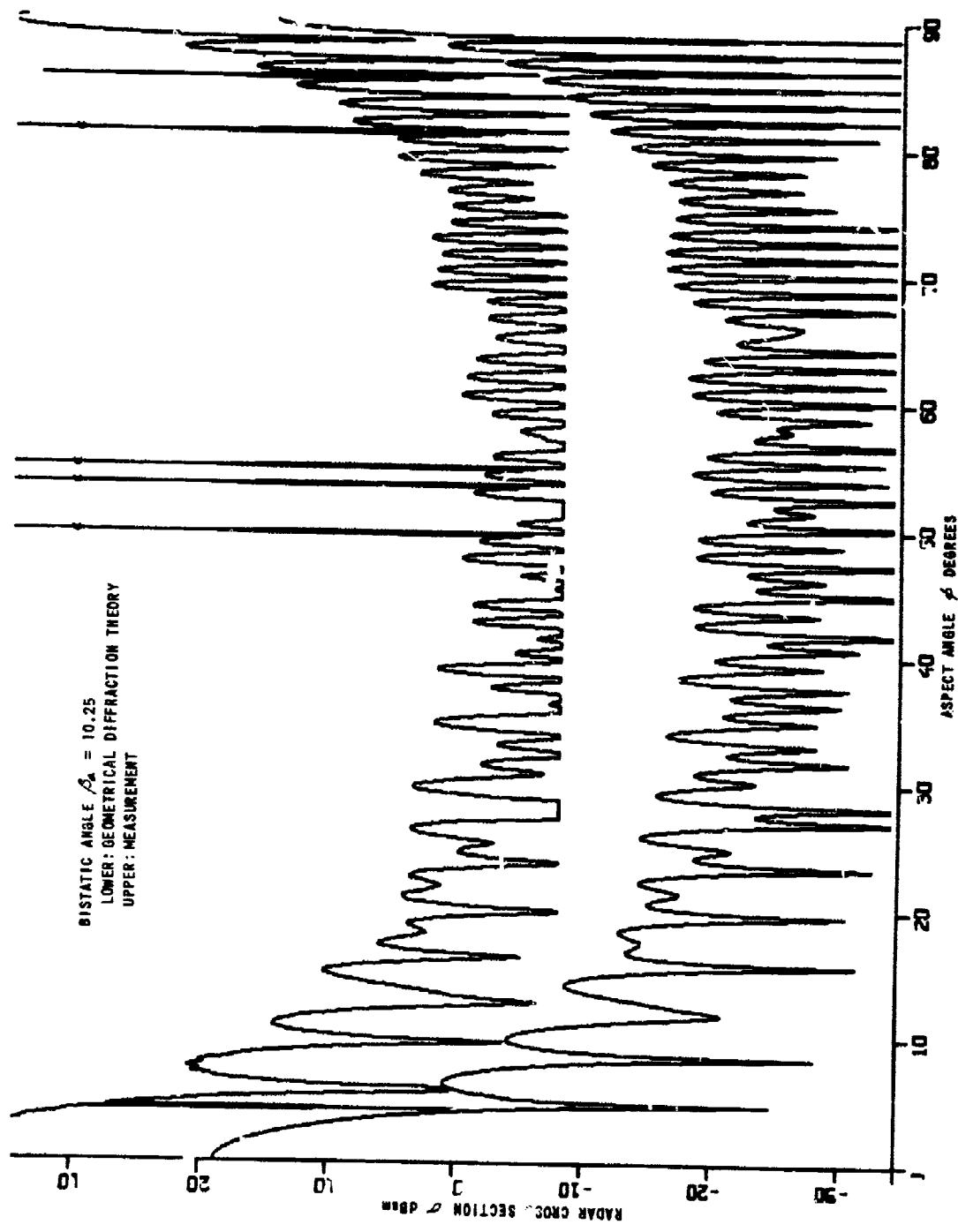


Figure 24 HORIZONTAL POLARIZATION RADAR CROSS SECTION. CYLINDER CY6, BISTATIC

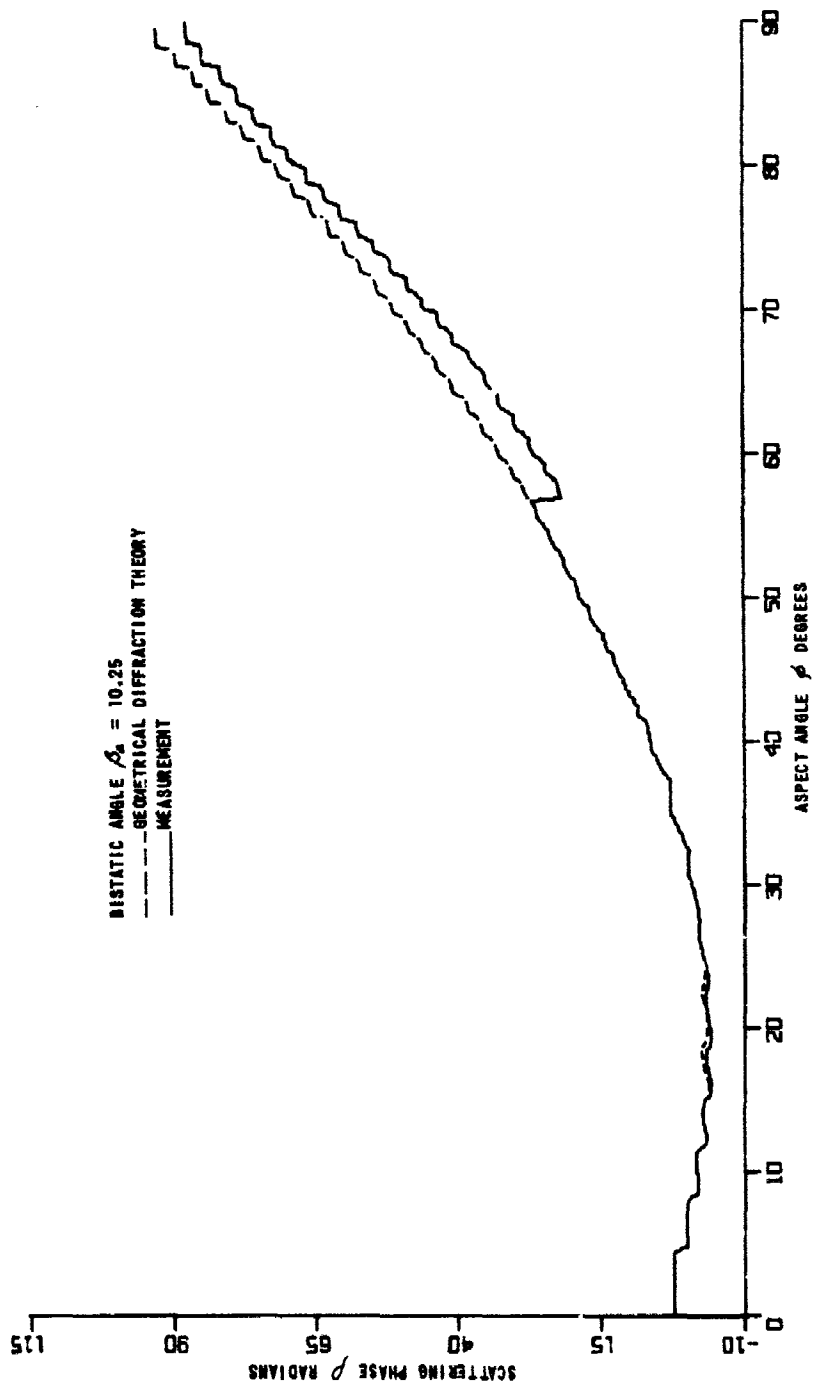


Figure 25 VERTICAL POLARIZATION SCATTERING PHASE. CYLINDER CYG, BISTATIC



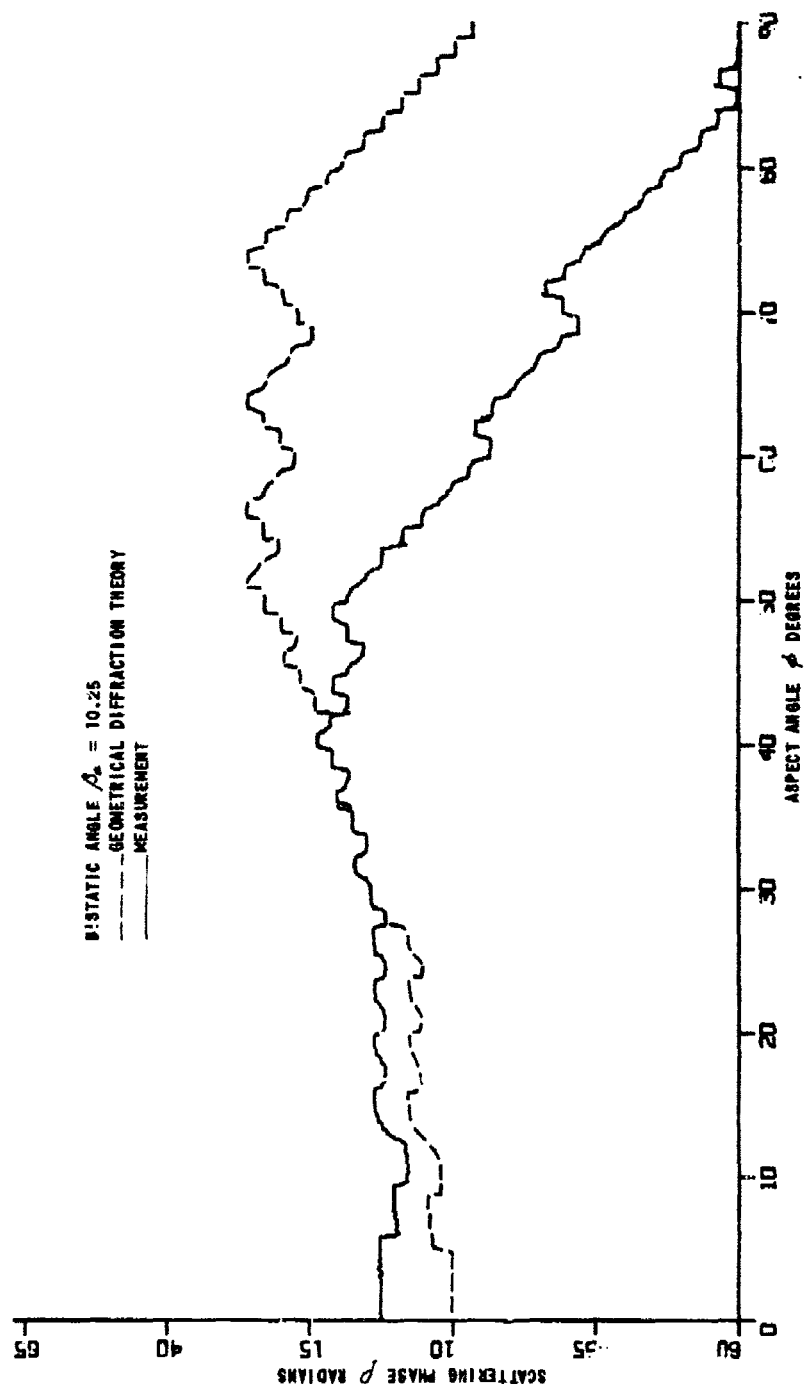


Figure 26 HORIZONTAL POLARIZATION SCATTERING PHASE. CYLINDER CYS, BISTATIC

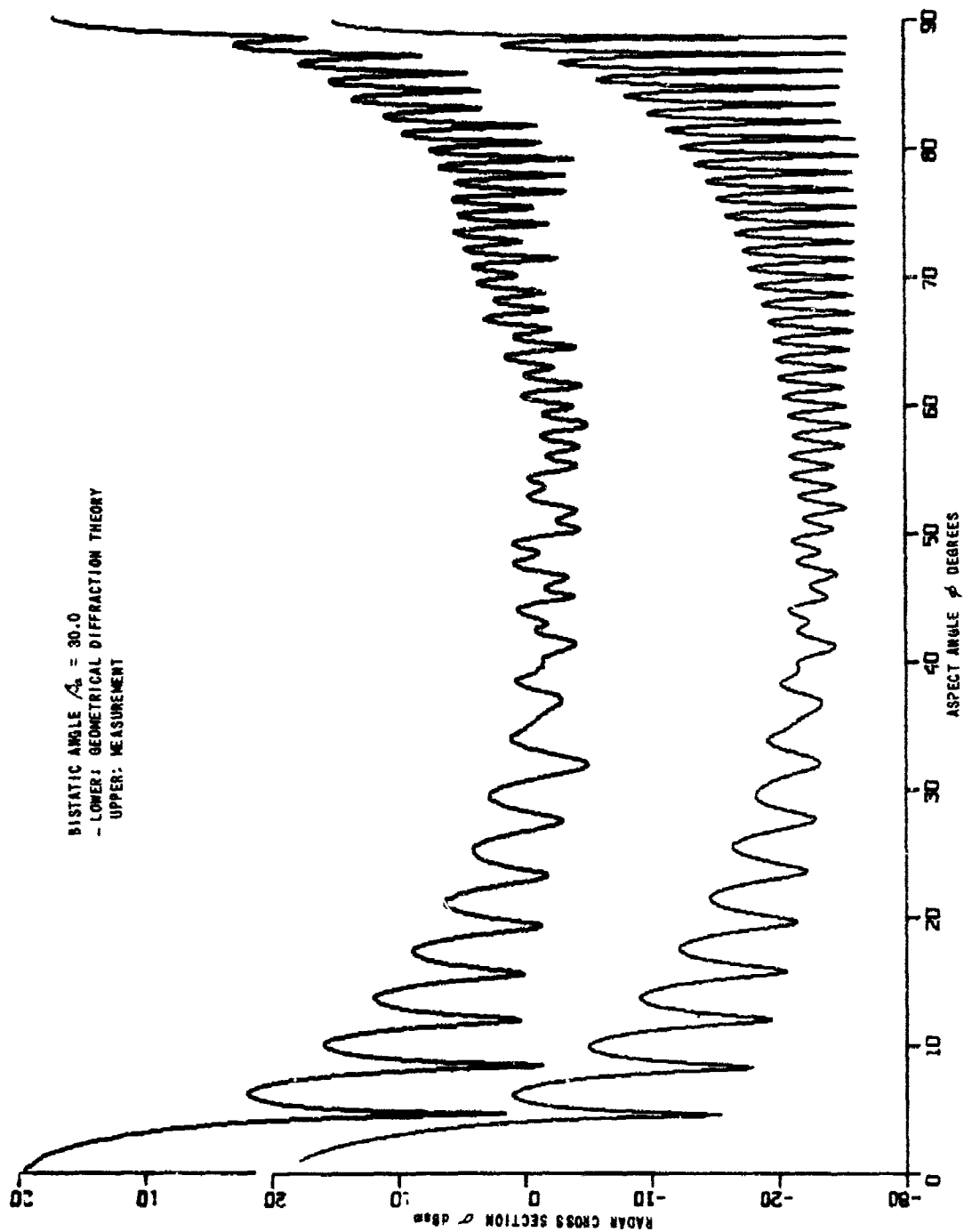


Figure 27 VERTICAL POLARIZATION RADAR CROSS SECTION. CYLINDER CY6, BISTATIC

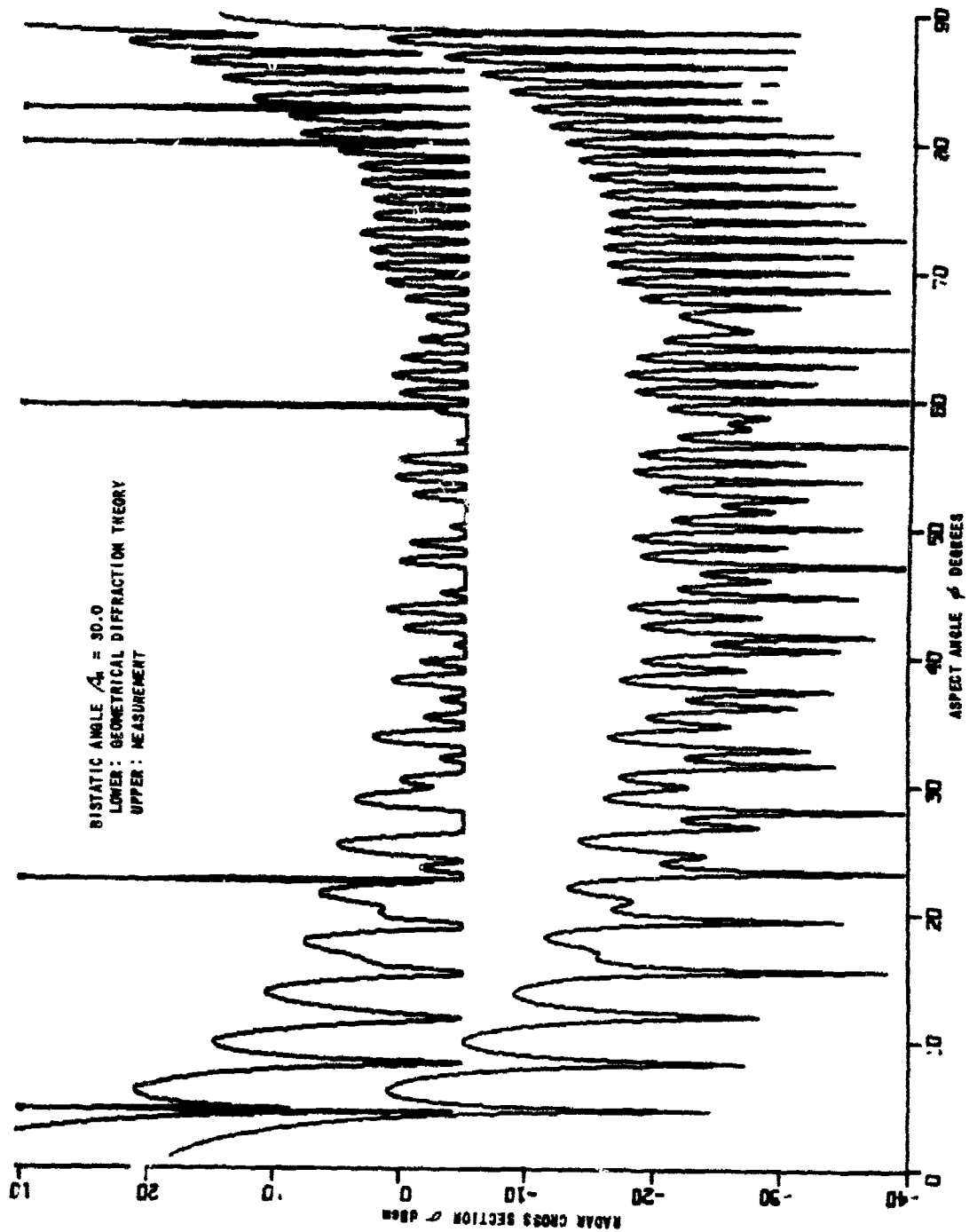


Figure 28 HORIZONTAL POLARIZATION RADAR CROSS SECTION. CYLINDER C76, BISTATIC

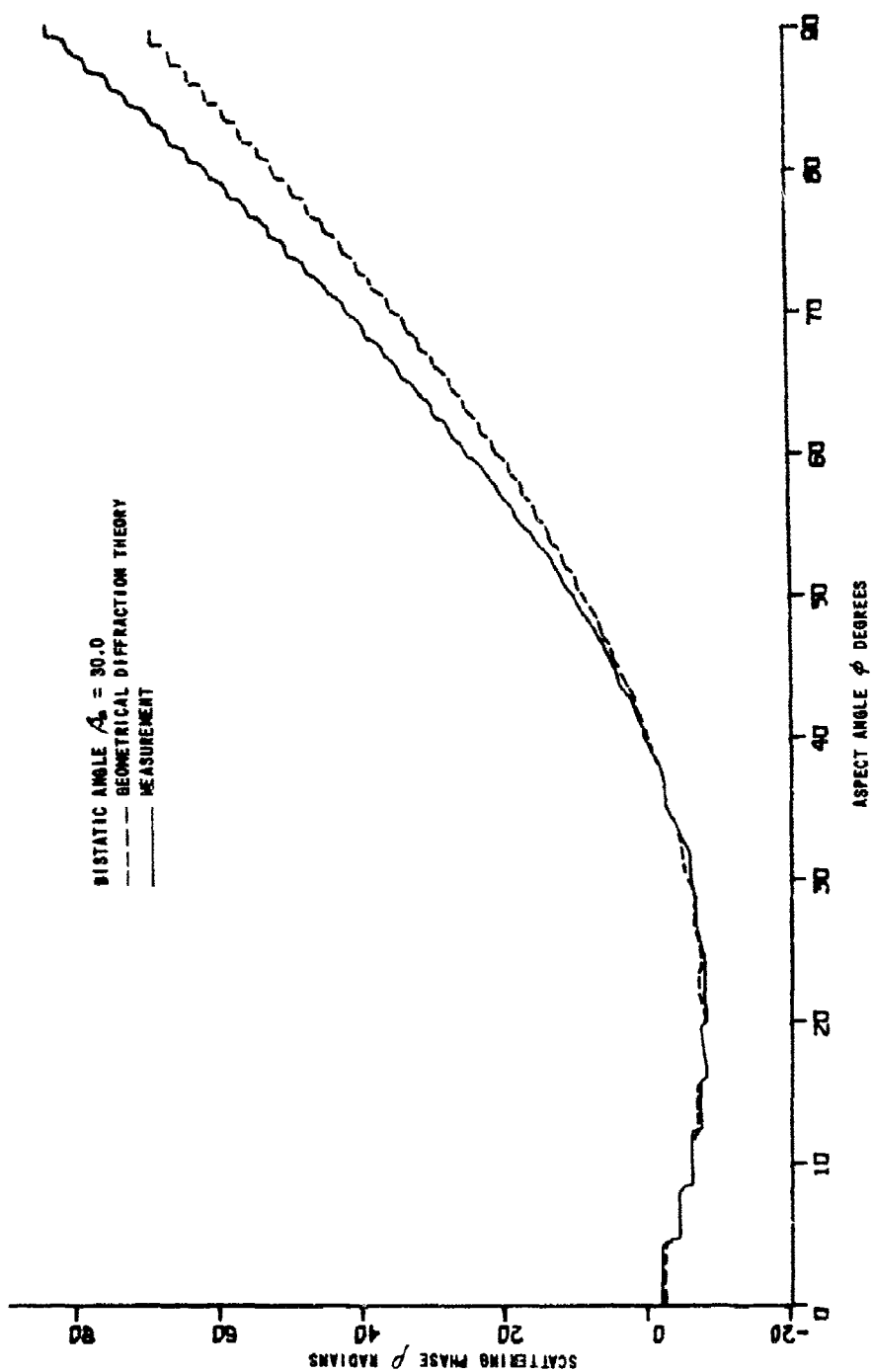


Figure 29 VERTICAL POLARIZATION SCATTERING PHASE. CYLINDER CY6, BISTATIC

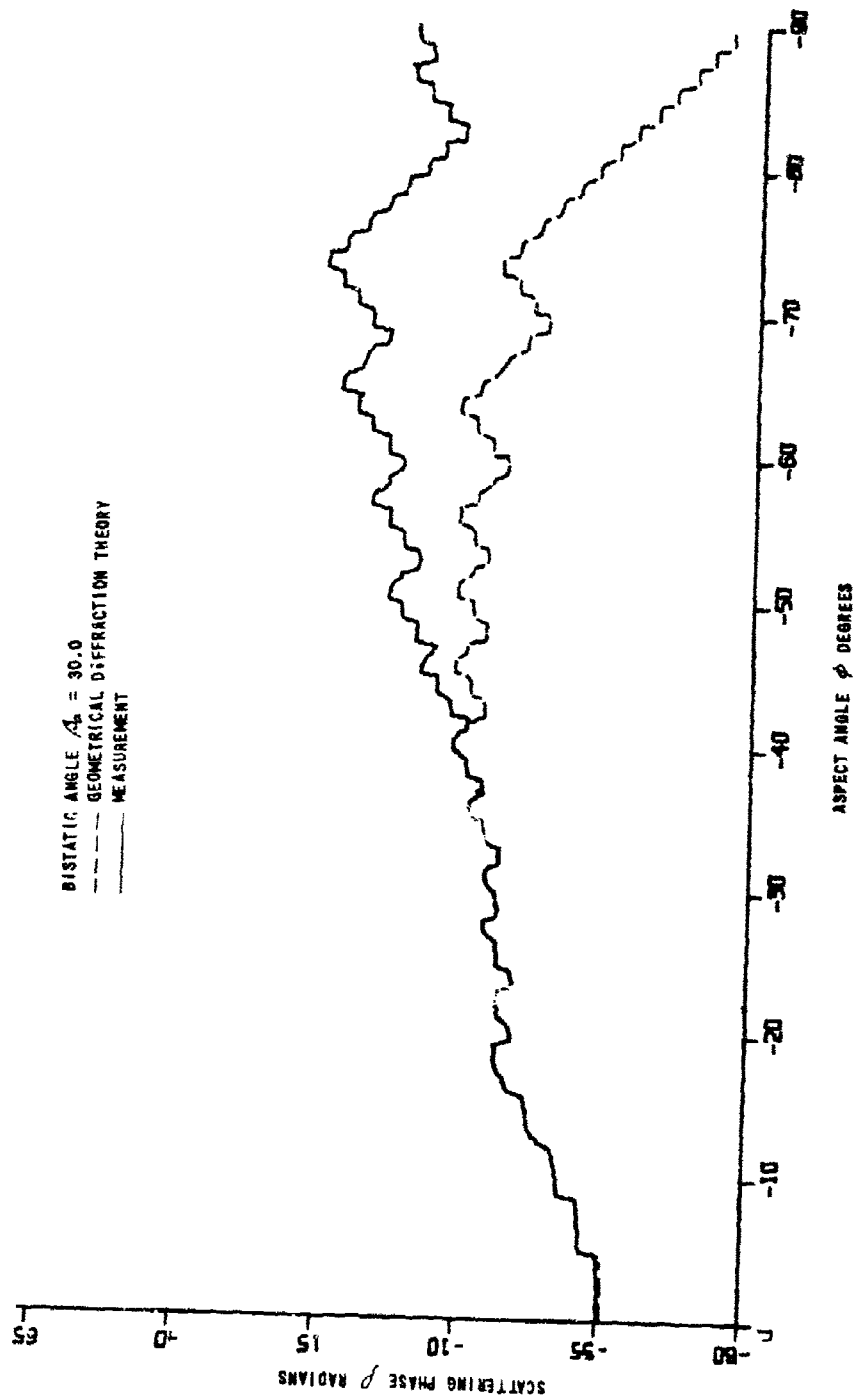


Figure 30 HORIZONTAL POLARIZATION SCATTERING PHASE. CYLINDER CV6, BISTATIC

## 4.2 FRUSTUM

### 4.2.1 Analytical Formulation

A frustum is a doubly truncated cone. Figure 31 illustrates the bistatic radar-target relationship: the axis of symmetry of the target and the bisector of the bistatic angle define an azimuth (x-y) plane. Two axially symmetric edges located at the extremities of the frustum give rise to four geometric discontinuities in the azimuth plane; these discontinuities, labelled  $S_1$ ,  $S_2$ ,  $S_3$ , and  $S_4$ , constitute the four scattering center on the target.

Scattering by a frustum is treated in Appendix B. Scattering center contributions based upon unmodified geometrical diffraction theory have amplitudes given by:

$$\sqrt{\sigma_1} = \frac{\sin(\pi/n_1)}{n_1} \sqrt{\frac{a_1 \csc \phi}{k \cos \beta/2}} \left[ \left\{ \cos(\pi/n_1) - \cos\left(\frac{\pi+2\phi}{n_1}\right) \right\}^{-1} \mp \left\{ \cos(\pi/n_1) - \cos\left(\frac{\beta_a}{n_1}\right) \right\}^{-1} \right] \quad (26)$$

$$= 0; \quad \phi > \pi - \alpha - \beta_a/2$$

$$\phi \leq \pi - \alpha - \beta_a/2$$

$$\sqrt{\sigma_2} = \frac{\sin(\pi/n_2)}{n_2} \sqrt{\frac{a_2 \csc \phi}{k \cos \beta/2}} \left[ \left\{ \cos\left(\frac{\pi}{n_2}\right) - \cos\left(\frac{3\pi-2\phi}{n_2}\right) \right\}^{-1} \mp \left\{ \cos\left(\frac{\pi}{n_2}\right) - \cos\left(\frac{\beta_a}{n_2}\right) \right\}^{-1} \right] \quad (27)$$

$$= 0; \quad \phi < -\alpha + \beta_a/2$$

$$\phi \geq -\alpha + \beta_a/2$$

$$\sqrt{\sigma_3} = \frac{\sin(\pi/n_1)}{n_1} \sqrt{\frac{a_1 \csc \phi}{k \cos \beta/2}} \left[ \left\{ \cos\left(\frac{\pi}{n_1}\right) - \cos\left(\frac{\pi-2\phi}{n_1}\right) \right\}^{-1} \mp \left\{ \cos\left(\frac{\pi}{n_1}\right) - \cos\left(\frac{\beta_a}{n_1}\right) \right\}^{-1} \right] \quad (28)$$

$$= 0; \quad \phi > \pi/2 - \beta_a/2$$

$$\phi \leq \pi/2 - \beta_a/2$$

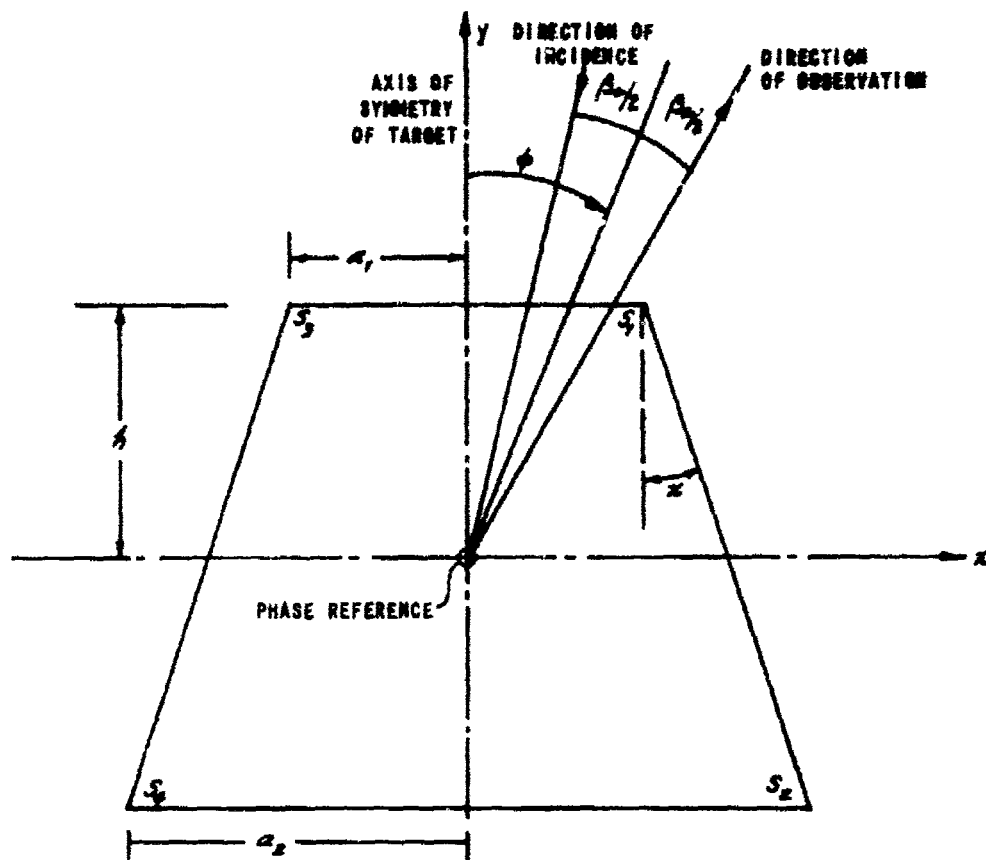


Figure 31 SCATTERING CENTERS ON FRUSTUM

$$\begin{aligned}
\sqrt{\sigma_4} &= \frac{\sin(\pi/n_2)}{n_2} \sqrt{\frac{a_2 \csc \phi}{k \cos \beta/2}} \left\{ \cos\left(\frac{\pi}{n_2}\right) - \cos\left(\frac{3\pi + 2\phi}{n_2}\right) \right\}^{-1} \times \left\{ \cos\left(\frac{\pi}{n_2}\right) - \cos\left(\frac{\beta_2}{n_2}\right) \right\}^{-1} \\
&= 0 ; \quad \pi/2 + \beta_2/2 = \phi > \pi - \beta_2/2 \quad \phi \leq \pi - \beta_2/2 \quad (29) \\
&= \frac{\sin(\pi/n_2)}{n_2} \sqrt{\frac{a_2 \csc \phi}{k \cos \beta/2}} \left\{ \cos\left(\frac{\pi}{n_2}\right) - \cos\left(\frac{-\pi + 2\phi}{n_2}\right) \right\}^{-1} \times \left\{ \cos\left(\frac{\pi}{n_2}\right) - \cos\left(\frac{\beta_2}{n_2}\right) \right\}^{-1} \\
&\quad \phi \leq \pi/2 + \beta_2/2
\end{aligned}$$

and phases given by:

$$f_1 = -2k \cos \beta/2 [a_1 \sin \phi + h \cos \phi] + \pi/4 \quad (30)$$

$$p_2 = -2k \cos \beta/2 [a_2 \sin \phi - h \cos \phi] + \pi/4 \quad (31)$$

$$p_3 = +2k \cos \beta/2 [a_1 \sin \phi - h \cos \phi] - \pi/4 \quad (32)$$

$$p_4 = +2k \cos \beta/2 [a_2 \sin \phi + h \cos \phi] - \pi/4 \quad (33)$$

where

- $\phi$  is an equivalent aspect angle, defined as the angle between the axis of symmetry of the frustum and the bisector of the bistatic angle  $\beta$  ( $\phi = 0$  for axial incidence and direct illumination of the smaller end of the frustum);
- $\beta$  is the bistatic angle between the transmitting direction and the receiving direction;
- $\beta_2$  is the azimuth bistatic angle, which should be considered as projecting into the plane containing both the axis of symmetry of the frustum and the line defining the direction of  $\phi$ ;



$a_1$  is the smaller radius of the frustum;

$a_2$  is the larger radius of the frustum;

$h$  is the half-height of the frustum;

$\alpha$  is the frustum angle ( $\alpha = \tan^{-1} \frac{a_2 - a_1}{2h}$ ) in radians

$$\eta_1 = \frac{3}{2} - \frac{\alpha}{\pi}$$

$$\eta_2 = \frac{3}{2} + \frac{\alpha}{\pi} \quad (34)$$

$k$  is the wave number ( $k = \frac{2\pi}{\lambda}$ ).

Equations 26 through 29 may contain singularities at aspects which produce specular scattering ( $\phi = 0, \pi/2 - \alpha, \pi$ ). At and near the nose-on axial aspect ( $\phi = 0$ ), the polarization-independent contribution from scattering centers  $S_1$  and  $S_3$  accounts for the specular return. According to the small angle analysis reported in subsection B.3 of Appendix B, we have

$$(\sqrt{\sigma_1} e^{j\rho_1} + \sqrt{\sigma_3} e^{j\rho_3})_{poli} = 2\sqrt{\pi} k \cos \beta/2 a_1^2 \frac{J_1(2ka_1 \cos \beta/2 \sin \phi)}{(2ka_1 \cos \beta/2 \sin \phi)} \times e^{-j\pi/2 - j2kh \cos \beta/2 \cos \phi} \quad (35)$$

We remove the remaining singularities in Equations 26 through 29 by applying the constraint  $\csc \phi \leq ka_1 \cos \beta/2$ . Estimates of scattering by a frustum are found to be continuous when we employ the axial cross-over angle  $\phi_{ca}$  given by  $2ka_1 \sin \phi_{ca} = 2.44$ . For  $0 \leq \phi \leq \phi_{ca}$  we use the modification of Equation 35.

At and near the tail-on axial aspect ( $\phi = \pi$ ), the term

$(\sqrt{\sigma_2} e^{j\rho_2} + \sqrt{\sigma_4} e^{j\rho_4})_{poli}$  produces the specular contribution, where

$$(\sqrt{\sigma_2} e^{j\rho_2} + \sqrt{\sigma_4} e^{j\rho_4})_{poli} = 2\sqrt{\pi} k \cos \beta/2 a_2^2 \frac{J_1(2ka_2 \cos \beta/2 \sin \phi)}{(2ka_2 \cos \beta/2 \sin \phi)} \times e^{-j\pi/2 + j2kh \cos \beta/2 \cos \phi} \quad (36)$$

and the remaining terms are constrained by the bound  $\csc \phi \leq k a_2 \cos \beta/2$ . Here the cross-over aspect becomes  $\pi - \phi_{ca}$  with  $\phi_{ca}$  now determined by the relation  $2k a_2 \sin \phi_{ca} = 2.44$ .

At and near the broadside aspect ( $\phi = \pi/2 - \alpha$ ), contributions from scattering centers  $S_1$  and  $S_2$  should account for the specular return. But the corresponding diffraction coefficients become singular for  $\phi = \pi/2 - \alpha$ . Although the small angle approximations do not allow removal of singularities in this instance, we have observed that unmodified geometrical diffraction theory fails gracefully at the broadside aspect (see Figure B-2 of Appendix B). In subsection B.4 of Appendix B, we report an analysis of broadside scattering by a frustum based upon physical optics. While the result obtained is valid, the physical optics expression is relatively complex compared to other expressions used throughout this program. For this reason a simple curve-fitting technique has been employed as a temporary alternative. Specifically, we curve fit the predictions based upon unmodified geometrical diffraction theory through the physical optics result

$$\sigma(\phi = \frac{\pi}{2} - \alpha) = \frac{8\pi}{9\lambda} \frac{[a_2^{3/2} - a_1^{3/2}]^2}{\sin^2 \alpha \cos \alpha} \cos \beta/2 \quad (37)$$

Further analysis of small angle approximations to unmodified geometrical diffraction theory in this aspect region is recommended to replace the curve-fitting operation.

#### 4.2.2 Results

Table 5 lists parameters used in the examination of frustum theory and experiment. The number of individual targets and bistatic situations contained in the table satisfy specifications noted in Table 1. The phase reference chosen for measurements was the center of the base of the frustum. For comparison purposes, the phase reference used in the analysis (see Figure 31) was translated to the base by adding the factor  $-2kh \cos \beta/2 \cos \phi$  to theoretical estimates of scattering phase.

Table 5  
PARAMETERS FOR FRUSTRUM STUDY

| MODEL<br>DESIGNATION | DIMENSIONS (INCHES) |                     |                | FREQUENCY<br>(GHz) | BISTATIC ANGLE<br>(DEGREES) |
|----------------------|---------------------|---------------------|----------------|--------------------|-----------------------------|
|                      | MIN. DIA.<br>$2a_1$ | MAX. DIA.<br>$2a_2$ | LENGTH<br>$2h$ |                    |                             |
| F3                   | 6.320               | 7.500               | 3.358          | 6.000              | 0                           |
| F4                   | 4.892               | 6.320               | 4.063          | 6.000              | 0                           |
|                      |                     |                     |                | 5.885              | 10.25                       |
|                      |                     |                     |                | 6.050              | 30.0                        |
| F5                   | 4.897               | 7.500               | 7.421          | 6.000              | 0                           |
|                      |                     |                     |                | 5.885              | 10.25                       |
|                      |                     |                     |                | 6.050              | 30.0                        |

Figures 32 through 35 compare monostatic theory and measurement for frustum F3. Notice that F3 does not satisfy the basic assumption underlying single-diffraction analyses — the height of this target is less than several wavelengths. When scattering centers  $J_1$  and  $J_2$  are the major contributors to the radar cross section of the target, predictions may be expected to be compromised. The effect observed in Figures 32 and 33 is that predictions tend to be larger than measurements. Vertical polarization phases shown in Figure 34 agree except for a slope factor. The basic shapes of the horizontal polarization phase curves agree except for displacements.

Monostatic results for F4 show better agreement due to an increase in the length of the target (see Figures 36 through 39). Furthermore, the capability of the theory seems to improve with increasing bistatic angle (see Figures 40 through 43 for  $\beta_a = 10.25$  degrees; see Figures 44 through 47 for  $\beta_a = 30.0$  degrees).

Frustum F5 is made by combining frustums F3 and F4. Monostatic results for F5 are given in Figures 48 through 51. Differences between theoretically and experimentally derived radar cross sections are maximum when the predicted return is determined by those scattering centers (  $S_1$  and  $S_2$  ) which have minimum separation. As noted in the table, a rather large offset error is present in monostatic measurements taken on frustum F5. This is because the actual phase reference used for measurements was the base of component F3, which is very close to the center of F5. To achieve the agreement shown in Figures 50 and 51, the phase reference for theoretical calculations was moved from the base of F5 to the center of the target. Accuracy of predictions improves when the bistatic angle is 10.25 degrees; the overall agreement between theory and measurement shown in Figures 52 through 55 is quite good. Finally, results for F5 with  $\beta_a = 30.0$  degrees are depicted in Figures 56 through 59. Here the agreement obtained between principal polarization radar cross sections is excellent. In the light of comments on the difficulties in comparing theoretical and experimental estimates of phase, the agreement obtained between principal polarization scattering phases is also excellent.

#### 4.2.3 Remarks

The study of frustum F3 is actually an examination of the low frequency capability of a high frequency technique. In this context, the agreement obtained is remarkable. Accuracy increases as the larger frustums (F4 and F5) are examined, and the results obtained for F5 with  $\beta_a = 30.0$  degrees are considered excellent.

Further analysis of scattering by this target at the broad-side aspect is required to eliminate the curve-fitting procedure presently employed.

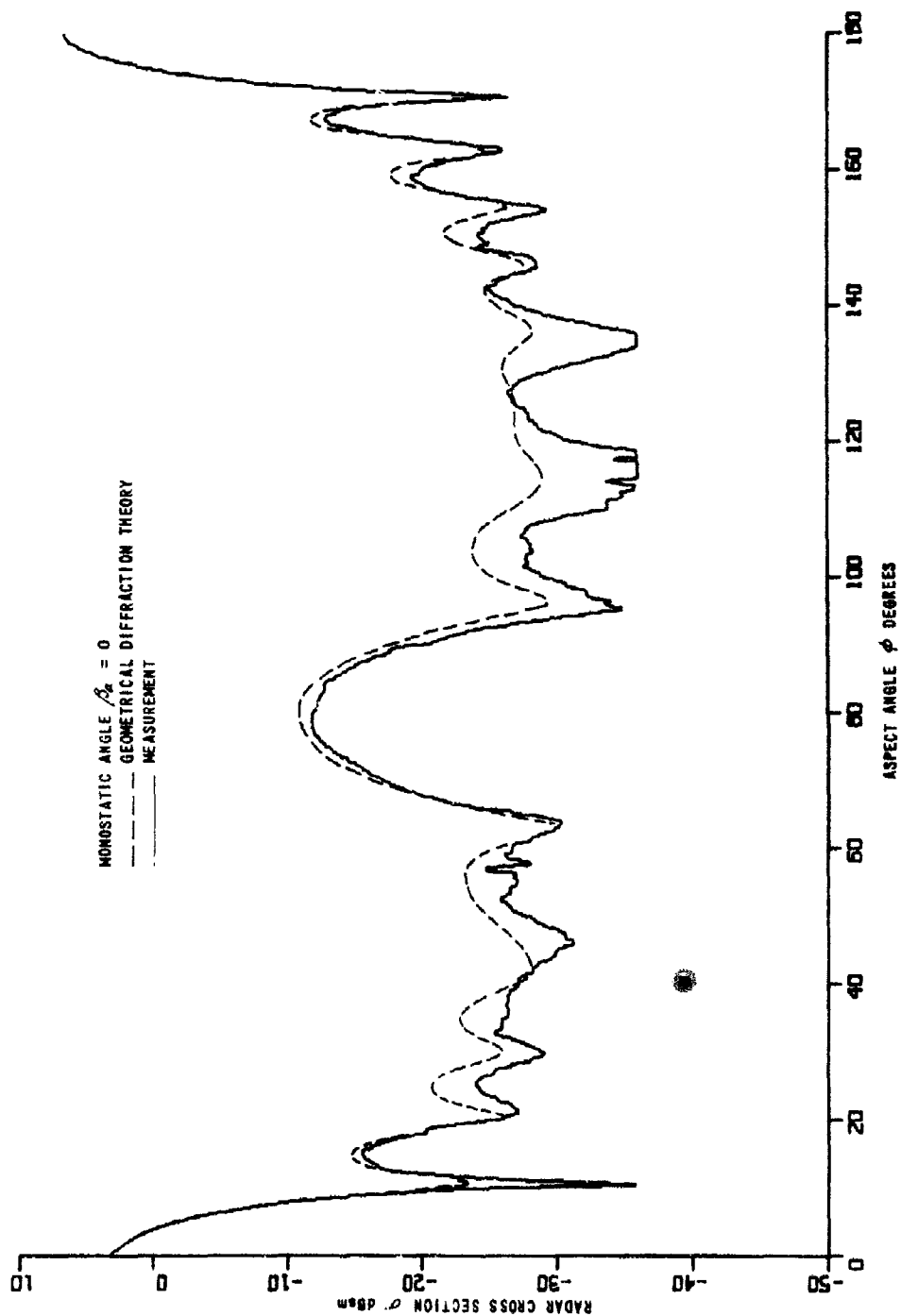


Figure 32 VERTICAL POLARIZATION RADAR CROSS SECTION. FRUSTUM F3 MONOSTATIC

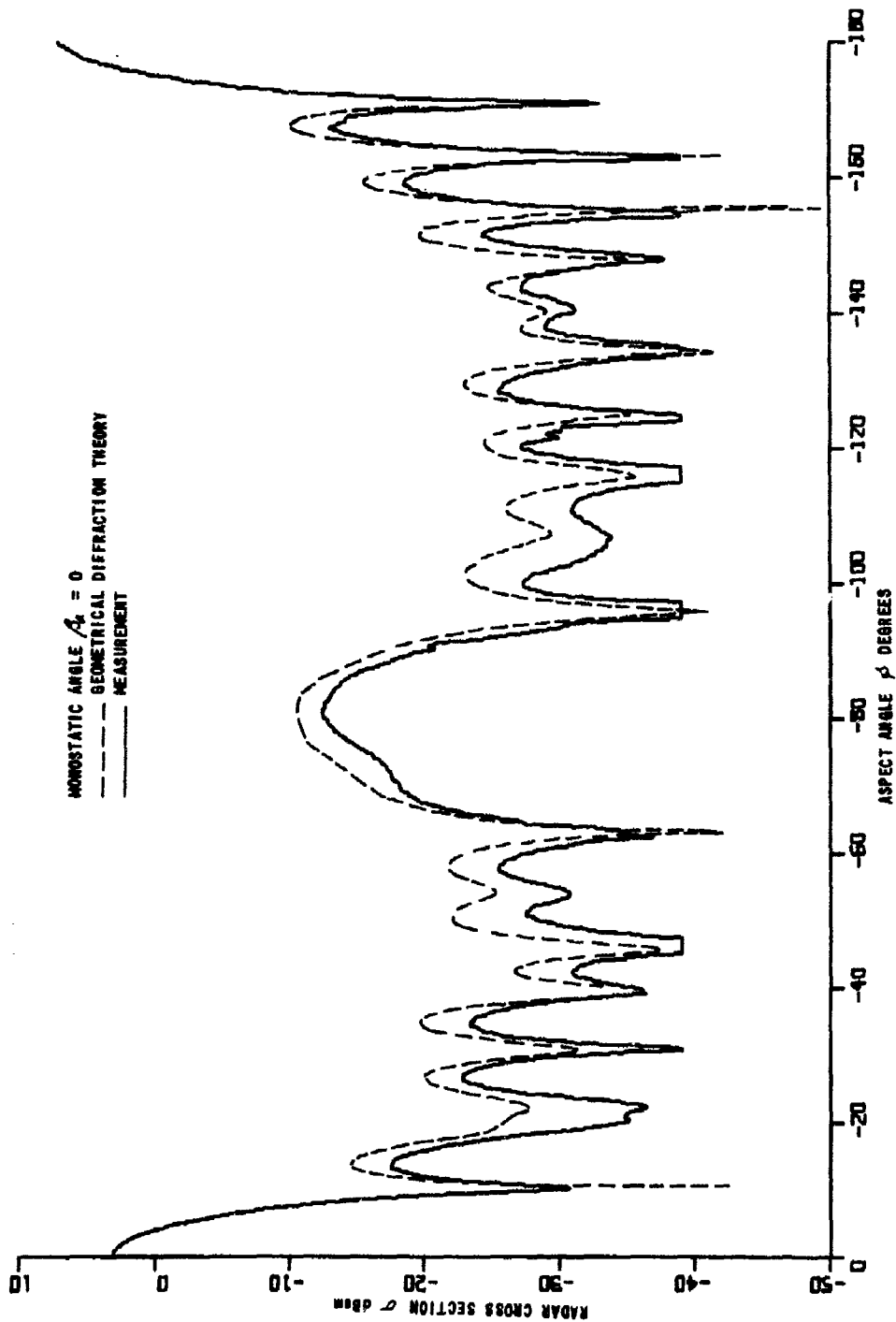


Figure 33 HORIZONTAL POLARIZATION RADAR CROSS SECTION. FRUSTUM F3, MONOSTATIC

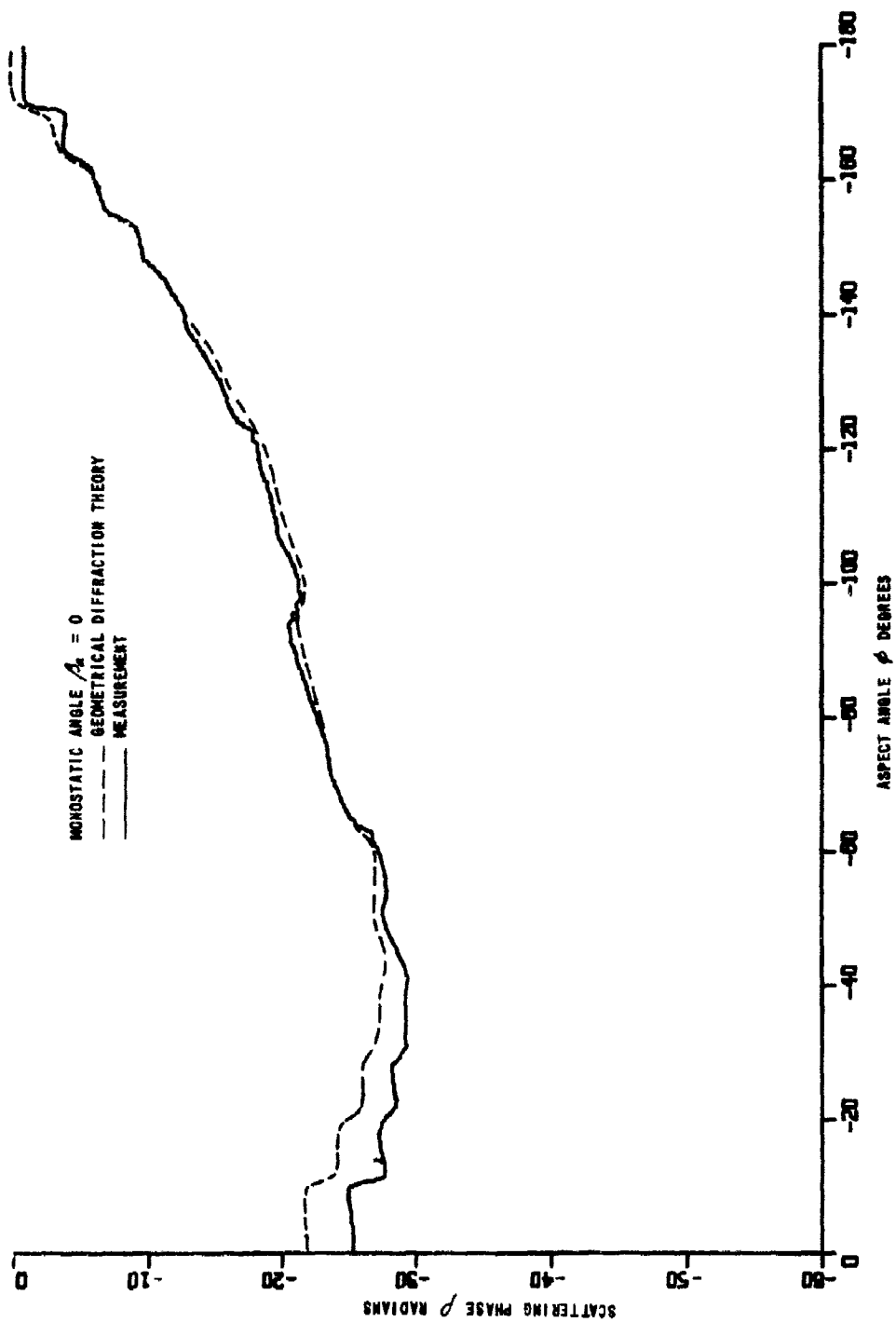


Figure 34 VERTICAL POLARIZATION SCATTERING PHASE. FRUSTUM F3, MONOSTATIC

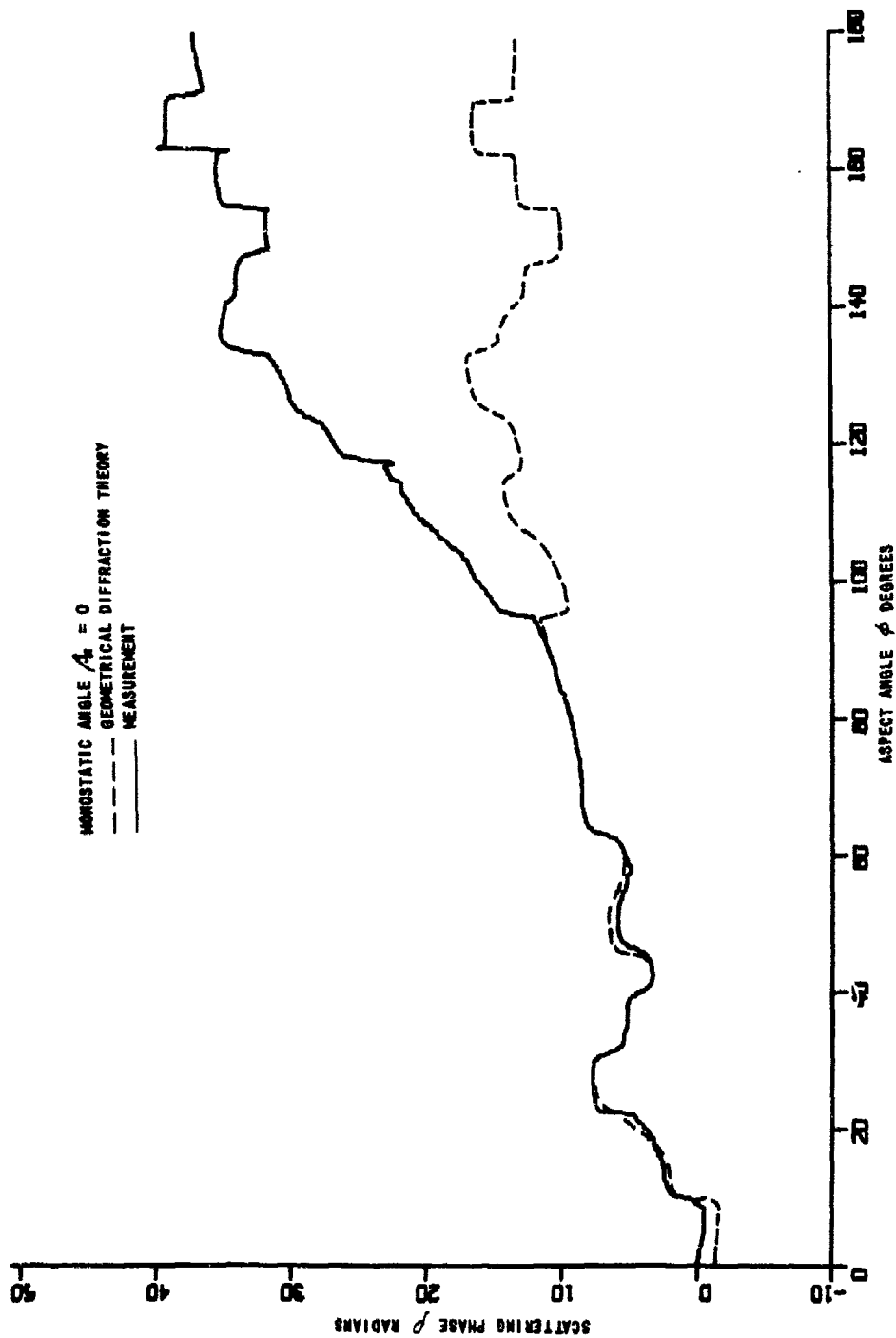


Figure 35 HORIZONTAL POLARIZATION SCATTERING PHASE. FRUSTUM F3, MONOSTATIC



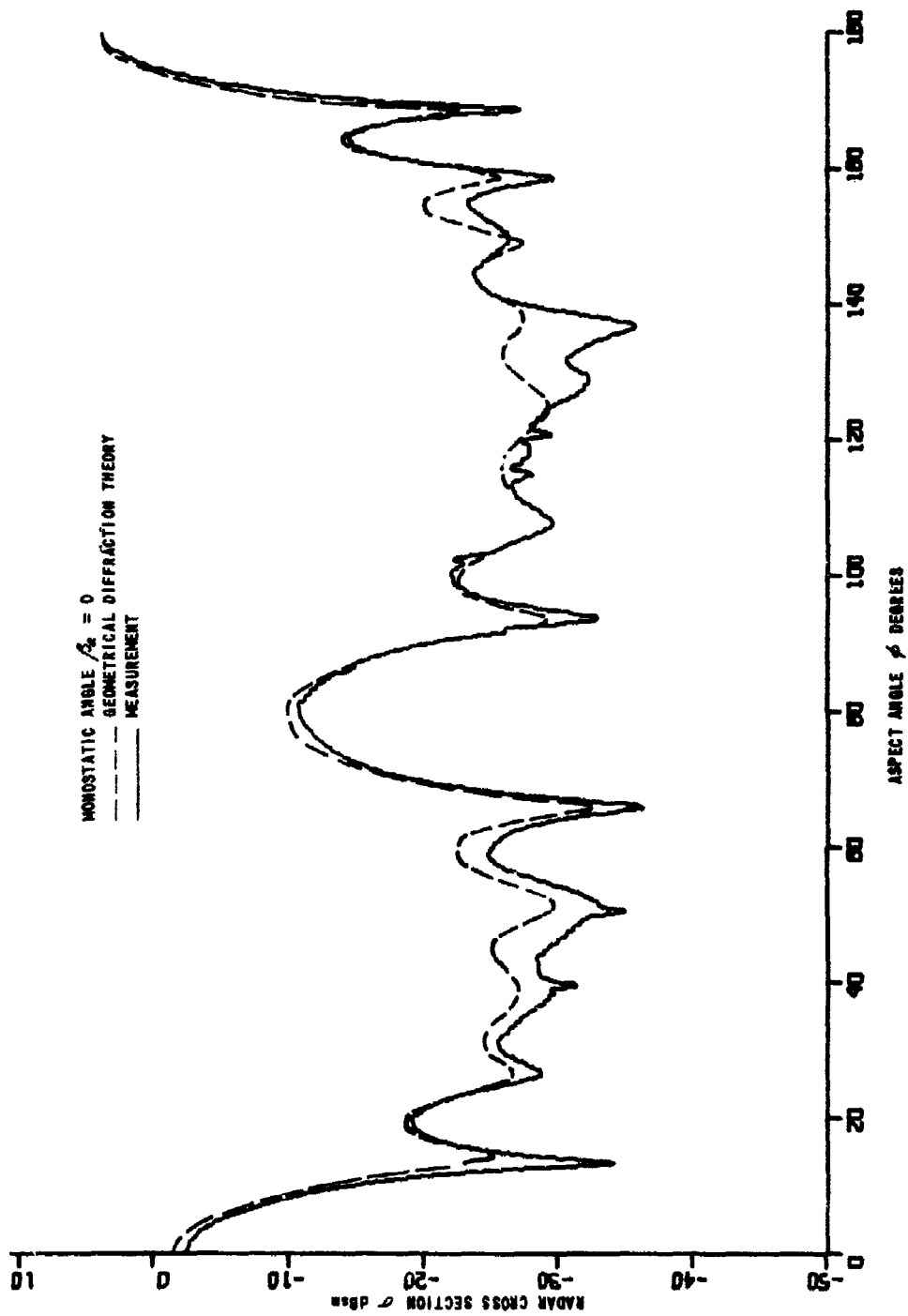


Figure 36 VERTICAL POLARIZATION RADAR CROSS SECTION. FRUSTUM F4, MONOSTATIC

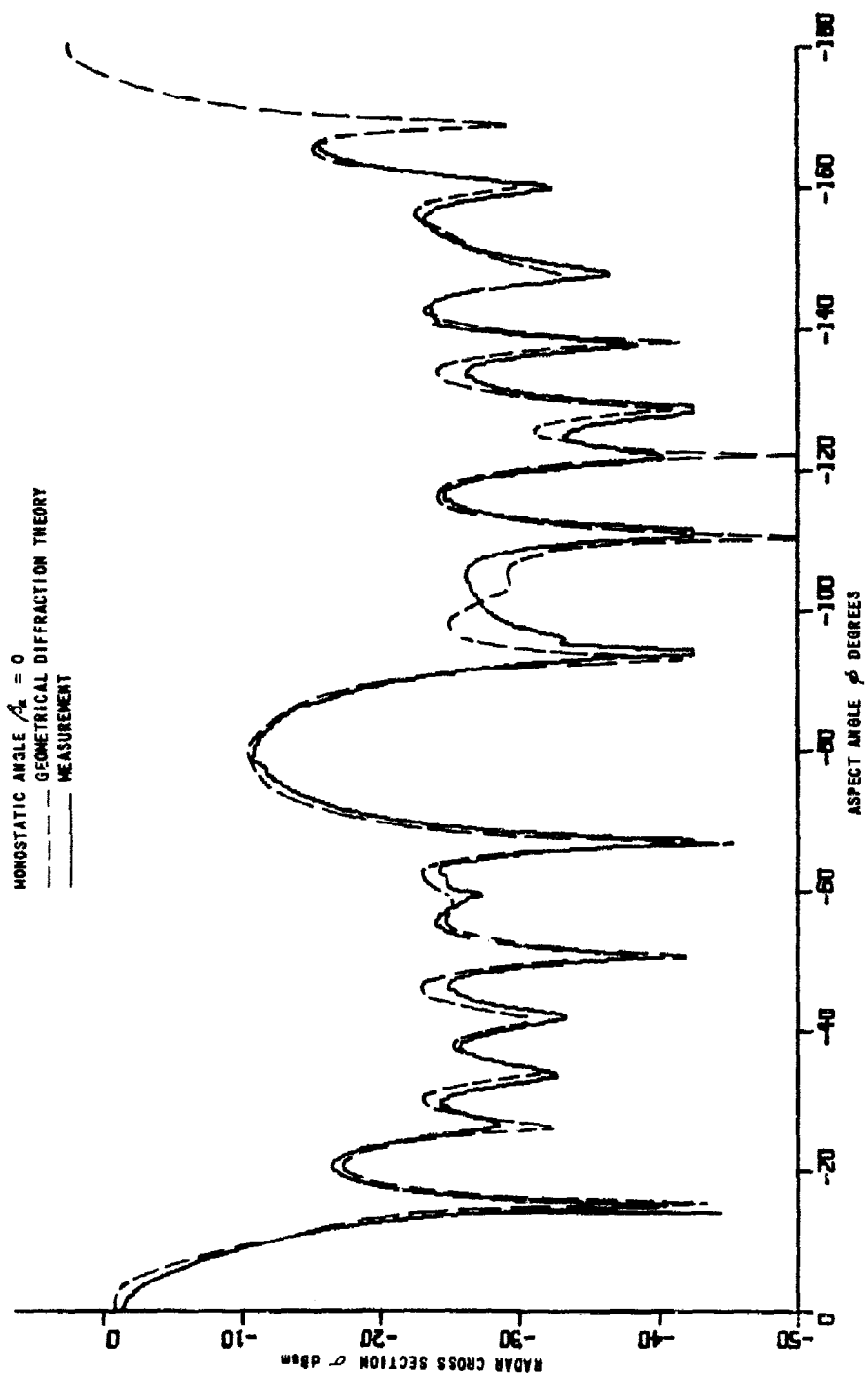


Figure 37 HORIZONTAL POLARIZATION RADAR CROSS SECTION. FRUSTUM FH, MONOSTATIC

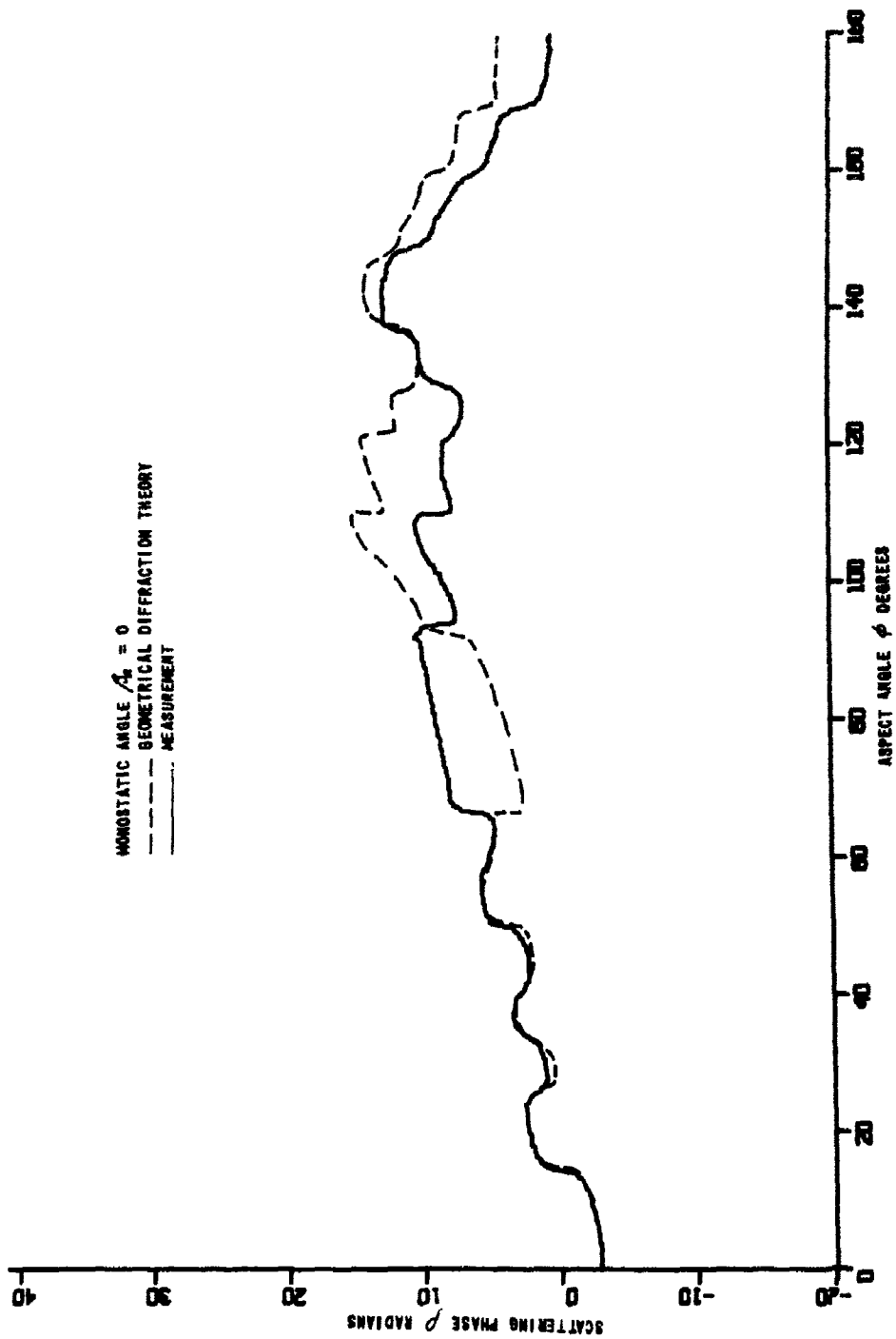


Figure 38 VERTICAL POLARIZATION SCATTERING PHASE. FRUSTUM F4, MONOSTATIC

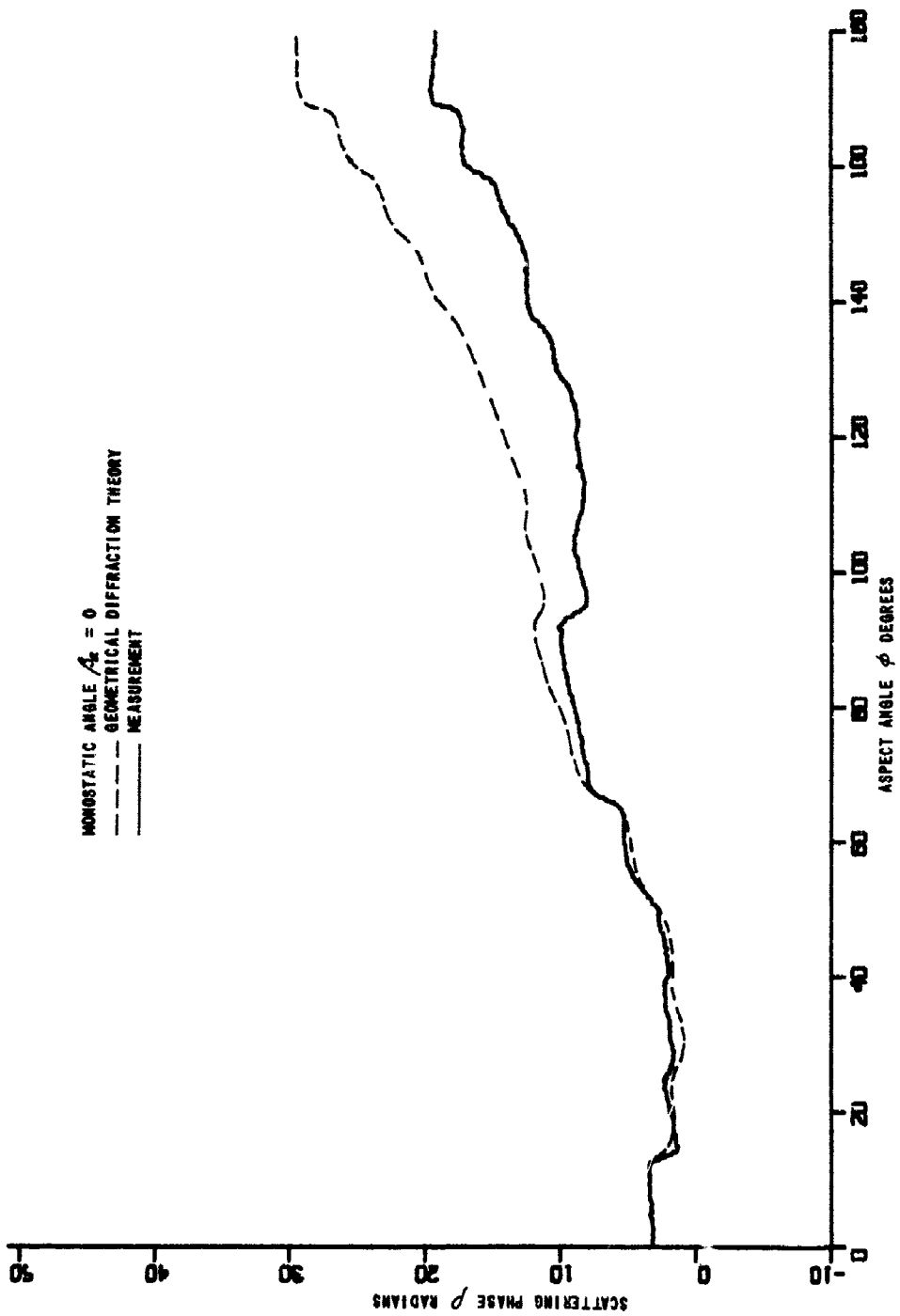


Figure 39 HORIZONTAL POLARIZATION SCATTERING PHASE, FRUSTUM F4, MONOSTATIC

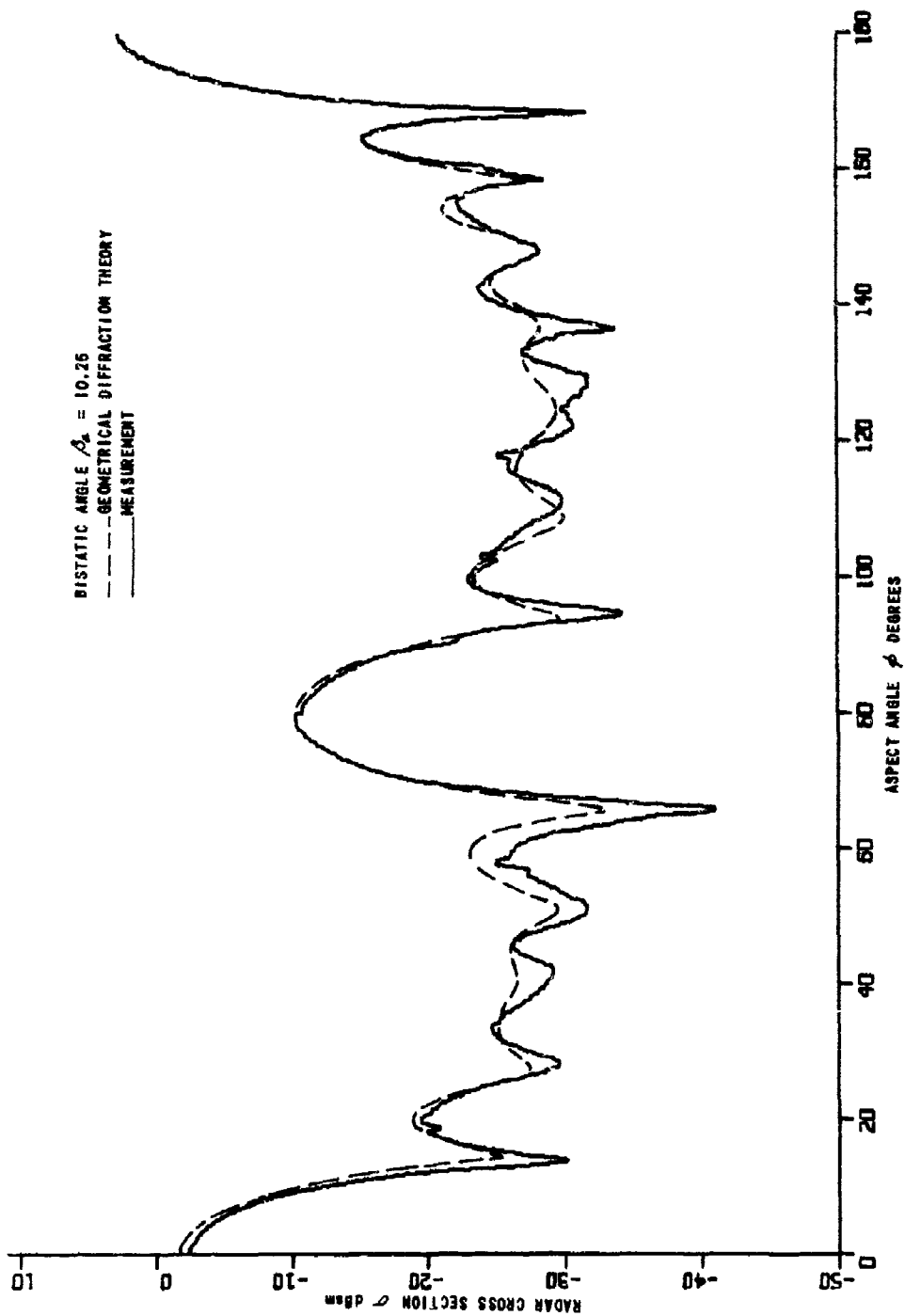


Figure 40 VERTICAL POLARIZATION RADAR CROSS SECTION. FRUSTUM F4, BISTATIC

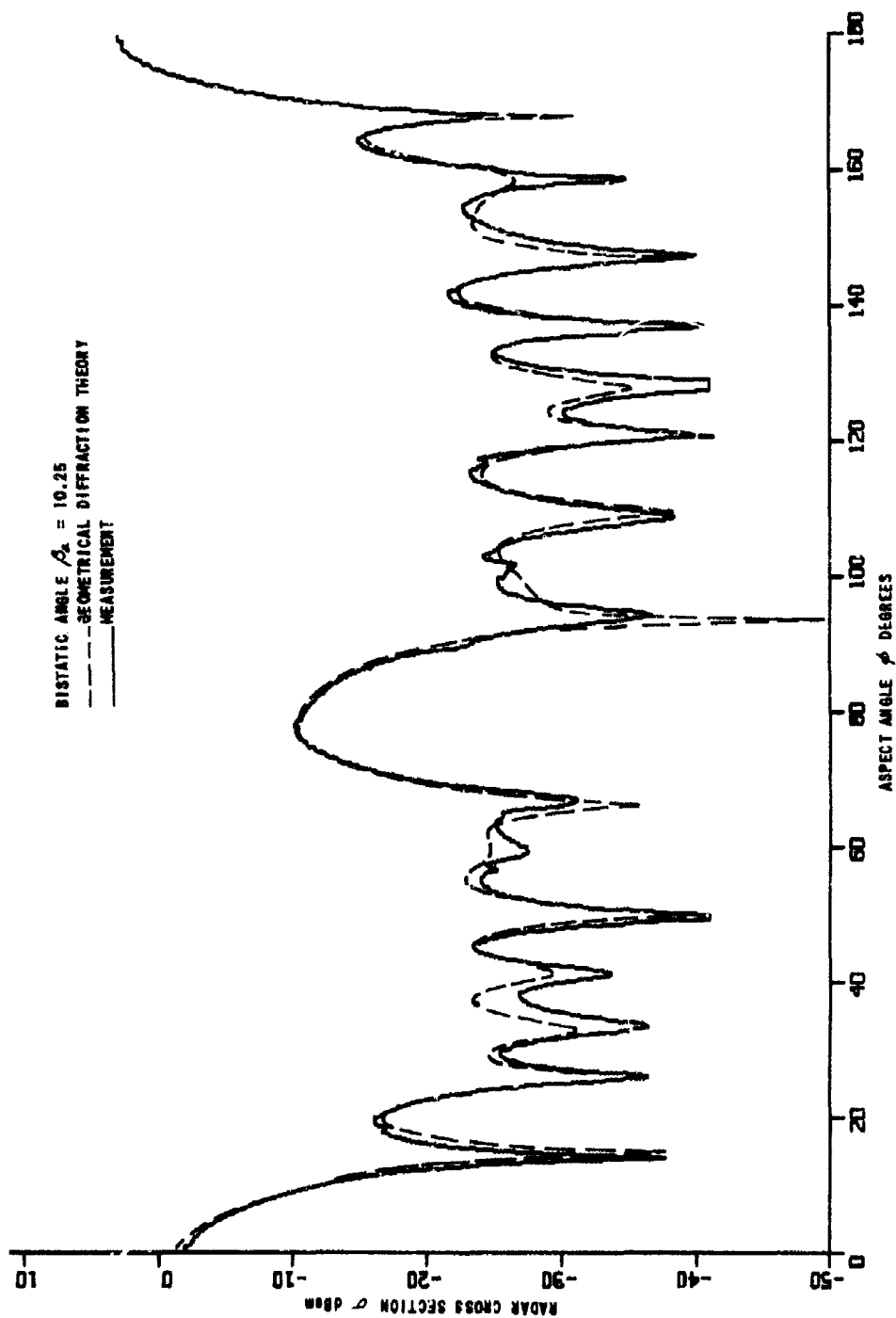


Figure 91 HORIZONTAL POLARIZATION RADAR CROSS SECTION. FRUSTUM PU, BISTATIC

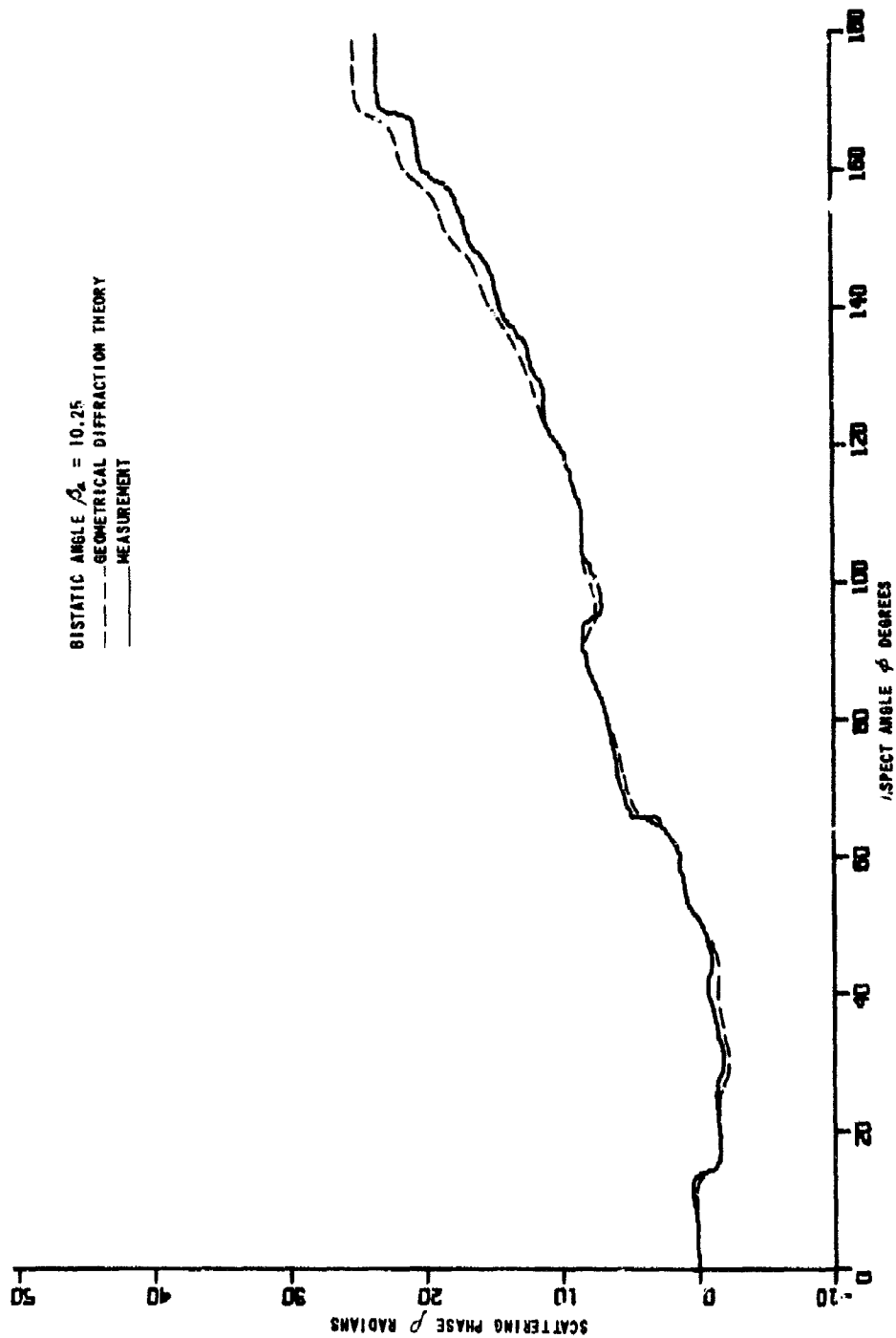


Figure 42 VERTICAL POLARIZATION SCATTERING PHASE. FRUSTRUM F4, BISTATIC

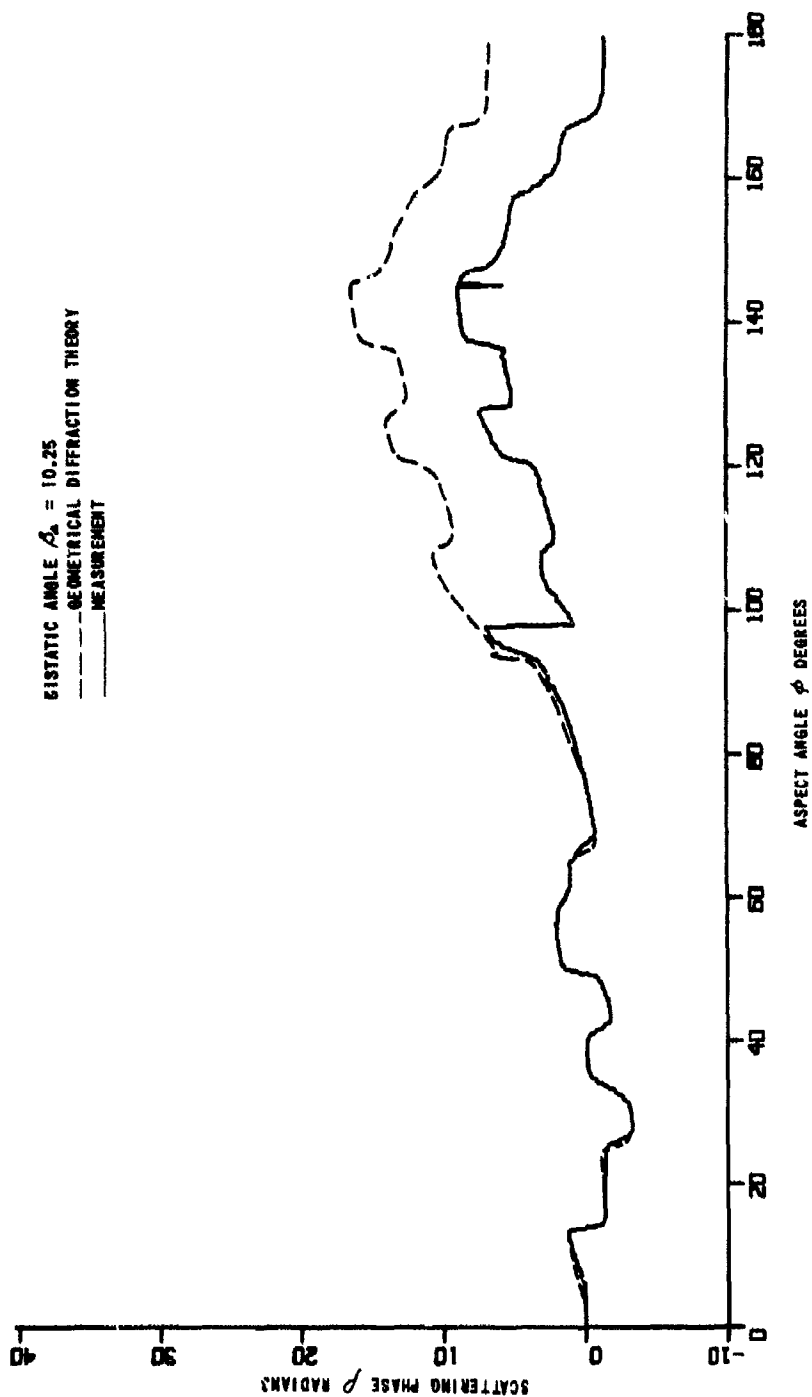


Figure N3 HORIZONTAL POLARIZATION SCATTERING PHASE. FRUSTUM F4, BISTATIC



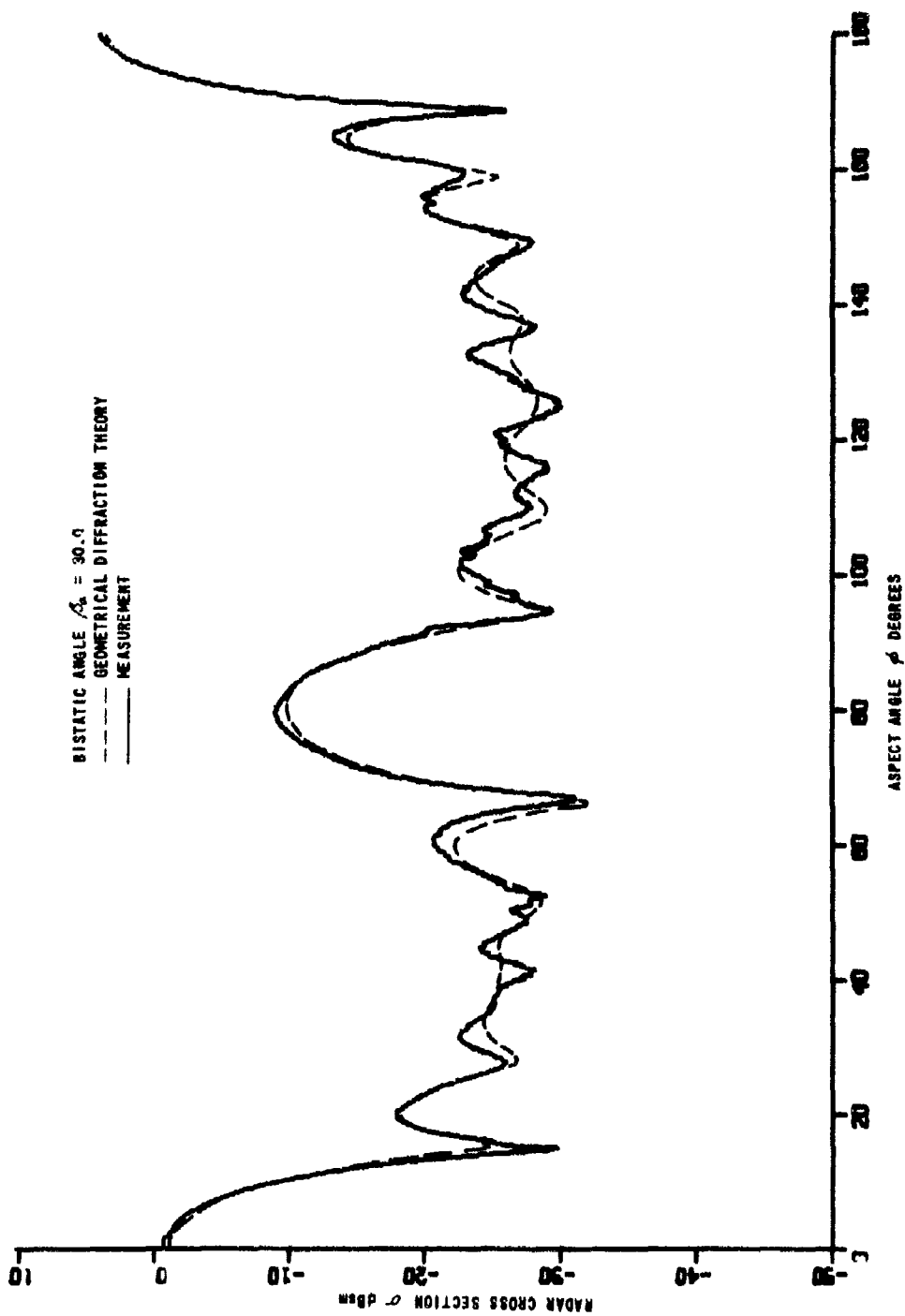


Figure 44 VERTICAL POLARIZATION RADAR CROSS SECTION. FRUSTUM F4, BISTATIC

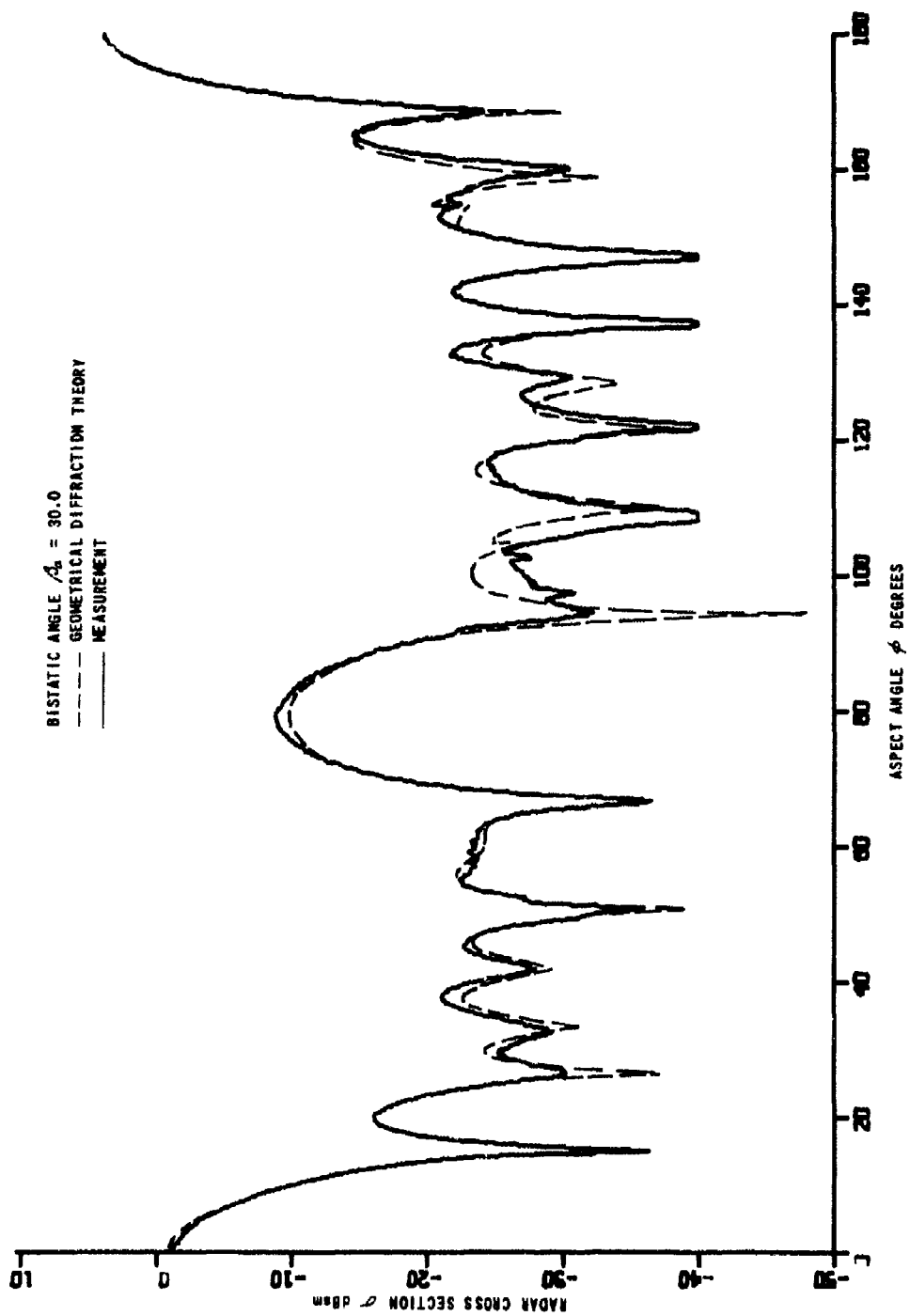


Figure 45 HORIZONTAL POLARIZATION RADAR CROSS SECTION. FRUSTUM F4, BISTATIC

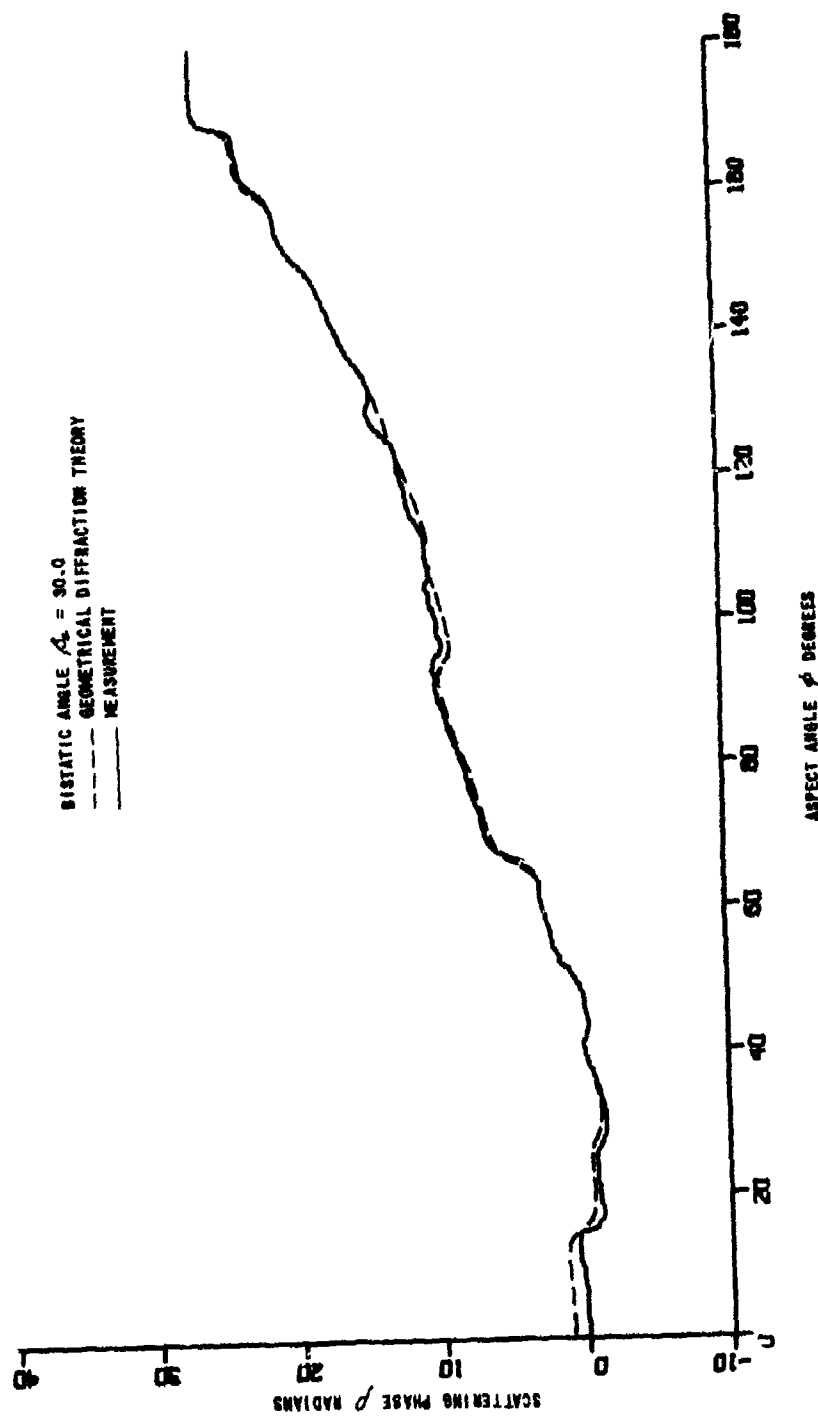


Figure 46 VERTICAL POLARIZATION SCATTERING PHASE. FRUSTUM F4, BISTATIC

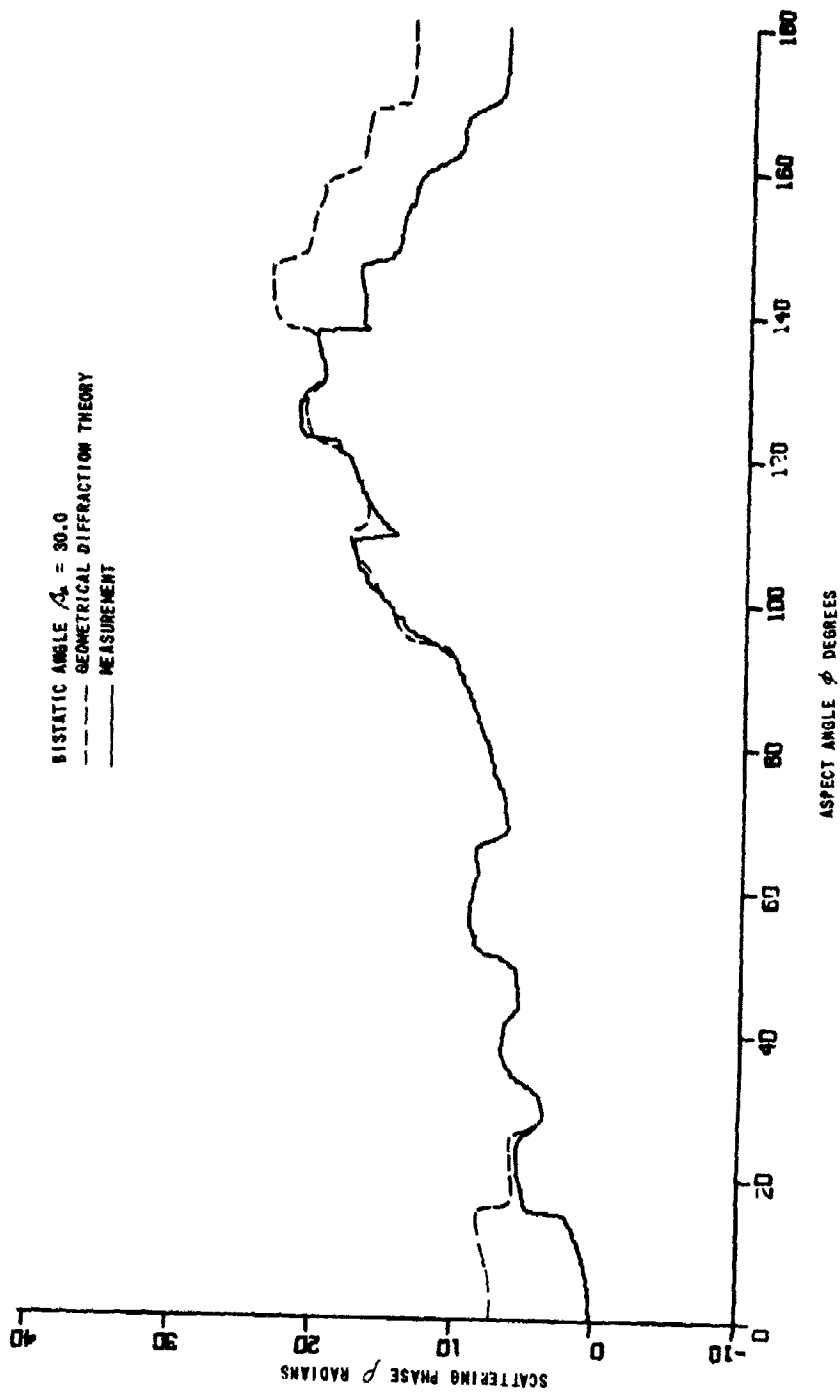


Figure 47 HORIZONTAL POLARIZATION SCATTERING PHASE. FRUSTUM F4, BISTATIC

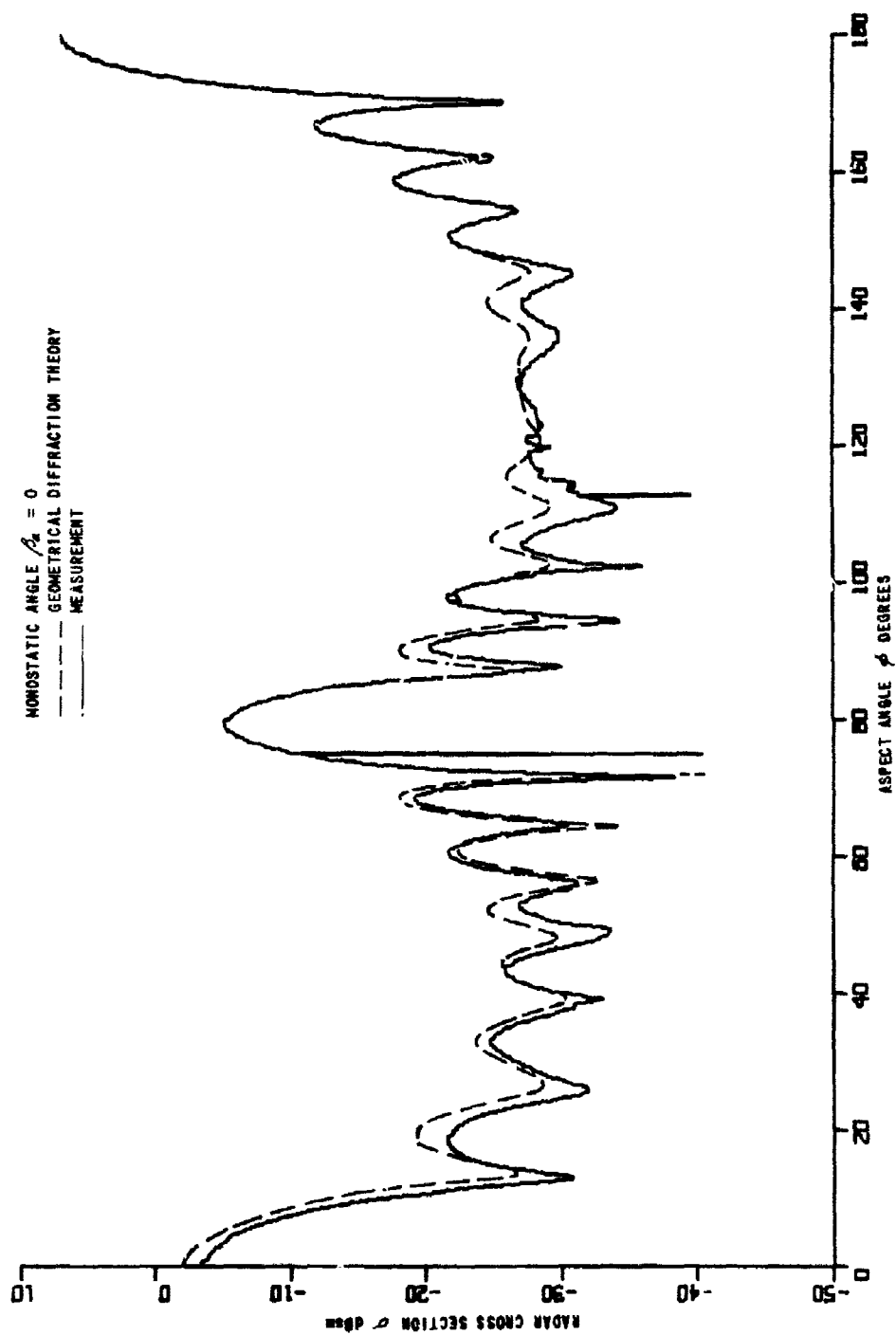


Figure 48 VERTICAL POLARIZATION RADAR CROSS SECTION. FRUSTUM F5, MONOSTATIC

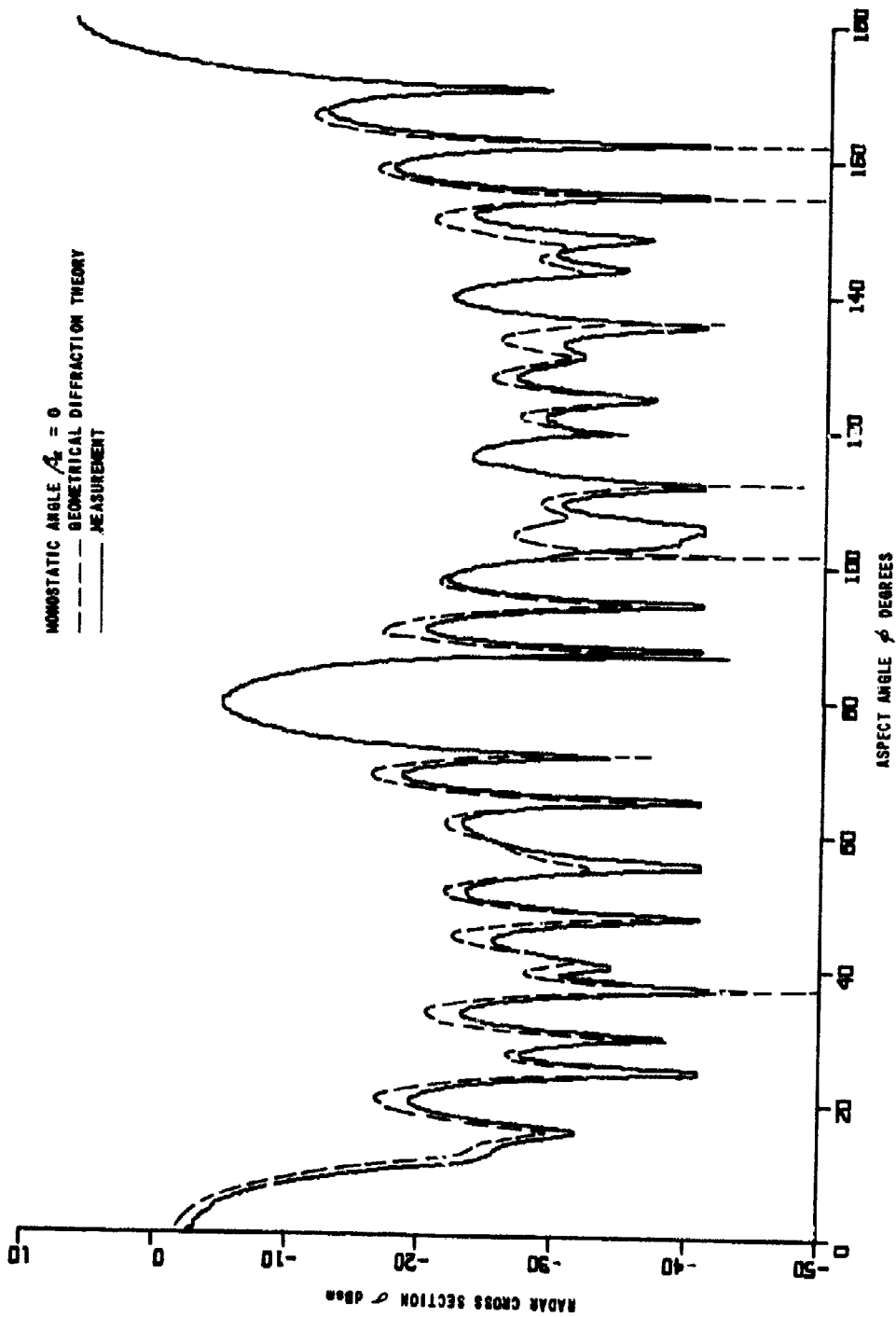


Figure 49 HORIZONTAL POLARIZATION RADAR CROSS SECTION. FRUSTUM F5, MONOSTATIC

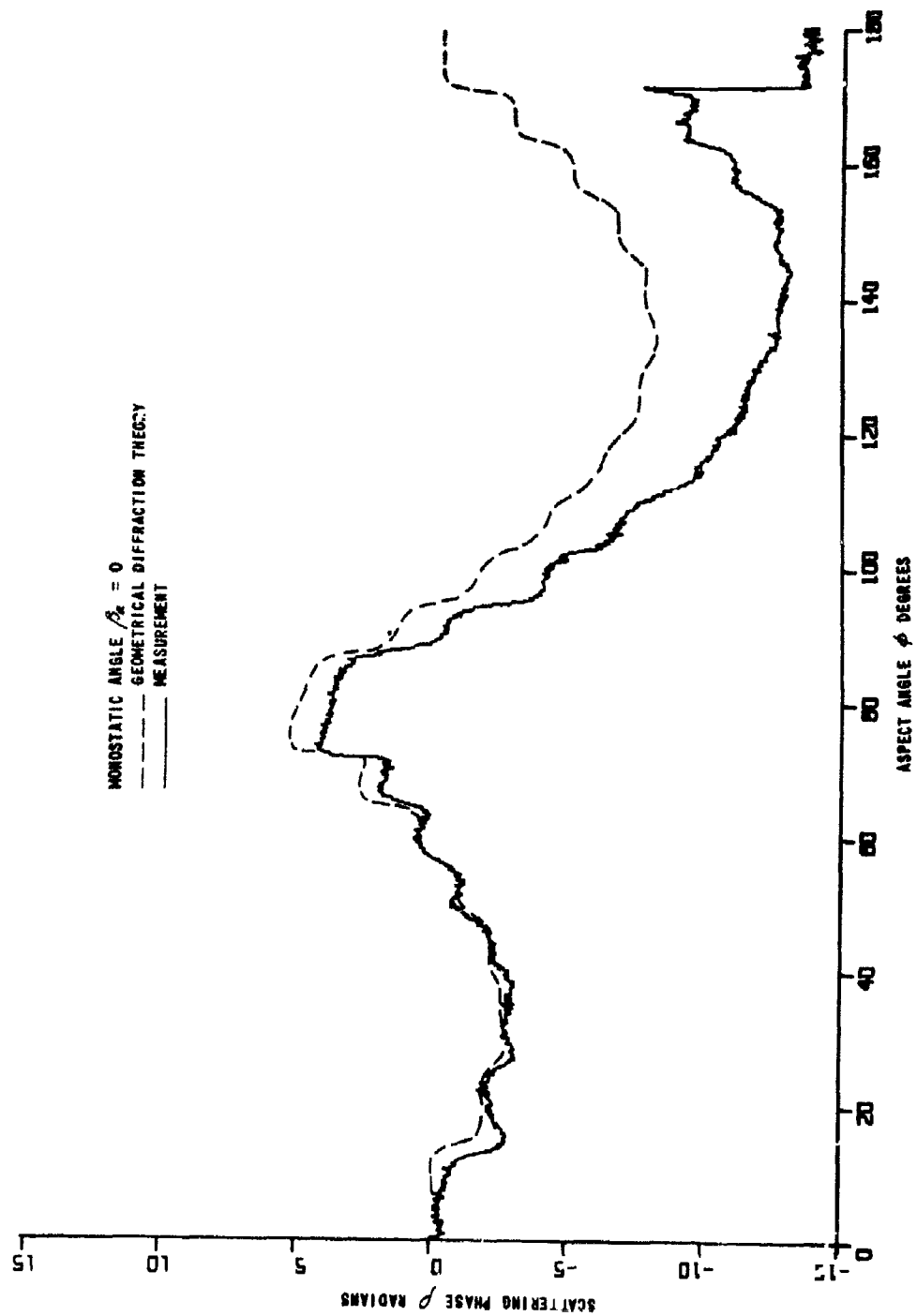


Figure 50 VERTICAL POLARIZATION SCATTERING PHASE. FRUSTUM F5, MONOSTATIC

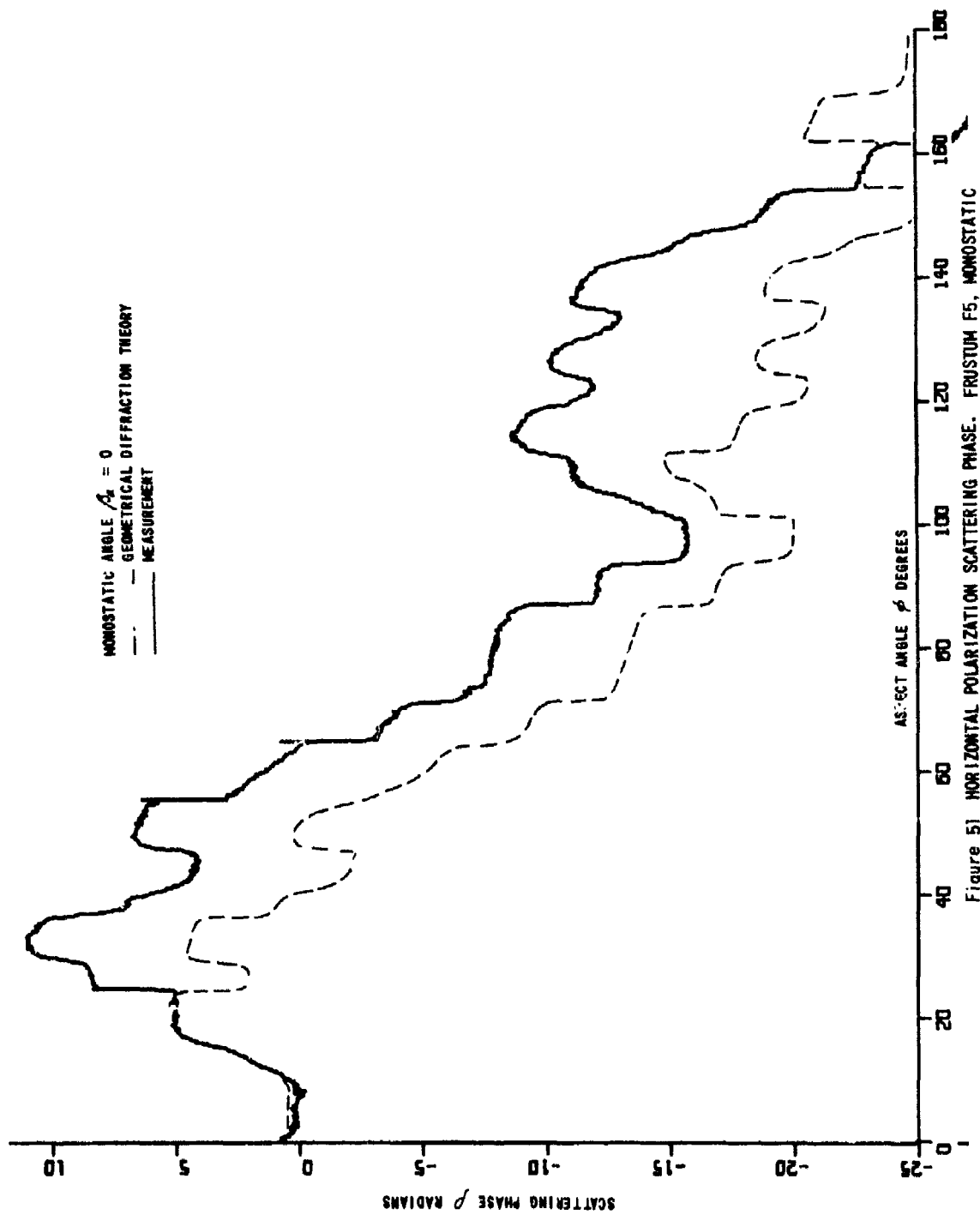


Figure 51 HORIZONTAL POLARIZATION SCATTERING PHASE. FRUSTUM F5, MONOSTATIC



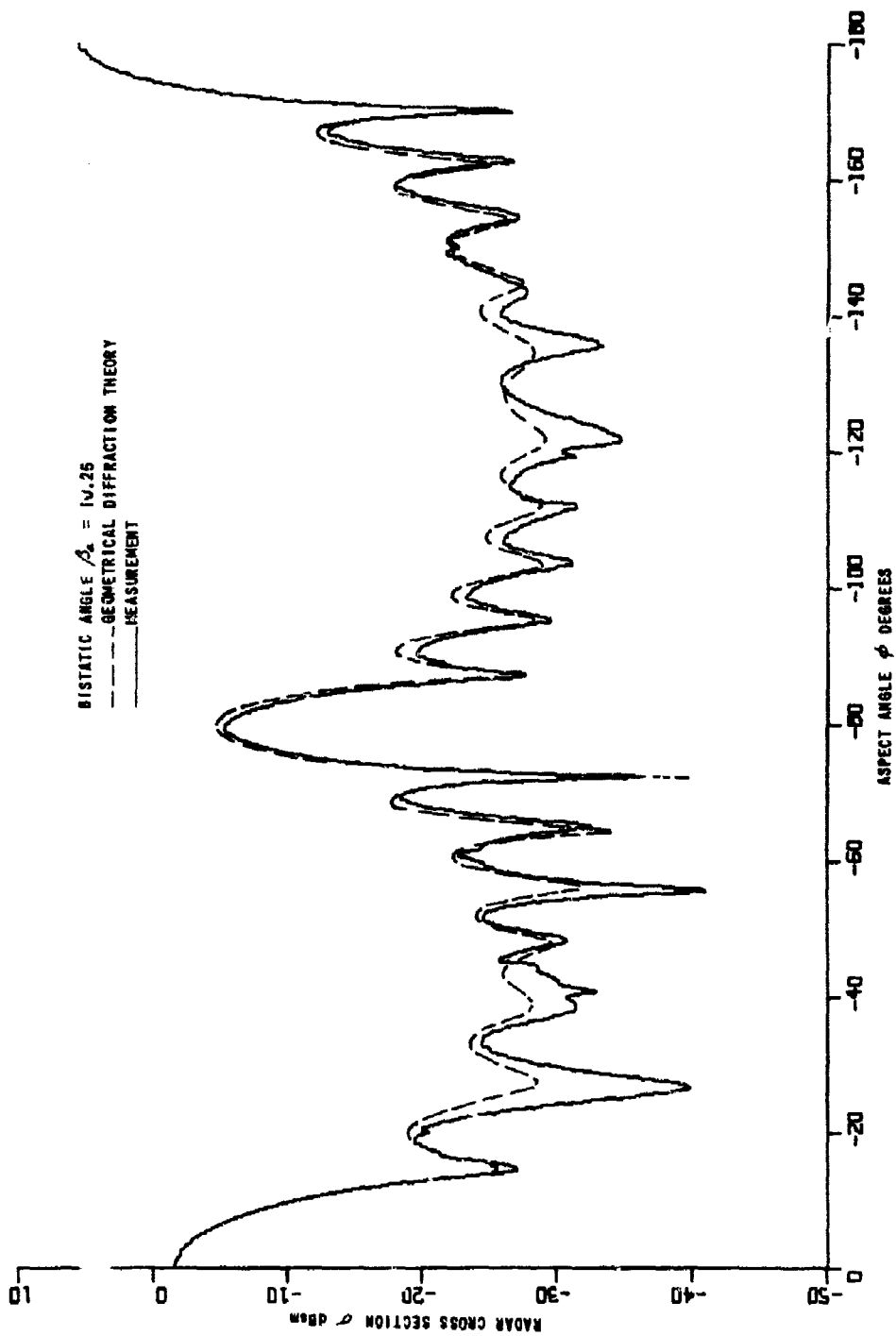


Figure 52 VERTICAL POLARIZATION RADAR CROSS SECTION. FRUSTUM F5, BISTATIC

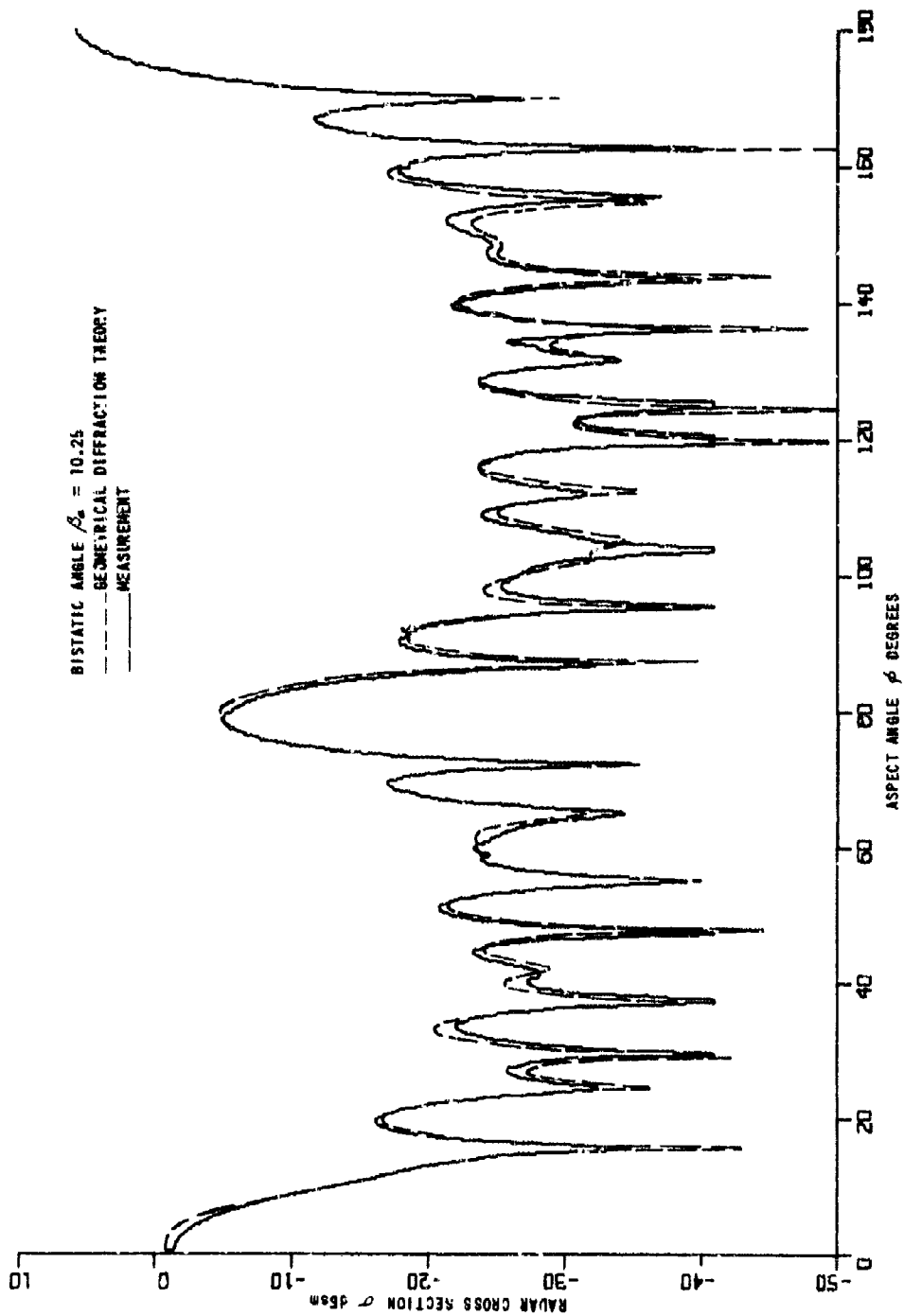


Figure 53 HORIZONTAL POLARIZATION RADAR CROSS SECTION. FRUSTUM F5, BISTATIC

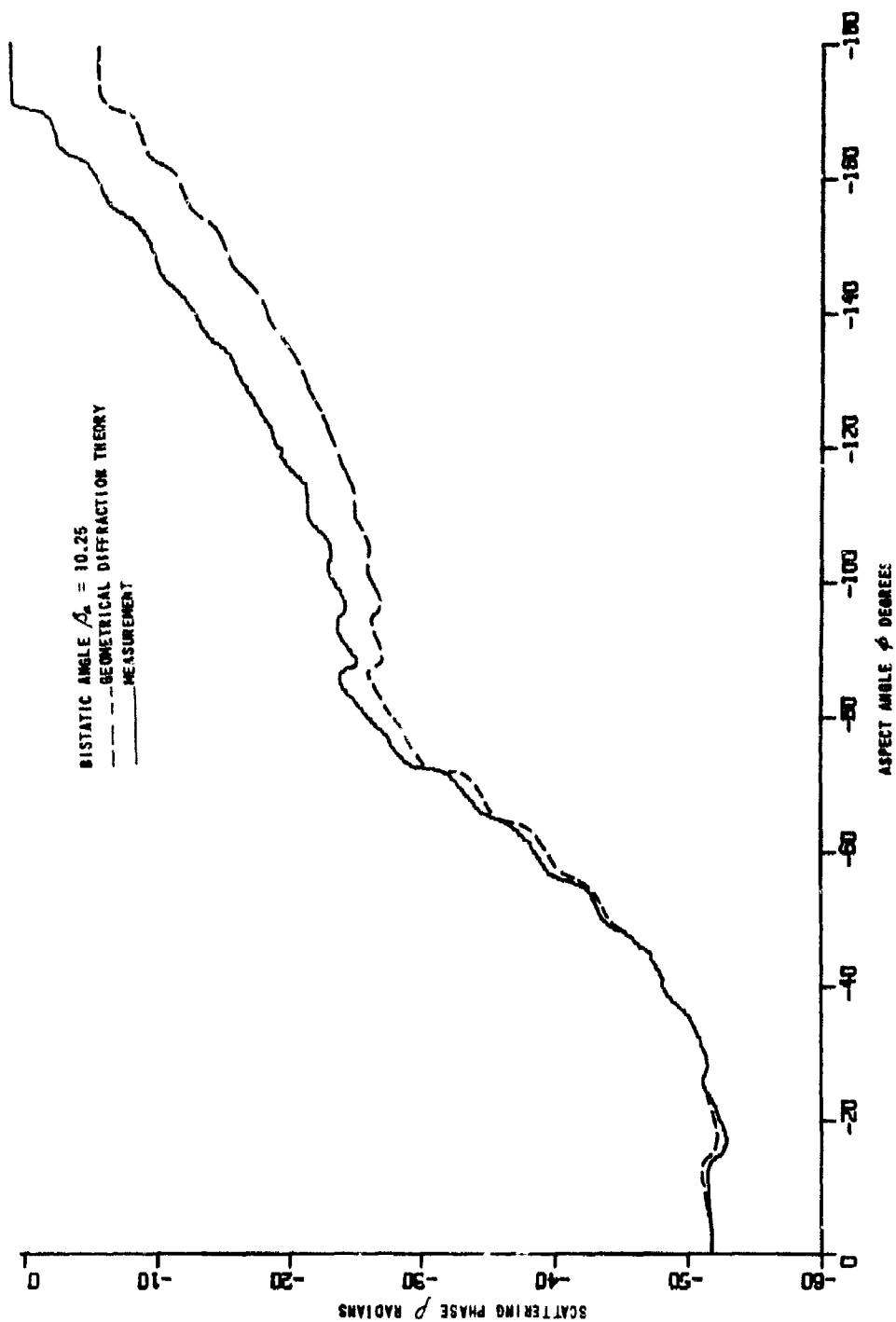


Figure 54 VERTICAL POLARIZATION SCATTERING PHASE. FRUSTUM F5, BISTATIC

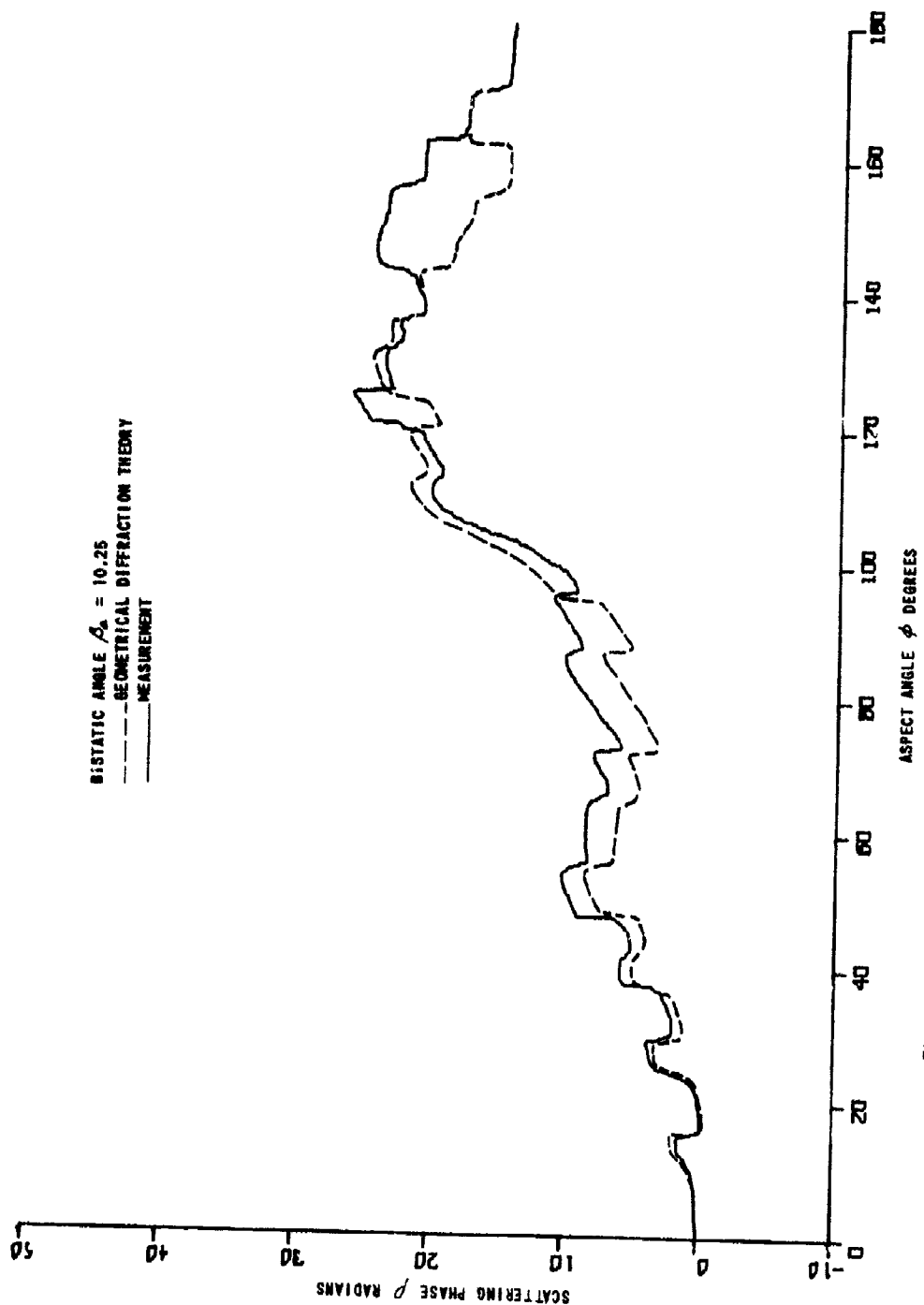


Figure 55 HORIZONTAL POLARIZATION SCATTERING PHASE. FRUSTUM F5, BISTATIC

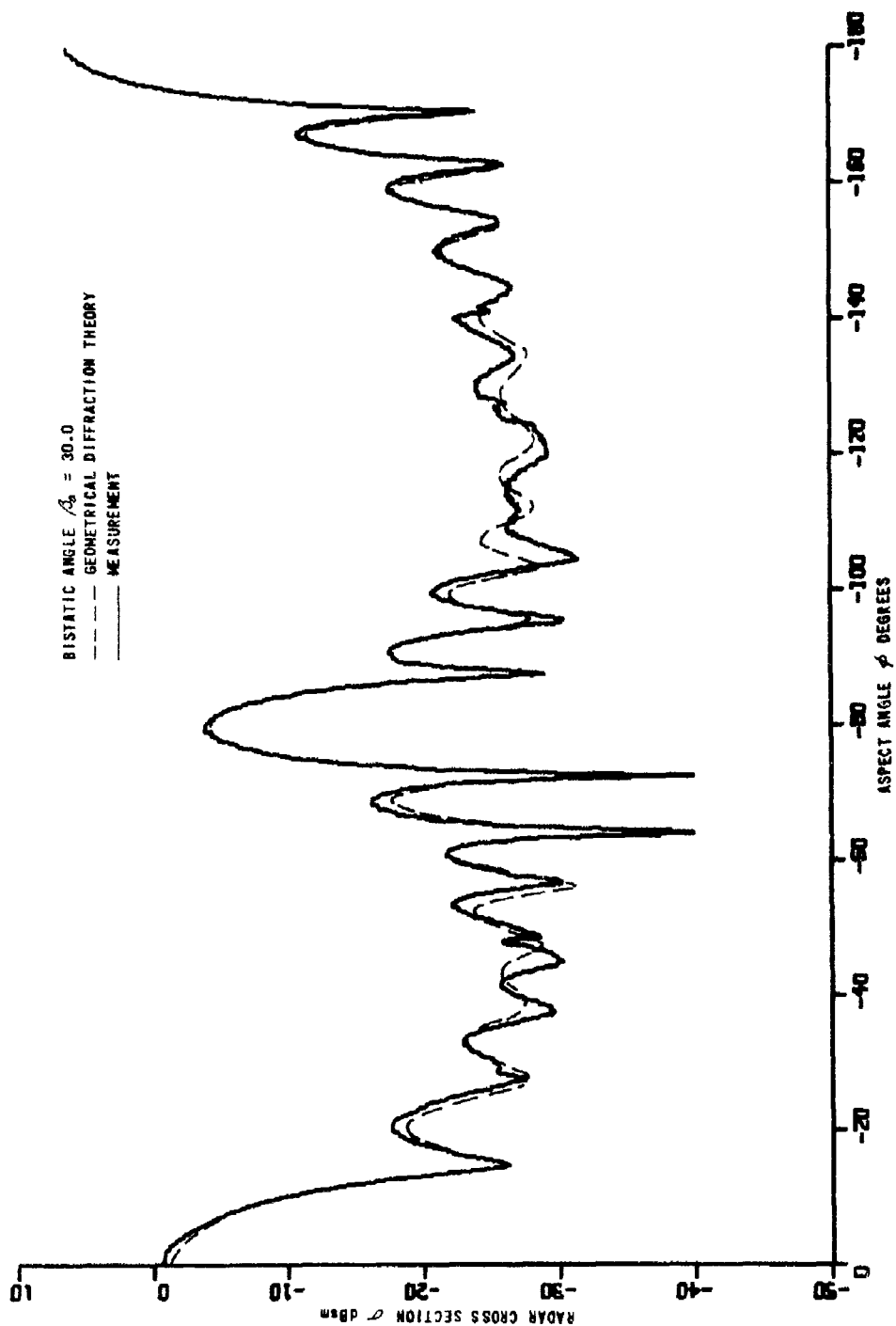


Figure 56 VERTICAL POLARIZATION RADAR CROSS SECTION. FRUSTUM F5, BISTATIC

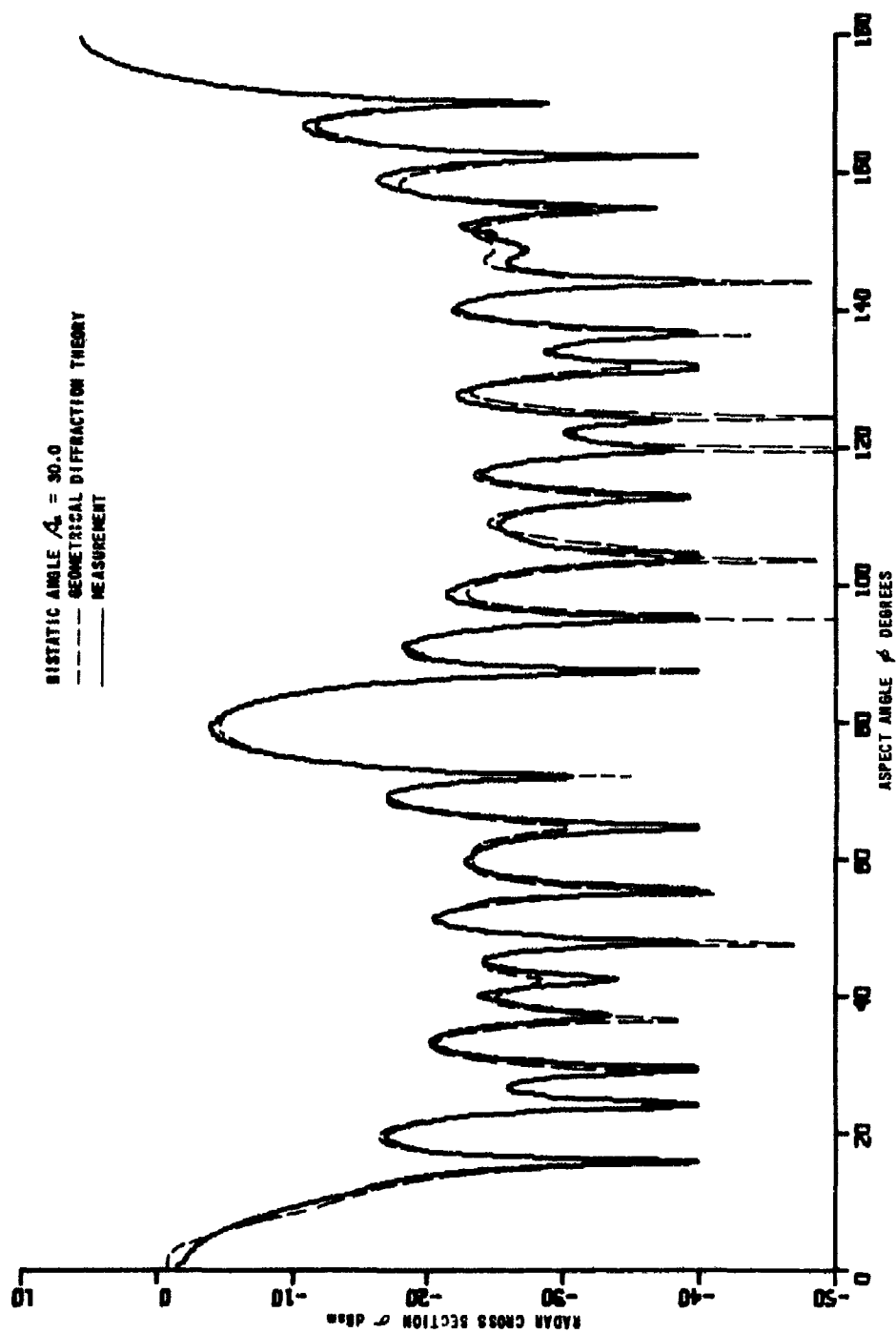


Figure 57 HORIZONTAL POLARIZATION RADAR CROSS SECTION. FRUSTUM F5, BISTATIC

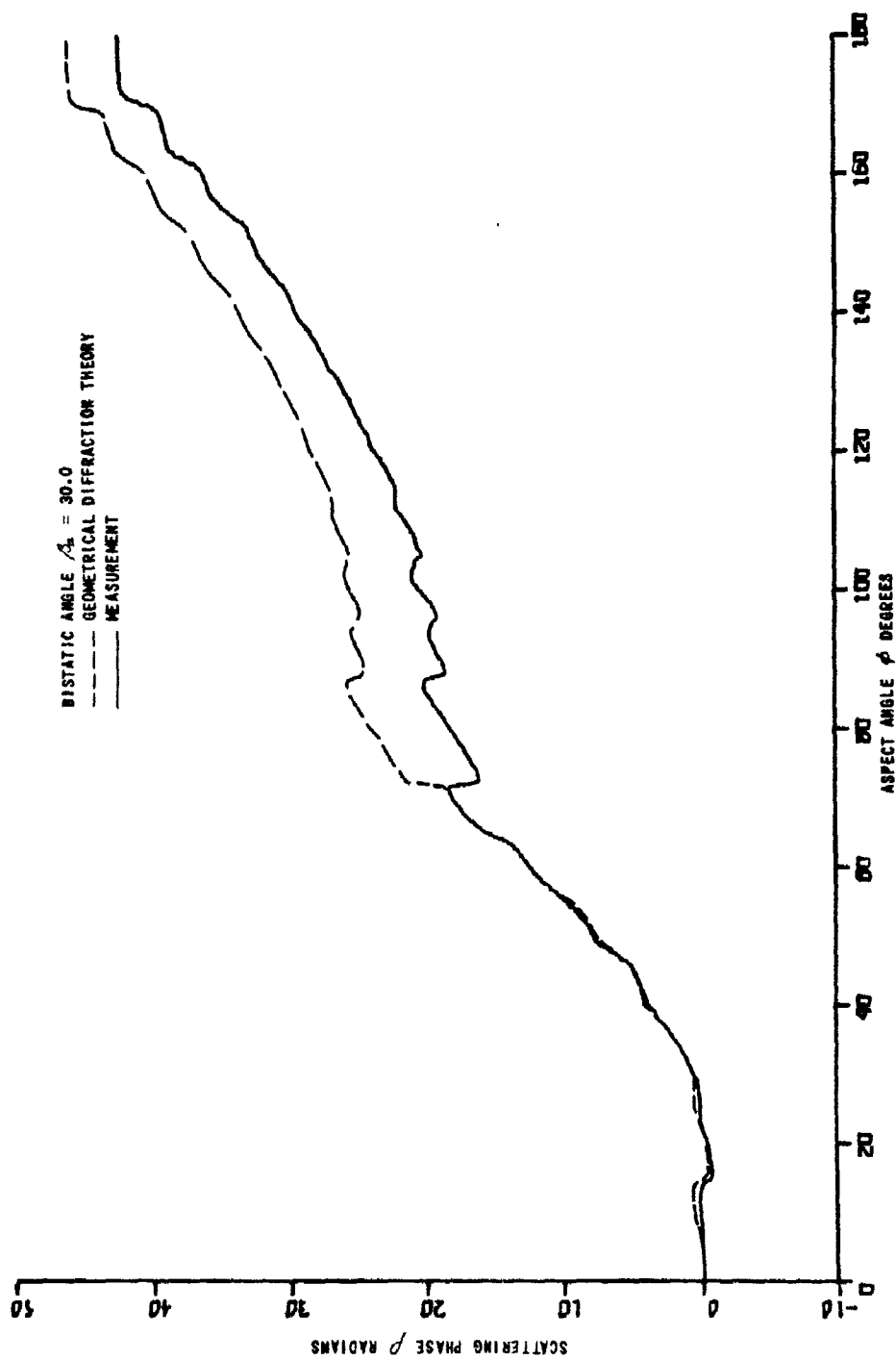


Figure 58 VERTICAL POLARIZATION SCATTERING PHASE. FRUSTUM F5, BISTATIC

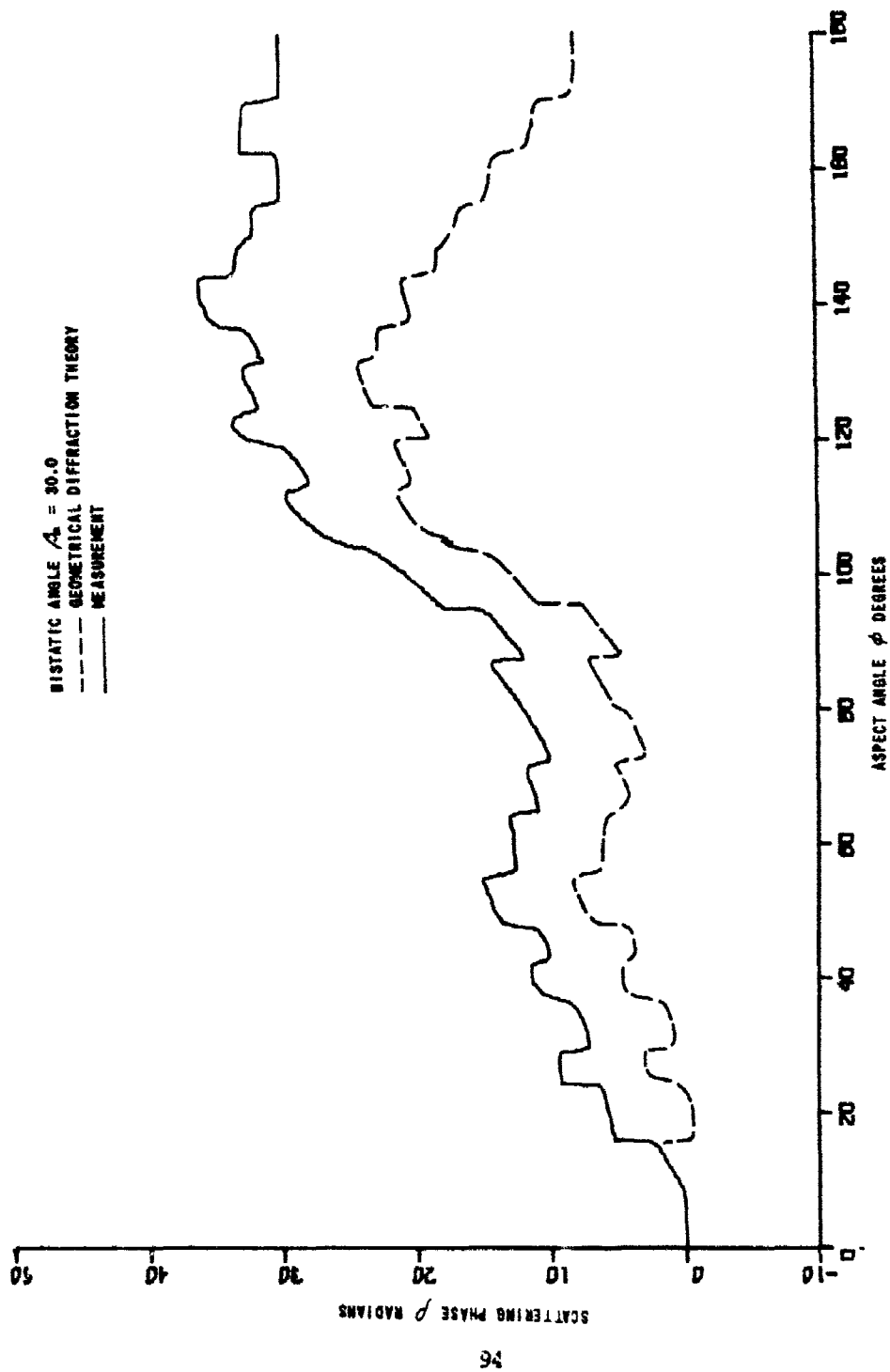


Figure 59 HORIZONTAL POLARIZATION SCATTERING PHASE. FRUSTUM F5, BISTATIC



### 4.3 CONE

Investigation of scattering by a cone is limited to preliminary analyses. It was recognized at the outset that the cone problem differed from the previously discussed problems of scattering by cylinders and frustums. The reason is that the creeping wave mechanism, which is of secondary importance in the case of the latter targets, is of primary importance for cones. For the cone, there exist no strong scattering centers to mask this contribution near axial aspects. An attempt to empirically upgrade the analysis using diagnostic short pulse data proved unsuccessful; no systematic creeping wave contribution was discovered (see subsection C.4 of Appendix C for a discussion of the diagnostic investigation). However, certain useful modifications to geometrical diffraction theory have been performed, and the present status of the cone problem is reported below.

#### 4.3.1 Analytical Formulation

Figure 60 illustrates monostatic illumination of a finite, right-circular cone of length  $2h$  and base diameter  $2a$ . The scattering

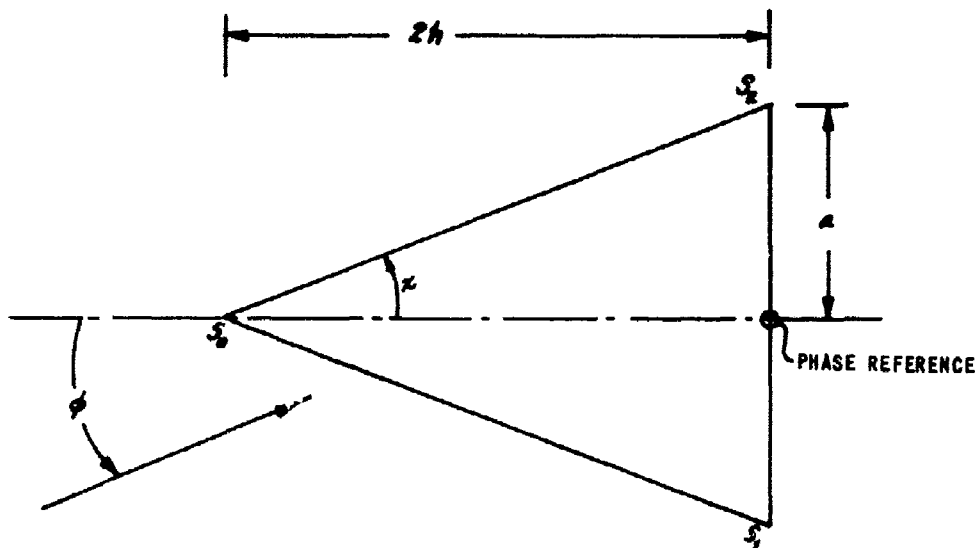


Figure 60 SCATTERING CENTERS ON CONE

matrix of the cone is to be found. The two extremities of the target are geometric discontinuities which form three scattering centers ( $S_0$ ,  $S_1$ , and  $S_2$  in Figure 60). Previously reported applications of geometrical diffraction theory to a cone are reviewed in Appendix C. They provide expressions for singly-diffracted contributions from centers  $S_1$  and  $S_2$ :

$$\sqrt{\sigma_1} = \frac{\sin(\pi/n_1)}{n_1} \sqrt{\frac{a \csc \phi}{k}} \left[ \left\{ \cos \frac{\pi}{n_1} - \cos \frac{3\pi - 2\phi}{n_1} \right\}^{-1} \mp \left\{ \cos \frac{\pi}{n_1} - 1 \right\}^{-1} \right] \quad (38)$$

$$\begin{aligned} \sqrt{\sigma_2} &= \frac{\sin(\pi/n_1)}{n_1} \sqrt{\frac{a \csc \phi}{k}} \left[ \left\{ \cos \frac{\pi}{n_1} - \cos \frac{3\pi + 2\phi}{n_1} \right\}^{-1} \mp \left\{ \cos \frac{\pi}{n_1} - 1 \right\}^{-1} \right] \\ &= 0; \quad \pi < \phi < \pi/2 \end{aligned} \quad (39)$$

$$\begin{aligned} &= \frac{\sin(\pi/n_1)}{n_1} \sqrt{\frac{a \csc \phi}{k}} \left[ \left\{ \cos \frac{\pi}{n_1} - \cos \frac{\pi - 2\phi}{n_1} \right\}^{-1} \right. \\ &\quad \left. \mp \left\{ \cos \frac{\pi}{n_1} - 1 \right\}^{-1} \right] \end{aligned}$$

$$\rho_1 = \frac{\pi}{4} - 2ka \sin \phi \quad (40)$$

$$\rho_2 = -\frac{\pi}{4} + 2ka \sin \phi \quad (41)$$

where  $n_1 = 3/2 + \pi/\pi$  and angular, polarization, and parametric conventions are those detailed in earlier discussions.

Singularities may arise in Equations 38 and 39 at axial aspects ( $\phi = 0, \pi$ ) and at the broadside aspect ( $\phi = \frac{\pi}{2} - \alpha$ ). For incidence at and near tail-on, we employ the small angle modification to obtain the specular contribution

$$(\sqrt{\sigma_1} e^{j\rho_1} + \sqrt{\sigma_2} e^{j\rho_2})_{poli} = 2\sqrt{\pi} ka \frac{J_1(2ka \sin \phi)}{(2ka \sin \phi)} e^{-j\pi/2} \quad (42)$$

Equation 42 applies for  $\phi > \pi - \phi_{ca}$  where the cross-over angle is given by  $2ka \sin \phi_{ca} = 2.44$ . Again the constraint  $\csc \phi \leq ka \cos \frac{\phi}{2}$  is introduced to limit the polarization-dependent terms in Equations 38 and 39. For incidence in the limited region near nose-on ( $0 \leq \phi \leq \alpha$ ), we modify the theory and replace Equations 38 through 41 with the expression

$$\begin{aligned} \sqrt{\sigma_1} e^{j\rho_1} + \sqrt{\sigma_2} e^{j\rho_2} = & \frac{2\sqrt{\pi} a \sin \pi/n_1}{n_1} \left[ \left\{ \cos \frac{\pi}{n_1} - \cos \frac{3\pi}{n_1} \right\}^{-1} J_0(2ka \sin \phi) \right. \\ & \left. - \frac{i \frac{2 \tan \phi}{n_1} \sin \frac{3\pi}{n_1}}{\left( \cos \frac{\pi}{n_1} - \cos \frac{3\pi}{n_1} \right)^2} J_1(2ka \sin \phi) + \left\{ \cos \frac{\pi}{n_1} - 1 \right\}^{-1} J_2(2ka \sin \phi) \right] \quad (43) \end{aligned}$$

A detailed derivation of Equation 43 is presented in subsection C.2.2 of Appendix C.

In the aspect region  $\alpha < \phi < \frac{\pi}{2}$ , the above description only allows a contribution from scattering center  $J_1$ . This angular interval includes the broadside aspect ( $\phi = \frac{\pi}{2} - \alpha$ ), for which case Equation 38 contains a singularity in the diffraction coefficient. Thus the theory in its present form predicts a smooth return throughout the interval  $\alpha < \phi < \frac{\pi}{2}$ , with a cusp when incidence is broadside. However, measurements reveal lobe structure in the same angular interval. In an attempt to extend the capability of geometrical diffraction theory, we introduce an approximate expression for the contribution from the cone tip: the result is approximate because the tip diffraction coefficient is unknown. Now we have contributions

from centers  $S_1$  and  $S_2$ , and the interaction will produce lobe structure. If the proper contribution from center  $S_0$  could be determined, we could expect the modified theory to fail gracefully at the broadside aspect, and the curve-fitting routine introduced in subsection 3.3.2.1 could be employed. Analysis has progressed to the point where an initial test function has been assigned to scattering center  $S_0$ . From Equation C-32 of Appendix C, we have

$$\sqrt{\sigma_0} e^{jP_0} = \frac{\sin \pi/\pi_0}{4k\sqrt{2\pi}\pi_0} \left[ \left\{ \cos \frac{\pi}{\pi_0} - \cos \frac{2(\pi - \chi - \phi)}{\pi_0} \right\}^{-1} \right] e^{j\pi/4 - j4kh \cos \phi} \quad (44)$$

$$= 0 ; \phi > \pi - \chi \quad 0 \leq \phi \leq \pi - \chi$$

where  $\pi_0 = 2 - \frac{2\chi}{\pi}$ . Equation 44 has negligible contribution to the total return from the cone for aspects near axial, as it should. The polarization dependent term associated with the contribution from center  $S_0$  is disregarded in keeping with the approximate nature of the present analysis.

#### 4.3.2 Preliminary Results

Table 6 lists designations, dimensions, and operating frequency for three cones which meet the specification noted in Table 1. Due to the preliminary nature of the cone investigation, only monostatic studies are called for.

Table 6  
PARAMETERS FOR CONE STUDY

| MODEL<br>DESIGNATION | DIMENSIONS (INCHES) |           | FREQUENCY<br>(GHz) |
|----------------------|---------------------|-----------|--------------------|
|                      | DIAMETER 2a         | LENGTH 2h |                    |
| C1                   | 6.320               | 11.783    | 6.000              |
| C2                   | 6.320               | 15.814    | 6.000              |
| C4                   | 7.500               | 13.983    | 5.975              |

Figures 61 through 72 compare theoretical and measured estimates of scattering matrix parameters for the three cones. The agreement obtained is considerably poorer than that achieved for other targets examined in this program. We note the following general observations. Modification to geometrical diffraction theory in the aspect region according to Equation 43 is valid: The predicted polarization dependence of vertical and horizontal polarization radar cross sections agrees with measurement data. Inclusion of a tip return according to Equation 44 broadens the specular cusp predicted at the broadside aspect, but the tip magnitude is insufficient to produce a specular which fails gracefully. For vertical polarization, the theoretical radar cross section agrees with measurement data in the angular region within 40 degrees of the tail-on aspect. For horizontal polarization, the corresponding interval is reduced to about 20 degrees due to the presence of finer structure in measured data. Better agreement can be achieved in the horizontal polarization case by extending the analysis to include interactions between centers  $S_1$  and  $S_2$  in the interval  $\frac{\pi}{2} \leq \phi \leq \pi$ . As discussed in Section 2, treatment of multiple-diffraction lies outside the scope of this program. Finally, examination of scattering phase data appears premature at this stage in the analysis. The gross patterns of phase progression show little correspondence. This is partially due to the large offset errors associated with cone measurements (see Table 3).

#### 4.3.3 Remarks

Preliminary analyses of scattering by a cone have been performed. These analyses were directed toward extension of theoretical capability at and near nose-on and tail-on axial aspects. Considerable success has been achieved in these aspect regions. However, evaluation of cone results shows that geometrical diffraction theory, in its present form, is severely limited in the aspect interval  $\alpha \leq \phi \leq \frac{\pi}{2} - \alpha$ , where  $\alpha$  is the cone half-angle. An attempt to empirically upgrade theory in this aspect region was unsuccessful; reduction of short pulse data failed to reveal any systematic secondary scattering mechanism.

A direction for future analysis has been outlined within the context of geometrical diffraction theory (see Appendix C).

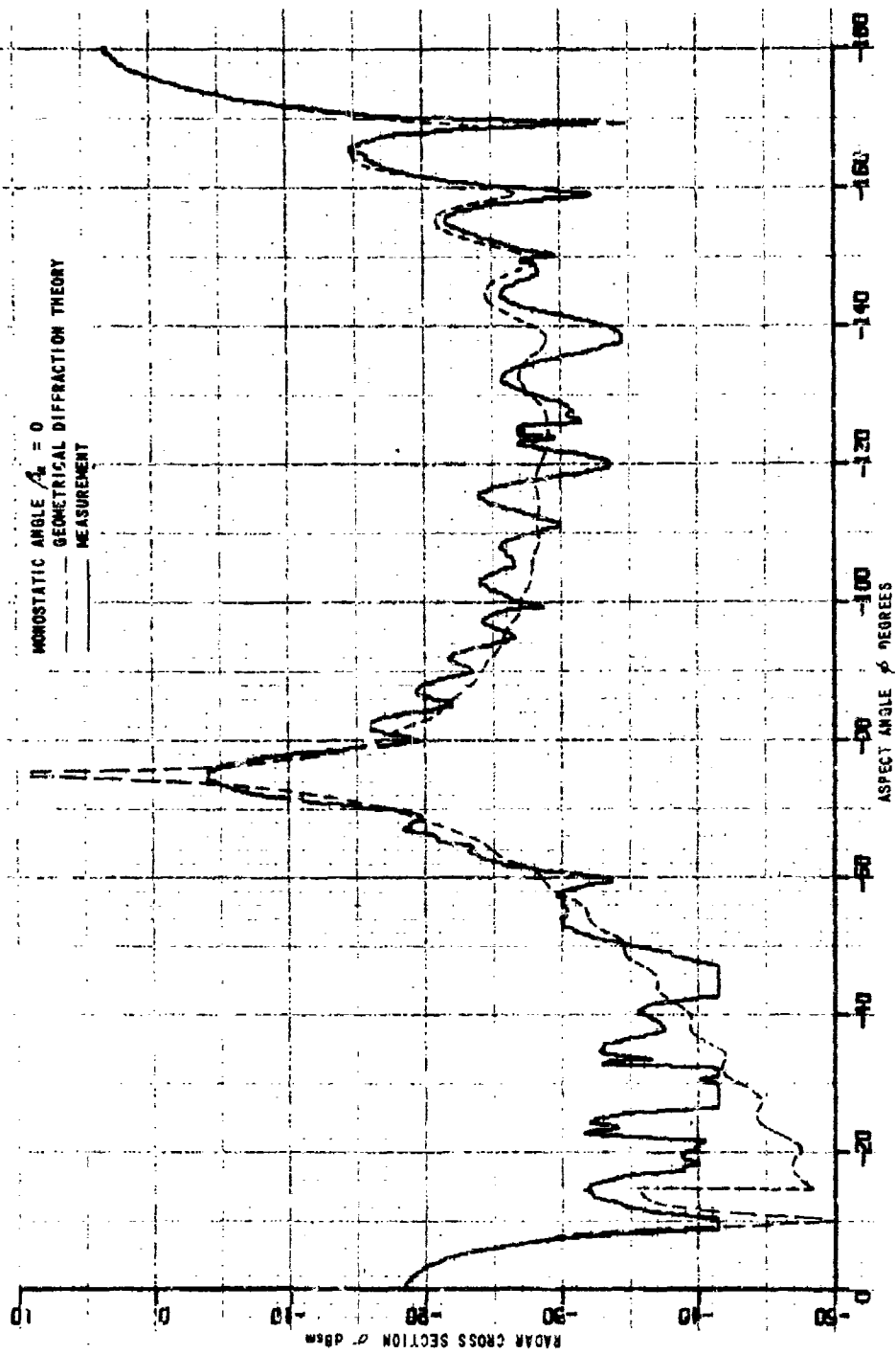


Figure 61 VERTICAL POLARIZATION RADAR CROSS SECTION. CONE C1, MONOSTATIC

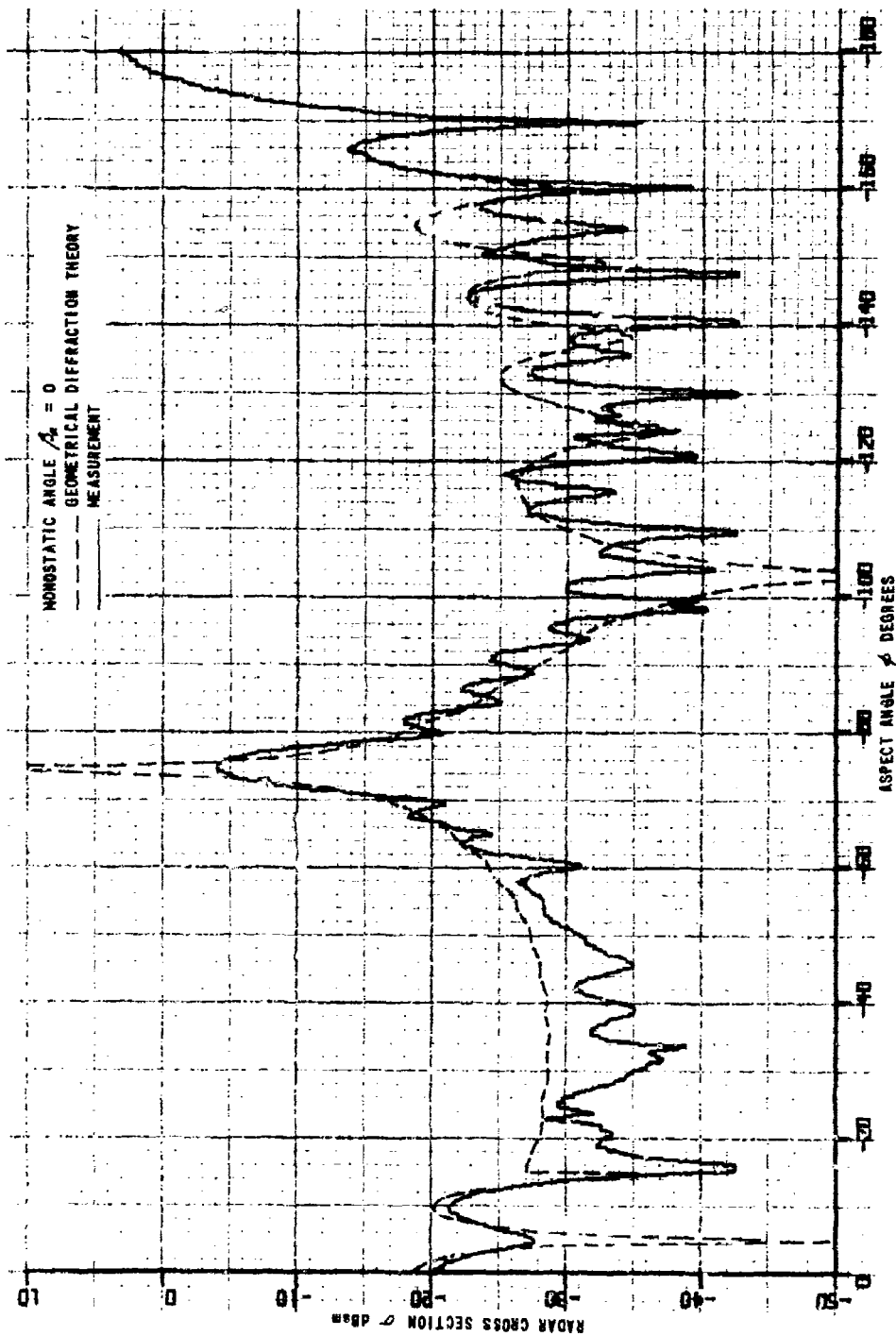


Figure 62 HORIZONTAL POLARIZATION RADAR CROSS SECTION. CONE C1, MONOSTATIC

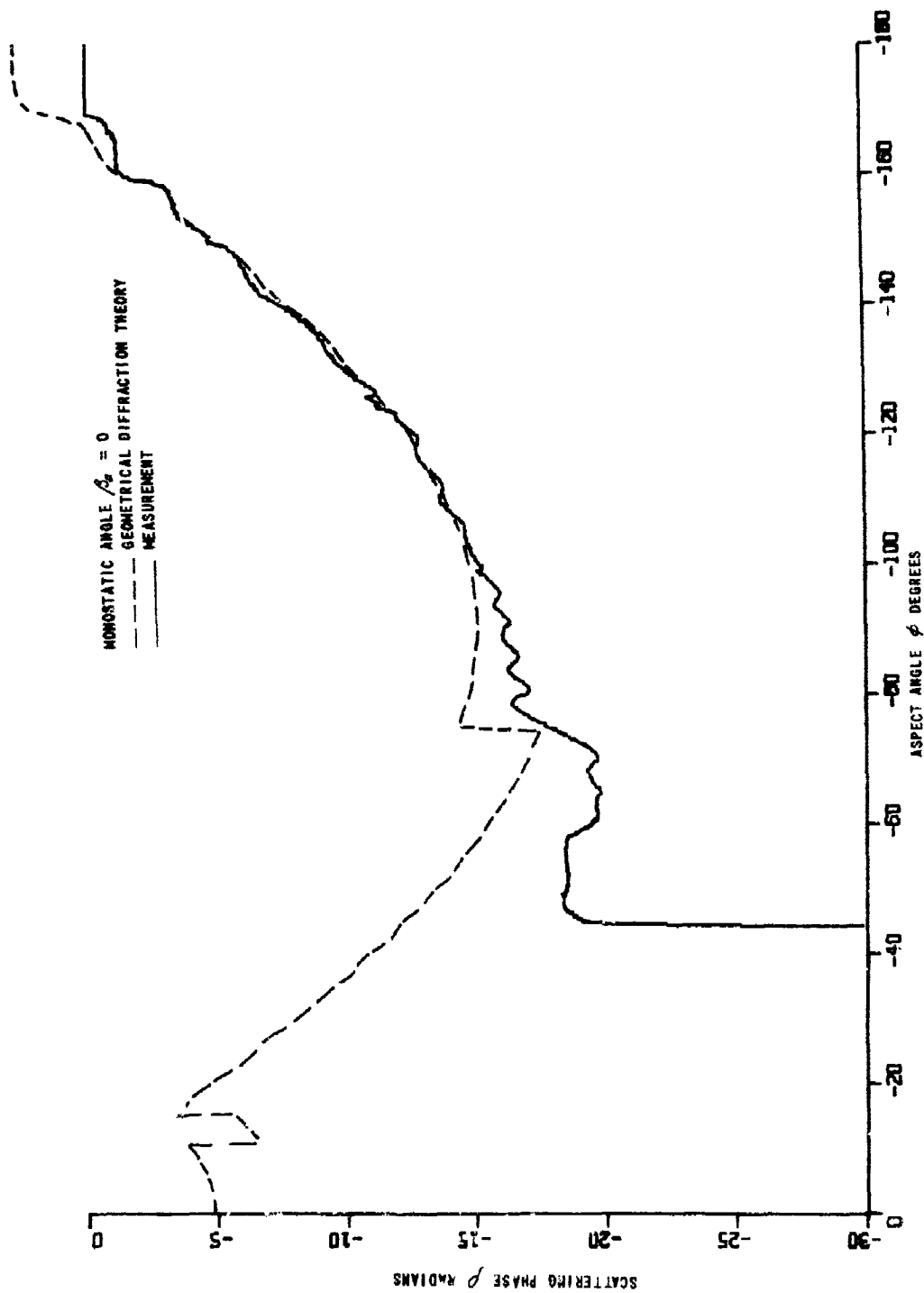


Figure 63 VERTICAL POLARIZATION SCATTERING PHASE. CONE C1, MONOSTATIC



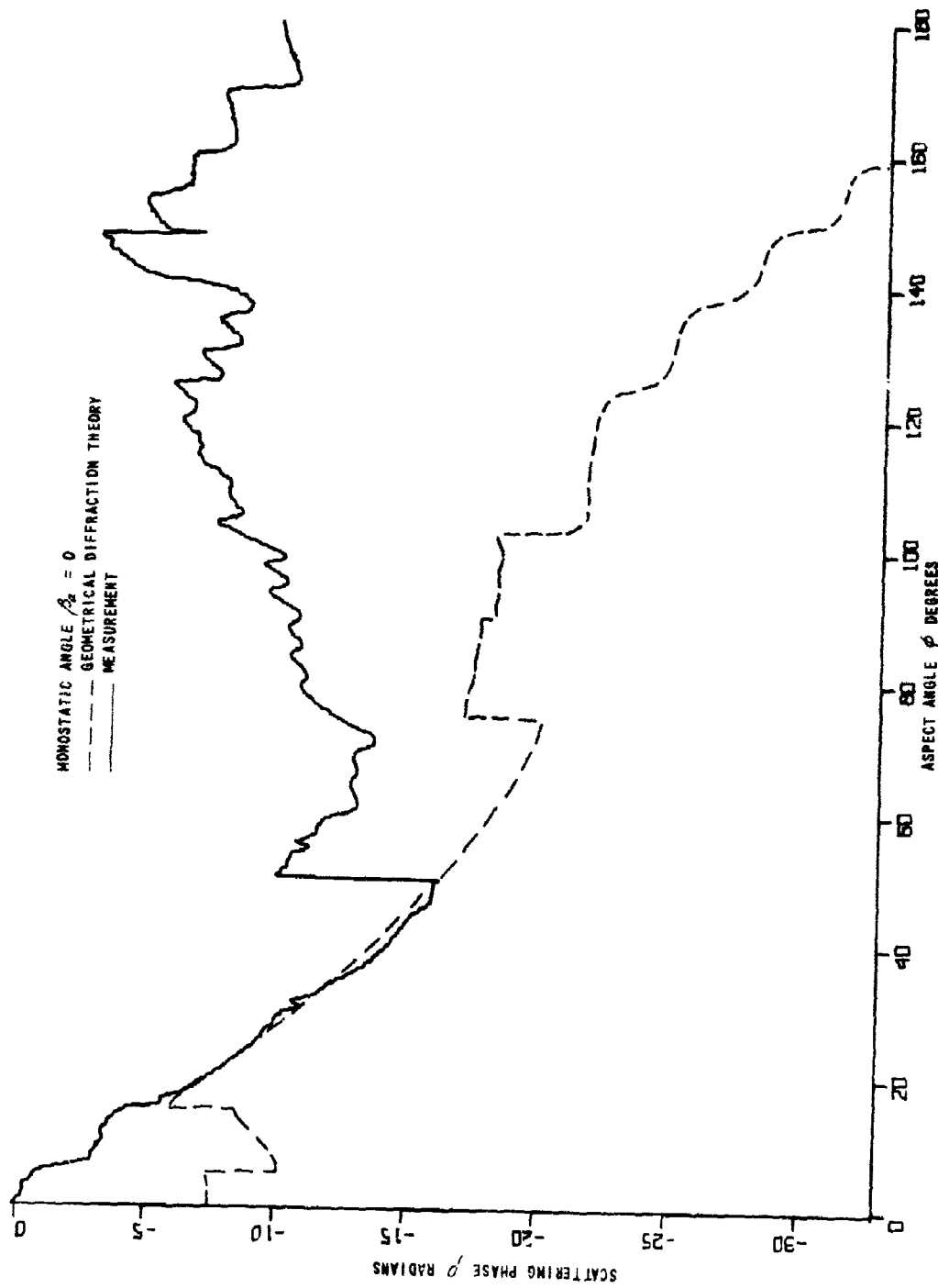


Figure 64 HORIZONTAL POLARIZATION SCATTERING PHASE. CONE C1, MONOSTATIC

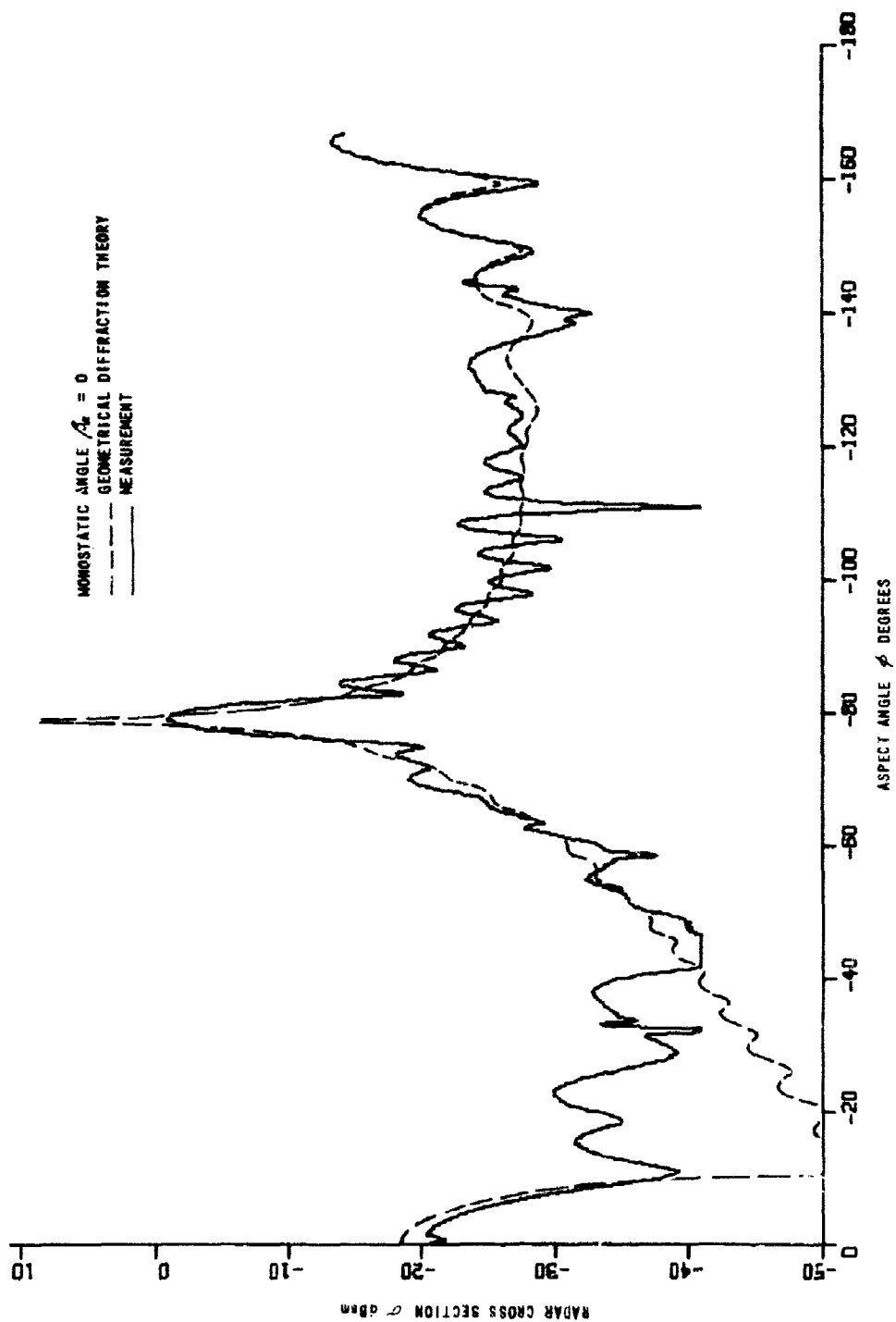


Figure 65 VERTICAL POLARIZATION RADAR CROSS SECTION. CONE C2, MONOSTATIC

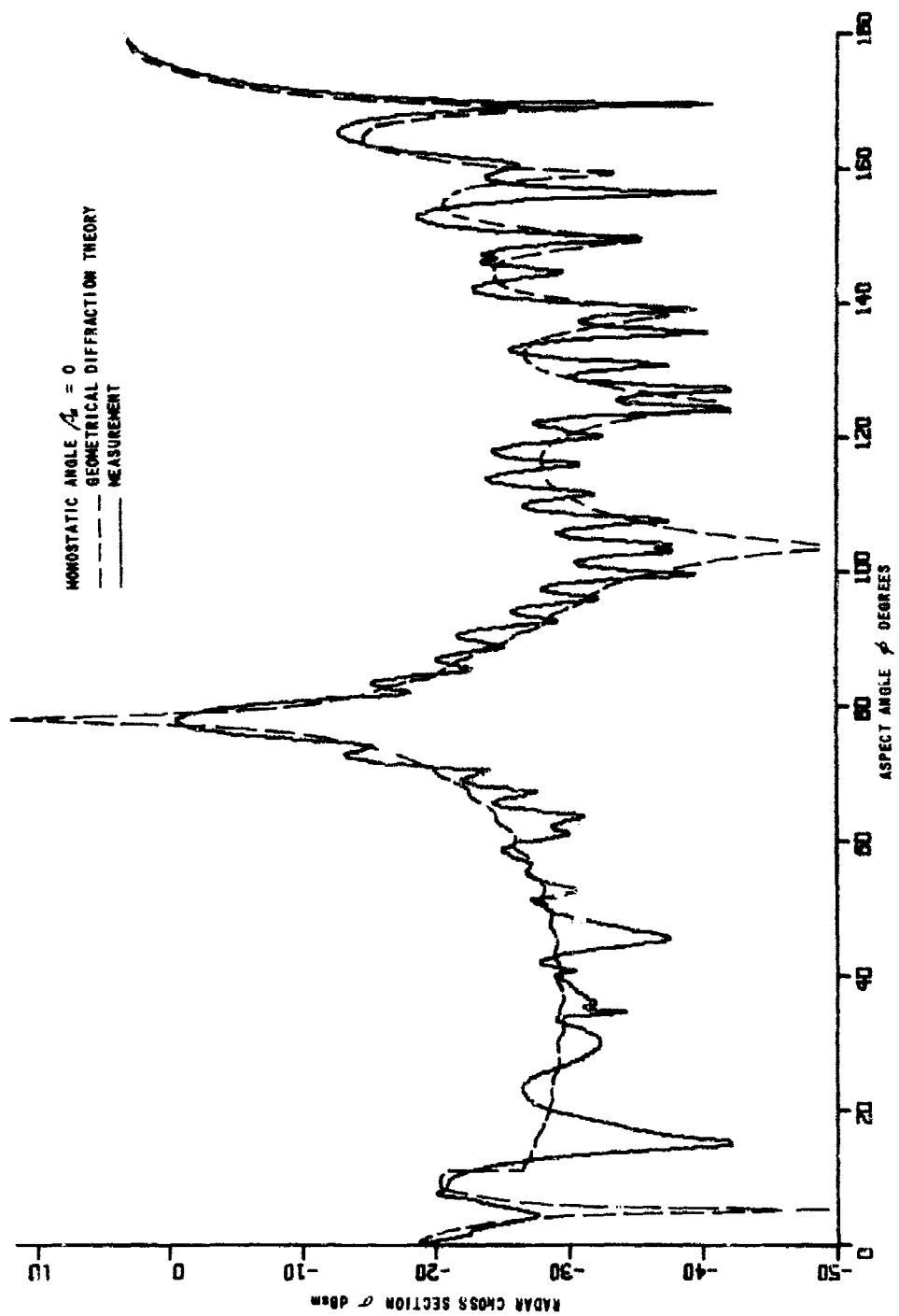


Figure 66 HORIZONTAL POLARIZATION RADAR CROSS SECTION. CONE C2, MONOSTATIC

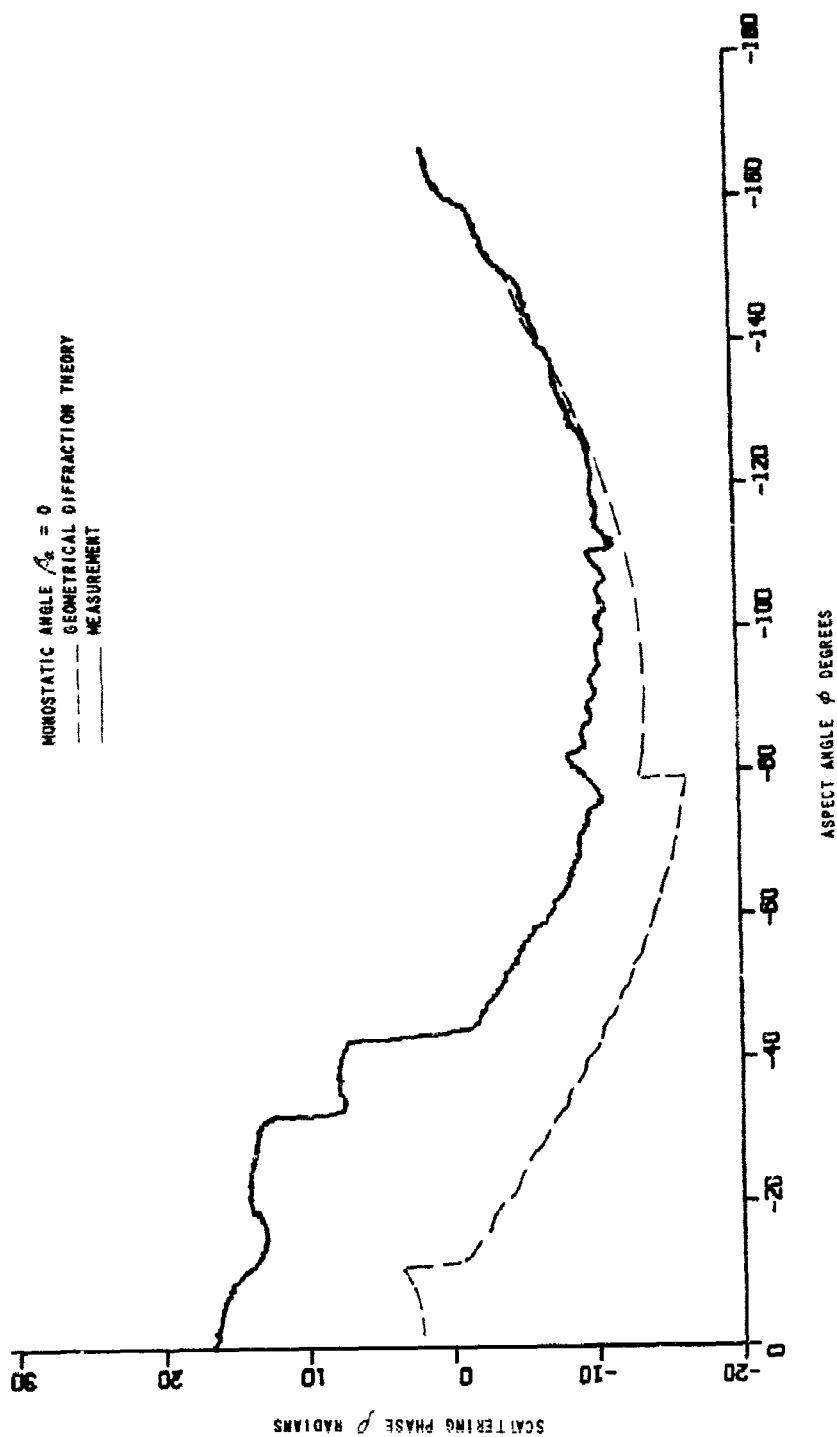


Figure 67 VERTICAL POLARIZATION SCATTERING PHASE. CONE C2, MONOSTATIC

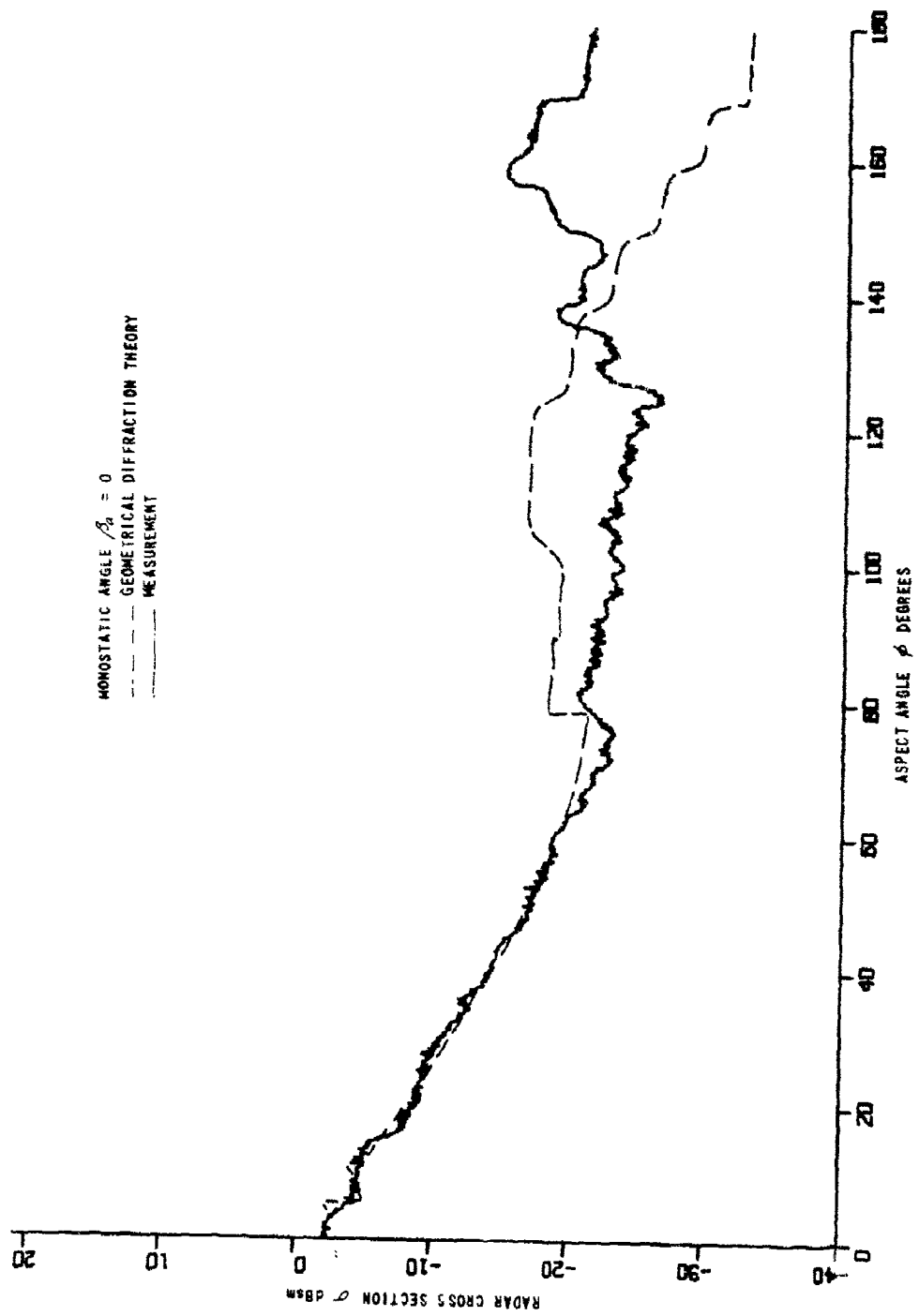


Figure 68 HORIZONTAL POLARIZATION SCATTERING PHASE. CONE C2, MONOSTATIC

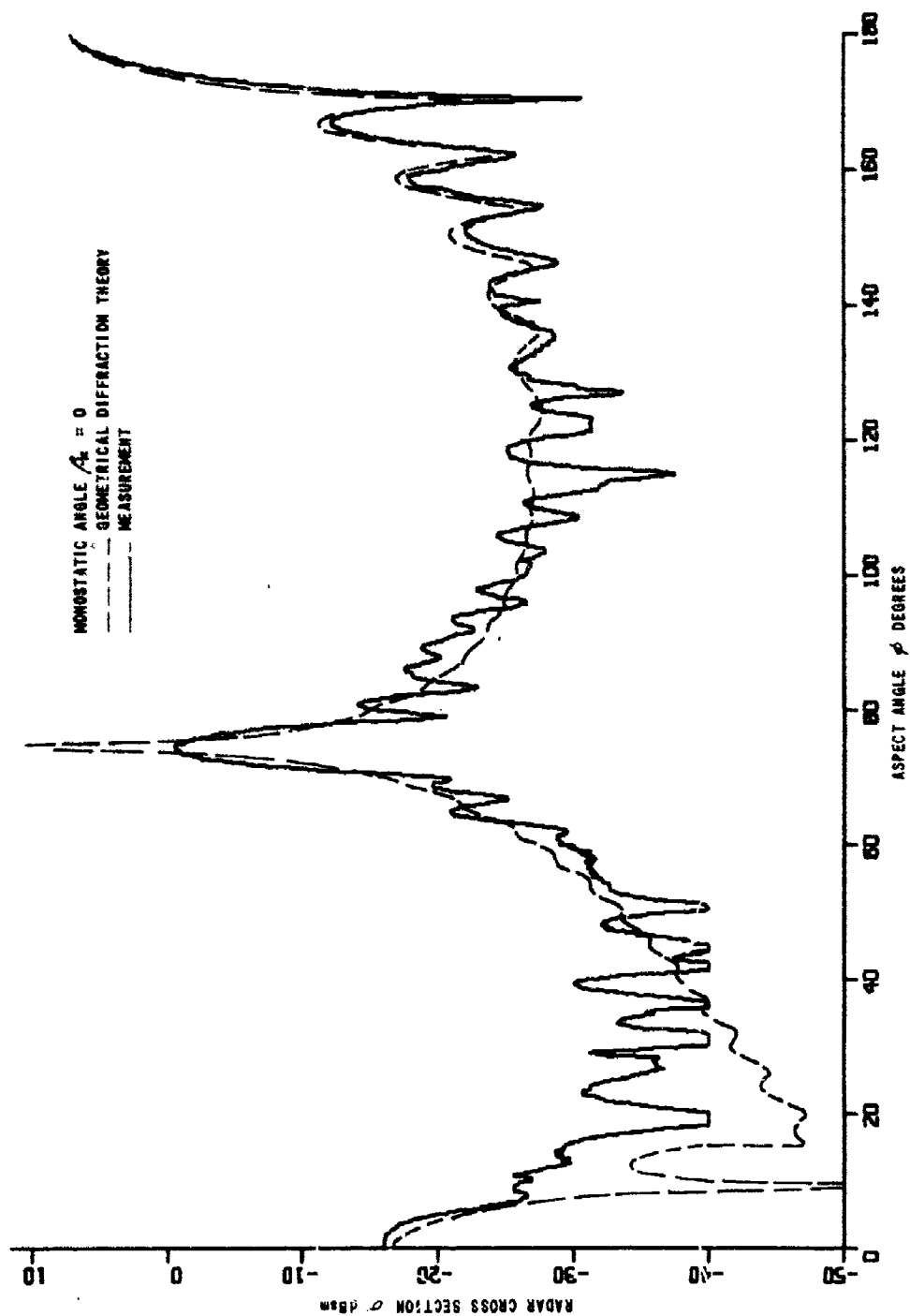


Figure 69 VERTICAL POLARIZATION RADAR CROSS SECTION. CONE C4, MONOSTATIC

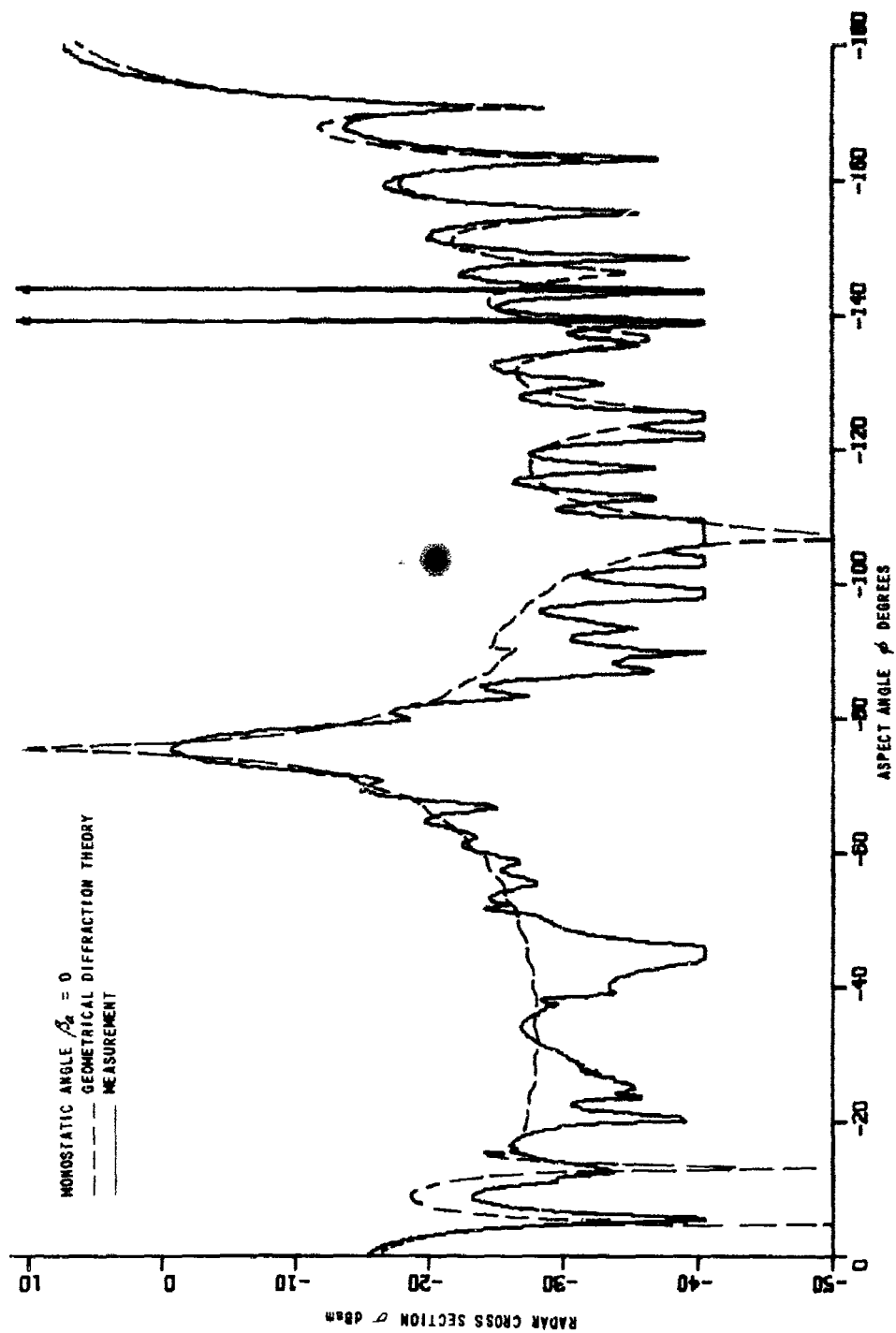


Figure 70 HORIZONTAL POLARIZATION RADAR CROSS SECTION. CONE CH, MONOSTATIC

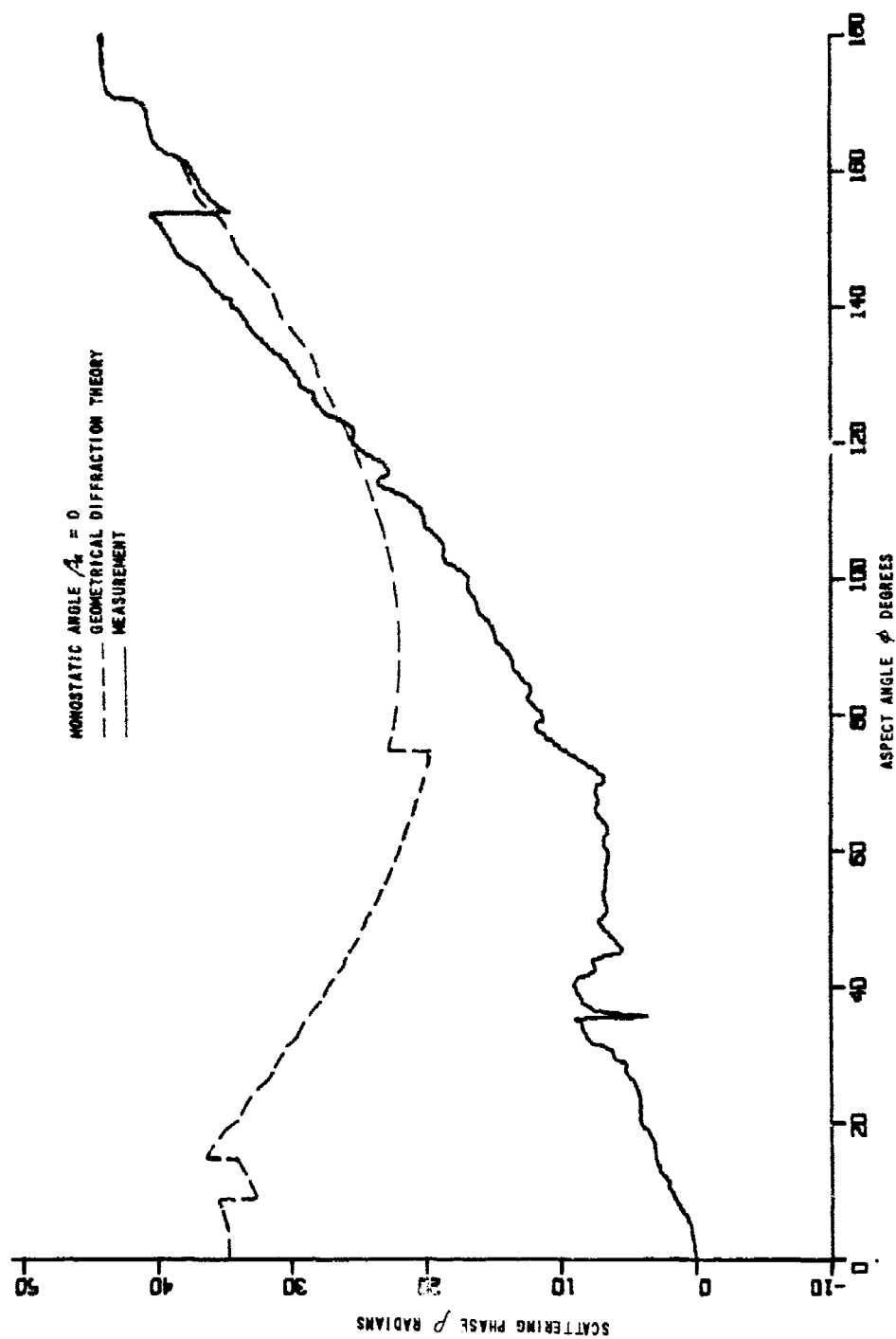


Figure 71 VERTICAL POLARIZATION SCATTERING PHASE. CONE CH, MONOSTATIC



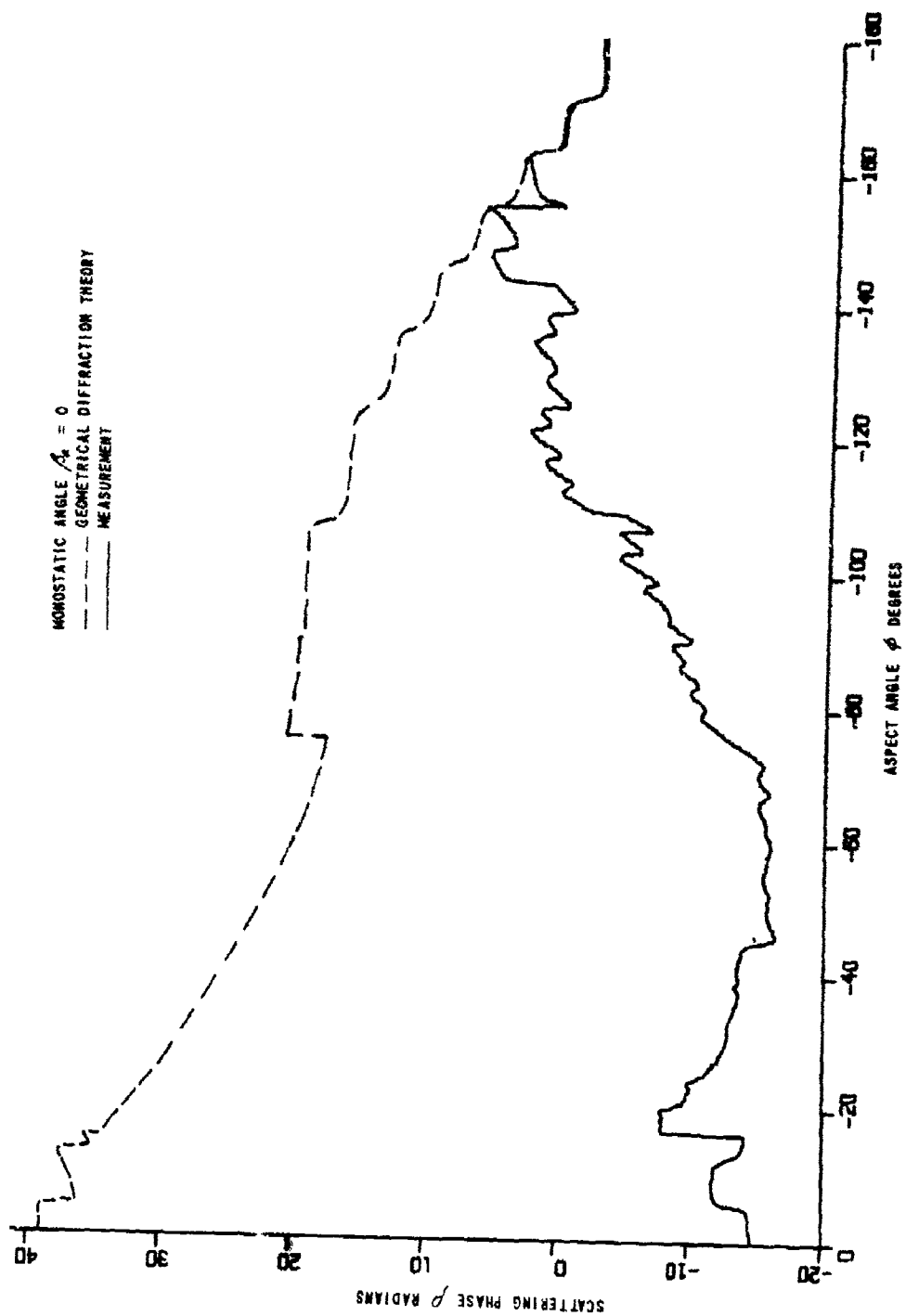


Figure 72 HORIZONTAL POLARIZATION SCATTERING PHASE. CONE C4, MONOSTATIC

#### 4.4 FRUSTUM-CYLINDER

##### 4.4.1 Analytical Formulation

The frustum-cylinder is a combinatorial shape formed by joining a frustum to a cylinder in the manner illustrated in Figure 73. The discontinuities on the target, labelled  $S_1$  through  $S_6$ , constitute the six important scattering centers.

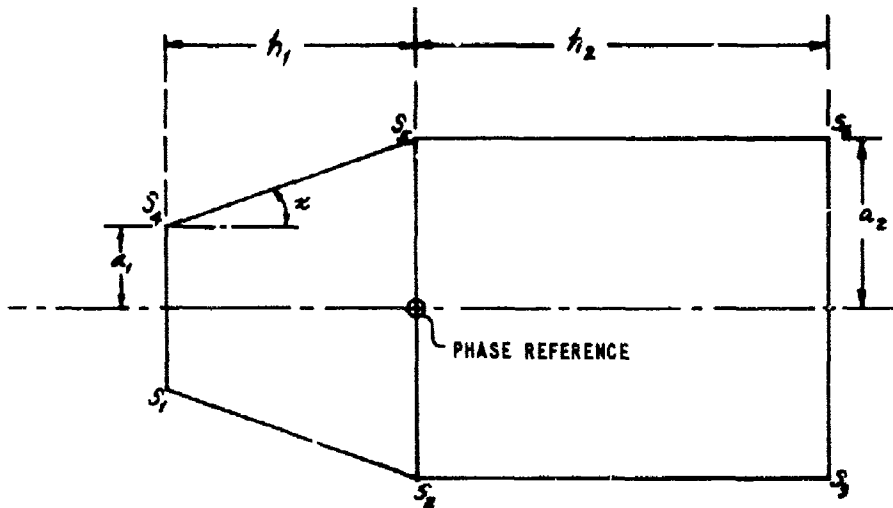


Figure 73 SCATTERING CENTERS ON A FRUSTUM CYLINDER

Notice that centers  $S_1$  and  $S_4$ , and  $S_3$  and  $S_6$  were investigated in the study of the frustum and the cylinder, respectively. Similarly, all the speculars occurring for a frustum-cylinder have been treated by modified geometrical diffraction theory in these two studies. We simply state the analytical results below.

$$\sqrt{\sigma_1} = \frac{\sin(\pi/n_1)}{n_1} \sqrt{\frac{a_1 \csc \phi}{k \cos \beta/2}} \left[ \left\{ \cos \frac{\pi}{n_1} - \cos \frac{\pi + 2\phi}{n_1} \right\}^{-1} \mp \left\{ \cos \frac{\pi}{n_1} - \cos \frac{\beta_a}{n_1} \right\}^{-1} \right] \quad (45)$$

$$\phi \leq \pi - \alpha - \beta_a/2$$

$$= 0 ; \phi > \pi - \alpha - \beta_a/2$$

$$\sqrt{\sigma_2} = \frac{\sin(\pi/n_2)}{n_2} \sqrt{\frac{a_2 \csc \phi}{k \cos \beta/2}} \left[ \left\{ \cos \frac{\pi}{n_2} - \cos \frac{2\pi - 2\phi}{n_2} \right\}^{-1} \mp \left\{ \cos \frac{\pi}{n_2} - \cos \frac{\beta_a}{n_2} \right\}^{-1} \right] \quad (46)$$

$$\phi \leq \pi - \beta_a/2$$

$$= 0 ; \phi > \pi - \beta_a/2$$

$$\sqrt{\sigma_3} = \frac{\sin(\pi/n_3)}{n_3} \sqrt{\frac{a_3 \csc \phi}{k \cos \beta/2}} \left[ \left\{ \cos \frac{\pi}{n_3} - \cos \frac{3\pi - 2\phi}{n_3} \right\}^{-1} \mp \left\{ \cos \frac{\pi}{n_3} - \cos \frac{\beta_a}{n_3} \right\}^{-1} \right] \quad (47)$$

$$\phi \geq \beta_a/2$$

$$= 0 ; \phi < \beta_a/2$$

$$\sqrt{\sigma_4} = \frac{\sin(\pi/n_1)}{n_1} \sqrt{\frac{a_1 \csc \phi}{k \cos \beta/2}} \left[ \left\{ \cos \frac{\pi}{n_1} - \cos \frac{\pi - 2\phi}{n_1} \right\}^{-1} \mp \left\{ \cos \frac{\pi}{n_1} - \cos \frac{\beta_a}{n_1} \right\}^{-1} \right] \quad (48)$$

$$\phi \leq \frac{\pi}{2} - \frac{\beta_a}{2}$$

$$= 0 ; \phi > \frac{\pi}{2} - \frac{\beta_a}{2}$$

$$\sqrt{\sigma_5} = \frac{\sin(\pi/n_2)}{n_2} \sqrt{\frac{a_2 \csc \phi}{k \cos \beta/2}} \left[ \left\{ \cos \frac{\pi}{n_2} - \cos \frac{2\pi + 2\phi}{n_2} \right\}^{-1} \mp \left\{ \cos \frac{\pi}{n_2} - \cos \frac{\beta_2}{n_2} \right\}^{-1} \right] \quad (49)$$

$$= 0; \quad \phi > \pi - \beta_2/2$$

$$\sqrt{\sigma_6} = \frac{\sin(\pi/n_3)}{n_3} \sqrt{\frac{a_2 \csc \phi}{k \cos \beta/2}} \left[ \left\{ \cos \frac{\pi}{n_3} - \cos \frac{-\pi + 2\phi}{n_3} \right\}^{-1} \mp \left\{ \cos \frac{\pi}{n_3} - \cos \frac{\beta_2}{n_3} \right\}^{-1} \right] \quad (50)$$

$$= 0; \quad \phi < \frac{\pi}{2} + \frac{\beta_2}{2}$$

$$\rho_1 = -2k \cos \beta/2 [a_1 \sin \phi + h_1 \cos \phi] + \pi/4 \quad (51)$$

$$\rho_2 = -2ka_2 \cos \beta/2 \sin \phi + \pi/4 \quad (52)$$

$$\rho_3 = -2k \cos \beta/2 [a_2 \sin \phi - h_2 \cos \phi] + \pi/4 \quad (53)$$

$$\rho_4 = +2k \cos \beta/2 [a_1 \sin \phi - h_1 \cos \phi] - \pi/4 \quad (54)$$

$$\rho_5 = +2ka_2 \cos \beta/2 \sin \phi - \pi/4 \quad (55)$$

$$\rho_6 = +2k \cos \beta/2 [a_2 \sin \phi + h_2 \cos \phi] - \pi/4 \quad (56)$$

with

$$\begin{aligned} n_1 &= 3/2 - \pi/\pi \\ n_2 &= 1 + \pi/\pi \\ n_3 &= 3/2 \end{aligned} \quad (57)$$

At and near the nose-on axial aspect ( $\phi = 0$ ), we describe specular scattering by the polarization independent terms in Equations 45 and 48 in the usual form

$$\begin{aligned} (\sqrt{\sigma_1} e^{jP_1} + \sqrt{\sigma_4} e^{jP_4})_{poli} &= 2\sqrt{\pi} k \cos \beta_{1/2} a_1^2 \frac{J_1(2ka_1 \cos \beta_{1/2} \sin \phi)}{(2ka_1 \cos \beta_{1/2} \sin \phi)} \times \\ &\quad e^{-j\pi/2 - 2kh_1 \cos \phi \cos \beta_{1/2}} \end{aligned} \quad (58)$$

Equation 58 is used for  $0 \leq \phi \leq \phi_{ca}$ , where the cross-over aspect is defined by the relation  $2ka_1 \sin \phi_{ca} = 2.44$ . The remaining contributions are well behaved when we apply the constraint  $\csc \phi \leq k a_1 \cos \beta_{1/2}$ . Similarly, at and near the tail-on aspect, we modify contributions from centers  $S_3$  and  $S_6$  to obtain

$$\begin{aligned} (\sqrt{\sigma_3} e^{jP_3} + \sqrt{\sigma_6} e^{jP_6})_{poli} &= 2\sqrt{\pi} k a_2^2 \cos \beta_{1/2} \frac{J_1(2ka_2 \cos \beta_{1/2} \sin \phi)}{(2ka_2 \cos \beta_{1/2} \sin \phi)} \times \\ &\quad e^{-j\pi/2 + j2kh_2 \cos \beta_{1/2} \cos \phi} \end{aligned} \quad (59)$$

Equation 59 is employed for  $\pi - \phi_{ca} \leq \phi \leq \pi$ , with the cross-over aspect now given by  $2ka_2 \sin \phi_{ca} = 2.44$ . Again the constraint on  $\csc \phi$  is introduced (here  $\csc \phi \leq k a_2 \cos \beta_{1/2}$ ) for the remaining contribution.

At and near broadside on the cylindrical section ( $\phi = \pi/2$ ), the polarization-independent terms in Equations 46 and 47 are combined to give

$$(\sqrt{\sigma_2} e^{j\beta_2} + \sqrt{\sigma_3} e^{j\beta_3})_{pol} = -\sqrt{\mu_2 k \cos \beta_2} h_2 \frac{\sin(k h_2 \cos \beta_2 \cos \phi)}{(k h_2 \cos \beta_2 \cos \phi)} \times e^{j\frac{3\pi}{4} - j2ka_2 \sin \phi \cos \beta_2 + kh_2 \cos \phi \cos \beta_2} \quad (60)$$

Equation 60 is used for  $\phi_{cb} \leq \phi \leq \pi - \phi_{cb}$ , with the cross-over aspect angle  $\phi_{cb}$  given by  $kh_2 \cos \phi_{cb} = 2.25$ . All other contributions are well behaved. Finally, we employ the curve-fitting technique discussed in the frustum study to suppress the singularities which arise in Equations 45 and 46 when incidence is broadside to the frustum segment ( $\phi = \pi/2 - \alpha$ ).

#### 4.4.2 Results

Table 7 lists parameters used in the study of the frustum-cylinder. The number of individual targets and bistatic situations contained in the table do not satisfy specifications noted in Table 1; the program specifies evaluation of the monostatic capability of theory using three models. Because measurement data on only one model was available for monostatic study, we have added available bistatic cases to bolster this investigation. Dimensions of each target may be obtained from Table 2.

Table 7  
PARAMETERS FOR FRUSTUM-CYLINDER STUDY

| MODEL DESIGNATION | FREQUENCY (GHz) | BISTATIC ANGLE $\beta_a$ (DEGREES) |
|-------------------|-----------------|------------------------------------|
| F4CY3             | 5.975           | 0                                  |
| F5CY5             | 5.885           | 10.25                              |
|                   | 6.050           | 30.0                               |

The phase reference chosen for measurements lay on the axis of symmetry of the target at the mid-point of the cylindrical section. Figure 73 shows the analytical phase reference located at the junction of the frustum and the cylinder. In order to compare theory and measurement then, a term of magnitude  $-kh_z \cos \beta_z \cos \phi$  was added to analytical estimates of scattering phase.

Figures 74 through 77 show monostatic results for frustum-cylinder F4CY3. Very good agreement between theory and measurement is evident for all parameters describing the scattering matrix of this target. Figures 78 through 81 show similar agreement for F5CY5 with bistatic angle  $\beta_a = 10.25$  degrees. Finally, calculations from theory for F5CY5 with  $\beta_a = 30.0$  degrees are given in Figures 82 through 85 and horizontal polarization experimental data are also presented in Figures 83 and 85. Notice that, for vertical polarization radar cross section and scattering phase, measurement data is not included in Figures 82 and 84. We were unable to plot these data in this instance. The computer provided an error message which indicates that the conventional format for recording measurement data was not employed. Again, Figures 83 and 85 indicate excellent agreement, when the caution about  $2\pi$  slippage of phase is observed.

#### 4.4.3 Remarks

Comparison of theory with measurement data shows that geometrical diffraction theory is an accurate description of scattering by a frustum-cylinder. Although a small portion of measurement data was unavailable for evaluation purposes, the overall agreement for the combinatorial shape is every bit as good as earlier results obtained for cylinders and frustums. Thus, the synthesis of combinatorial shapes in terms of scattering centers is well founded.

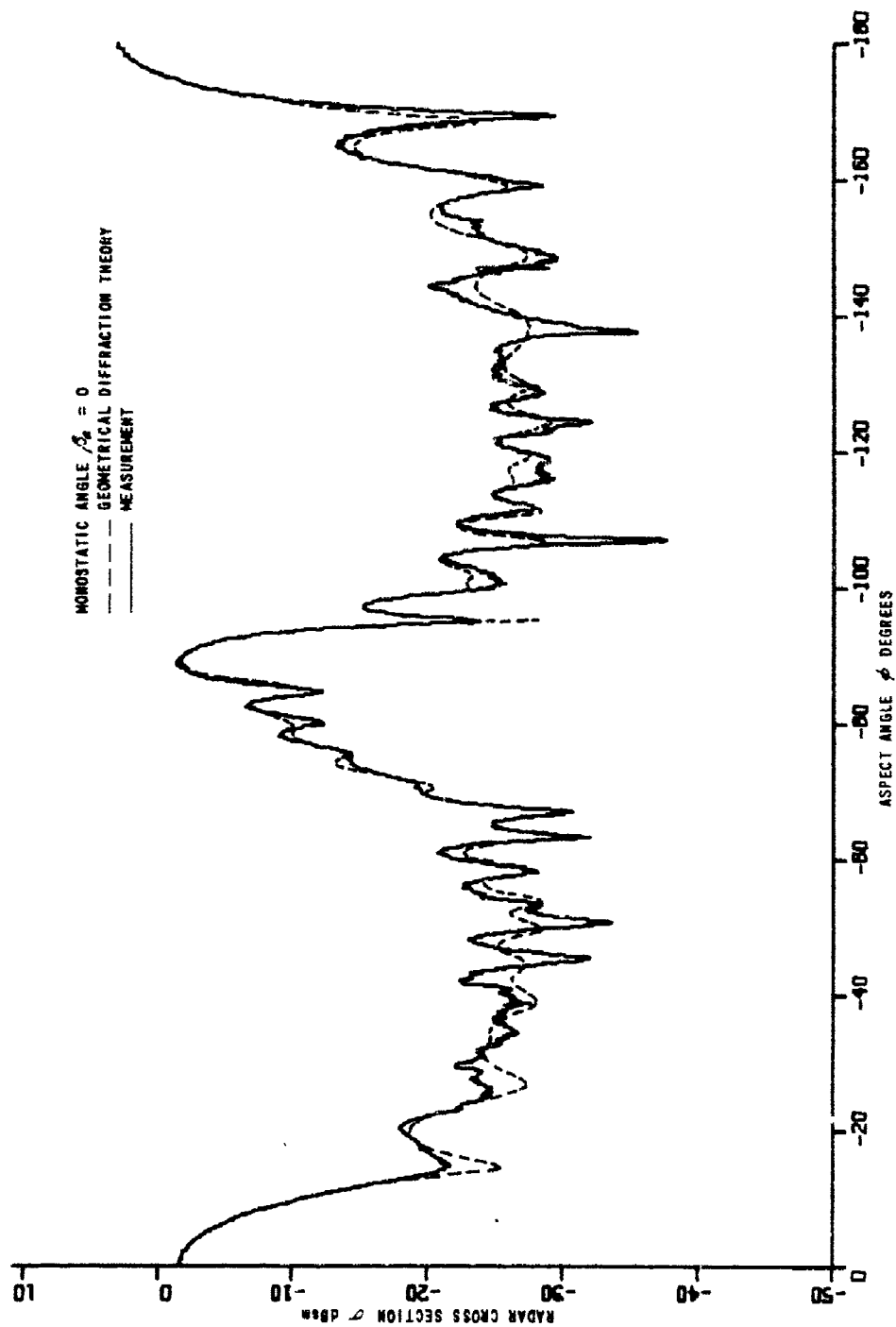


Figure 74 VERTICAL POLARIZATION RADAR CROSS SECTION. FRUSTUM-CYLINDER F4CY3, MONOSTATIC



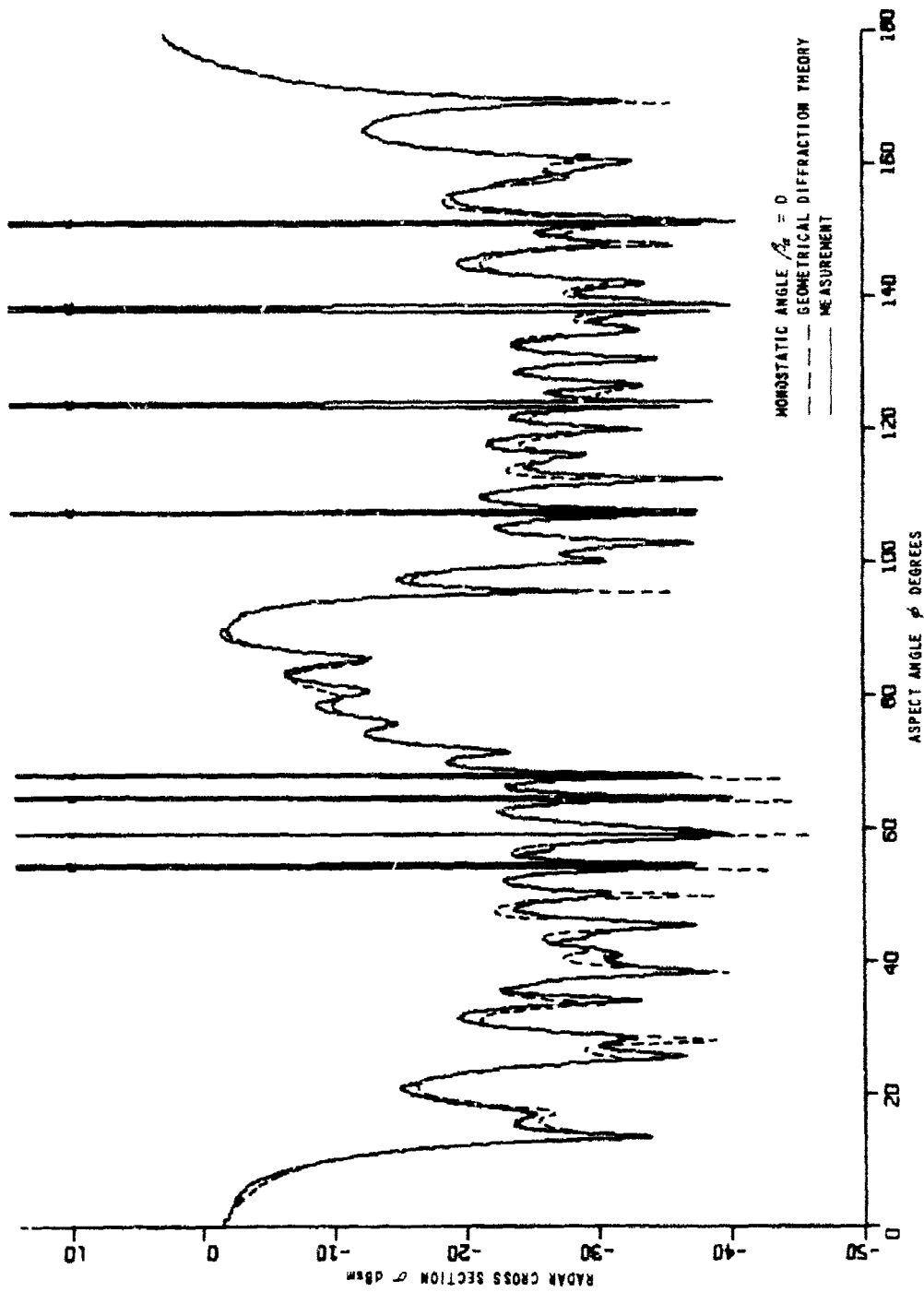


Figure 75 HORIZONTAL POLARIZATION RADAR CROSS SECTION. FRUSTUM-CYLINDER FNCY3. MONOSTATIC

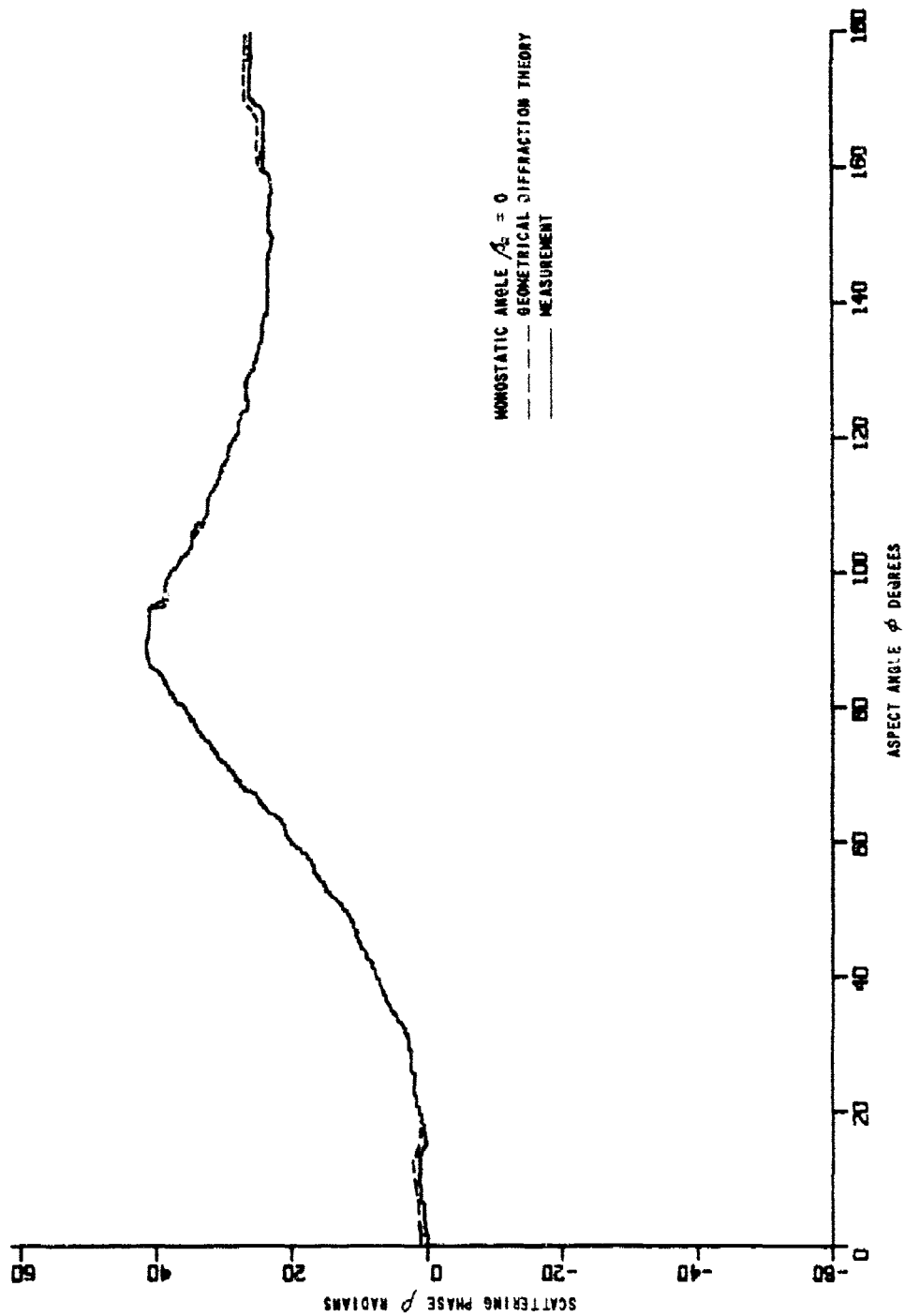


Figure 76 VERTICAL POLARIZATION SCATTERING PHASE. FRUSTUM-CYLINDER F4CY3, MONOSTATIC

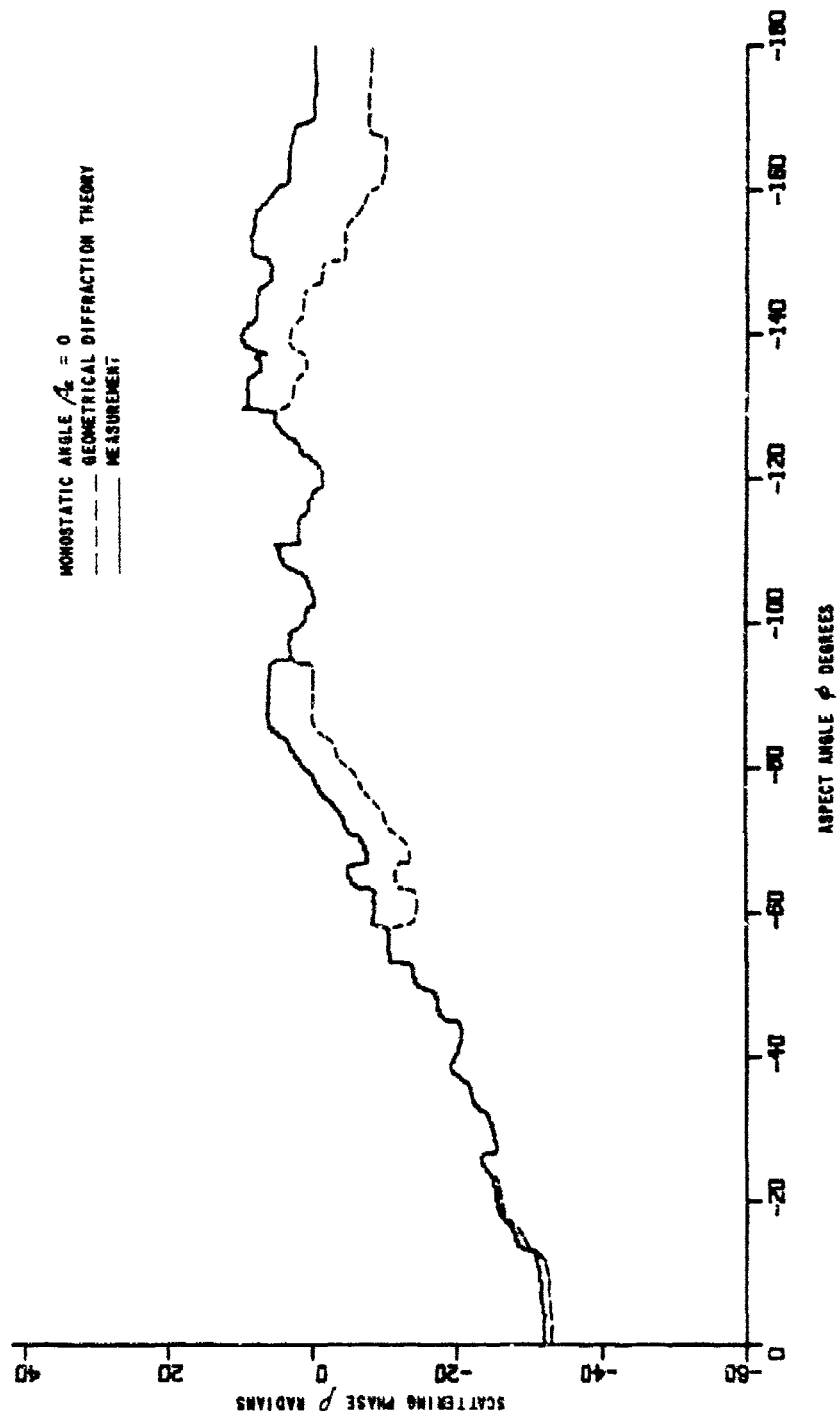


Figure 77 HORIZONTAL POLARIZATION SCATTERING PHASE. FRUSTUM-CYLINDER  $P^{H/CY3}$ , MONOSTATIC

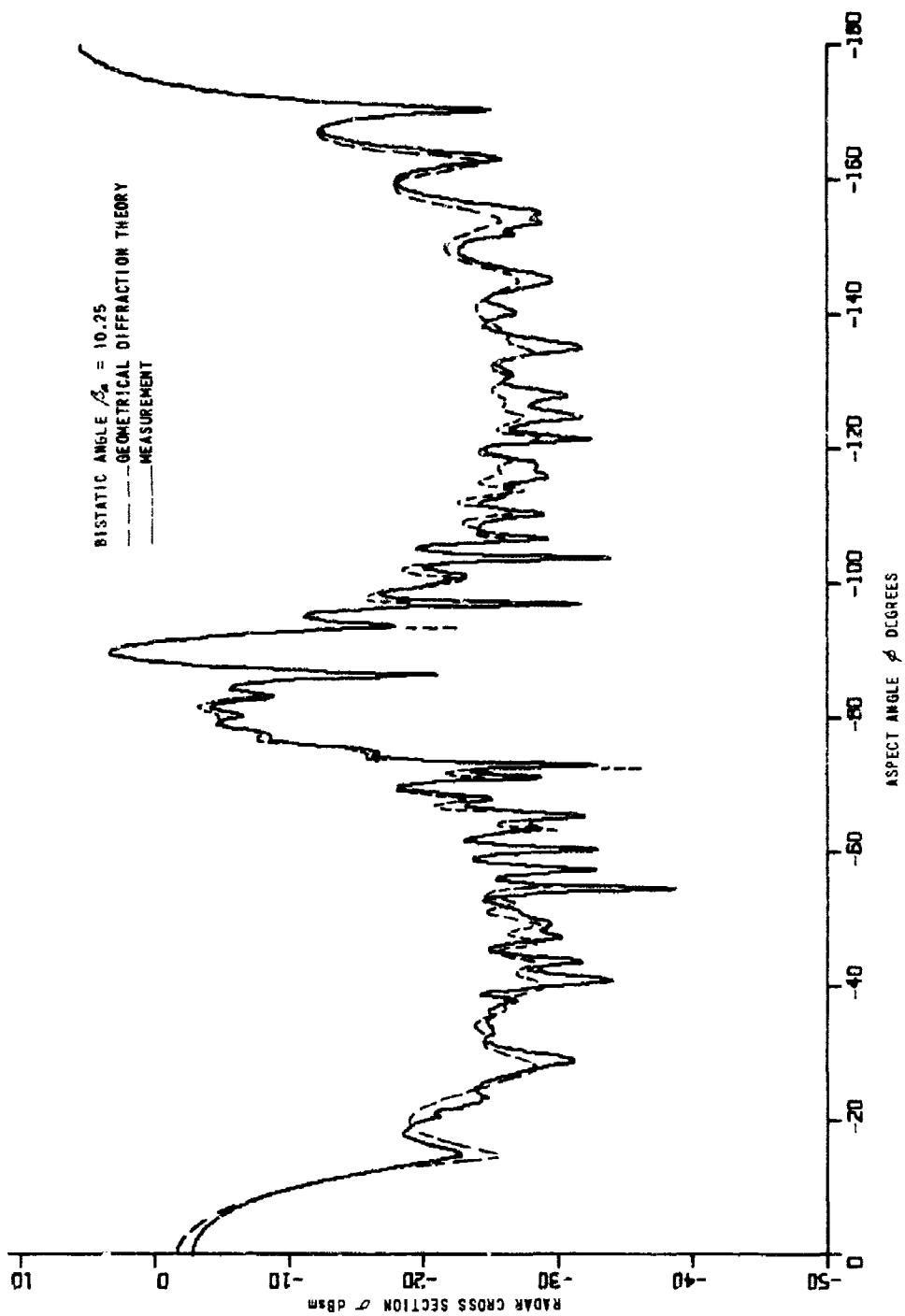


Figure 78 VERTICAL POLARIZATION RADAR CROSS SECTION. FRUSTUM-CYLINDER F5CV5, BISTATIC

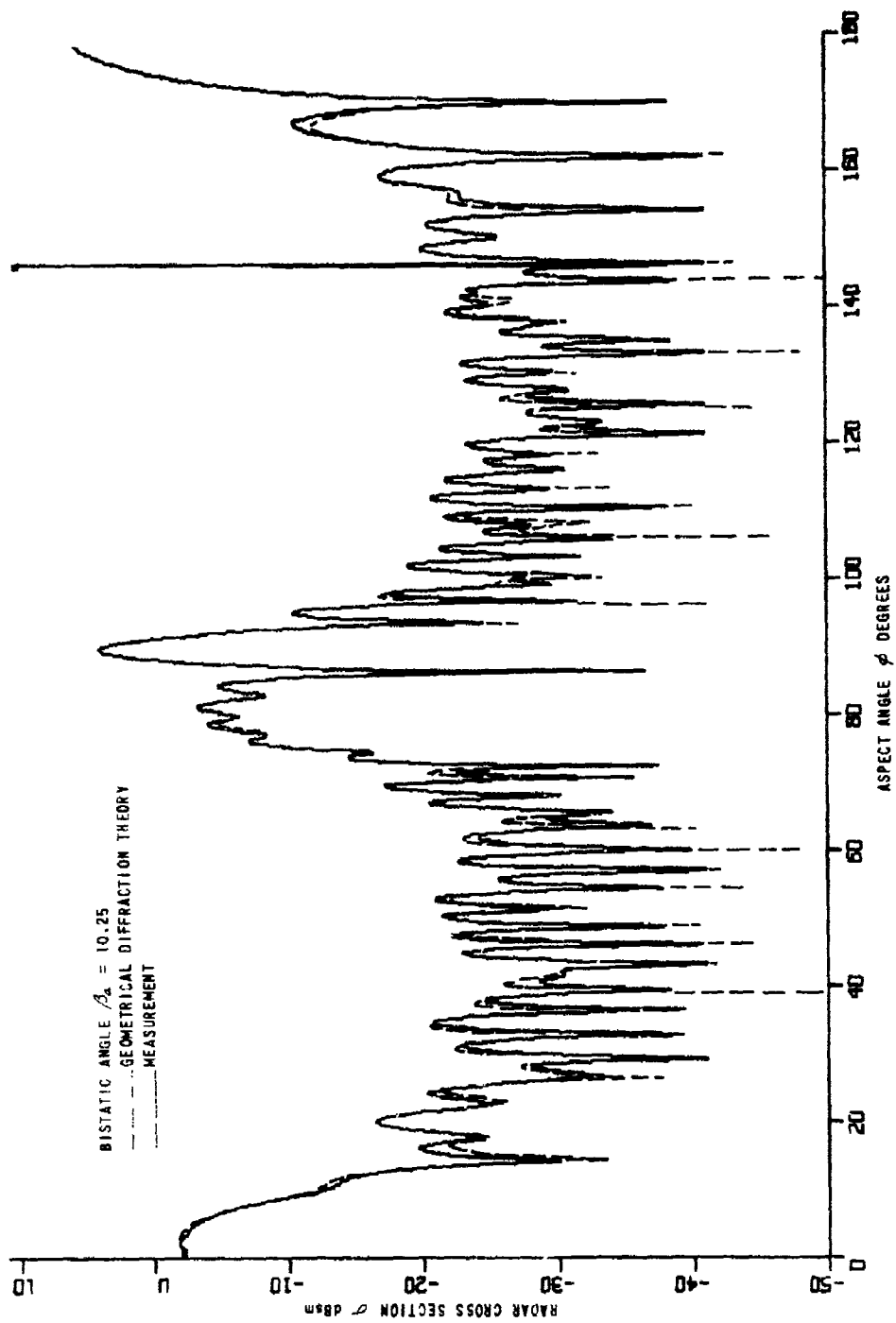


Figure 79 HORIZONTAL POLARIZATION RADAR CROSS SECTION. FRUSTUM-CYLINDER FSCY5, BISTATIC

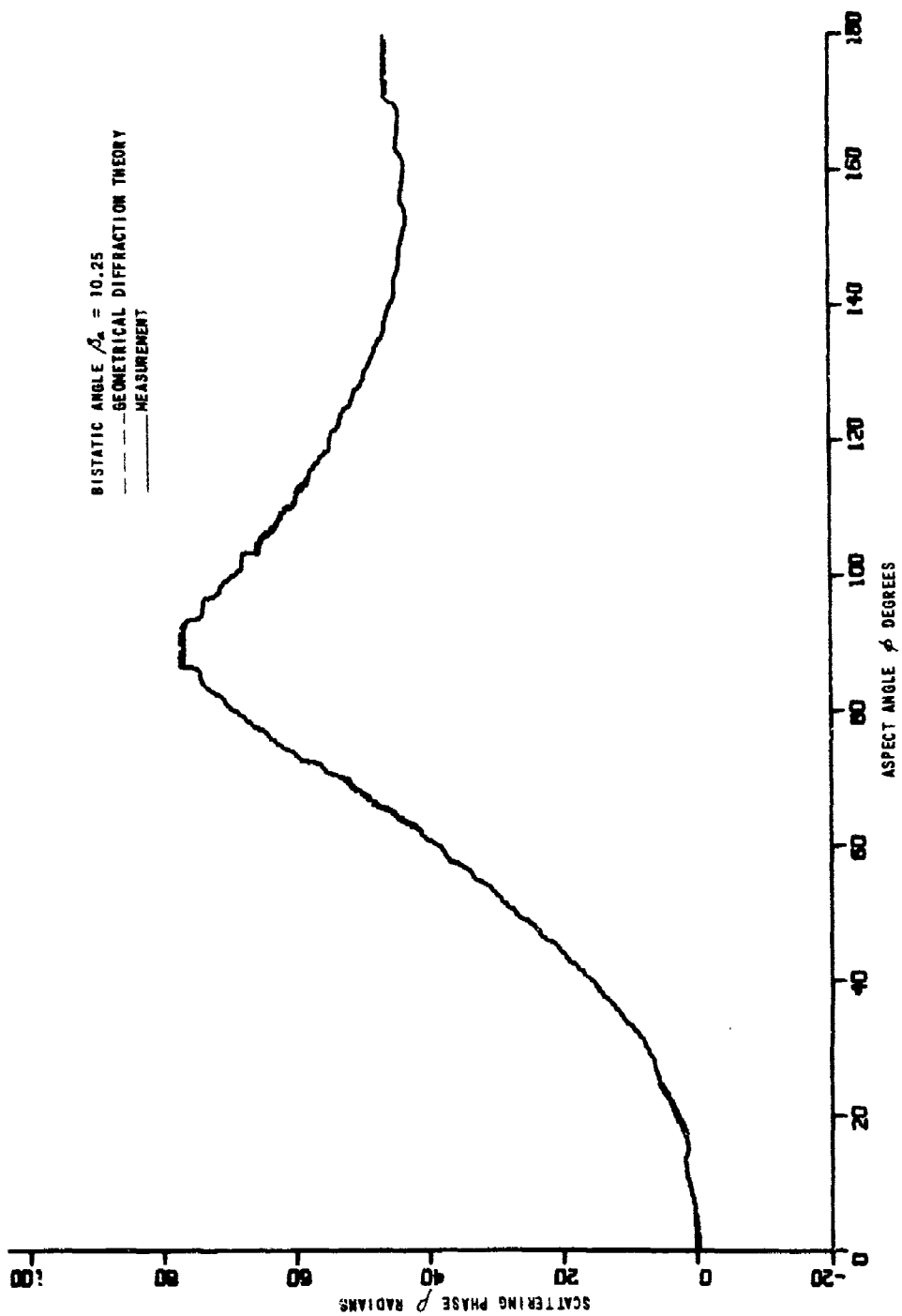


Figure 80 VERTICAL POLARIZATION SCATTERING PHASE. FRUSTUM-CYLINDER F5CY5, BISTATIC

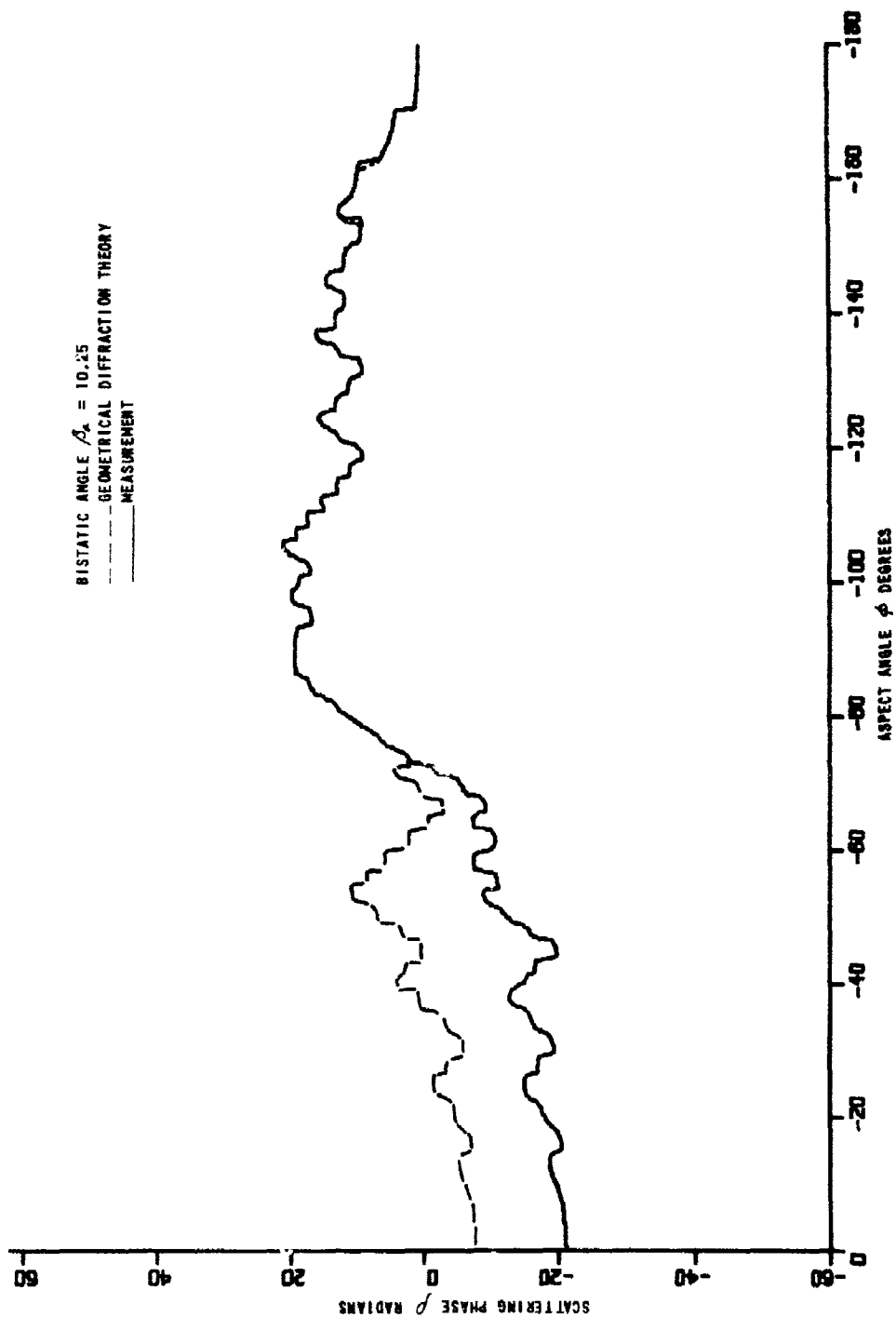


Figure 81 HORIZONTAL POLARIZATION SCATTERING PHASE. FRUSTUM-CYLINDER F5CY5, BISTATIC

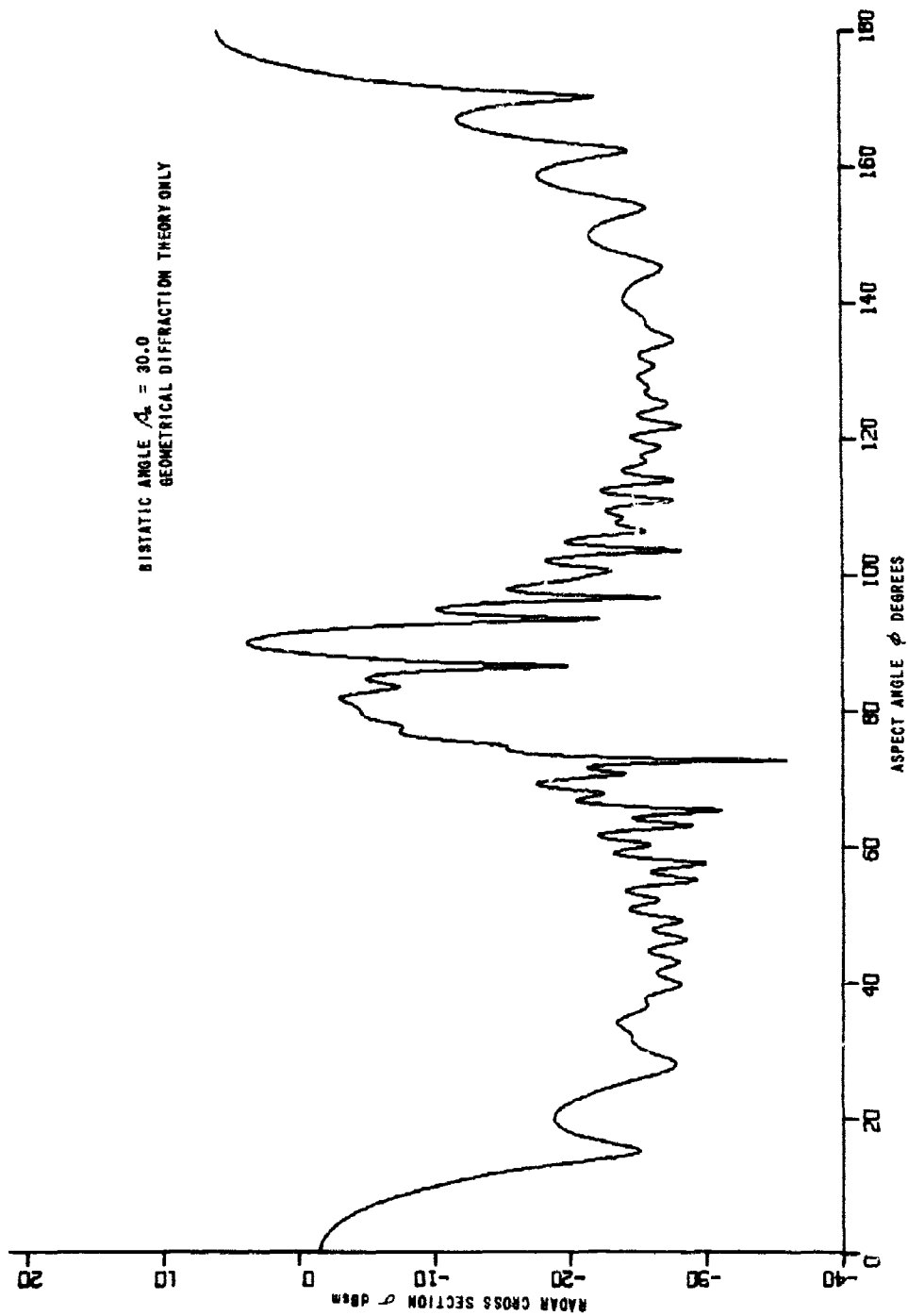


Figure 82 VERTICAL POLARIZATION RADAR CROSS SECTION. FRUSTUM-CYLINDER FSCV5, BISTATIC



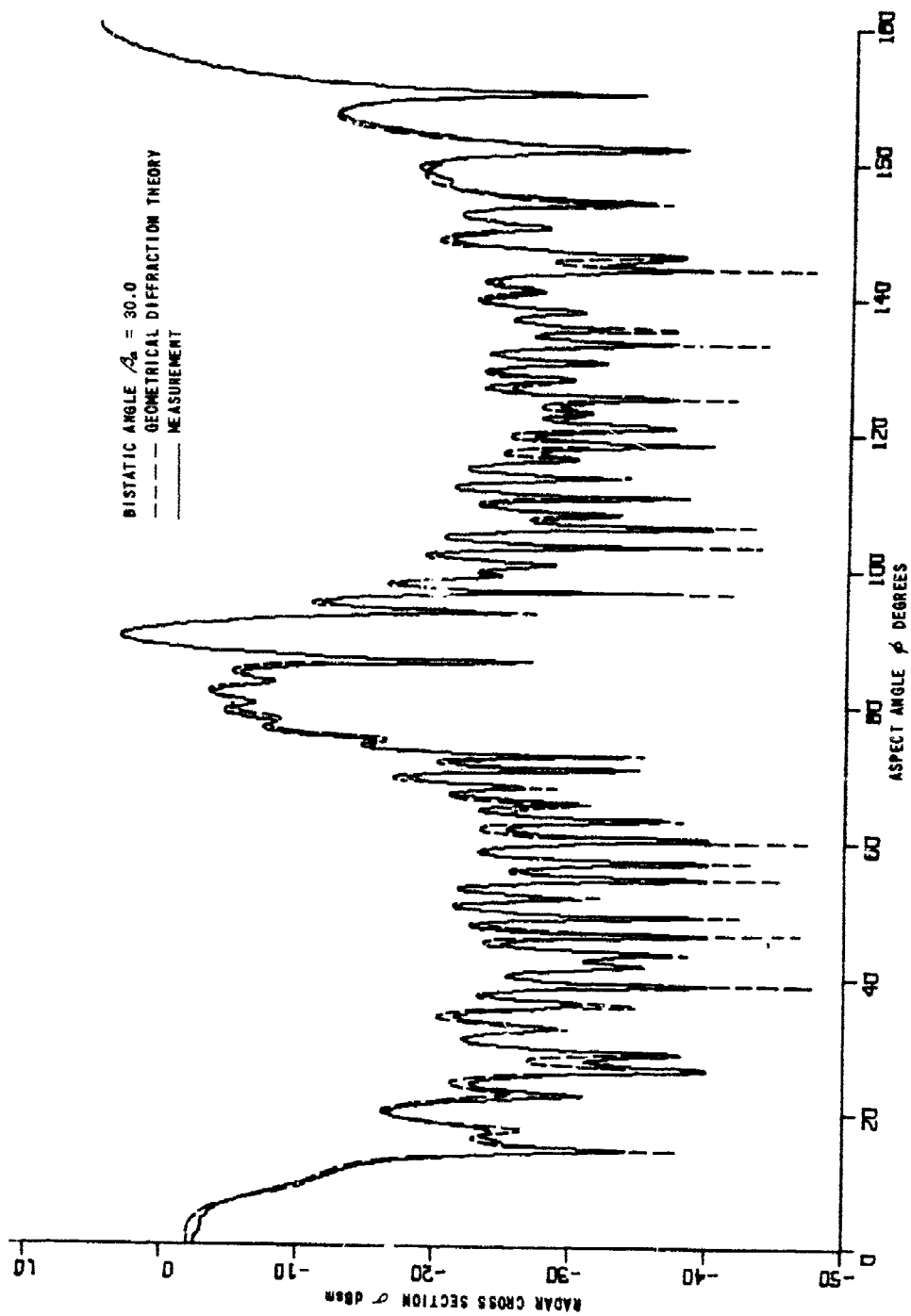


Figure 83 HORIZONTAL POLARIZATION RADAR CROSS SECTION. FRUSTUM-CYLINDER F5CV5, BISTATIC

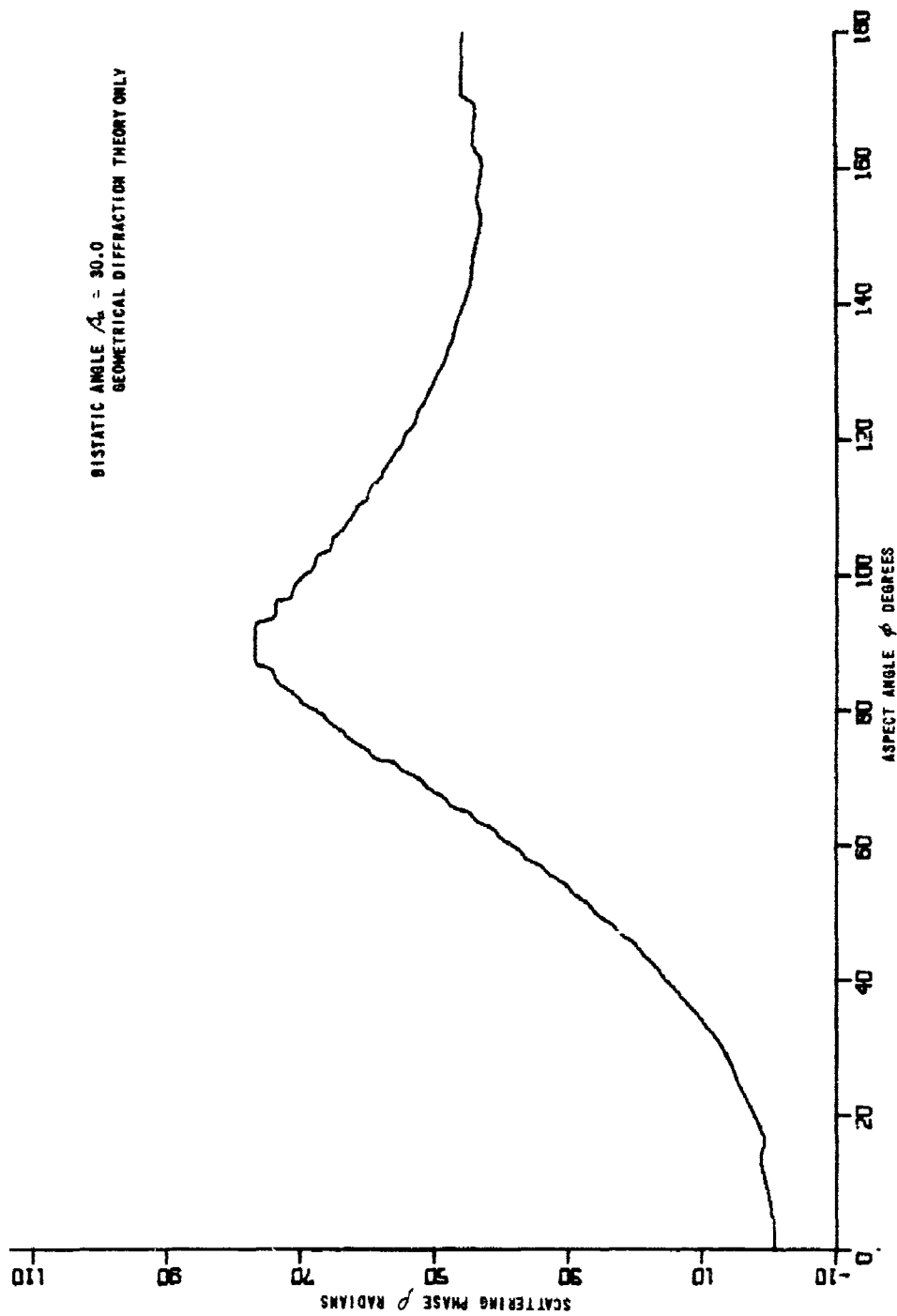


Figure 84 HORIZONTAL POLARIZATION SCATTERING PHASE. FRUSTUM-CYLINDER F50V5, BISTATIC

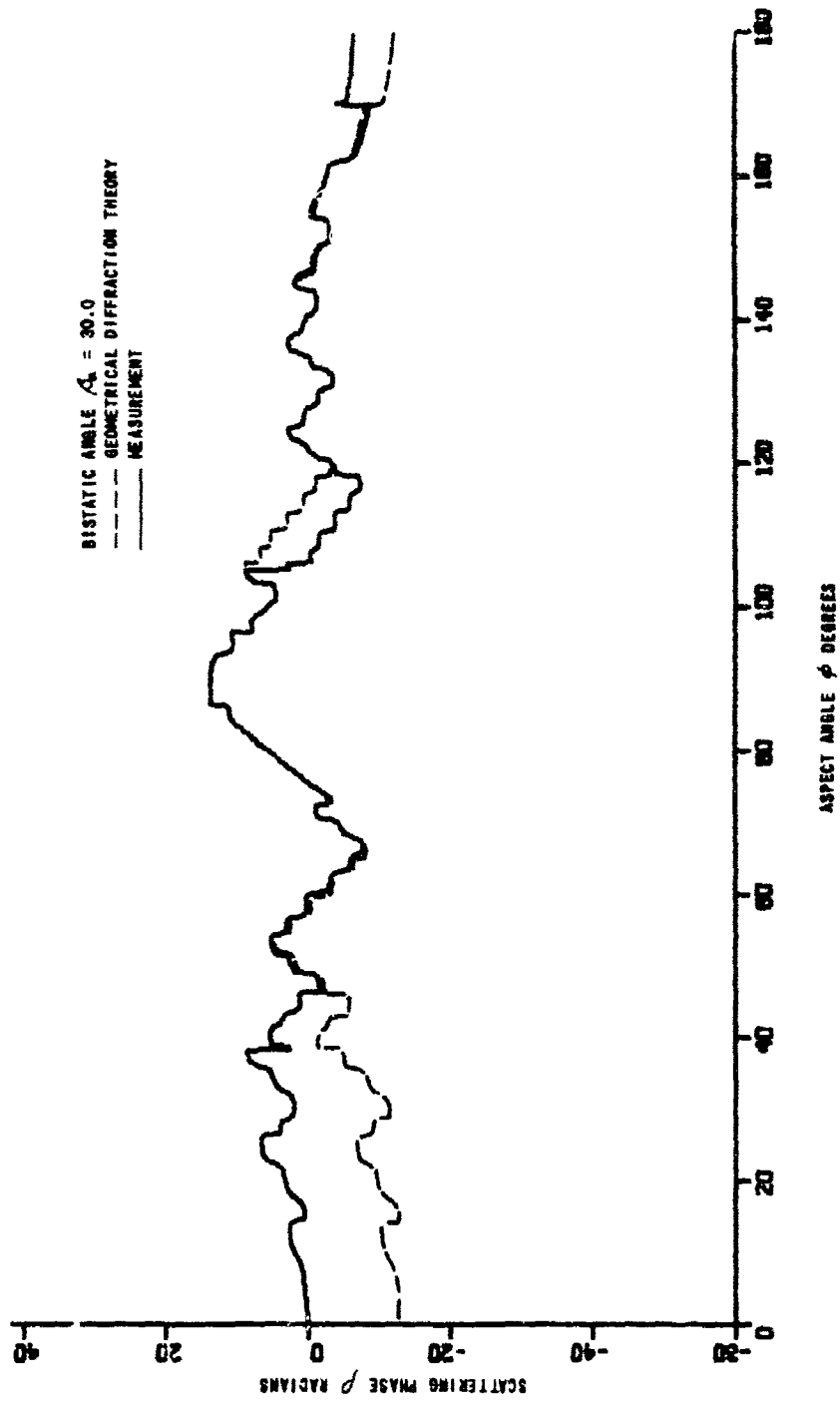


Figure 85 VERTICAL POLARIZATION SCATTERING PHASE. FRUSTUM-CYLINDER F5C75, BISTATIC

## 4.5 CYLINDER-FLARE

### 4.5.1 Analytical Formulation

A cylinder-flare is also formed by combining a cylinder and a frustum (see Figure 86). We use the term cylinder-flare to denote the combined shape when the junction between simple shapes forms a concave edge (see scattering center  $S_2$  in the figure). The presence of a concave edge introduces the possibility of considerable interaction between scattering centers even though they may be separated by many wavelengths. The strength of such interaction will be determined by the degree of concavity of the edge. Referring to Figure 86, if  $\alpha$  is allowed to approach 90 degrees, one can expect a reentrant scattering phenomenon much like the mechanism associated with a dihedral corner reflector. In our case,  $\alpha$  is small (usually about 15 degrees), and interactions may be ignored.

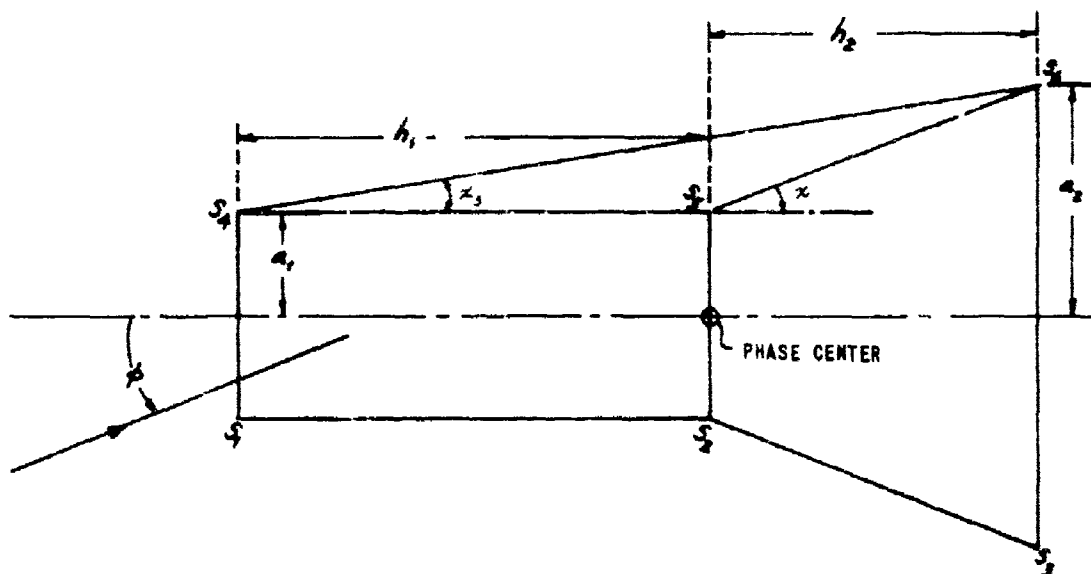


Figure 86 SCATTERING CENTERS ON A CYLINDER-FLARE

Figure 86 shows the location of the six important scattering centers on a cylinder-flare. In the light of previous analyses, we write by inspection

$$\sqrt{\sigma_1} = \frac{\sin(\pi/n_1)}{n_1} \sqrt{\frac{a_1 \csc \phi}{k \cos \beta/2}} \left[ \left\{ \cos \frac{\pi}{n_1} - \cos \left( \frac{\pi + 2\phi}{n_1} \right) \right\}^{-1} \mp \left\{ \cos \frac{\pi}{n_1} - \cos \frac{\beta_0}{n_1} \right\}^{-1} \right] \quad (61)$$

$$\phi \leq \pi - \alpha_3 - \beta_0/2$$

$$= 0; \quad \phi > \pi - \alpha_3 - \beta_0/2$$

$$\sqrt{\sigma_2} = \frac{\sin(\pi/n_2)}{n_2} \sqrt{\frac{a_1 \csc \phi}{k \cos \beta/2}} \left[ \left\{ \cos \frac{\pi}{n_2} - \cos \left( \frac{2\phi}{n_2} \right) \right\}^{-1} \mp \left\{ \cos \frac{\pi}{n_2} - \cos \frac{\beta_0}{n_2} \right\}^{-1} \right] \quad (62)$$

$$\phi \leq \pi - \alpha - \beta_0/2$$

$$= 0; \quad \phi > \pi - \alpha - \beta_0/2$$

$$\sqrt{\sigma_3} = \frac{\sin(\pi/n_3)}{n_3} \sqrt{\frac{a_2 \csc \phi}{k \cos \beta/2}} \left[ \left\{ \cos \frac{\pi}{n_3} - \cos \left( \frac{3\pi - 2\phi}{n_3} \right) \right\}^{-1} \mp \left\{ \cos \frac{\pi}{n_3} - \cos \frac{\beta_0}{n_3} \right\}^{-1} \right] \quad (63)$$

$$\sqrt{\sigma_4} = \frac{\sin(\pi/n_1)}{n_1} \sqrt{\frac{a_1 \csc \phi}{k \cos \beta/2}} \left[ \left\{ \cos \frac{\pi}{n_1} - \cos \left( \frac{\pi - 2\phi}{n_1} \right) \right\}^{-1} \mp \left\{ \cos \frac{\pi}{n_1} - \cos \frac{\beta_0}{n_1} \right\}^{-1} \right] \quad (64)$$

$$\phi \leq \pi/2 - \beta_0/2$$

$$= 0; \quad \phi > \pi/2 - \beta_0/2$$

$$\sqrt{\sigma_5} = 0$$

$$\sqrt{\sigma_6} = \frac{\sin(\pi/n_3)}{n_3} \sqrt{\frac{a_2 \csc \phi}{k \cos \beta/2}} \left[ \left\{ \cos \frac{\pi}{n_3} - \cos \left( \frac{3\pi + 2\phi}{n_3} \right) \right\}^{-1} \mp \left\{ \cos \frac{\pi}{n_3} - \cos \frac{\beta_0}{n_3} \right\}^{-1} \right] \quad (65)$$

$$= 0; \quad \alpha_2 - \beta_0/2 < \phi < \pi/2 + \beta_0/2$$

$$\phi \leq \alpha_2 - \beta_0/2$$

$$= \frac{\sin(\pi/n_3)}{n_3} \sqrt{\frac{a_2 \csc \phi}{k \cos \beta/2}} \left[ \left\{ \cos \frac{\pi}{n_3} - \cos \left( \frac{-\pi + 2\phi}{n_3} \right) \right\}^{-1} \mp \left\{ \cos \frac{\pi}{n_3} - \cos \frac{\beta_0}{n_3} \right\}^{-1} \right]$$

$$\phi \geq \pi/2 + \beta_0/2$$

$$\rho_1 = \frac{\pi}{4} - 2k [a_1 \sin \phi + h_1 \cos \phi] \quad (66)$$

$$\rho_2 = \frac{\pi}{4} - 2ka_1 \sin \phi \quad (67)$$

$$\rho_3 = \frac{\pi}{4} - 2k [a_2 \sin \phi - h_2 \cos \phi] \quad (68)$$

$$\rho_4 = -\frac{\pi}{4} + 2k [a_1 \sin \phi - h_1 \cos \phi] \quad (69)$$

$$\rho_6 = -\frac{\pi}{4} + 2k [a_2 \sin \phi + h_2 \cos \phi] \quad (70)$$

where

$$n_1 = 3/2$$

$$n_2 = 1 - \alpha/\pi \quad (71)$$

$$n_3 = 3/2 + \alpha/\pi$$

$$\alpha = \tan^{-1} \frac{a_2 - a_1}{h_2}$$

$$\alpha_2 = \tan^{-1} \frac{a_2 - a_1}{h_1 + h_2} \quad (72)$$

When incidence is at and near the nose-on axial aspect ( $\phi = 0$ ), we modify the polarization-independent terms in Equations 61 and 64. The combined result is

$$\left(\sqrt{\sigma_1} e^{j\beta_1} + \sqrt{\sigma_2} e^{j\beta_2}\right)_{poli} = 2\sqrt{\pi} k \cos \beta/2 a_z^2 \frac{J_1(2ka_z \cos \beta/2 \sin \phi)}{(2ka_z \cos \beta/2 \sin \phi)} \times e^{-j\pi/2 - j2kh_z \cos \beta/2 \cos \phi} \quad (73)$$

Equation 73 is employed for  $0 \leq \phi \leq \phi_{ca}$  where  $2ka_z \sin \phi_{ca} = 2.44$ . All other terms are modified by the constraint  $\csc \phi \leq ka_z \cos \beta/2$ . When incidence is at and near the tail-on axial aspect ( $\phi = \pi$ ), we modify the polarization-independent terms in Equations 63 and 65. The combined result is

$$\left(\sqrt{\sigma_3} e^{j\beta_3} + \sqrt{\sigma_4} e^{j\beta_4}\right)_{poli} = 2\sqrt{\pi} k \cos \beta/2 a_z^2 \frac{J_1(2ka_z \cos \beta/2 \sin \phi)}{(2ka_z \cos \beta/2 \sin \phi)} \times e^{-j\pi/2 + j2kh_z \cos \beta/2 \cos \phi} \quad (74)$$

Equation 74 is used for  $\pi - \phi_{ca} \leq \phi \leq \pi$  where  $2ka_z \sin \phi = 2.44$ . The polarization-dependent terms in Equations 63 and 65 are modified by the constraint  $\csc \phi \leq ka_z \cos \beta/2$ .

When incidence is at and near broadside on the cylinder section ( $\phi = \pi/2$ ), we modify the polarization-independent terms in Equations 61 and 62. The combined result is

$$\left(\sqrt{\sigma_1} e^{j\beta_1} + \sqrt{\sigma_2} e^{j\beta_2}\right)_{poli} = -\sqrt{a_z k \cos \beta/2} h_z \frac{\sin(kh_z \cos \beta/2 \cos \phi)}{(kh_z \cos \beta/2 \cos \phi)} \times e^{j3\pi/4 - j2ka_z \cos \beta/2 \sin \phi - jkh_z \cos \beta/2 \cos \phi} \quad (75)$$

Equation 74 is employed for  $\phi_{cb} \leq \phi \leq \pi - \phi_{cb}$  with  $\phi_{cb}$  given by  $kh, \cos \phi_{cb} = 2.25$ . All other contributions are well behaved. We employ the curve-fitting technique to eliminate singularities which arise in Equations 62 and 63 when incidence is broadside to the flare section ( $\phi = \pi/2 - \alpha$ ).

#### 4.5.2 Results

Table 8 lists parameters employed in the study of the cylinder-flare. Whereas the study is limited to bistatic situations, the number of targets listed does not satisfy specifications given in Table 1; bistatic data on one additional target are called for. However, measurement data taken on only one cylinder-flare has been supplied to CAL. Dimensions of the target CY4F4 may be obtained from Table 2. Again, the phase reference chosen for measurements was the centroid of the cylindrical segment of the target. A common phase reference is achieved by adding the term  $kh, \cos \beta/2 \cos \phi$  to analytical estimates of scattering phase.

Table 8  
PARAMETERS FOR CYLINDER-FLARE STUDY

| MODEL<br>DESIGNATION | FREQUENCY<br>(GHz) | BISTATIC ANGLE $\beta_a$<br>(DEGREES) |
|----------------------|--------------------|---------------------------------------|
| CY4F4                | 5.885              | 10.25                                 |
|                      | 6.050              | 30.0                                  |

Figures 87 through 90 show results for cylinder-flare CY4F4 for bistatic angle  $\beta_a = 10.25$  degrees. Agreement between theory and measurement is considered very good. Differences in radar cross section noted at and near the aspect which is broadside to the flare ( $\phi = \pi/2 - \alpha$ ) may be due to interactions between the cylinder and the frustum. As noted in subsection 4.5.1, these interaction effects are neglected in the present formulation. Figures 91 through 94 depict scattering matrix data for cylinder-flare CY4F4 with bistatic angle  $\beta_a = 30.0$  degrees. Horizontal



polarization results shown in Figures 92 and 94 exhibit very good correspondence. Vertical polarization data given in Figures 91 and 93 are theoretical predictions only; experimental values were contained on the magnetic tape in a format which did not plot. Notice that Figure 91 reveals a discontinuity in predicted radar cross section for  $\phi \approx 84$  degrees. This discontinuity arises due to the use of cross-over aspect angles originally developed for use with simple shapes.

#### 4.5.3 Remarks

On the basis of available comparisons between theory and measurement, we can conclude that agreement between theory and experiment for the cylinder-flare is comparable with that reported for the cylinder, frustum, and frustum-cylinder.

Interactions between component shapes should be negligible provided the junction edge is no more slightly concave than the 15 degrees used here.

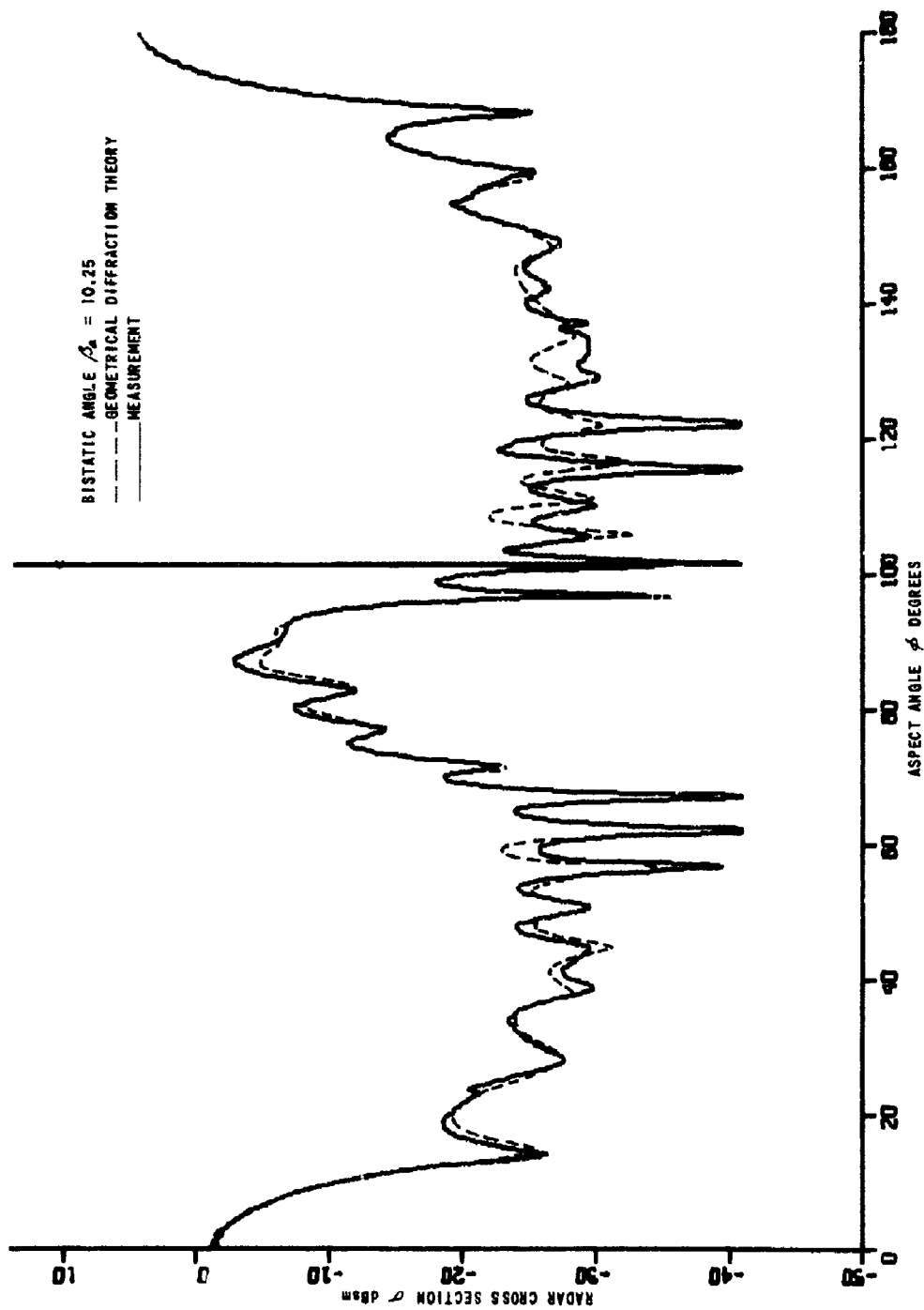


Figure 87 VERTICAL POLARIZATION RADAR CROSS SECTION. CYLINDER-FLARE C/MFL, BISTATIC

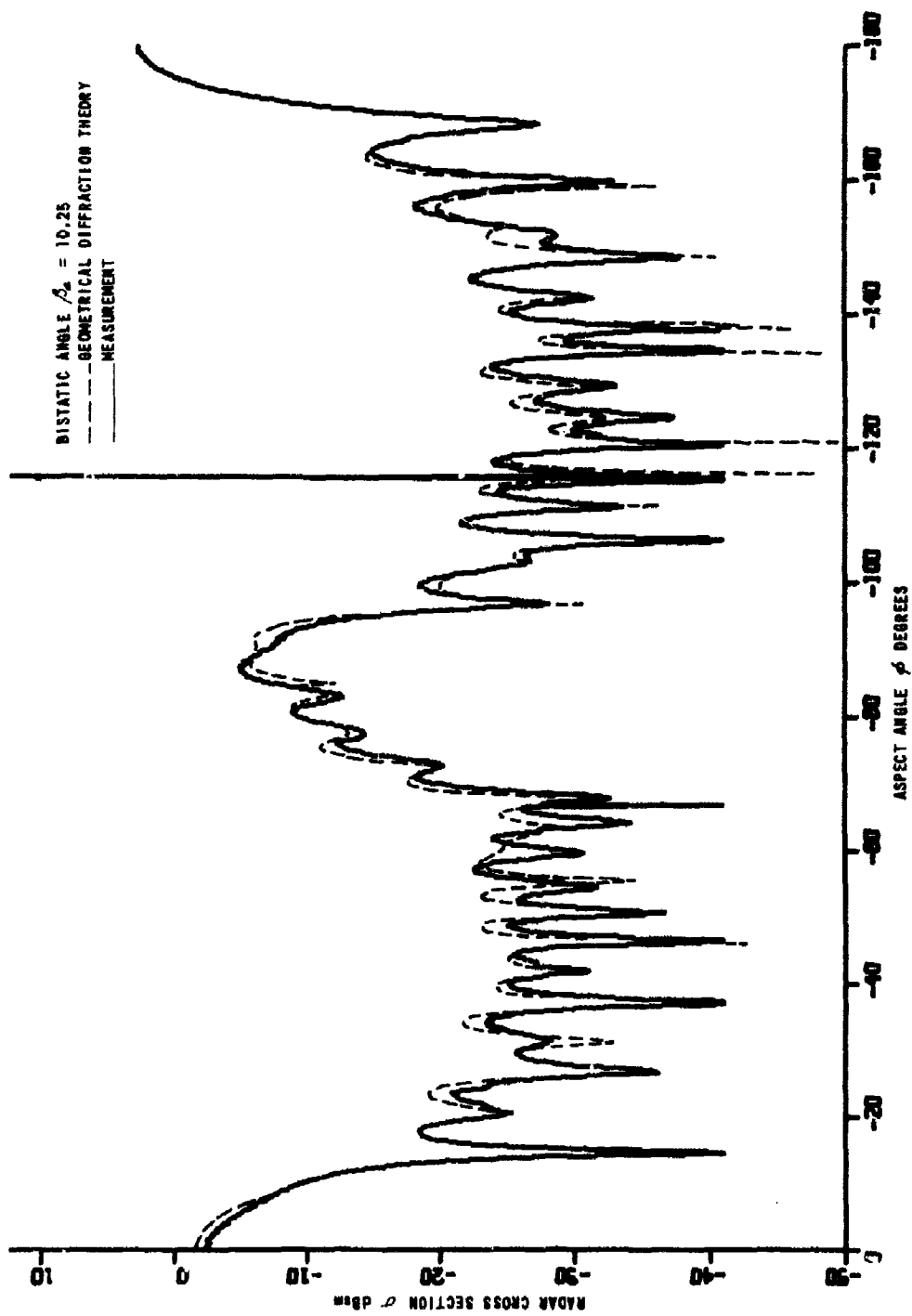


Figure 88 HORIZONTAL POLARIZATION RADAR CROSS SECTION. CYLINDER-FLARE CY4FN, BISTATIC

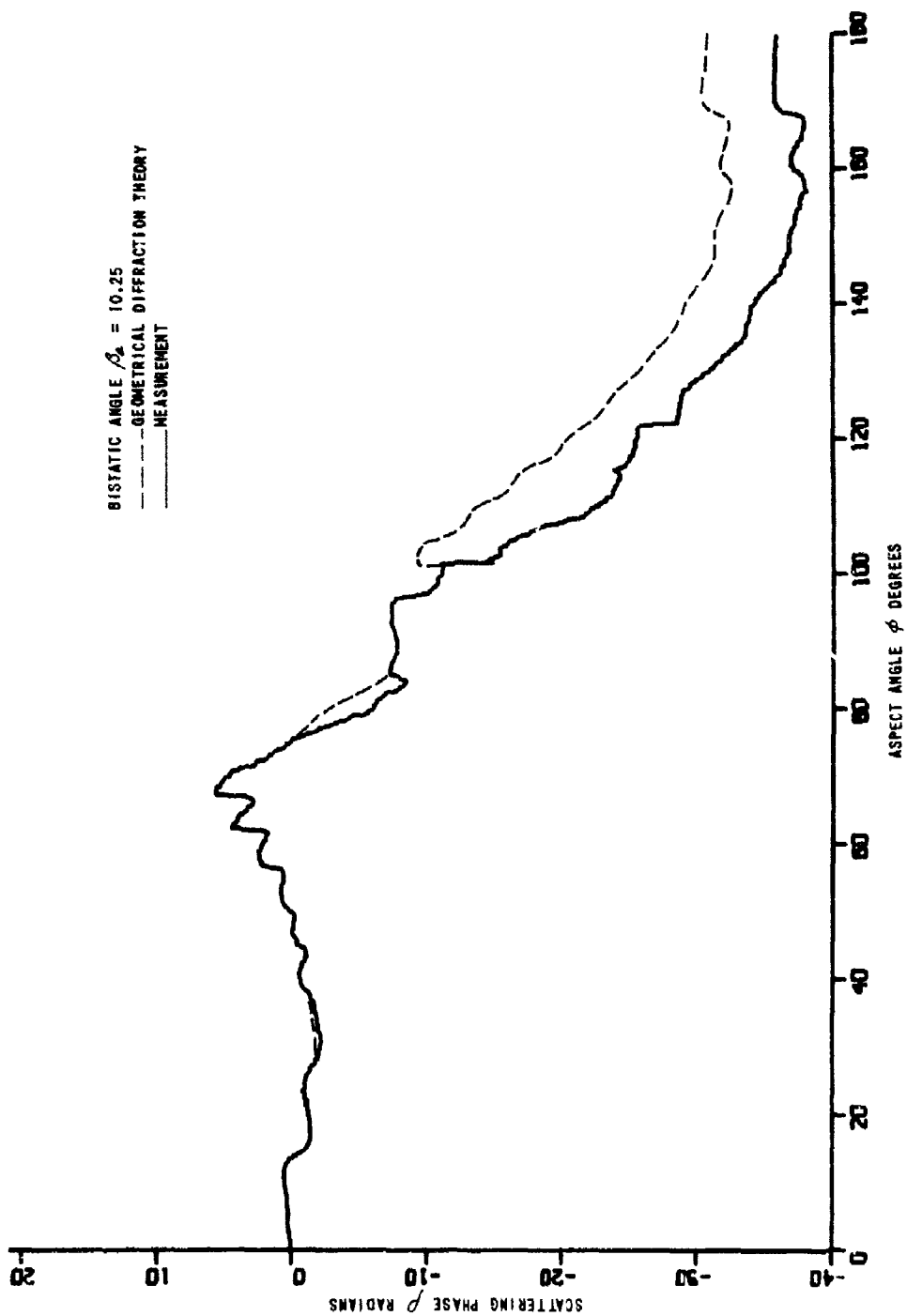


Figure 89 VERTICAL POLARIZATION SCATTERING PHASE, CYLINDER-FLARE CY4FH, BISTATIC

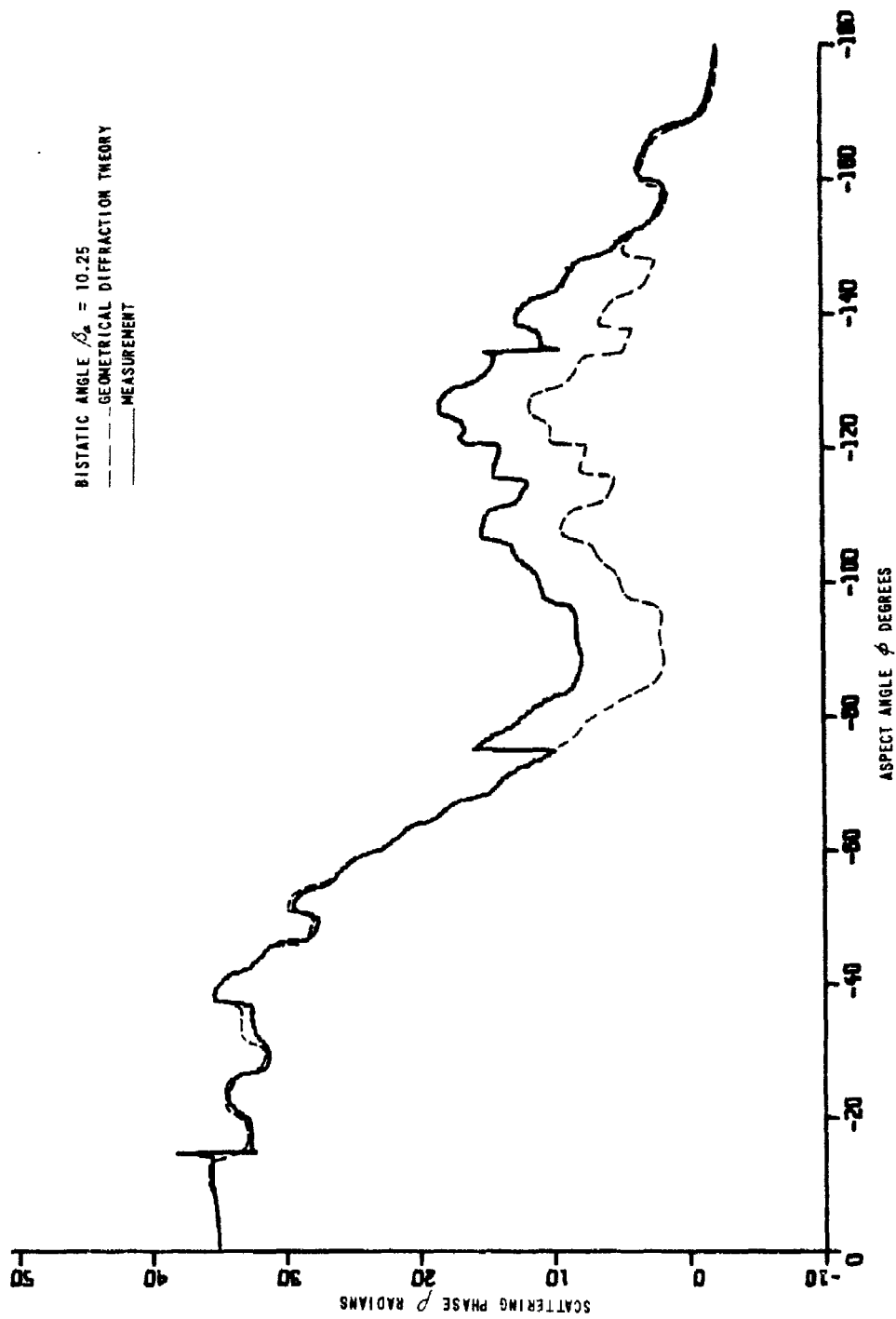


Figure 90 HORIZONTAL POLARIZATION SCATTERING PHASE. CYLINDER-FLARE CY4F4, BISTATIC

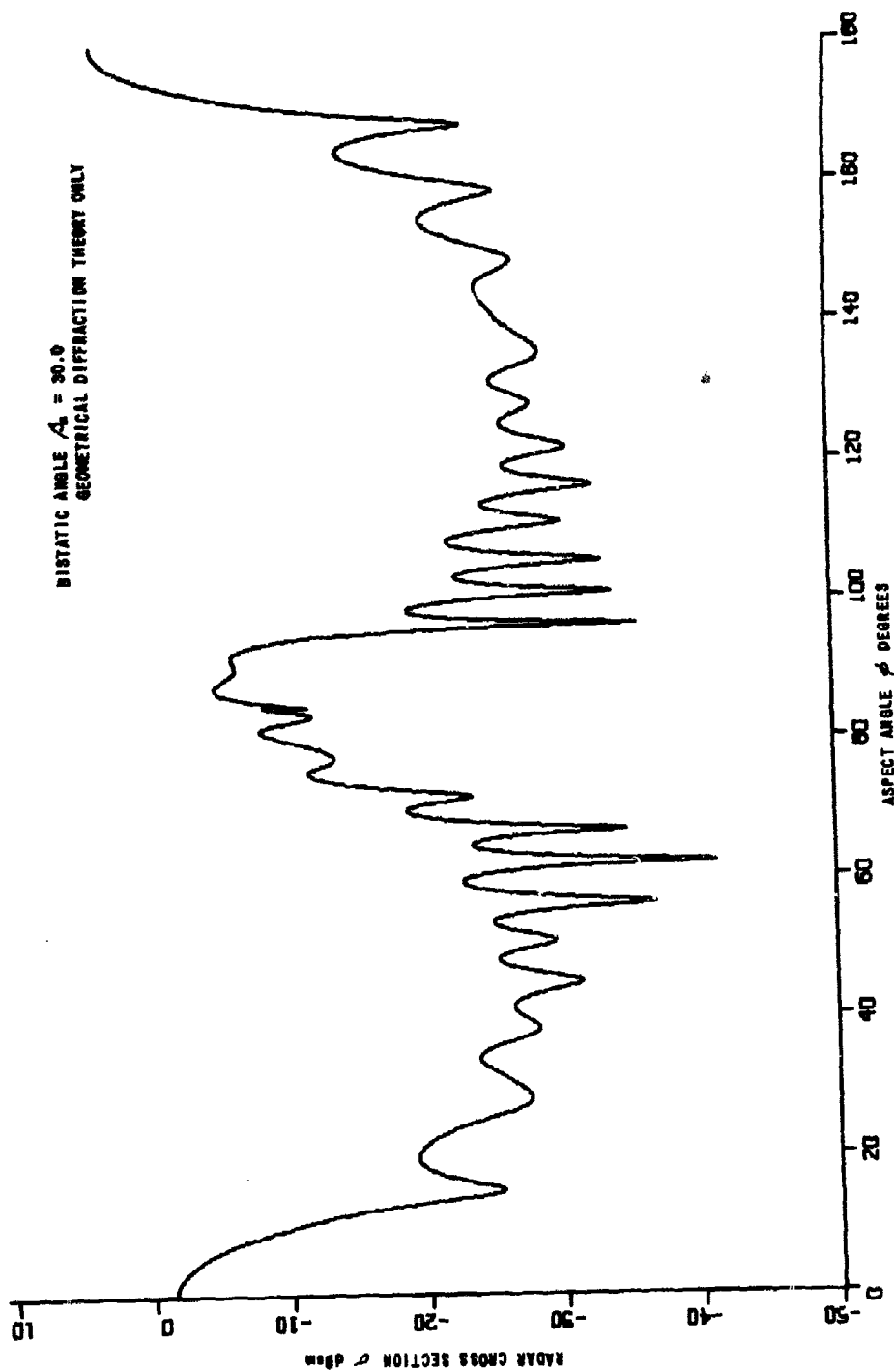


Figure 91 VERTICAL POLARIZATION RADAR CROSS SECTION. CYLINDER-FLARE CUSP, BISTATIC

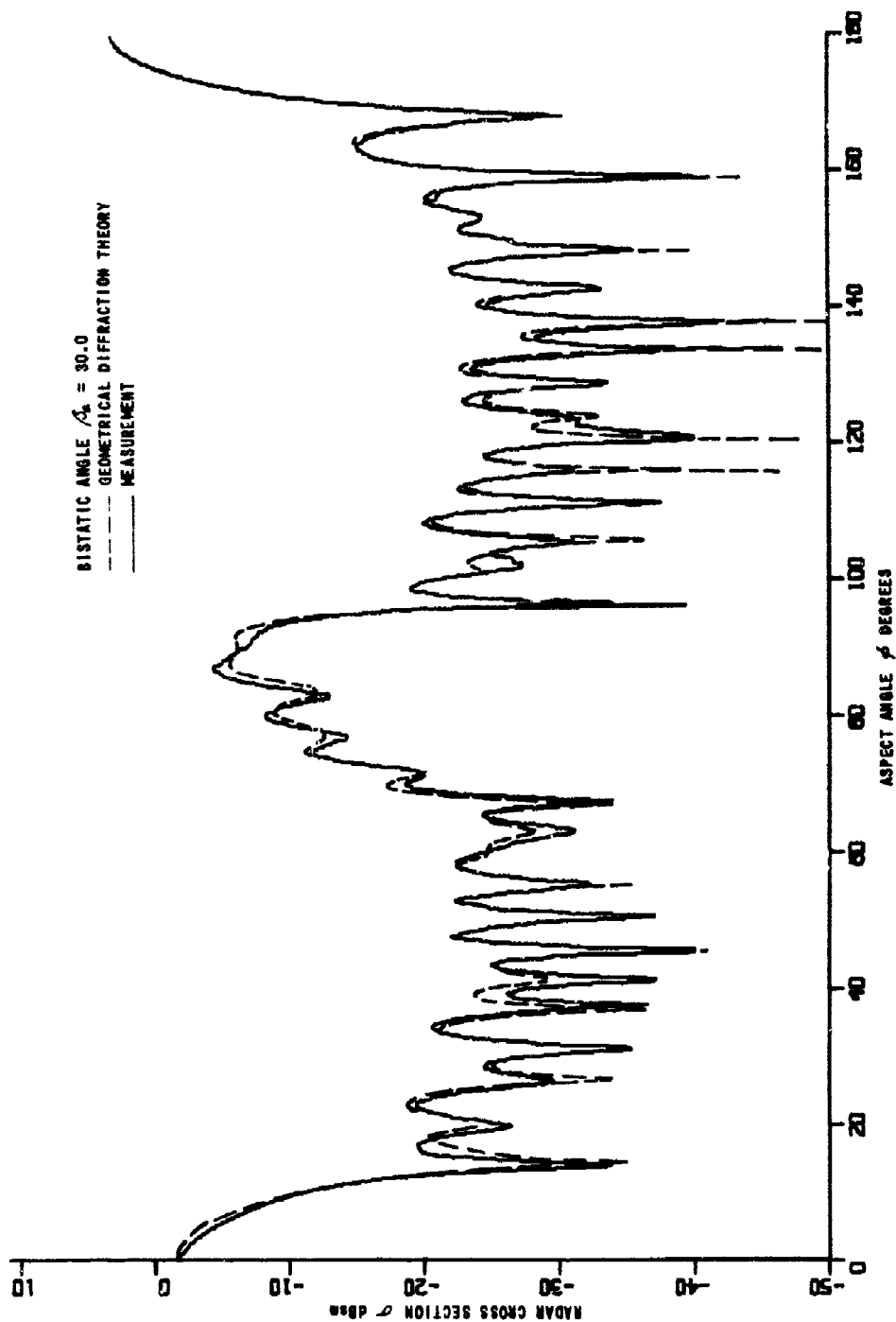


Figure 92 HORIZONTAL POLARIZATION RADAR CROSS SECTION. CYLINDER-FLARE CYLINDER, BISTATIC

BISTATIC ANGLE  $\chi_0 = 30.0$   
GEOMETRICAL DIFFRACTION THEORY

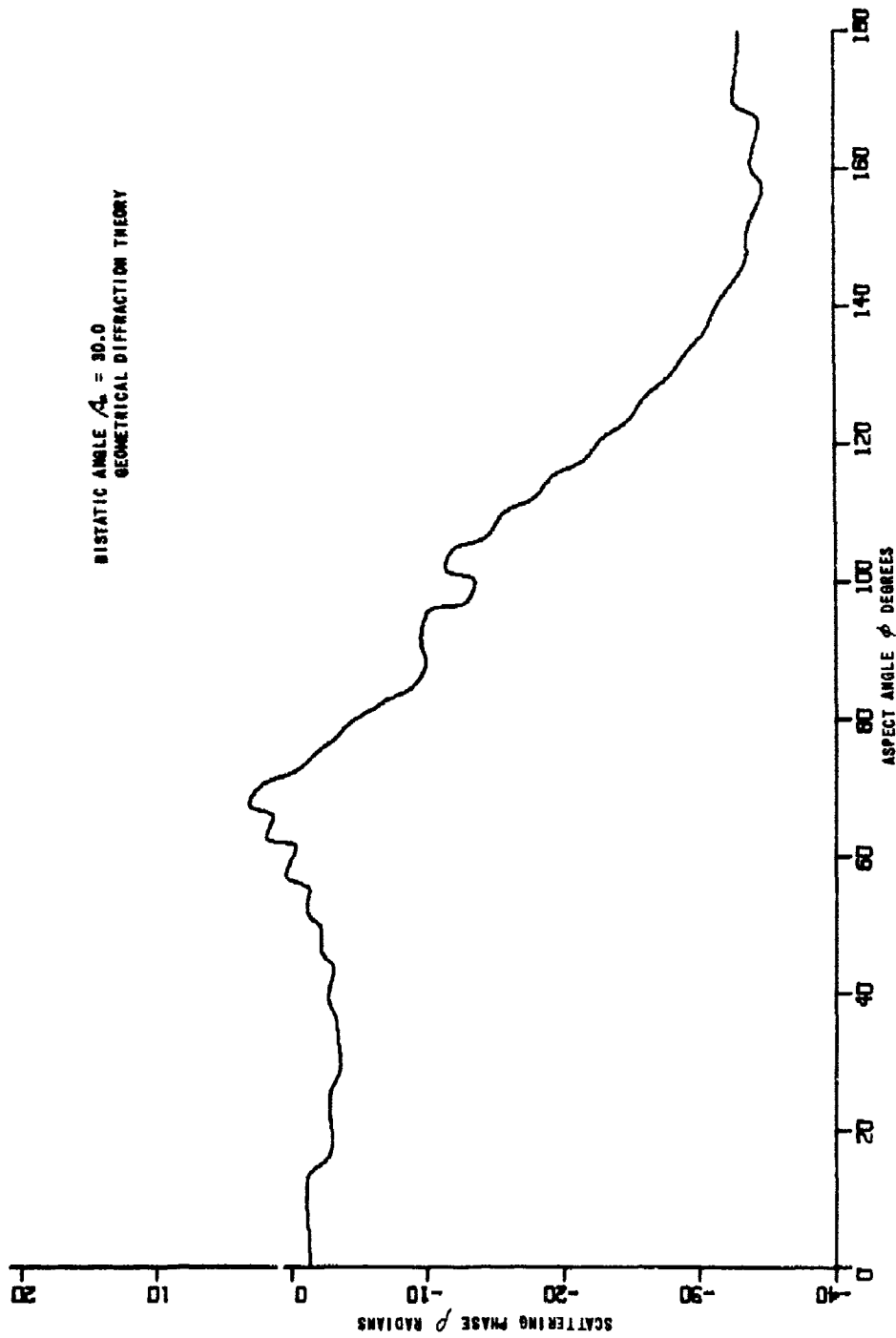


Figure 93 VERTICAL POLARIZATION SCATTERING PHASE. CYLINDER-FLARECYU4M, BISTATIC



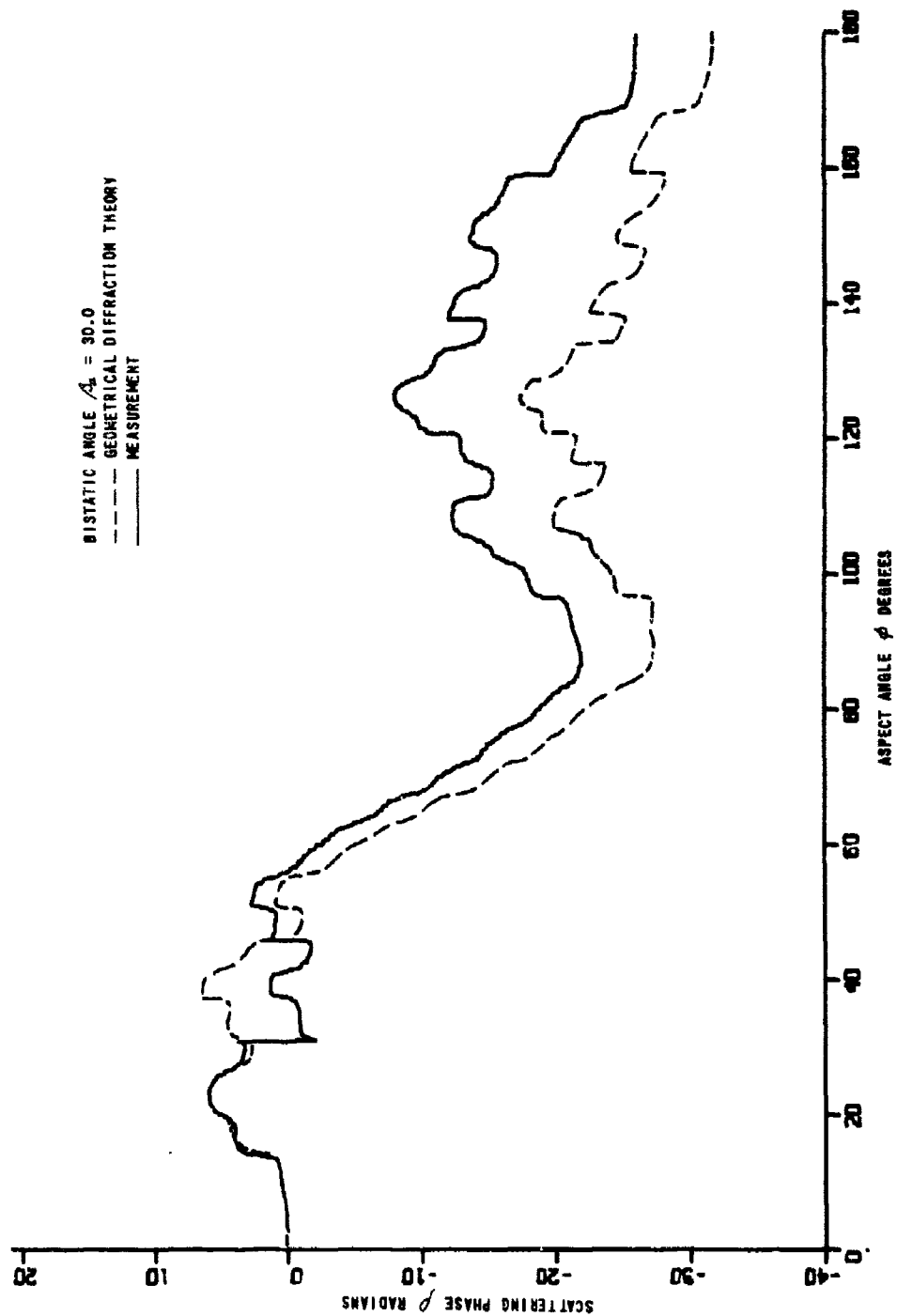


Figure 94 HORIZONTAL POLARIZATION SCATTERING PHASE. CYLINDER-FLARE CYNF4, BISTATIC

## 4.6 CONE-CYLINDER

### 4.6.1 Analytical Formulation

The cone-cylinder is a combinatorial shape formed by joining a cone to a cylinder in the manner depicted in Figure 95. The five important scattering centers on the target are labelled in the figure. Each scattering center has been subject to analysis in previous investigations. Based upon work already discussed, we write by inspection

$$\sqrt{\sigma_1} = \frac{\sin(\pi/n_1)}{4k\sqrt{2\pi} n_1} \left[ \cos \frac{\pi}{n_1} - \cos \frac{2(\pi - \alpha - \phi)}{n_1} \right]^{-1} \quad (76)$$

$$= 0 ; \phi > \pi - \alpha \quad \phi \leq \pi - \alpha$$

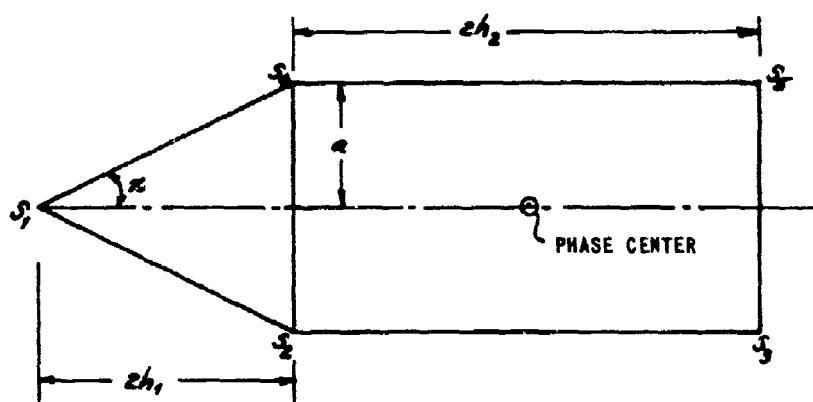


Figure 95 SCATTERING CENTERS ON A CONE-CYLINDER

$$\sqrt{\sigma_2} = \frac{\sin(\pi/n_2)}{n_2} \sqrt{\frac{a \csc \phi}{k}} \left[ \left\{ \cos \frac{\pi}{n_2} - \cos \frac{2\pi - 2\phi}{n_2} \right\}^{-1} \right. \\ \left. \mp \left\{ \cos \frac{\pi}{n_2} - 1 \right\}^{-1} \right] \quad (77)$$

$$\sqrt{\sigma_3} = \frac{\sin(\pi/n_3)}{n_3} \sqrt{\frac{a \csc \phi}{k}} \left[ \left\{ \cos \frac{\pi}{n_3} - \cos \frac{3\pi - 2\phi}{n_3} \right\}^{-1} \right. \\ \left. \mp \left\{ \cos \frac{\pi}{n_3} - 1 \right\}^{-1} \right] \quad (78)$$

$$\sqrt{\sigma_4} = \frac{\sin(\pi/n_2)}{n_2} \sqrt{\frac{a \csc \phi}{k}} \left[ \left\{ \cos \frac{\pi}{n_2} - \cos \frac{2\pi + 2\phi}{n_2} \right\}^{-1} \right. \\ \left. \mp \left\{ \cos \frac{\pi}{n_2} - 1 \right\}^{-1} \right] \quad (79)$$

$= 0; \phi > \pi$ 
 $\phi \leq \pi$

$$\sqrt{\sigma_5} = \frac{\sin(\pi/n_3)}{n_3} \sqrt{\frac{a \csc \phi}{k}} \left[ \left\{ \cos \frac{\pi}{n_3} - \cos \frac{-\pi + 2\phi}{n_3} \right\}^{-1} \right. \\ \left. \mp \left\{ \cos \frac{\pi}{n_3} - 1 \right\}^{-1} \right] \quad (80)$$

$= 0; \phi \leq \pi/2$ 
 $\phi \geq \pi/2$

$$\rho_1 = \frac{\pi}{4} - 2k [2h_1 \cos \phi + h_2 \cos \phi + a \sin \phi] \quad (81)$$

$$\rho_2 = \frac{\pi}{4} - 2k [a \sin \phi + h_2 \cos \phi] \quad (82)$$

$$\rho_3 = \frac{\pi}{4} - 2k [a \sin \phi - h_2 \cos \phi] \quad (83)$$

$$\rho_4 = -\frac{\pi}{4} + 2k [a \sin \phi - h_2 \cos \phi] \quad (84)$$

$$\rho_5 = -\frac{\pi}{4} + 2k [a \sin \phi + h_2 \cos \phi] \quad (85)$$

where

$$\begin{aligned} n_1 &= 2 - \frac{2x}{\pi} \\ n_2 &= 1 + \frac{x}{\pi} \\ n_3 &= \frac{3}{2} \end{aligned} \quad (86)$$

When incidence is at and near the nose-on axial aspect ( $0 \leq \phi \leq x$ ), we replace Equations 77 and 79 by the expression

$$\begin{aligned} \sqrt{\sigma_2} e^{j\rho_2} + \sqrt{\sigma_4} e^{j\rho_4} &= \frac{2\sqrt{\pi} a \sin(\pi/n_2)}{n_2} \left[ \left\{ \cos \frac{\pi}{n_2} - \cos \frac{2\pi}{n_2} \right\}^{-1} J_0(2ka \sin \phi) \right. \\ &\quad - \frac{i \frac{2 \tan \phi}{n_2} \sin \frac{2\pi}{n_2}}{\left( \cos \frac{\pi}{n_2} - \cos \frac{2\pi}{n_2} \right)^2} J_1(2ka \sin \phi) + \left\{ \cos \frac{\pi}{n_2} - 1 \right\}^{-1} J_2(2ka \sin \phi) \left. \right] \quad (87) \\ &\quad e^{-j2kh_2 \cos \phi} \end{aligned}$$

where Equation 87 is recognized as a variant of the result obtained for the flat-backed cone. The return from center  $S_3$  is well behaved when we apply the constraint  $\csc \phi \leq ka$  in Equation 78. When incidence is at and near the tail-on axial aspect, we modify the polarization-independent terms in Equations 78 and 80. The combined result is

$$\left( \sqrt{\sigma_3} e^{j\rho_3} + \sqrt{\sigma_5} e^{j\rho_5} \right)_{\text{poli}} = 2\sqrt{\pi} ka^2 \frac{J_1(2ka \sin \phi)}{(2ka \sin \phi)} \times e^{-j\frac{\pi}{2} + j2kh_2 \cos \phi} \quad (88)$$

where Equation 88 applies in the interval  $\pi - \phi_{cl} \leq \phi \leq \pi$ , with the cross-over aspect given by  $2ka \sin \phi = 2.44$ . The polarization-dependent terms in Equations 78 and 80, and the contribution from center  $S_2$  (Equation 77) are subject to the constraint  $\csc \phi \leq ka$

At and near the broadside aspect ( $\phi = \pi/2$ ) the polarization-independent terms in Equations 77 and 78 are replaced by the combined expression

$$\left( \sqrt{\sigma_2} e^{j\rho_2} + \sqrt{\sigma_3} e^{j\rho_3} \right)_{\text{poli}} = -\sqrt{ak} 2h_2 \frac{\sin(2kh_2 \cos \phi)}{(2kh_2 \cos \phi)} \times e^{j\frac{\pi}{4} - j2ka \sin \phi} \quad (89)$$

Equation 89 applies in the aspect interval  $\phi_{cb} \leq \phi \leq \pi - \phi_{cb}$  where the cross-over aspect is given by the relation  $2kh_2 \cos \phi_{cb} = 2.25$ . All other contributions to the total return from the target are well behaved in this angular region.

#### 4.6.2 Results

Table 9 lists targets employed in the evaluation of monostatic theory for the cone-cylinder. The number of models given in the table agrees with specifications contained in Table 1. Dimensions of each target may be obtained from Table 2.

Table 9  
PARAMETERS FOR CONE-CYLINDER STUDY

| MODEL<br>DESIGNATION | FREQUENCY<br>(GHz) |
|----------------------|--------------------|
| C1CY3                | 6.000              |
| C2CY3                | 5.975              |
| C4CY5                | 6.000              |

Figures 96 through 99 show results for cone-cylinder C1CY3. Consider first radar cross sections in the aspect region  $0 \leq \phi \leq 60$  and near the broadside aspect ( $\phi = \pi/2 - \alpha$ ). These are the ranges of viewing angles where scattering by the combinatorial shape is determined by the cone section. Then the same shortcomings noted in discussion of cone theory apply here.

In remaining aspect intervals, theory and measurement show close correspondence except for horizontal polarization results for  $120 < \phi < 160$  degrees, where experimental data exhibit finer lobe structure than theory. Figures 98 and 99 show theoretical phase data only; corresponding measurement data were not plotted.

Results for C2CY3 and C4CY5 confirm observations noted above (see Figures 100 through 107). Here we may compare phase data. The theory is useful for estimating the gross dependence of phase upon aspect angle.

#### 4.6.3 Remarks

Theory for the cone-cylinder exhibits the same failings as theory for the simple cone. Until the latter analysis is upgraded, it is not advisable to apply geometrical diffraction theory to predict scattering by combinatorial shapes which include a pointed cone.

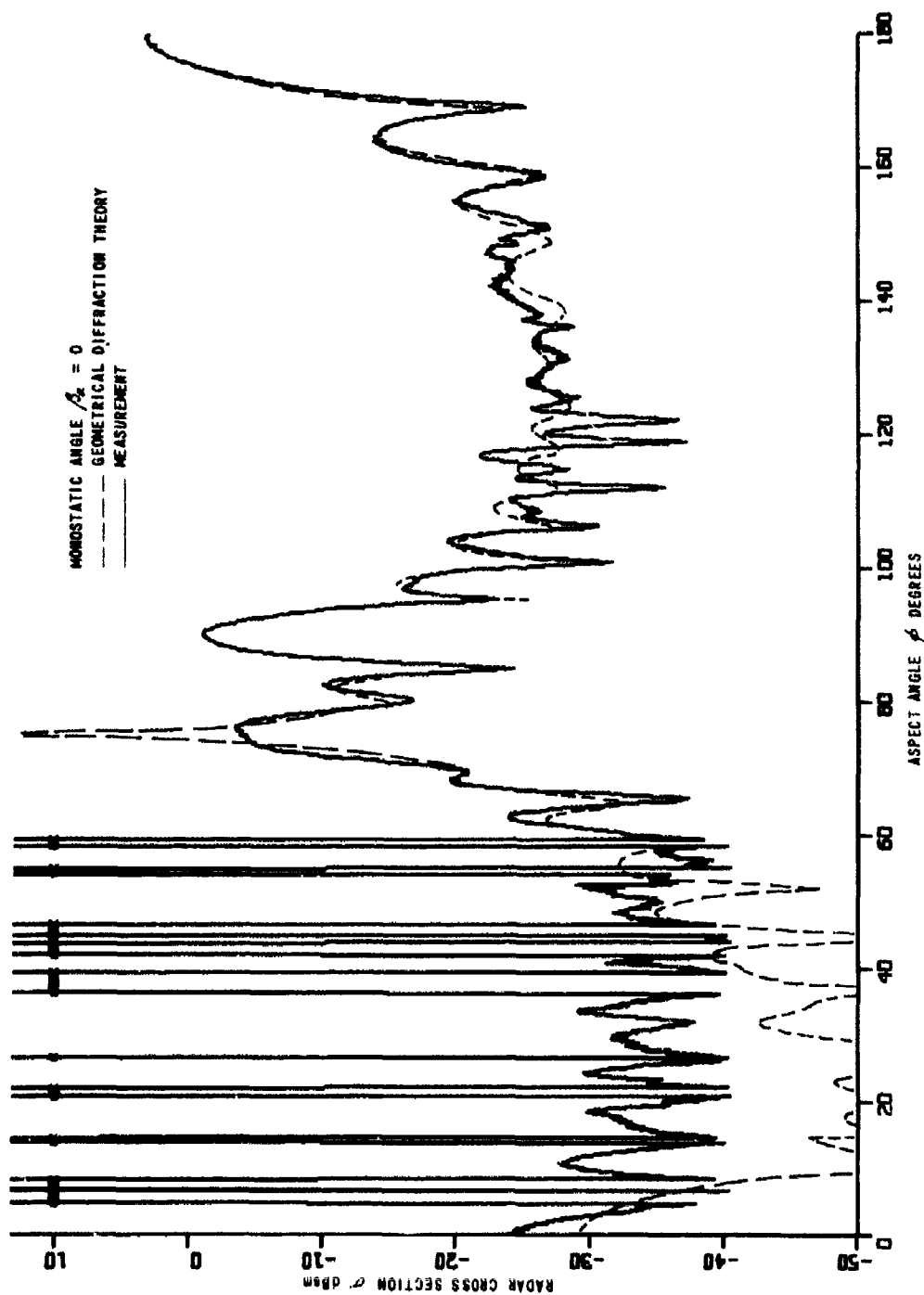


Figure 96 VERTICAL POLARIZATION RADAR CROSS SECTION. CONE-CYLINDER C1C1V3, MONOSTATIC



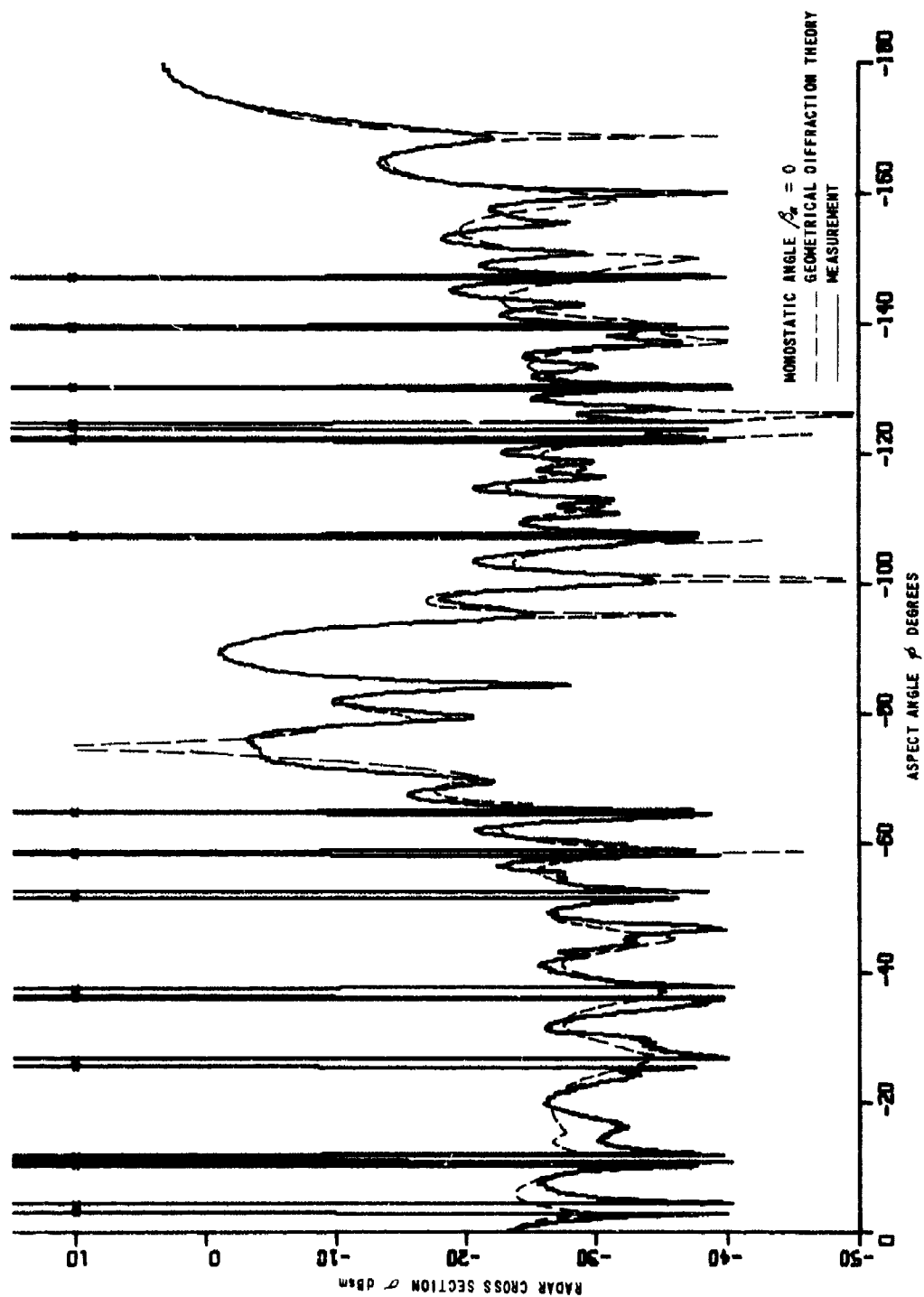


Figure 97 HORIZONTAL POLARIZATION RADAR CROSS SECTION. CONE-CYLINDER C1C13, MONOSTATIC

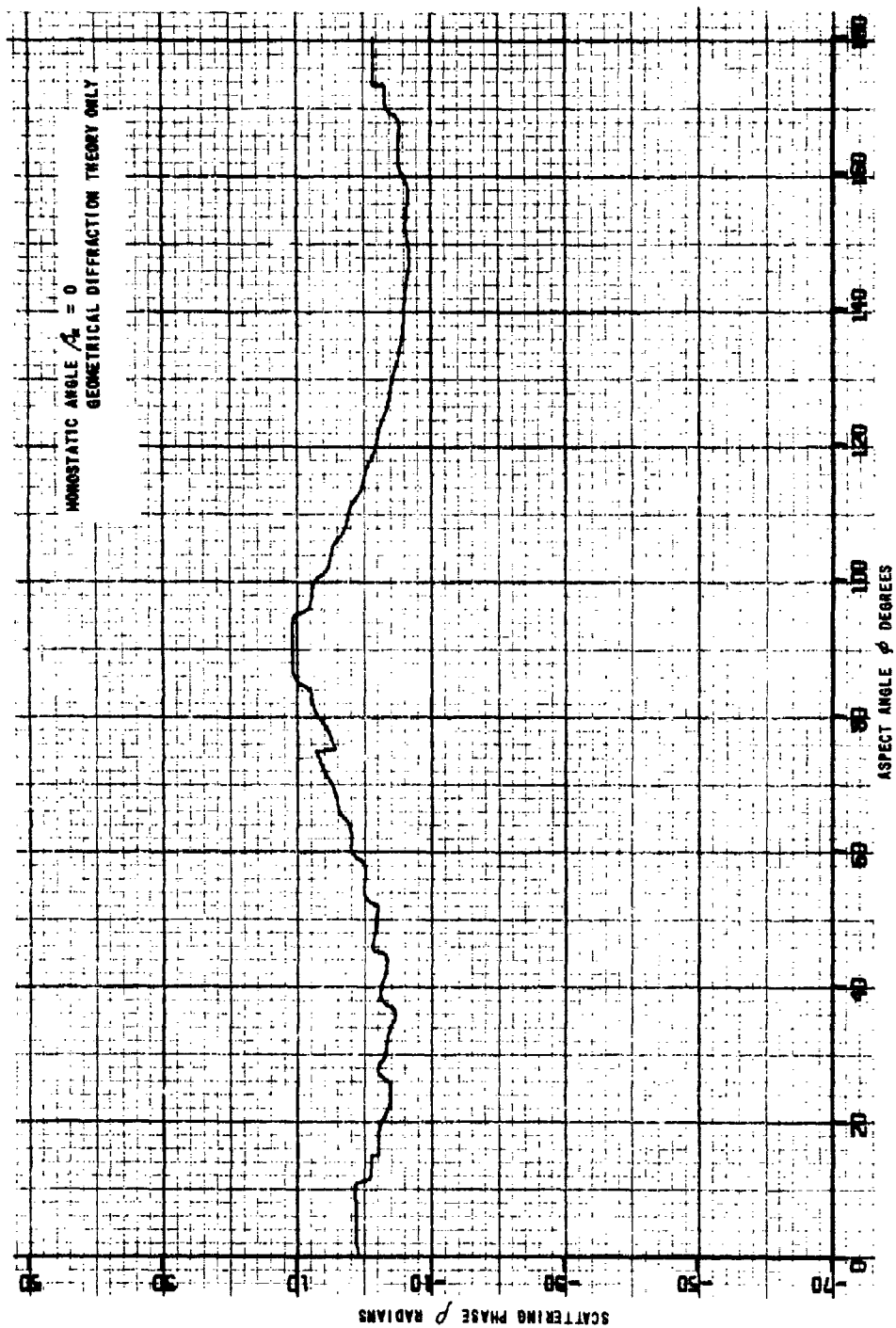


Figure 98 VERTICAL POLARIZATION SCATTERING PHASE. CONE-CYLINDER CICY3, MONOSTATIC

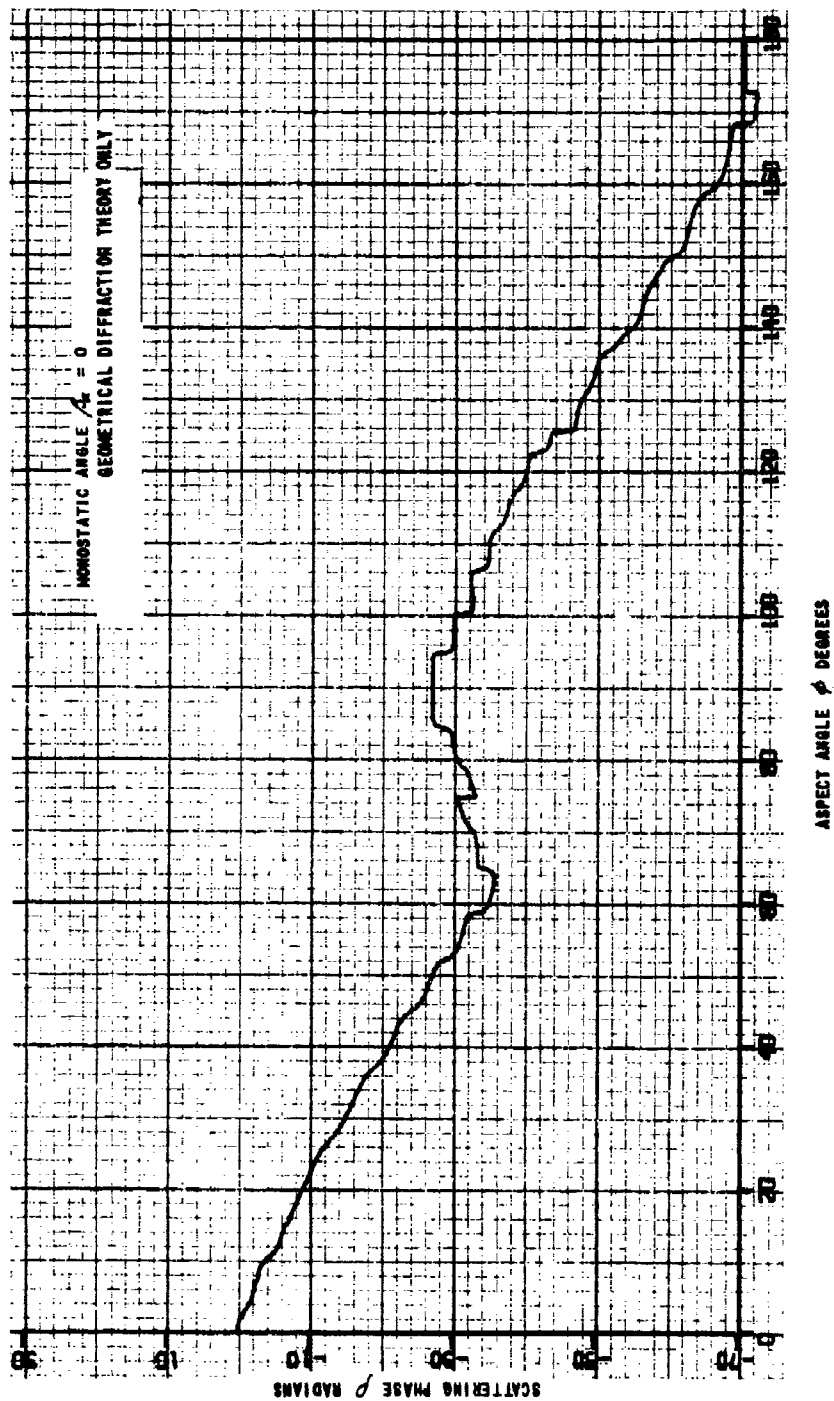


Figure 99 HORIZONTAL POLARIZATION SCATTERING PHASE. CONE CYLINDER CICY3, MONOSTATIC C

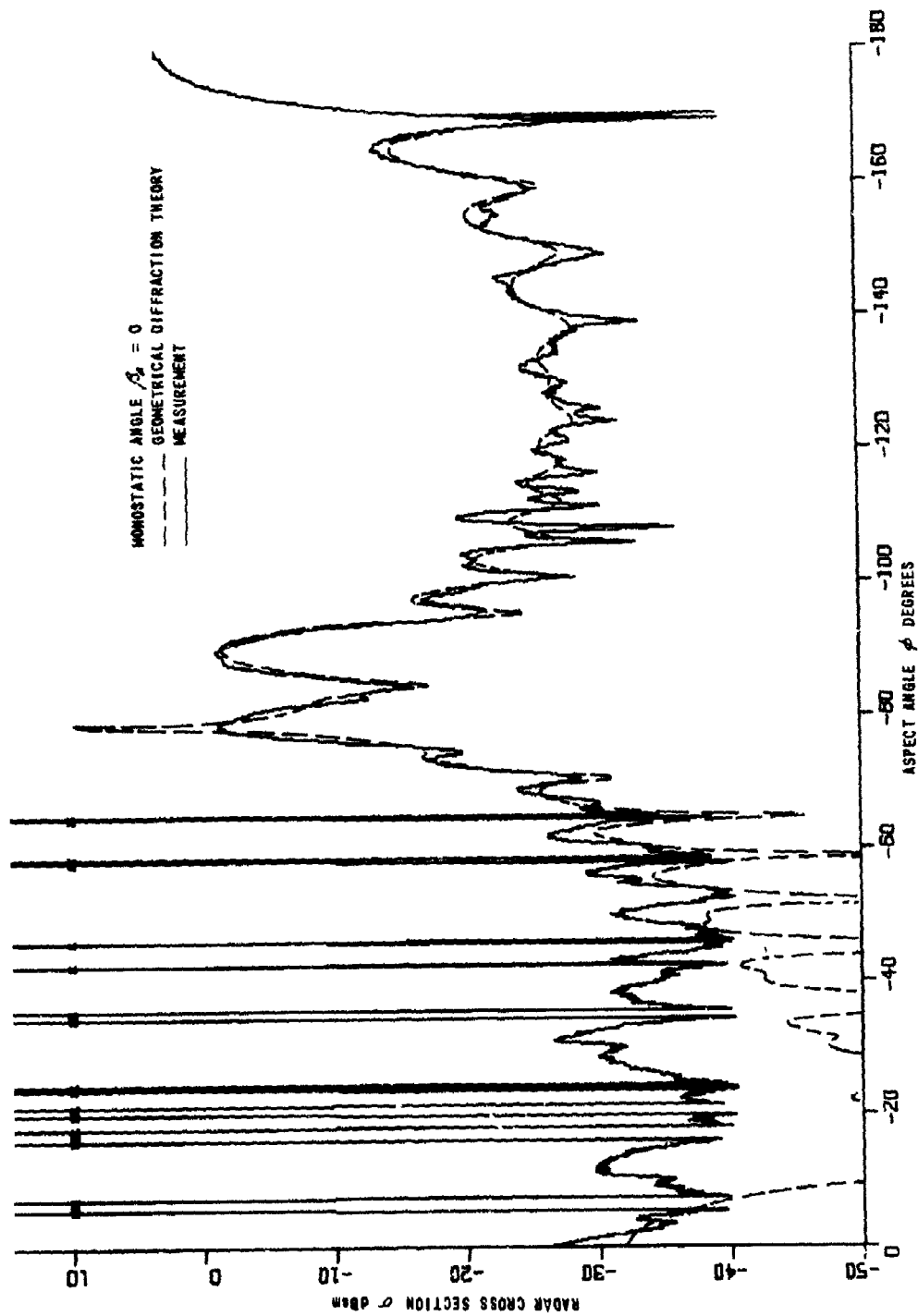


Figure 100 VERTICAL POLARIZATION RADAR CROSS SECTION. CONE-CYLINDER C2C33, MONOSTATIC

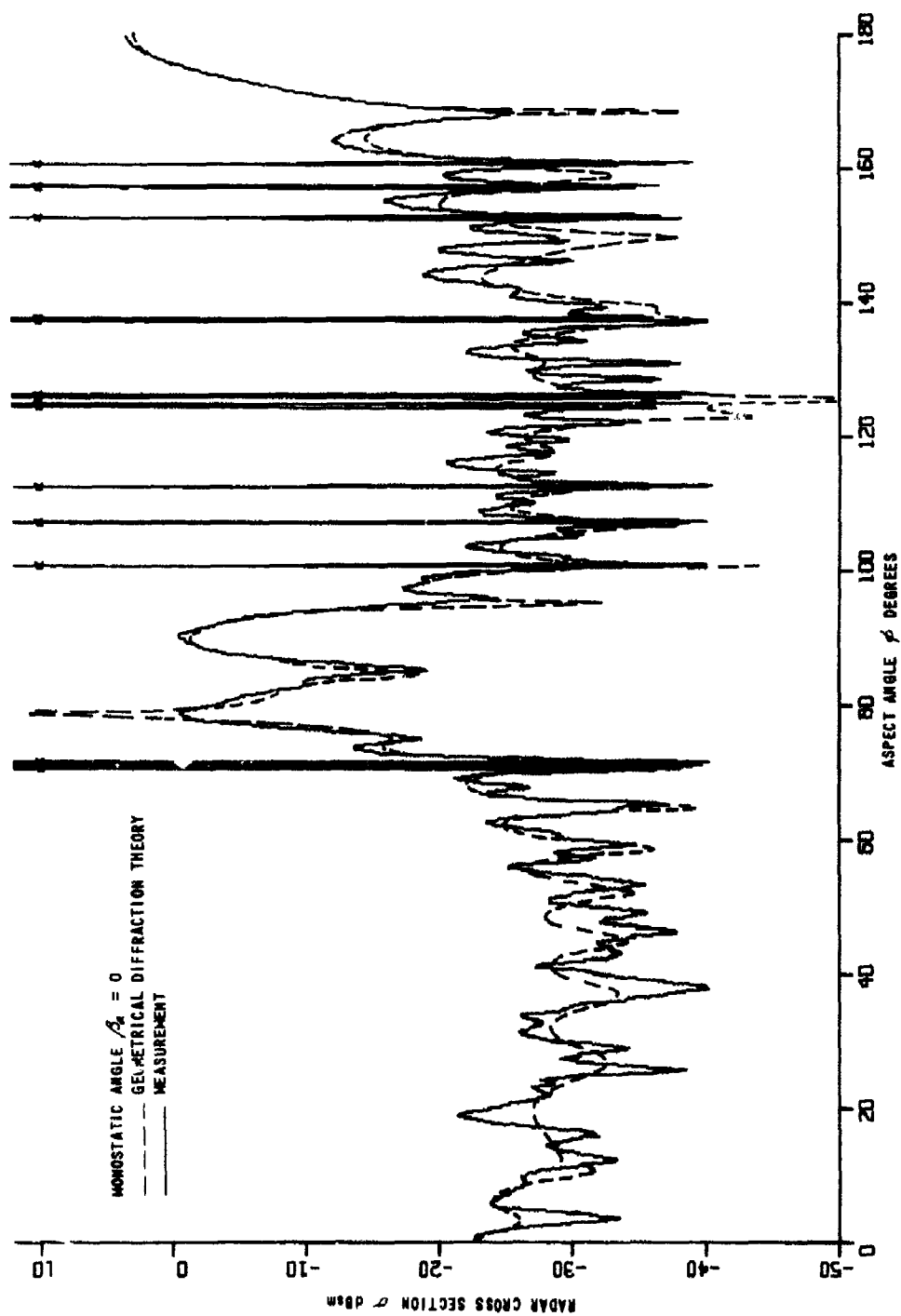


Figure 101 HORIZONTAL POLARIZATION RADAR CROSS SECTION. CONE-CYLINDER C2CY3, MONOSTATIC

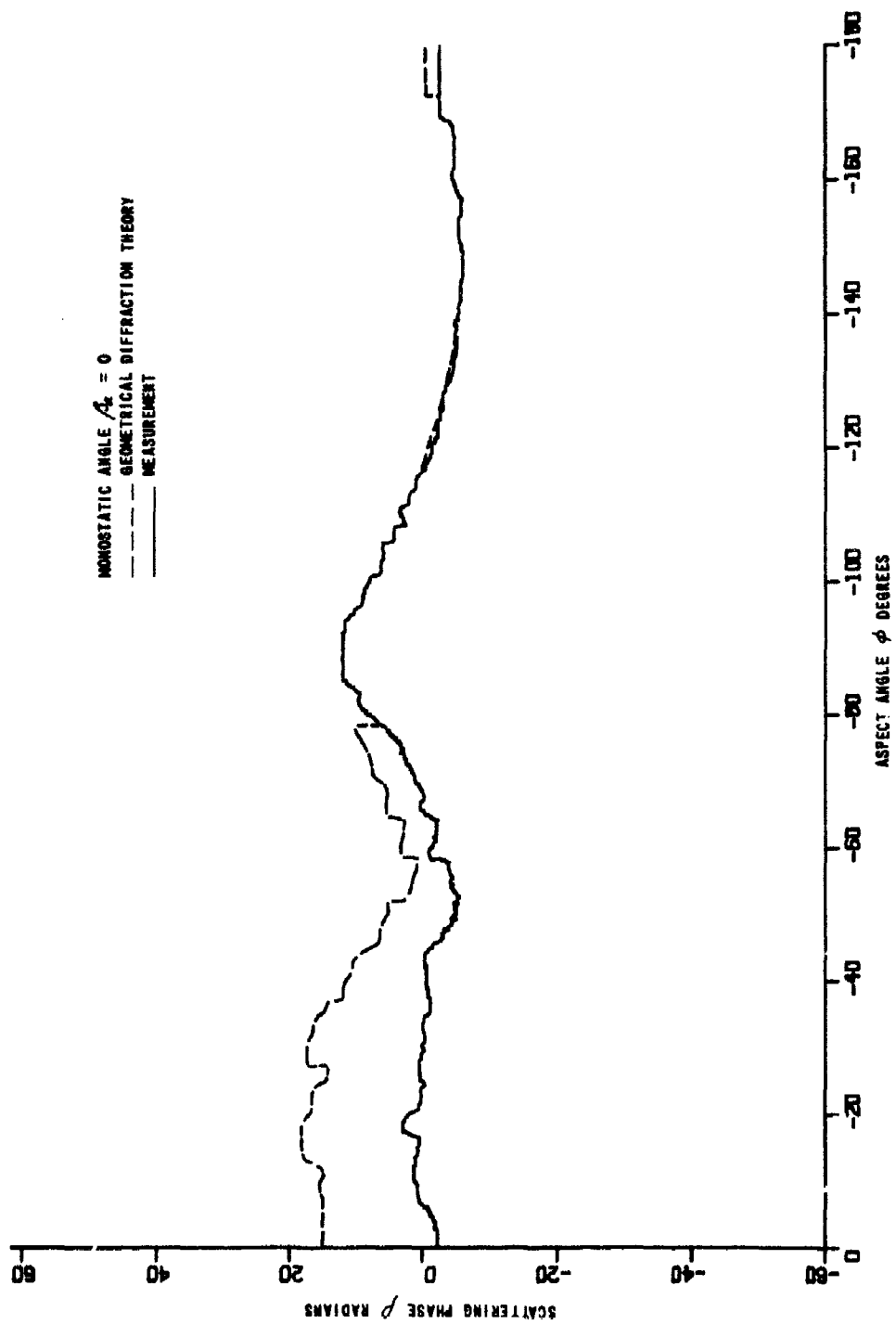


Figure 102 VERTICAL POLARIZATION SCATTERING PHASE. CONE CYLINDER C2CY3, MONOSTATIC

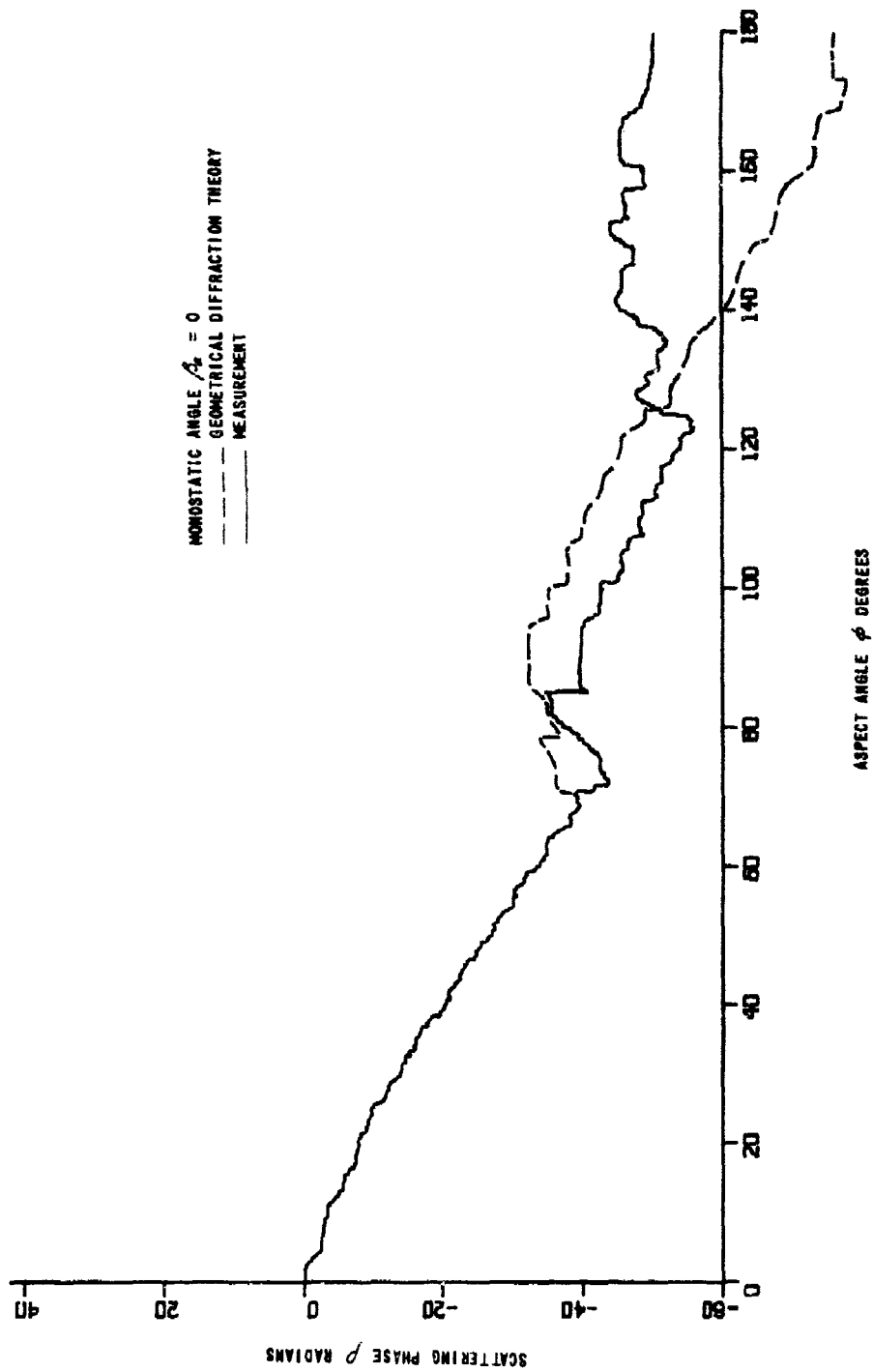


Figure 103 HORIZONTAL POLARIZATION SCATTERING PHASE. CONE-CYLINDER C2CY3, MONOSTATIC

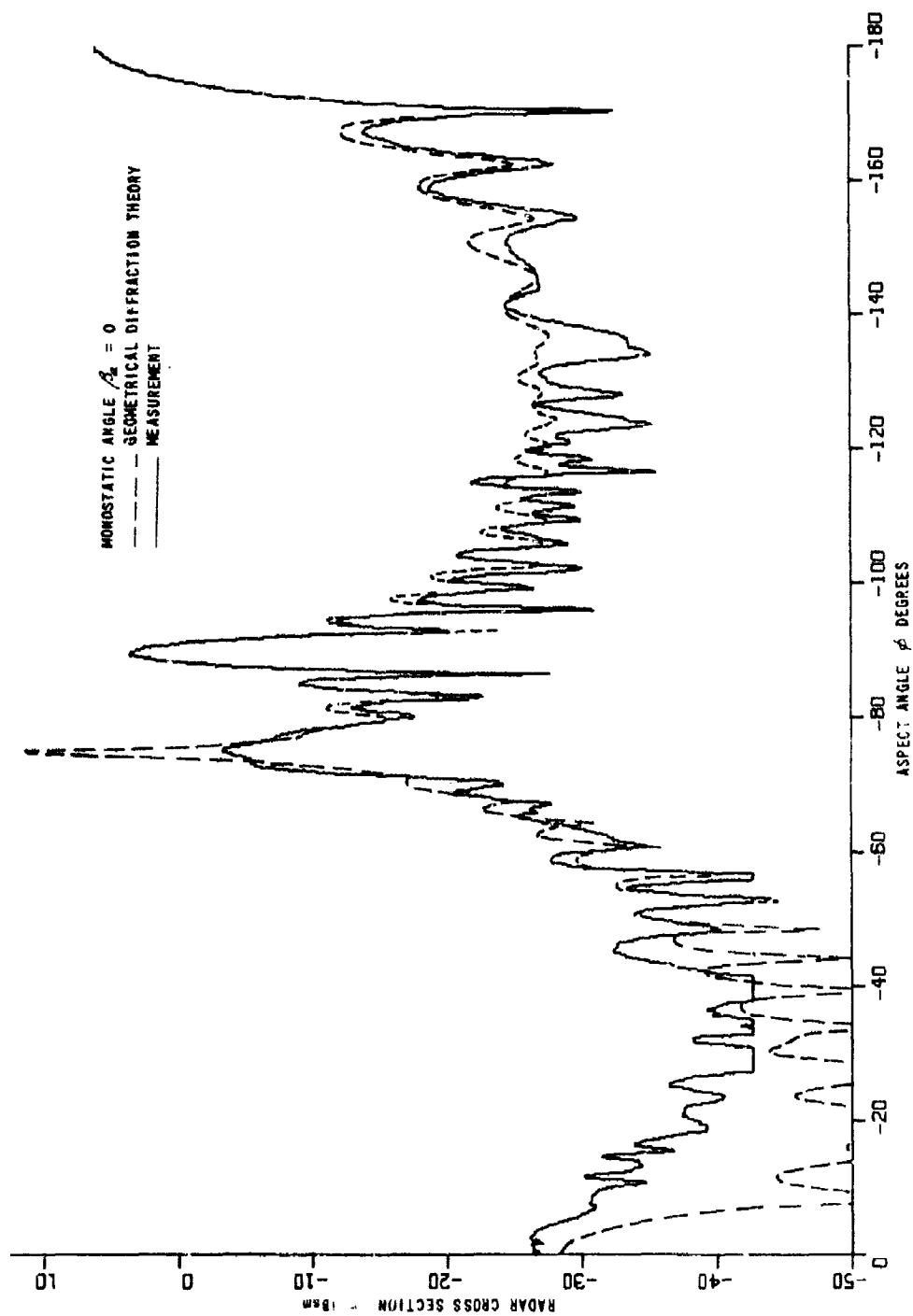


Figure 104 VERTICAL POLARIZATION RADAR CROSS SECTION. CONE-CYLINDER CROSS SECTION. MONOSTATIC



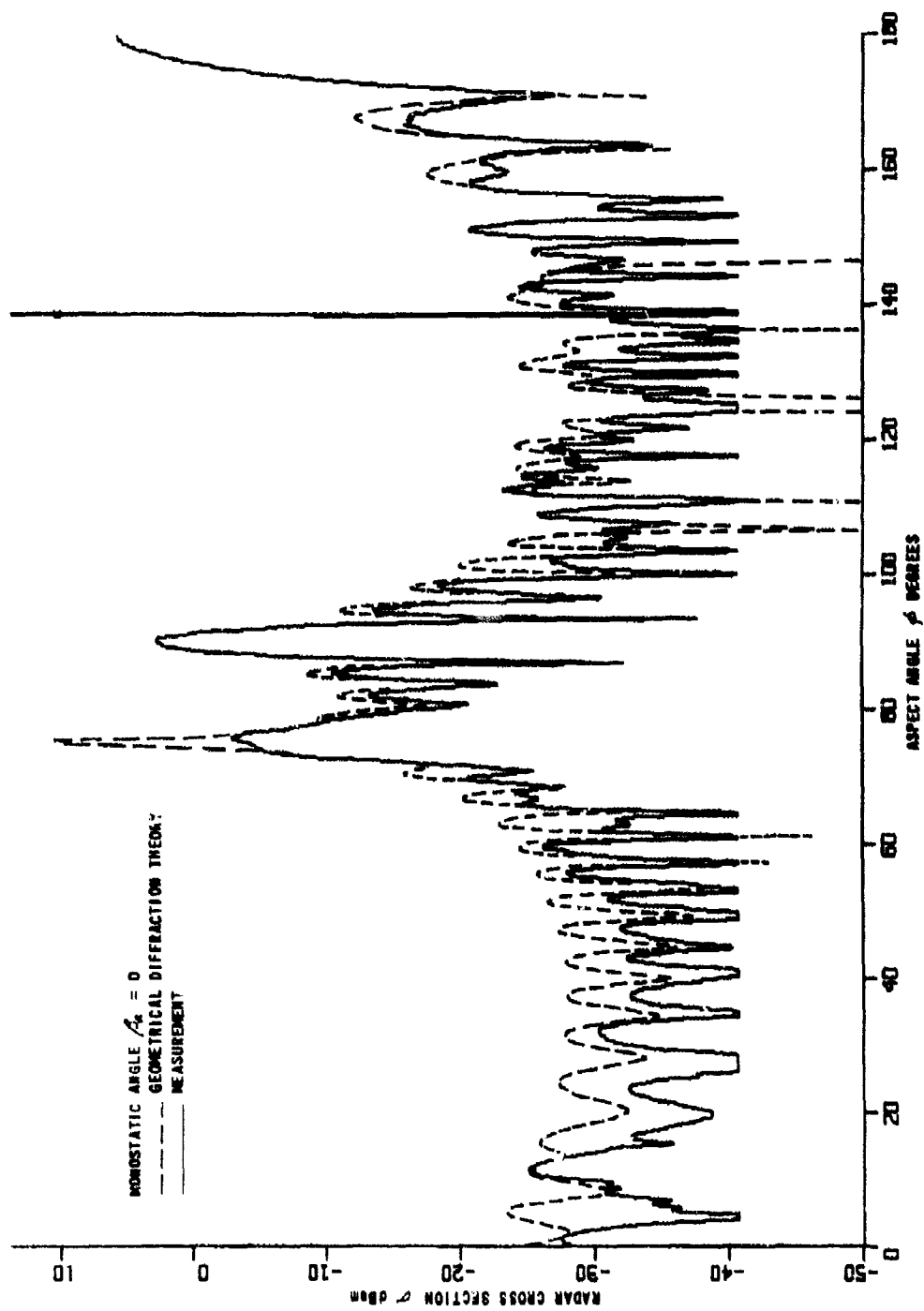


Figure 105 HORIZONTAL POLARIZATION RADAR CROSS SECTION. CONE-CYLINDER OBJECT, MONOSTATIC

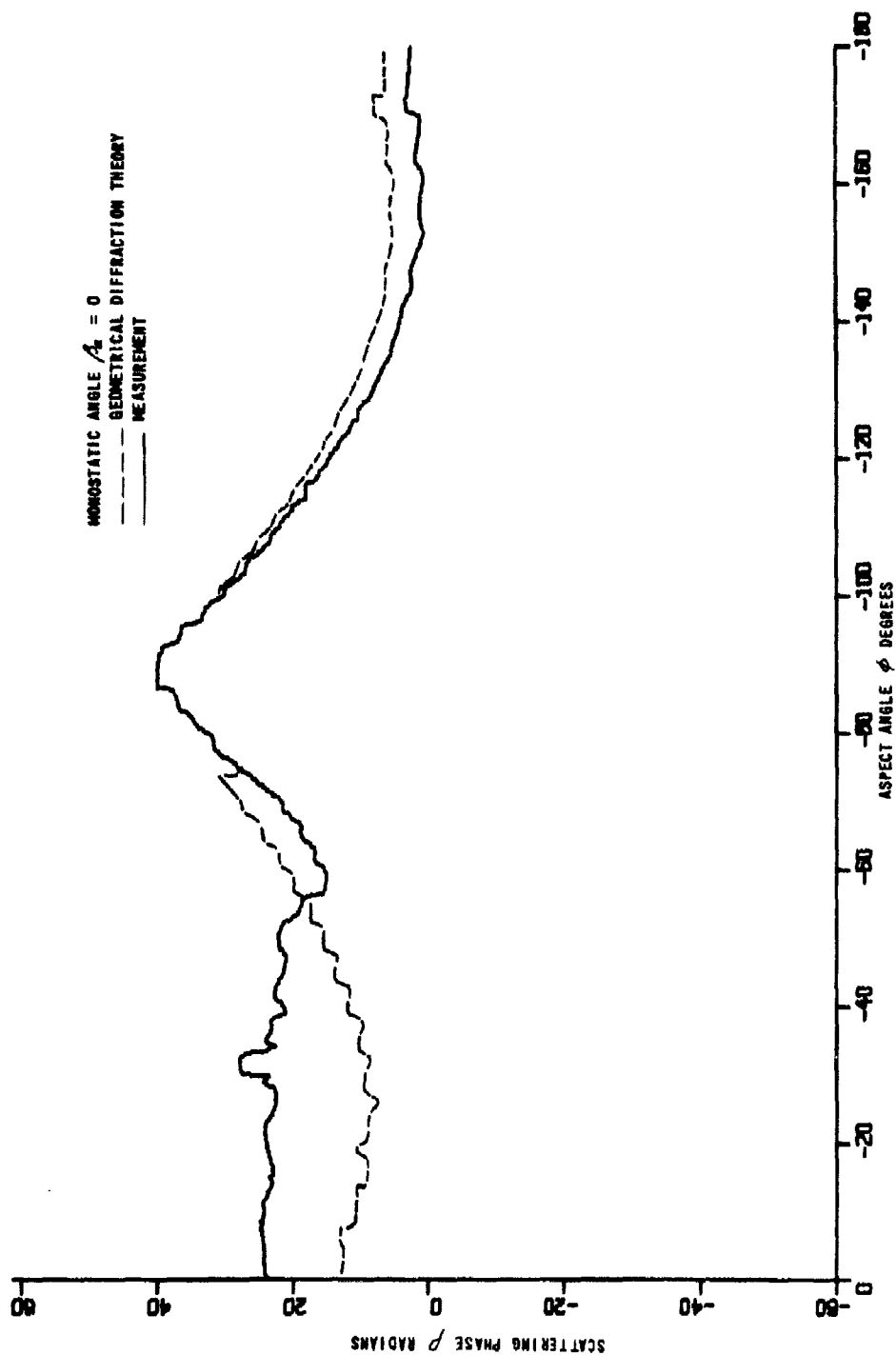


Figure 106 VERTICAL POLARIZATION SCATTERING PHASE. CONE-CYLINDER CUCYS, MONOSTATIC

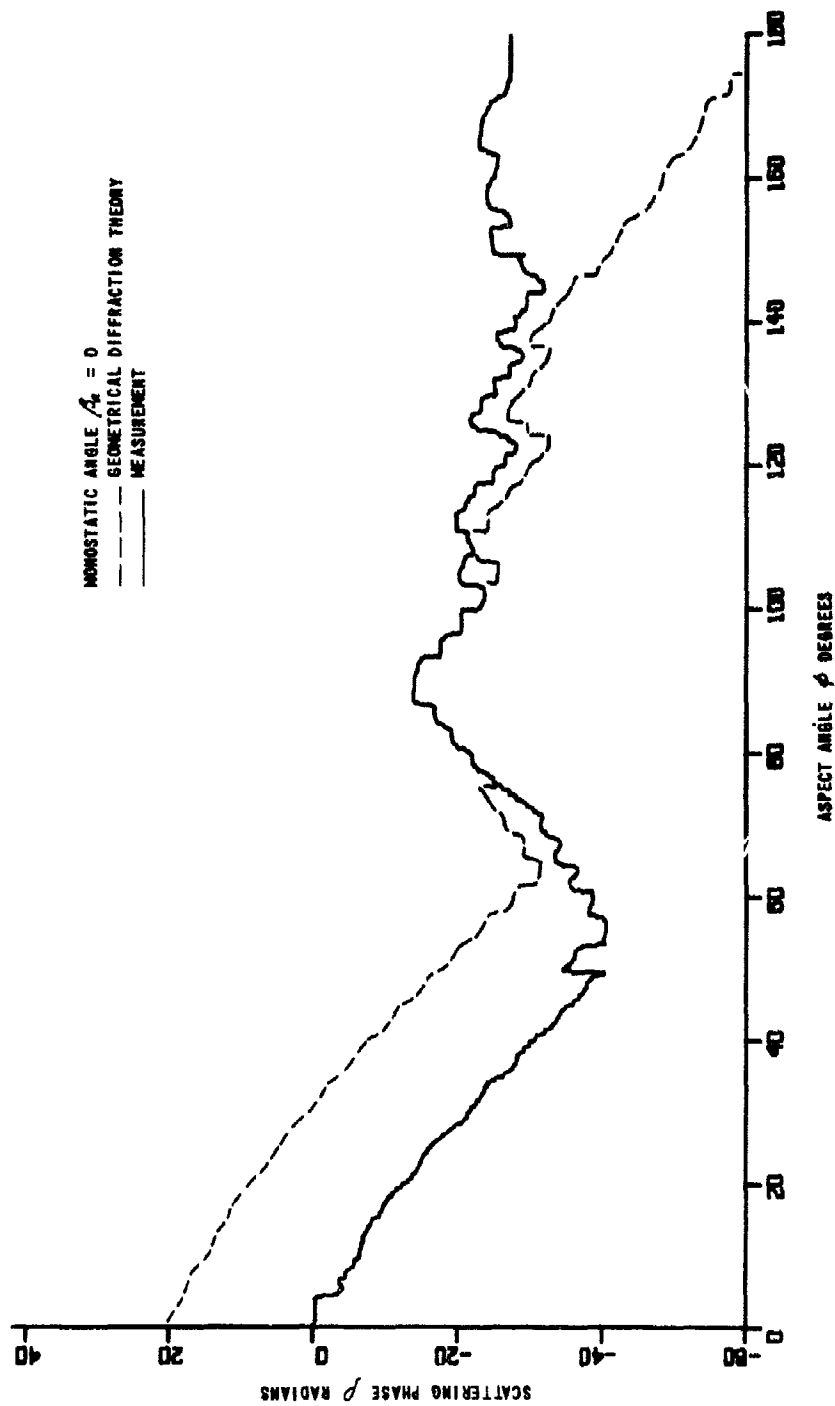


Figure 107 HORIZONTAL POLARIZATION SCATTERING PHASE. CONE-CYLINDER CAVES, MONOSTATIC

## 4.7 HEMISPHERE-CYLINDER

### 4.7.1 Analytical Formulation

A hemisphere-cylinder is formed by placing a spherical cap on one end of a finite cylinder as shown in Figure 108. The discontinuities on the target, labelled  $S_1$ ,  $S_2$  and  $S_3$ , constitute four scattering centers required to describe reradiation in the aspect interval  $0 \leq \phi \leq \pi$ .

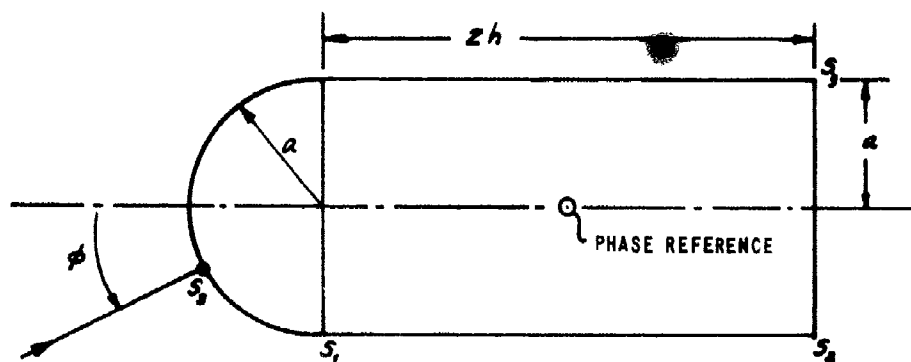


Figure 108 SCATTERING CENTERS ON A HEMISPHERE-CYLINDER

The scattering center denoted by the symbol  $S_3$  gives rise to a specular return from the hemispherical segment. The location of  $S_3$  is a function of aspect angle  $\phi$ , its position being determined by the normal to the surface which lies parallel to the direction of incidence. Such a center is termed a "slippery" center. Notice that a return from  $S_3$  is present in the limited aspect interval  $0 \leq \phi \leq \frac{\pi}{2}$ . Scattering center  $S_1$  is formed by the hemisphere-cylinder junction. Since there exists no discontinuity in the shape of the target at this point, the return from  $S_1$  is determined by discontinuities in the derivatives of shape. The return is thus much less than the return from other centers on the body. However, contributions from  $S_1$  can be important for  $\phi > \frac{\pi}{2}$ , where  $S_3$  no longer contributes to the total scattered field. Because the diffraction coefficient assigned to center  $S_1$  is presently unknown, we limit analysis to the aspect

region  $0 \leq \phi \leq \frac{\pi}{2}$ . Finally, contributions from centers  $S_2$  and  $S_3$  are known from the analysis of a cylinder.

Geometrical optics, physical optics, and geometrical diffraction theory provide identical estimates of the contribution from center  $S_3$ :

$$\sqrt{\sigma_3} e^{j\beta_3} = -\sqrt{\pi} a e^{+jzk(a+h\cos\phi)} \quad (90)$$

For scattering center  $S_2$  we have

$$\begin{aligned} \sqrt{\sigma_2} e^{j\beta_2} = & \frac{2}{3} \sin\left(\frac{2\pi}{3}\right) \sqrt{\frac{a \csc\phi}{k}} \left[ \left\{ \cos\frac{2\pi}{3} - \cos\frac{\phi}{3} \right\}^{-1} \left\{ \cos\frac{2\pi}{3} - 1 \right\}^{-1} \right] \\ & \times e^{+j\frac{\pi}{4} - jzk(a\sin\phi - h\cos\phi)} \end{aligned} \quad (91)$$

At and near the axial aspect ( $\phi = 0$ ), we limit the singularity in Equation 91 by the constraint  $\csc\phi \leq ka$ . At and near the broadside aspect ( $\phi = \pi/2$ ) we replace Equations 90 and 91 by the specular contribution

$$\begin{aligned} & -\sqrt{a k \csc\phi} \frac{2h \sin(2kh \cos\phi)}{(2kh \cos\phi)} e^{j\frac{3\pi}{4} - jka \sin\phi} \\ & + \frac{2}{3} \sin\frac{2\pi}{3} \sqrt{\frac{a \csc\phi}{k}} \left\{ \cos\frac{2\pi}{3} - 1 \right\}^{-1} \cos(2kh \cos\phi) \times \\ & e^{j\frac{\pi}{4} - j2ka \sin\phi} \end{aligned} \quad (92)$$

Equation 92 is used for  $\phi_{cb} \leq \phi \leq \frac{\pi}{2}$ , where  $\phi_{cb}$  is given by  $2kh \cos\phi_{cb} = 2.25$ .

#### 4.7.2 Results

Table 10 indicates the designation, dimensions, and operating frequency for the target employed in the examination of monostatic theory for the hemisphere-cylinder. The number of targets listed does not meet the specification of Table 1; measurement data were supplied to CAL for only one hemisphere-cylinder. Further, the aspect interval being studied is restricted to the region  $0 \leq \phi \leq \frac{\pi}{2}$  due to analytical limitations.

Table 10  
PARAMETERS FOR HEMISPHERE-CYLINDER STUDY

| MODEL<br>DESIGNATION | DIMENSIONS (INCHES) |           | FREQUENCY<br>(GHz) |
|----------------------|---------------------|-----------|--------------------|
|                      | DIAMETER 2a         | LENGTH 2h |                    |
| H3CY3                | 6.320               | 10.513    | 5.975              |

Figures 109 through 112 show results for hemisphere-cylinder H3CY3. The overall agreement between theoretical and experimental estimates of scattering matrix parameters is very good. Results shown in Figure 109 show that predicted interference between scattering centers is slightly less than that observed in measurement data at and near the nose-on axial aspect ( $0 \leq \phi \leq 30$ ). Notice that the measured lobe structure in this region is not related to interference between the two major scattering centers  $S_1$  and  $S_2$  introduced in Figure 108: the period of lobes associated with this interference, shown in Figure 110, is about half that observed in Figure 109. Thus, the measured lobe structure shown in Figure 109 for  $0 \leq \phi \leq 30$  degrees is associated with two sources of scattering that are separated by approximately half the total length of the target. Disagreement between vertical polarization theory and measurement apparent near the broadside aspect is due to the use of the cross-over aspect  $\phi_{cb}$  generated for the cylinder. A new cross-over aspect  $\phi_{cb}$  should be

developed specifically for hemisphere-cylinders. Horizontal polarization results shown in Figure 110 are very good: note that agreement between theoretical and experimental radar cross sections at and very near the nose-on axial aspect ( $\phi = 0$ ) may be improved by replacing the constraint with the proper form of the polarization-dependent return from center  $S_2$  based upon analyses performed in Appendix C. Figures 111 and 112 show that principal polarization phases are smooth functions of aspect angle: in this case comparison with theory is straightforward, and excellent agreement is evidenced.

#### 4.7.3 Remarks

Geometrical diffraction theory has been applied to predict the scattering matrix of a hemisphere-cylinder in the limited aspect region  $0 \leq \phi \leq \pi/2$ . Very good agreement between theory and measurement is reported. Theoretical capability may be improved by: 1) replacing the  $ka$  constraint on the contribution from scattering center  $S_2$  with the proper polarization dependent term, which has  $J_2(x)$  dependence; and 2) generating a cross-over aspect angle  $\phi_{cb}$  for specific application with hemisphere-cylinder targets.

The analysis may be extended to the aspect region  $\pi/2 < \phi \leq \pi$  upon further examination of the return from the hemisphere-cylinder junction (denoted by scattering center  $S_1$  in Figure 108).

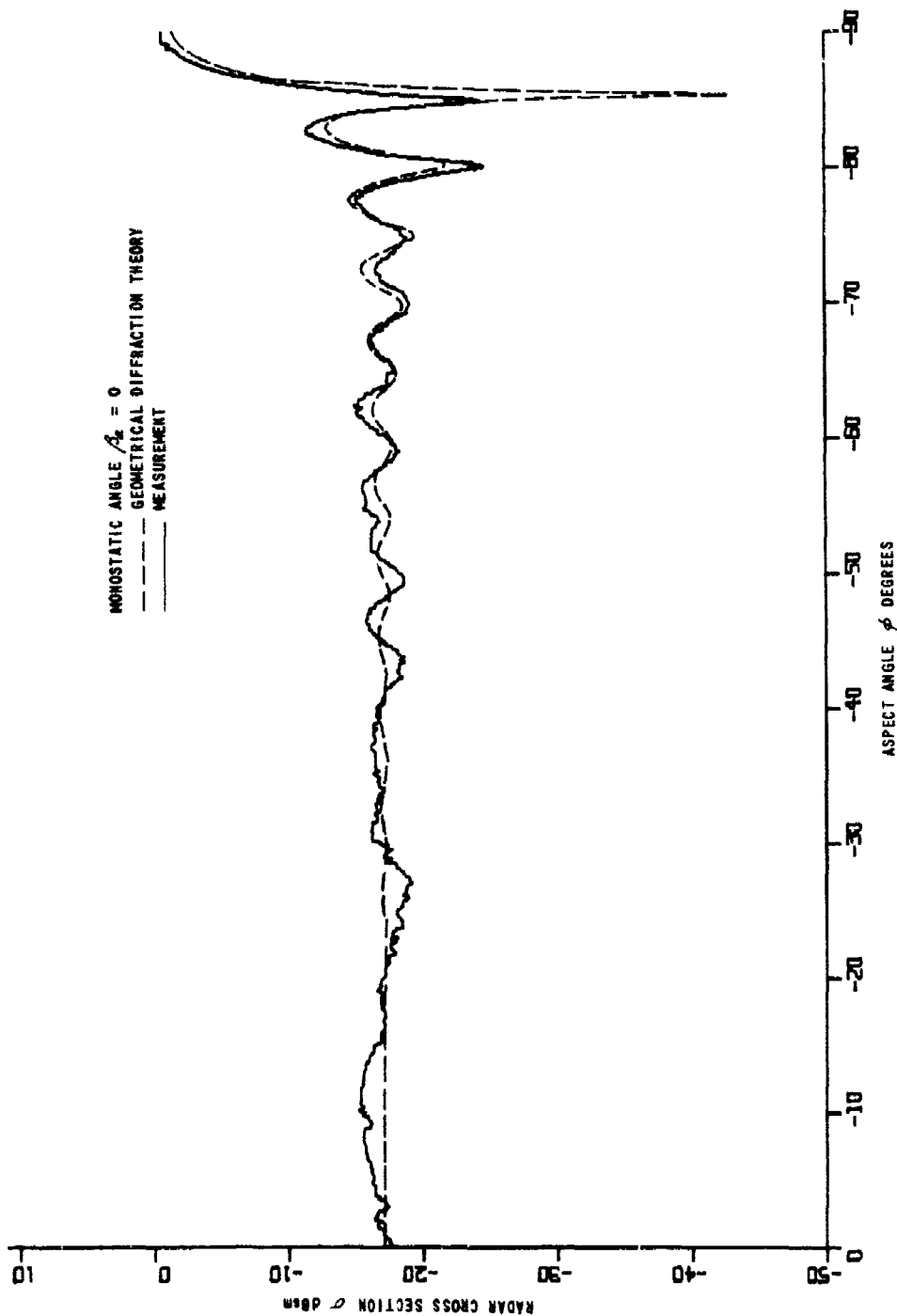


Figure 109 VERTICAL POLARIZATION RADAR CROSS SECTION. HEMISPHERE-CYLINDER H3C13, MONOSTATIC



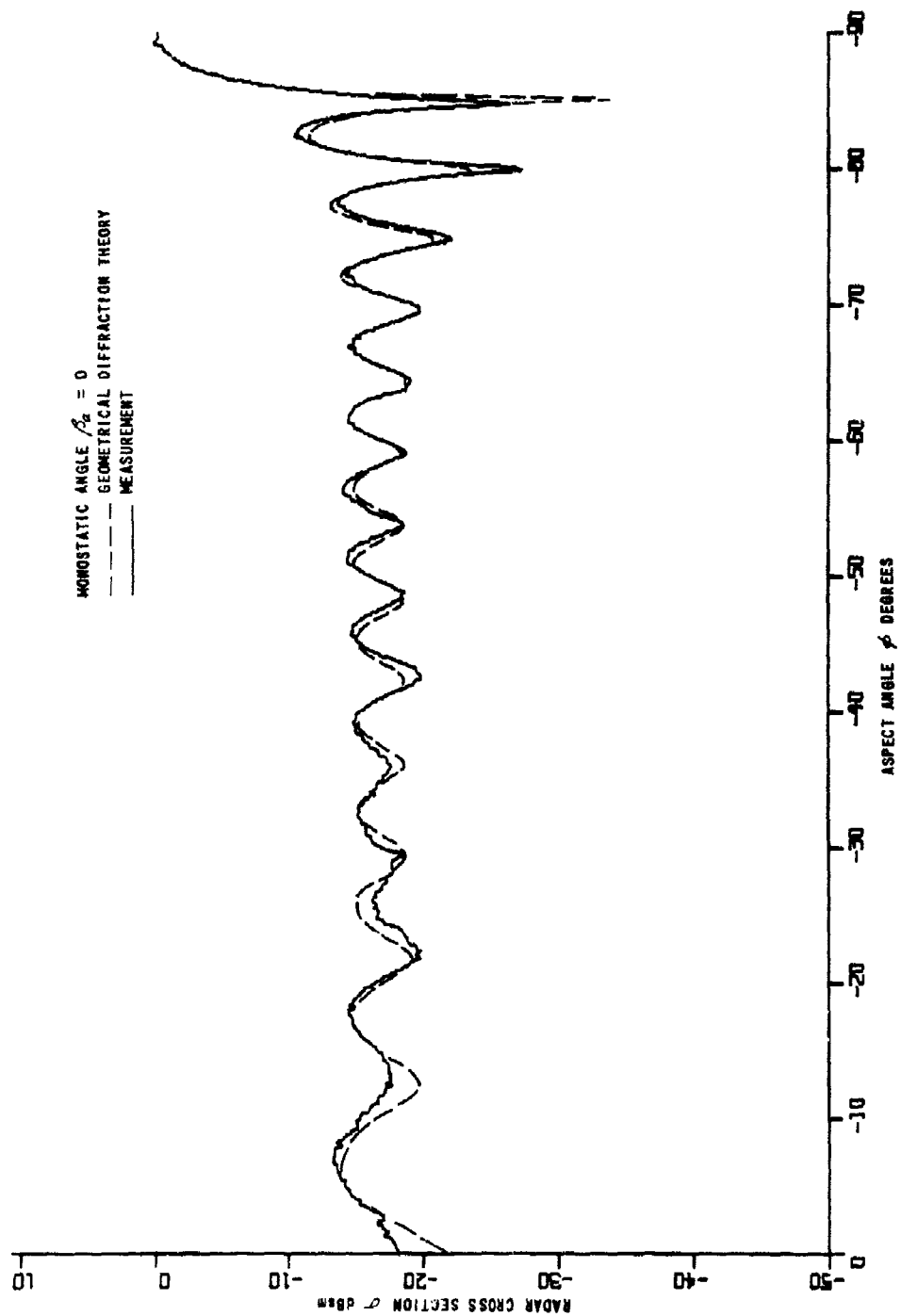


Figure 110 HORIZONTAL POLARIZATION RADAR CROSS SECTION. HEMISPHERE-CYLINDER HSCY3, MONOSTATIC

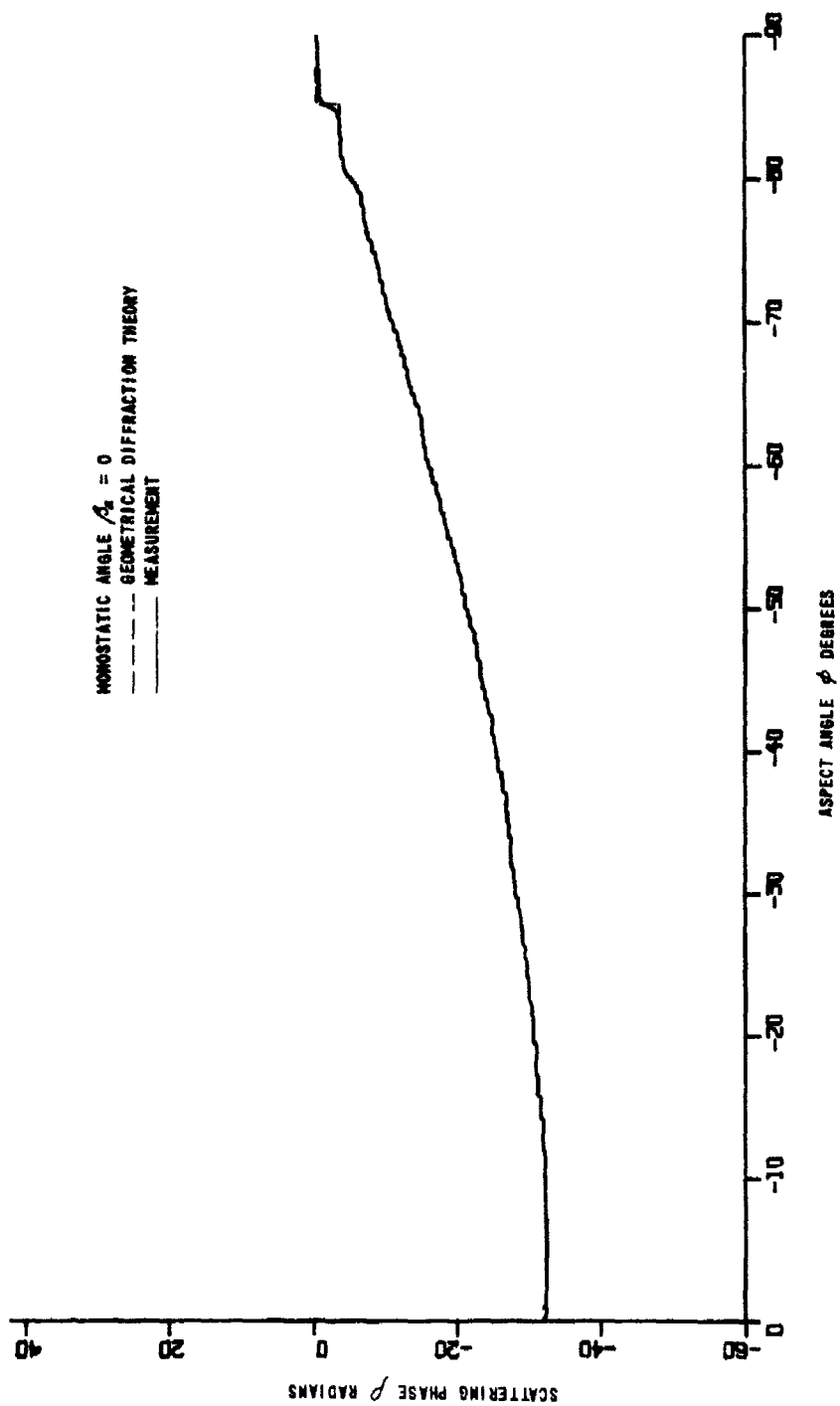


Figure 111 VERTICAL POLARIZATION SCATTERING PHASE. HEMISPHERE-CYLINDER H3C3, MONOSTATIC

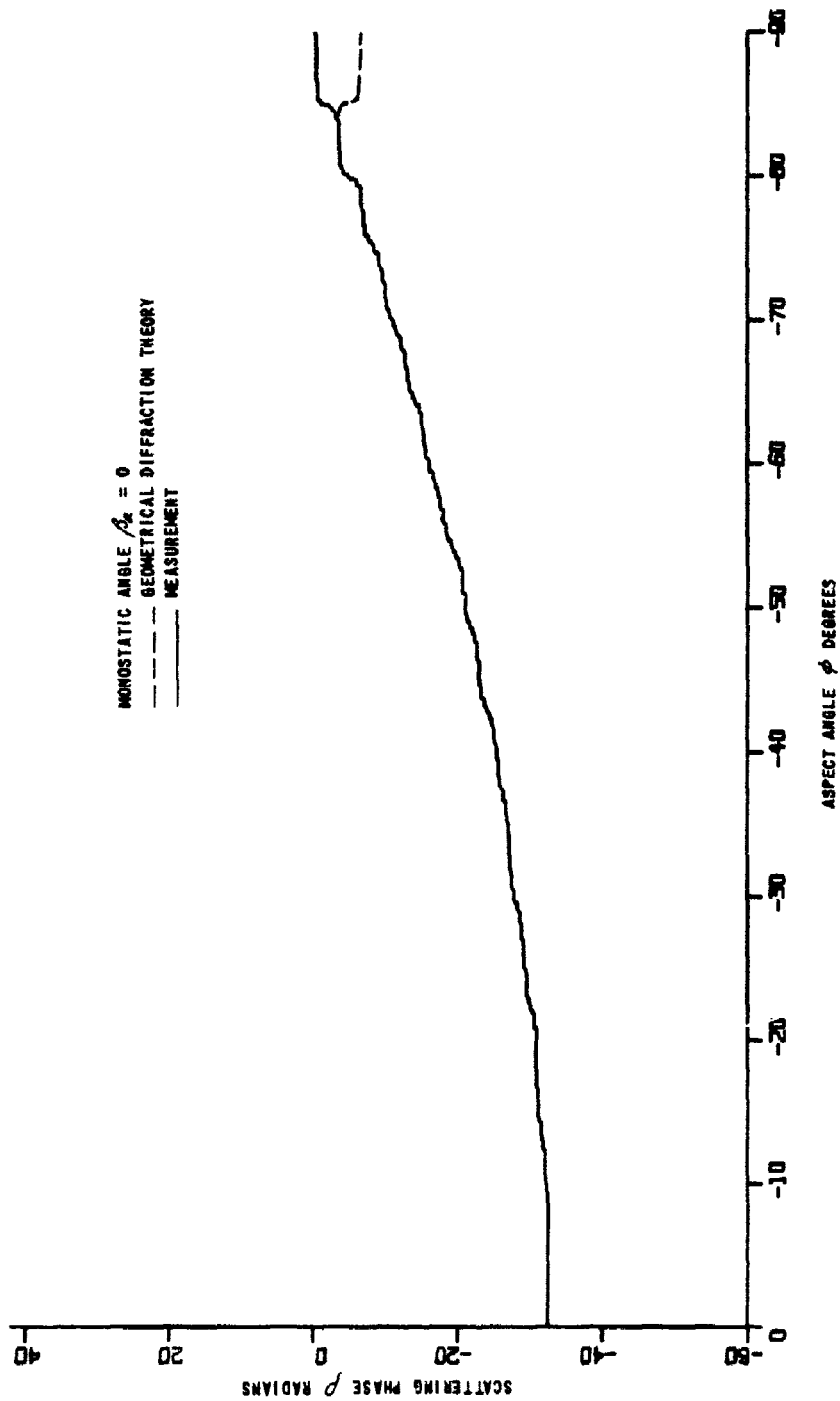


Figure 112 HORIZONTAL POLARIZATION SCATTERING PHASE. HEMISPHERE-CYLINDER H3CY3, MONOSTATIC

## 5. SUMMARY AND CONCLUSIONS

Coordination between CAL and GD/FW has led to the definition of measurement models and parameter variations necessary to conduct scattering formula investigations detailed in this report. The basic analyses involved application of unmodified geometrical diffraction theory to predict scattering by cylinders, frustums, cones, and derivable shapes. Extensions to theory performed under this contract involved modifications of basic analyses for application at and near aspects which give rise to specular scattering, and at and near nose-on aspects for a cone.

Resultant formulations were programmed for the IBM 360 digital computer for the following shapes: cylinder, frustum, cone, frustum-cylinder, cylinder-flare, cone-cylinder, and hemisphere-cylinder. Theory was evaluated by comparing predicted and experimental values of principal polarization radar cross section and cumulative scattering phases. Both monostatic and bistatic situations were investigated.

Results obtained under this contract attest the validity of geometrical diffraction theory for predicting the bistatic scattering matrix of cylinders, frustums, frustum-cylinders and cylinder-flares. Very good agreement with measurement data is generally observed when the minimum target dimension is at least several wavelengths in extent. Further modification of geometrical diffraction theory is required to generate equivalent capability for a cone and a cone-cylinder.

A direction for additional analytical effort has been outlined within the context of geometrical diffraction theory. Furthermore, the very rapid phase changes occurring in plots of predicted and measured values of horizontal polarization phase need to be followed more closely to resolve ambiguities.

Computer time is not a limitation when calculations are based upon geometrical diffraction theory; the complete scattering matrix of each target was predicted at 1801 aspect angles in less than two minutes on an IBM 360/65.

## REFERENCES

1. NORAIR Div. Report NOR65-271, Phase I Report, AD No. 624 586, "A Source Distribution Technique for the Solution of General Electro-Magnetic Scattering Problems," 13 October 1965.
2. TRG, Inc., Report W-121, "Calculations of Scattering from Two- and Three-Dimensional Bodies," Final Report, Contract DA-01-021-AMC-14204(Z), June 1966.
3. Harrington, R.F., "Matrix Methods for Field Problems," Proc. IEEE, 55, pp. 136-149, February, 1967.
4. Oshiro, F.K., Torres, F.P., and Heath, H.C., "Numerical Procedures for Calculating Radar Cross Section of Arbitrarily-Shaped Three-Dimensional Geometries," AFAL-TR-66-162, May 1966, Volume I.
5. Ross, R.A., "Investigation of Scattering Center Theory," Final Report, CAL Report No. UA-2462-E-2, January 1968.
6. Keller, J.B., "Geometrical Theory of Diffraction," Jour. Opt. Soc. Amer., 52, pp. 116-130, 1962
7. Kline, M. and Kay, I.W., "Electromagnetic Theory and Geometrical Optics, (New York: Interscience, 1965).
8. Bechtel, M.E. and Ross, R.A., "Radar Scattering Analysis," Cornell Aeronautical Laboratory Report No. ER/RIS-10, August 1966.
9. Kouyoumjian, R.G., "An Introduction to Geometrical Optics and the Geometrical Theory of Diffraction," Antenna and Scattering Theory: Recent Advances, Volume I, Short Course at Ohio State University, March 1966.
10. Ross, R.A., "Investigation of Scattering Matrix Measurements and Suspension Target Supports," CAL Report No. UB-1806-P-1, January 1964.
11. Kell, R.E., "On the Derivation of Bistatic RCS from Monostatic Measurements," Proc. IEEE, 53, pp. 983-988, August 1965.
12. Crispin, J.W., Jr., Goodrich, R.F., and Seigel, K.M., "A Theoretical Method for the Calculation of the Radar Cross Sections of Aircraft and Missiles," University of Michigan Rad. Lab Report No. 2591-1-H, July 1959.

13. Helstrom, C.W., "Backscattering of Radio Waves," Westinghouse Research Laboratories, Research Report No. 412-F8573-R1, December 15, 1960
14. Keller, J.B., "Backscattering from a Finite Cone," Trans. IRE, AP-8, pp. 175-182, 1960
15. Keller, J.B., "Backscattering from a Finite Cone -- Comparison of Theory and Experiment," Trans IRE, AP-9, pp. 411-412, 1961
16. Bechtel, M.E., "Application of Geometric Diffraction Theory to Scattering from Cones and Discs," Proc. IEEE, Vol. 53, pp. 877-882, August 1965.
17. Ross, R.A., "Radar Cross Section of Rectangular Flat Plates," Trans. IEEE, AP-14, May 1966
18. Ross, R.A., "Scattering by a Finite Cylinder," Proc. IEE, 114, pp. 864-868, 1967
19. Mentzer, J.W., Scattering and Diffraction of Radio Waves (Pergamon, 1955).
20. Keller, J.B., "Diffraction by an Aperture," Jour. App. Phys., 28, pp. 426-444, 1957
21. Raybin, D.M., "Radar Cross Section of Spherical Shell Segments," Trans IEEE, AP-13, pp. 754-759, 1965
22. "Investigation of Scattering Principles, Volume I," General Dynamics Report FZE-791, 15 August 1968
23. "Investigation of Scattering Principles, Volume II, Scattering Matrix Measurements," General Dynamics Report FZE-792, 15 July 1968
24. "Investigation of Scattering Principles, Volume IV, Inverse Scattering Analysis," General Dynamics Report FZE-794, 15 August 1968

## Appendix A

### SCATTERING BY A CYLINDER

#### A.1 INTRODUCTION

High-frequency scattering of an incident plane wave by a finite, perfectly conducting, right-circular cylinder is treated by the geometrical theory of diffraction. The analysis begins with Keller's formula for the field singly diffracted at the edge of a perfectly conducting wedge. Here reradiation is interpreted in terms of three distinct quantities: a diffraction coefficient, a divergence factor, and an associated geometrical phase angle. Each quantity is evaluated for the four scattering centers (edges) on a finite cylinder. A single-diffraction expression for the amplitude and phase of the complex far field scattered by the target is obtained as functions of cylinder's dimensions and aspect angle, and the radar bistatic angle, frequency and polarization. Next, the fields diffracted at scattering centers are interpreted in terms of radar cross sections and phases for convenience in describing scattering center contributions. The formulation is valid except: 1) at aspects which give rise to specular scattering, and 2) for the forward-scattering bistatic situation.

Modification of geometrical diffraction theory for application at and near specular aspects is effected using a small angle approximation technique. These analyses extend the capability of the theory for application at arbitrary aspect angles.

## A.2

## FIELDS SINGLY DIFFRACTED AT CYLINDER EDGES

## A.2.1

General

According to geometrical diffraction theory, the field  $\mu$  singly-diffracted at a scattering center is given by:

$$\mu = \text{GDT} \quad (\text{A-1})$$

where T denotes an incident plane wave, D is a coefficient of proportionality called the diffraction coefficient, and G is a geometrical factor which accounts for divergence of the diffracted field. Keller introduced an expanded statement of Equation (A-1) for diffraction at the edge of a wedge (see Equation (12) of Reference 20):

$$\mu_{\text{edge diff}} = D [A(1 + \rho_1^{-1}A)]^{-1/2} A e^{ik(\psi + A)} \quad (\text{A-2})$$

where  $A e^{ik\psi}$  is the incident plane field, D is that diffraction coefficient for a two-dimensional wedge, and the term  $[A(1 + \rho_1^{-1}A)]^{-1/2}$  is a divergence factor based upon the optical form of the principal of conservation of energy. Divergence is seen to be a function of A, the separation between the edge and the receiving antenna, and  $\rho_1$ , the radius of curvature of the diffracted wavefront.

In order that Equation (A-2) be complete for eventual application within the scattering matrix, we introduce the following modification at this point:

$$\mu_{\text{edge diff}} = \bar{F} D [A(1 + \rho_1^{-1}A)]^{-1/2} A e^{ik(\psi + A)} \quad (\text{A-3})$$



where the choice of signs in Equation (A-3) relates to polarization dependence; use the upper sign for vertical polarization (E vectors associated with incident and scattered fields parallel to edge of wedge at point of diffraction), and use the lower sign for horizontal polarization (E vectors lie perpendicular to edge of wedge at point of diffraction). The rationale behind the above modification is discussed by Helstrom on pages 37 and 38 of Reference 13.

Individual treatment of the diffraction coefficient, the divergence factor, and the geometrical phase  $k(\pi - \alpha)$  precedes application of Equation (A-3) in describing principal polarization contributions singly-diffracted at the four scattering centers on a cylinder.

### A.2.2 Diffraction Coefficient

The diffraction coefficient appropriate for our problem is determined from the first term in the asymptotic expansion of Oberhettinger's exact solution for scattering by a two-dimensional wedge. Keller introduced a general expression for this diffraction coefficient as a footnote correction in Reference 14.

$$D = \frac{e^{i\frac{\pi}{4}} \sin(\pi/n)}{n \sin \beta_k \sqrt{2\pi k}} \left[ \left\{ \cos\left(\frac{\pi}{n}\right) - \cos\left(\frac{\theta_k - \alpha_k}{n}\right) \right\}^{-1} + \left\{ \cos\left(\frac{\pi}{n}\right) - \cos\left(\frac{\pi + \theta_k + \alpha_k}{n}\right) \right\}^{-1} \right] \quad (\text{A-4})$$

where the subscript k on angular symbols denotes Keller's terminology and

$\alpha_k$  is the angle of incidence

$\theta_k$  is the angle of diffraction

$n$  is  $\frac{\gamma_k}{\pi}$  ( $\gamma_k$  being the exterior wedge angle)

$\beta_k$  is the angle between the incident ray and the positive tangent to the wedge

and  $k$  is the wave number ( $k = \frac{2\pi}{\lambda}$  where  $\lambda$  is the wavelength).

The angles  $\alpha_k$  and  $\theta_k$  introduced in Equation (A-4) are defined as follows: Project the incident and diffracted rays onto a plane normal to the edge at the point of diffraction; the angles between these projections and the normal to the wedge are  $\theta_k$  and  $\alpha_k$  respectively.

Figure A-1 illustrates the coordinate convention employed in describing diffraction at the edge of a two-dimensional wedge having interior angle  $2\pi - \gamma_k$ . An X-Y-Z coordinate system has been chosen such that the Z-axis is coincident with the edge of the wedge, the Y-axis is perpendicular to one face of the wedge, and the X-Y plane is normal to the edge at the point

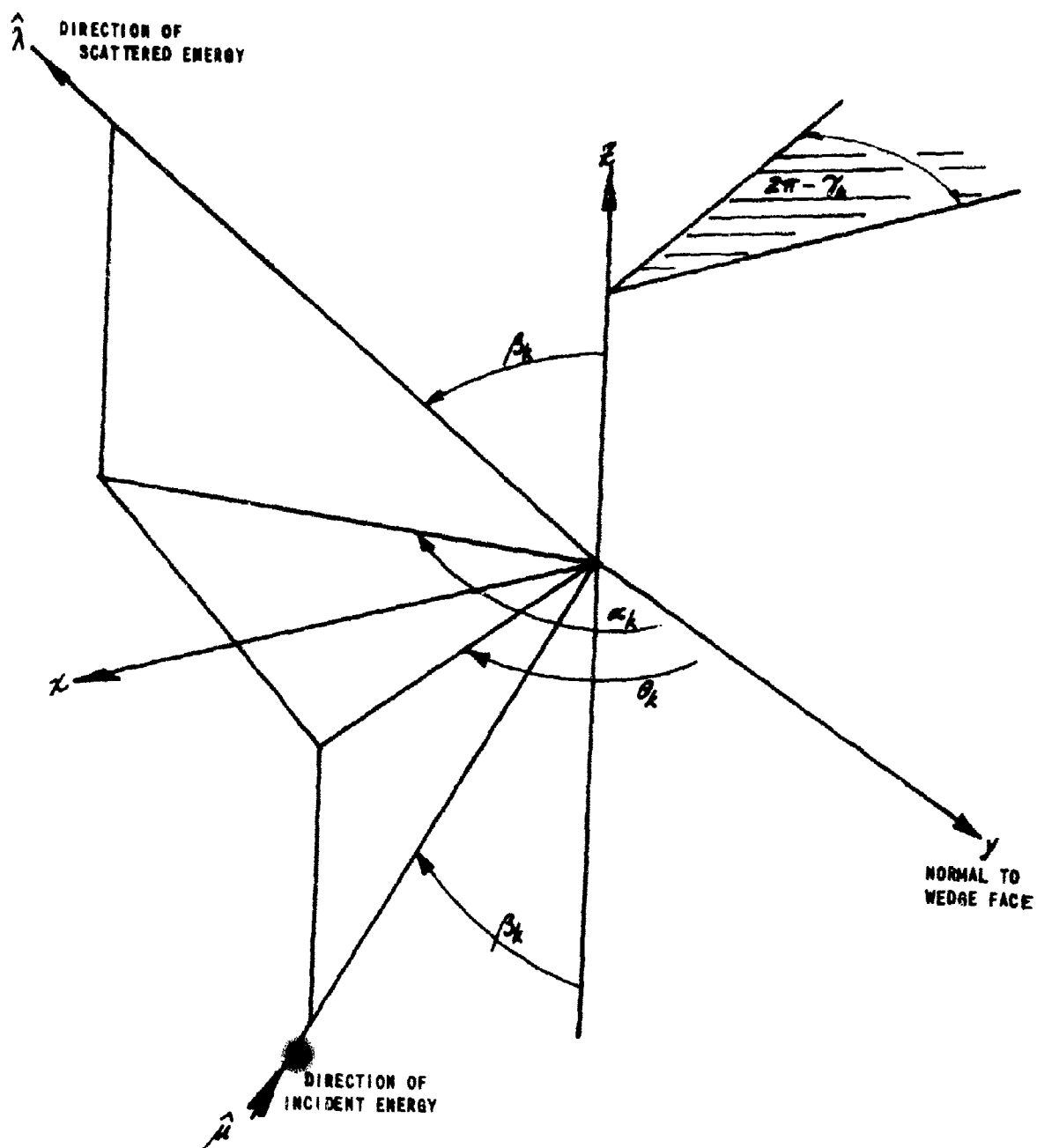


Figure A-1 DIFFRACTION AT A POINT ON THE EDGE OF A TWO-DIMENSIONAL WEDGE

of diffraction. The vector  $\hat{\mu}$  represents the sense and arbitrary direction on an incident ray. The angle between the incident ray and the positive tangent to the edge (negative - Z-axis) is denoted by  $\beta_k$ . The angle between the projection of the direction of incidence in the plane normal to the edge at the point of diffraction (X-Y or azimuth plane), and the normal to the wedge (Y-axis) is denoted by  $\theta_k$ . According to the law of edge diffraction, the family of rays diffracted at the edge lie on the surface of a cone with apex located at the point of diffraction (coordinate origin), and with half-cone angle equal to  $\beta_k$ . One member of this family of diffracted rays is illustrated by the vector  $\hat{\lambda}$ . Here the projection of  $\hat{\lambda}$  in the azimuth plane makes an angle  $\alpha_k$  with the Y-axis.

Figure A-2 illustrates the angular relations employed throughout our analysis. We define the bistatic angle between the directions of incidence and observation by the angle  $\beta$ . The projection of the bistatic angle  $\beta$  in the azimuth plane is denoted by  $\beta_a$ , where  $\beta_a = \alpha_k - \theta_k$ . Similarly, the projection of  $\beta$  in the elevation plane is denoted by  $\beta_e$ , where  $\frac{\beta_e}{2} = \pi/2 - \beta_k$ . Having referenced bistatic characteristics to the azimuth plane, we note that the law of edge diffraction requires that the bisector of the bistatic angle  $\beta$  must lie in the azimuth plane: we interpret this bisector as an equivalent azimuth aspect angle  $\phi$ , where  $\phi = \frac{\alpha_k + \theta_k}{2}$ .

Next we observe that cylinder edges are formed by right-angle wedges, so that  $\gamma_k = \frac{\pi}{2}$  and  $n = 3/2$ . Having defined bistatic and aspect angles in the manner noted above, we rewrite Equation (A-4) as

$$D = \frac{e^{i\frac{\pi}{4}} \sin\left(\frac{2\pi}{3}\right)}{\frac{3}{2} \cos\left(\frac{\beta_e}{2}\right) \sqrt{2\pi k}} \left[ \left\{ \cos\left(\frac{2\pi}{3}\right) - \cos\left(\frac{2\beta_a}{3}\right) \right\}^{-1} \left\{ \cos\left(\frac{2\pi}{3}\right) - \cos\left(\frac{\pi + 2\phi}{3/2}\right) \right\}^{-1} \right] \quad (A-5)$$

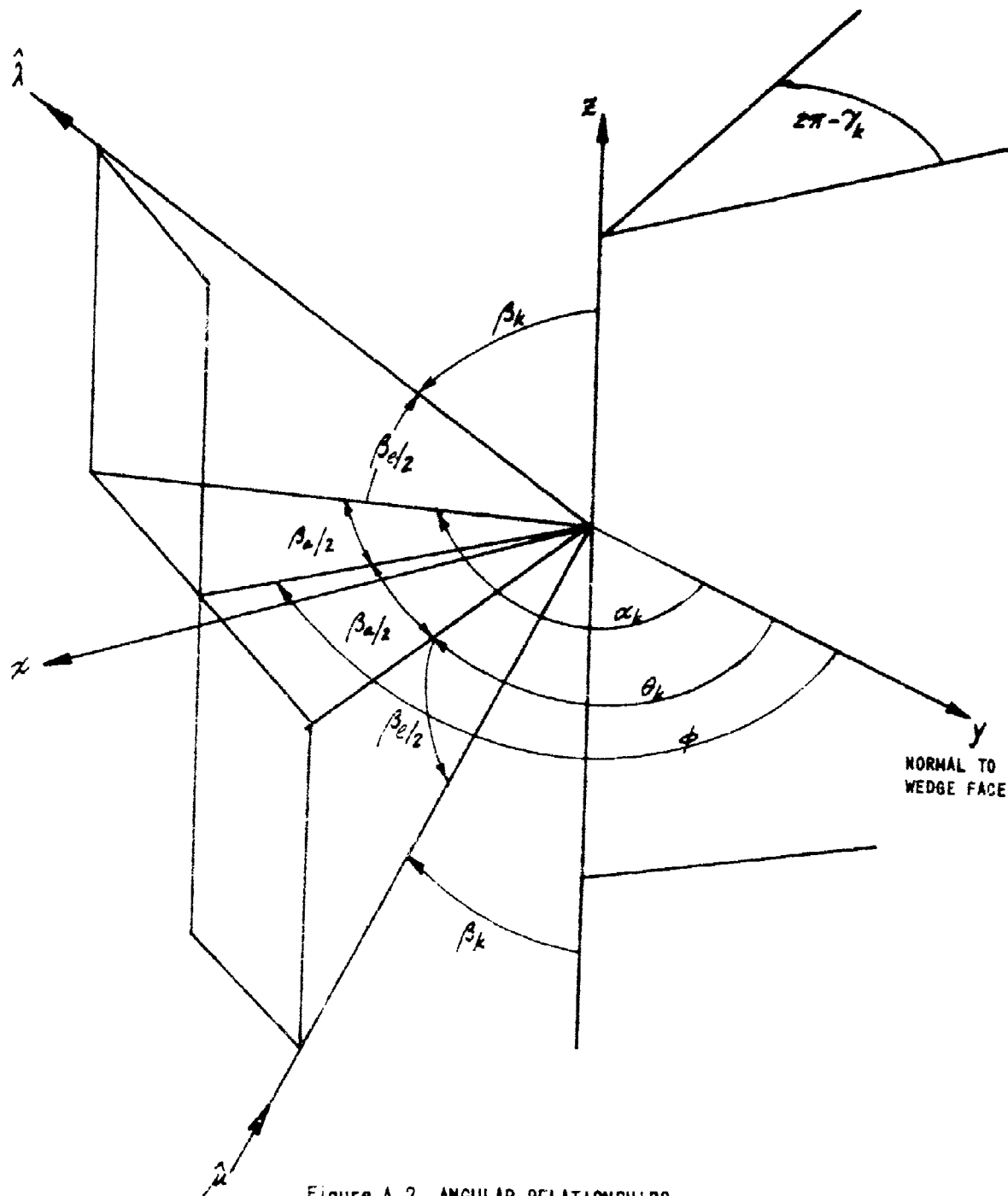


Figure A-2 ANGULAR RELATIONSHIPS

Notice that the diffraction coefficient satisfies reciprocity; i. e., interchange of the roles of transmitter and receiver does not alter bistatic dependencies revealed in Equation (A-5).

It remains to evaluate the diffraction coefficient at the four edges of a cylinder. Figure A-3 depicts a two-dimensional, rectangular cylinder having generator coincident with the Z-axis of a cartesian coordinate system. The four edges of the cylinder lying in the X-Y plane are labelled  $S_1$ ,  $S_2$ ,  $S_3$  and  $S_4$ . An equivalent azimuth aspect angle  $\phi$  is referenced to the Y-axis. Angular transformations appropriate to each edge are noted in the figure. Substituting these relations into Equation (A-5) we have

$$D_1 = \frac{\frac{2}{3} e^{i\frac{\pi}{3}} \sin\left(\frac{2\pi}{3}\right)}{\cos\frac{\beta_a}{2} \sqrt{2\pi k}} \left[ \left\{ \cos\left(\frac{2\pi}{3}\right) - \cos\left(\frac{2\beta_a}{3}\right) \right\}^{-1} \mp \left\{ \cos\left(\frac{2\pi}{3}\right) - \cos\left(\frac{\pi+2\phi}{3/2}\right) \right\}^{-1} \right] \quad (A-6)$$

$$D_2 = \frac{\frac{2}{3} e^{i\frac{\pi}{3}} \sin\left(\frac{2\pi}{3}\right)}{\cos\frac{\beta_a}{2} \sqrt{2\pi k}} \left[ \left\{ \cos\left(\frac{2\pi}{3}\right) - \cos\left(\frac{2\beta_a}{3}\right) \right\}^{-1} \mp \left\{ \cos\left(\frac{2\pi}{3}\right) - \cos\left(\frac{4\phi}{3}\right) \right\}^{-1} \right] \quad (A-7)$$

$$= 0; \phi < \beta_a/2 \qquad \phi \geq \beta_a/2$$

$$D_3 = \frac{\frac{2}{3} e^{i\frac{\pi}{3}} \sin\left(\frac{2\pi}{3}\right)}{\cos\frac{\beta_a}{2} \sqrt{2\pi k}} \left[ \left\{ \cos\left(\frac{2\pi}{3}\right) - \cos\left(\frac{2\beta_a}{3}\right) \right\}^{-1} \mp \left\{ \cos\left(\frac{2\pi}{3}\right) - \cos\left(\frac{\pi-2\phi}{3/2}\right) \right\}^{-1} \right] \quad (A-8)$$

$$= 0; \phi > \frac{\pi}{2} - \beta_a \qquad \phi \leq \frac{\pi}{2} - \beta_a/2$$

$$D_4 = \frac{\frac{2}{3} e^{i\frac{\pi}{3}} \sin\left(\frac{2\pi}{3}\right)}{\cos\frac{\beta_a}{2} \sqrt{2\pi k}} \left[ \left\{ \cos\left(\frac{2\pi}{3}\right) - \cos\left(\frac{4\pi}{3} - \frac{2\beta_a}{3}\right) \right\}^{-1} \mp \left\{ \cos\left(\frac{2\pi}{3}\right) - \cos\left(\frac{\pi+2\phi}{3/2}\right) \right\}^{-1} \right] \quad (A-9)$$

$$= 0; \beta_a/2 < \phi < \frac{\pi}{2} - \beta_a/2 \qquad \frac{\pi}{2} - \beta_a/2 \leq \phi \leq \beta_a/2$$

where the aspect angle transformation performed at the fourth edge required

a bistatic transformation  $\beta_a \rightarrow 2\pi - \beta_a$ .

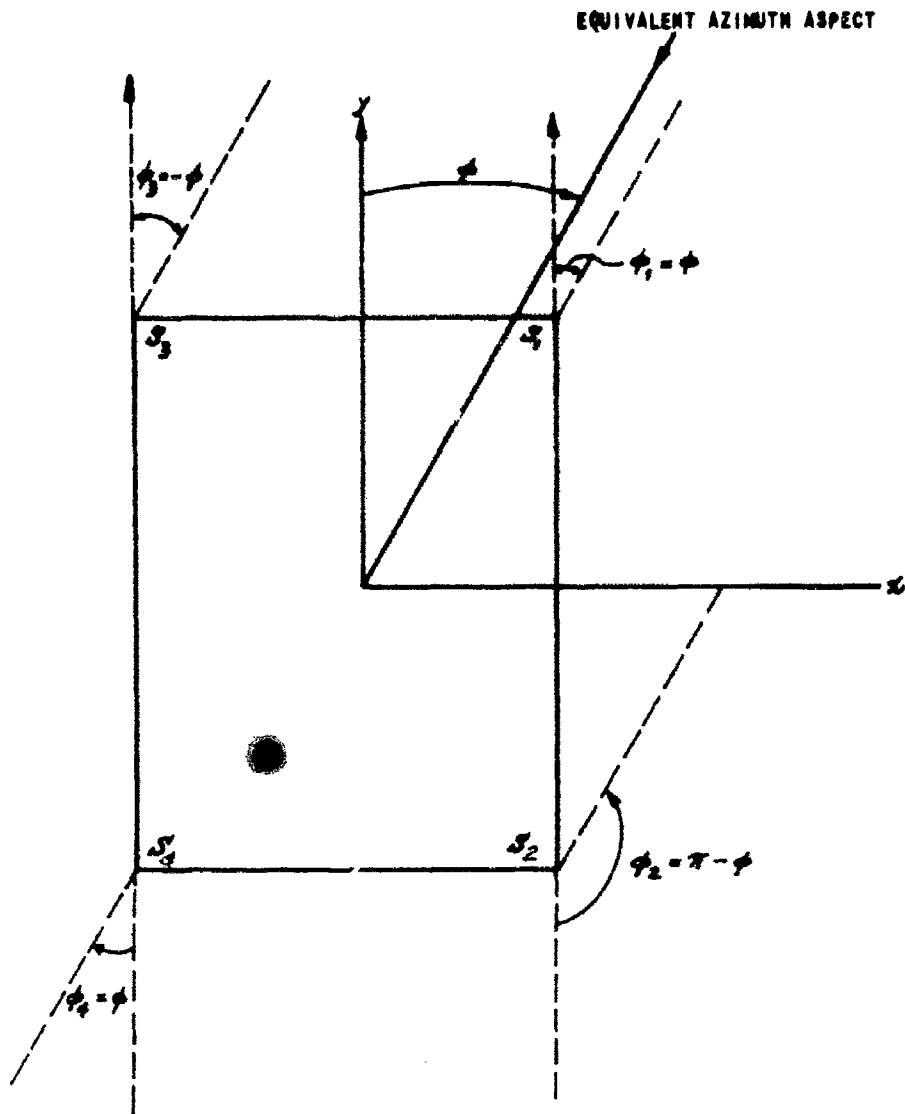


Figure A-3 ANGULAR TRANSFORMATION: TWO-DIMENSIONAL RECTANGULAR CYLINDER

Angular restrictions on Equations (A-6) through (A-9) are a consequence of a single diffraction analysis: individual scattering centers contribute to the total scattered field only when they are directly illuminated by the transmitter and directly "observed" by the receiver.

### A.2.3 Divergence Factor

The diffraction coefficients listed above were derived from the asymptotic solution for scattering at the edge of an infinite, right-angle wedge. Fields diffracted at such two-dimensional edges fall as  $\rho^{-1/2}$ , where  $\rho$  is the distance separating the edge and the receiver. In contrast, edges on finite targets are three dimensional. Field diffracted at three-dimensional edges drop as  $\rho^{-1}$

For far field diffraction, the separation between the edge and receiver  $\rho$  is much greater than the radius of curvature of the diffracted wavefront  $\rho_1$ . Then, for  $\rho \gg \rho_1$ , the divergence factor introduced in Equation (A-2) becomes

$$\left[ \rho (1 + \rho_1^{-1} \rho) \right]^{-1/2} \rightarrow \frac{\sqrt{\rho_1}}{\rho} \quad (\text{A-10})$$

The divergence factor is known when we have solved for the radius of curvature of the diffracted wavefront. One may choose two methods of solution for  $\rho_1$ . First, he may employ Keller's basic definition presented as Equation (11) of Reference 20.

$$\rho_1 = - \frac{\rho \sin^2 \beta_k}{\rho \dot{\beta}_k \sin \beta_k + \cos \delta_k} \quad (\text{A-11})$$

where  $\rho \geq 0$  is the radius of curvature of the edge (i. e.,  $\rho = a$  for a right-circular cylinder)

$\beta_k$  is the angle between the incident (diffracted) ray and the positive (negative) tangent to the edge

$\dot{\beta}_k$  is the derivative of  $\beta$  with respect to arc length along the edge

and  $\delta_k$  is the angle between the diffracted ray and the normal to the edge.



(Here the normal to the edge, which lies in the X-Z plane, is supposed to point toward the center of curvature of the edge.) Equation (A-11) is a convenient geometrical interpretation of the quantity  $\beta_1$ ; however, it does not offer the simplicity of a formulation discussed by Helstrom. From Equation (C-13) of Reference 13, we introduce the alternate formula

$$\beta_1 = -\frac{\rho \sin^2 \beta_k}{\hat{\mu} \cdot \hat{n} - \hat{\lambda} \cdot \hat{n}} \quad (\text{A-12})$$

where  $\rho$  and  $\beta_k$  are as defined above, and

$\hat{\lambda}$  is a unit vector specifying a direction parallel to which incident rays move

$\hat{\mu}$  is a unit vector specifying a direction parallel to which diffracted rays move, and

$\hat{n}$  is a unit vector in the direction of the principal normal to the edge.

The difference between Equations (A-12) and (A-11) involves the denominators: note that in the denominator of Equation (A-12),  $\hat{\mu} \cdot \hat{n} (\hat{\lambda} \cdot \hat{n})$  is the cosine of the angle between the incidence (diffraction) vector and the principal normal to the edge. Then Equation (A-12) is easily evaluated in terms of  $\beta_e$ ,  $\beta_a$ ,  $\alpha$  and  $\rho$  using the appropriate modification to Figure A-2. Diffraction at the edge of a cylinder edge is illustrated in Figure A-4. The angle between the incident vector  $\hat{\mu}$  and diffraction vector  $\hat{\lambda}$  is  $\beta$ . The bistatic angle  $\beta$  has angular projections  $\beta_a$  and  $\beta_e$  in the azimuth and elevation planes. Finally, the angle between the bisector of  $\beta$  and the Y-axis is the equivalent azimuth aspect angle  $\phi$ .

Thus for scattering center  $S_1$ , the following relations obtain

$$\begin{aligned} \beta_k &= \frac{\pi}{2} - \frac{\beta_e}{2} \\ \hat{\mu} \cdot \hat{n} &= -\cos(\beta_e/2) \cos\left(\frac{\pi}{2} - \phi + \frac{\beta_a}{2}\right) \\ \hat{\lambda} \cdot \hat{n} &= \cos(\beta_e/2) \cos\left(\phi + \frac{\beta_a}{2} - \frac{\pi}{2}\right) \end{aligned} \quad (\text{A-13})$$

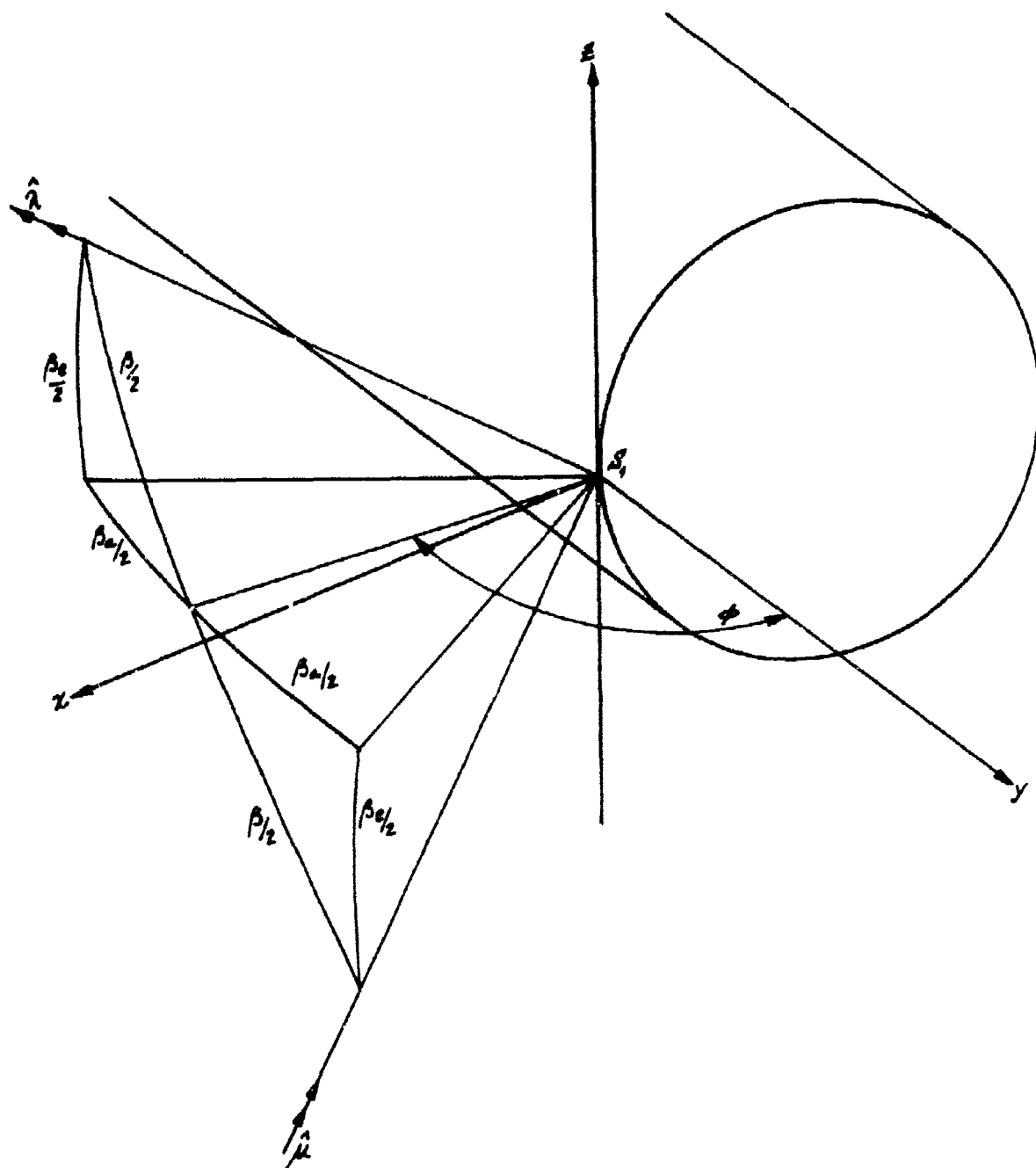


Figure A-4 ANGULAR RELATIONS FOR RIGHT-CIRCULAR CYLINDER

and the radius of curvature of the diffracted wavefront given by Equation (A-12) becomes

$$f_1 = \frac{a \cos(\beta_a/2)}{2 \cos(\beta_a/2) \sin \phi} \quad (\text{A-14})$$

The appropriate divergence factors  $G_1$ ,  $G_2$ ,  $G_3$  and  $G_4$  follow from Equations (A-14), (A-10) and the angular transformations noted at the end of Subsection A.2.2. They are

$$G_1 = \sqrt{\frac{a \cos \beta_0/2}{2 \cos \beta_a/2 \sin \phi}} = G_2 \quad (\text{A-15})$$

$$G_3 = \sqrt{\frac{a \cos \beta_0/2}{2 \cos \beta_a/2 \sin \phi}} e^{-i\frac{\pi}{2}} \quad (\text{A-16})$$

$$G_4 = \sqrt{\frac{a \cos \beta_0/2}{2 \cos \beta_a/2 \sin \phi}} e^{-i\frac{\pi}{2}} \quad (\text{A-17})$$

where the phase factor  $e^{-i\frac{\pi}{2}}$  enters Equation (A-16) from the factor  $\frac{1}{\sqrt{\sin(-\phi)}}$  and enters Equation (A-17) from the factor  $\frac{1}{\sqrt{\cos(\frac{2\pi - \beta_a}{2})}}$ .

## A.2.4

Geometric Phase

According to Equation (A-3) of Subsection A.2.1, each diffracted field includes a geometric phase angle  $k(\psi + s)$  where  $\psi$  is the separation between the transmitting antenna and edge (at the point of diffraction),  $s$  is the separation between the edge and the receiving antenna, and  $k$  is the wave number. For convenience, we choose a phase reference located at the center of the cylinder. Figure A-5 illustrates the geometry where  $a$  is the radius of the cylinder,  $h$  is the half-length, and the phase reference is taken to be the origin of the coordinate system. Let the separation between the phase reference and the radar antennas be denoted by  $r$ . The radar transmitter and receiver are constrained to be on a circle of radius  $r$ . This is a definite limitation for investigating a bistatic array, however it represents a realistic condition on a radar scattering range. For the case where the bistatic angle is zero, this condition is not a limitation. Let the distance between the edge  $S_1$  and the phase reference, projected along the direction of incidence (scattering), be denoted by  $d_i(d_s)$ . Then  $\psi = r - d_i$ ,  $s = r - d_s$  and the geometric phase becomes

$$k(\psi + s) = k(2r - (d_i + d_s))$$

(A-18)

Prior to evaluating the general case, the planar case will be considered.

In this case,  $\beta_e = 0$  and  $\beta = \beta_s$ . This case is illustrated in Figure A-5a.



•

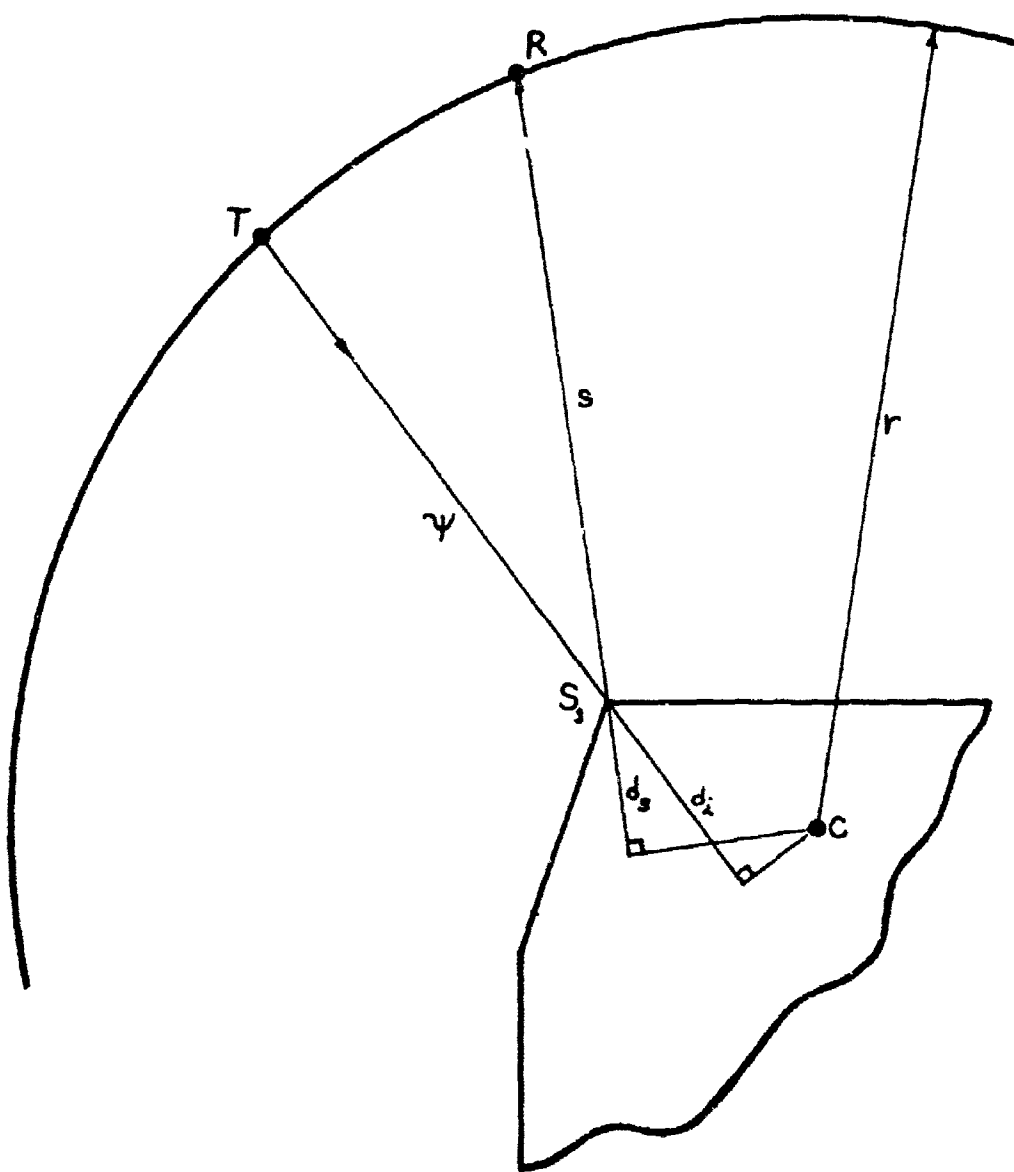


Figure A-5a DEFINITION OF GEOMETRICAL PHASE TERMS

The geometrical distances  $d_i$  and  $(d_s)$  are shown as the distances measured along the incident (scattered) ray between the edge  $S_i$  and the line passing through the phase reference which is perpendicular to the incident (scattered) ray. Note, that if the bistatic angle is zero,  $d_i = d_s$ ,  $\phi = s$  and the geometrical phase becomes  $2k\phi = 2k(r-d_i)$ . We now evaluate the distance  $(d_i + d_s)$  as functions of the equivalent azimuth aspect angle  $\phi$  and the unrestricted bistatic angle  $\beta$ . Then the distances  $d_i(d_s)$  are measured on the surface of a cone with axis coincident with the aspect angle  $\phi$ , with apex located in the X-Y plane at the edge, and with base defined by the plane normal to the directions of incidence (observation) and passing through the origin. According to Figure A-5, the edge lies in the X-Y plane a distance  $d$  along a line oriented at an angle  $T$  to the X-axis. The equivalent azimuth aspect direction intersects this line at an angle  $R$ , where  $R = \phi - (\frac{\pi}{2} - \tau)$ . The bistatic angle  $\beta$  is contained in a plane which rotates about the equivalent azimuth aspect direction. This plane intersects the cone to generate lines containing segments  $d_i$  and  $d_s$ . In Figure A-5, the plane is shown rotated an angle  $\xi$  out of the X-Y plane. If we observe along the line OC, the spherical geometry illustrated in Figure A-6 is obtained.

Then

$$d_i + d_s = d (\cos \theta_i + \cos \theta_s) \quad (A-19)$$

where

$$\begin{aligned} \cos \theta_i &= \cos R \cos \beta/2 + \sin R \sin \beta/2 \cos \xi \\ \cos \theta_s &= \cos R \cos \beta/2 + \sin R \sin \beta/2 \cos(\pi - \xi) \end{aligned} \quad (A-20)$$

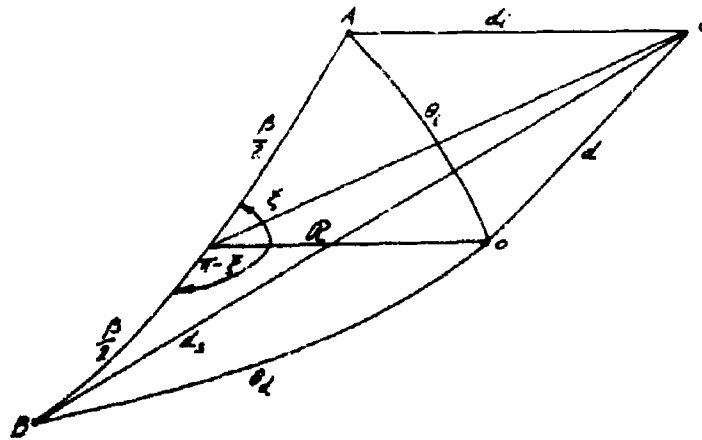


Figure A-6 SPHERICAL GEOMETRY: VIEW ALONG LINE OC

Substituting Equation (A-20) into Equation (A-19) and simplifying, we have

$$d_i + d_3 = 2(d \cos R) \cos \beta/2 \quad (\text{A-21})$$

where

$$\begin{aligned} d \cos R &= d \cos \left( \phi - \frac{\pi}{2} + \tau \right) \\ &= a \sin \phi + h \cos \phi \end{aligned} \quad (\text{A-22})$$

Finally, substituting Equation (A-21) and Equation (A-22) into Equation (A-18), we obtain the geometric phase for the edge  $S_1$

$$k(\psi + \lambda)_1 = k(2r - 2[a \sin \phi + h \cos \phi] \cos \beta/2) \quad (\text{A-23})$$

Employing the angular transformations noted at the end of Subsection A.2.1, we now write the geometric phase for the remaining three edges.

$$k(\psi + \lambda)_2 = k(2r - 2[a \sin \phi - h \cos \phi] \cos \beta/2) \quad (\text{A-24})$$

$$k(\psi + \lambda)_3 = k(2r + 2[a \sin \phi - h \cos \phi] \cos \beta/2) \quad (\text{A-25})$$

$$k(\psi + \lambda)_4 = k(2r + 2[a \sin \phi + h \cos \phi] \cos \beta/2) \quad (\text{A-26})$$



A.3

### SINGLE DIFFRACTION EXPRESSIONS FOR SCATTERING BY A FINITE, RIGHT-CIRCULAR CYLINDER

The total field  $\mu$  scattered by the cylinder is the vector and phasor sum of the fields diffracted at edges  $S_1$ ,  $S_2$ ,  $S_3$  and  $S_4$ . That is

$$\mu_{\text{TOTAL}} = \mu_1 + \mu_2 + \mu_3 + \mu_4 \quad (\text{A-27})$$

Each contribution  $\mu_i$  is determined according to Equation (A-3) using results derived in Subsections A.2.2 through A.2.4. For cylinder edge  $S_1$ , use Equations (A-6), (A-15), and (A-23) to obtain

$$\begin{aligned} \mu_1 = & \frac{A}{3} \frac{\sin\left(\frac{2\pi}{3}\right)}{\sqrt{\pi k r}} \sqrt{\frac{a}{\cos \beta/2 \sin \phi}} \left[ \left\{ \cos\left(\frac{2\pi}{3}\right) - \cos\left(\frac{\pi + 2\beta/2}{3/2}\right) \right\}^{-1} \right. \\ & \left. \mp \left\{ \cos\left(\frac{2\pi}{3}\right) - \cos\left(\frac{2\beta_a}{3}\right) \right\}^{-1} \right] e^{i[2kr + \frac{\pi}{4} - 2k(a \sin \phi + h \cos \phi) \cos \beta/2]} \quad (\text{A-28}) \end{aligned}$$

where  $\beta$  is approximated by  $r$  in the magnitude of the field. In the case of cylinder edge  $S_2$ , use Equations (A-7), (A-15) and (A-24) to obtain

$$\begin{aligned} \mu_2 = & \frac{A}{3} \frac{\sin\left(\frac{2\pi}{3}\right)}{\sqrt{\pi k r}} \sqrt{\frac{a}{\cos \beta/2 \sin \phi}} \left[ \left\{ \cos\left(\frac{2\pi}{3}\right) - \cos\left(\frac{4\phi}{3}\right) \right\}^{-1} \right. \\ & \left. \mp \left\{ \cos\left(\frac{2\pi}{3}\right) - \cos\left(\frac{2\beta_a}{3}\right) \right\}^{-1} \right] e^{i[2kr + \frac{\pi}{4} - 2k(a \sin \phi - h \cos \phi) \cos \beta/2]} \quad (\text{A-29}) \\ & \phi \geq \beta_a/2 \\ & = 0; \quad \phi < \beta_a/2 \end{aligned}$$

Similarly, cylinder edge  $S_3$  involves Equations (A-8), (A-16), and (A-25)

$$\begin{aligned} \mu_3 = & \frac{A}{3} \frac{\sin\left(\frac{2\pi}{3}\right)}{\sqrt{\pi k r}} \sqrt{\frac{a}{\cos \beta/2 \sin \phi}} \left[ \left\{ \cos\left(\frac{2\pi}{3}\right) - \cos\left(\frac{\pi - 2\phi}{3/2}\right) \right\}^{-1} \right. \\ & \left. \mp \left\{ \cos\left(\frac{2\pi}{3}\right) - \cos\left(\frac{2\beta_a}{3}\right) \right\}^{-1} \right] e^{i[2kr - \frac{\pi}{4} + 2k(a \sin \phi - h \cos \phi) \cos \beta/2]} \quad (\text{A-30}) \\ & \phi \leq \frac{\pi}{2} - \frac{\beta_a}{2} \\ & = 0; \quad \phi > \frac{\pi}{2} - \frac{\beta_a}{2} \end{aligned}$$

Finally, for cylinder edge  $S_4$ , use Equations (A-9), (A-17), and (A-26)

$$\begin{aligned} \mu_4 &= \frac{A}{3} \frac{\sin\left(\frac{2\pi}{3}\right)}{\sqrt{\pi k r}} \sqrt{\frac{a}{\cos\beta/2 \sin\phi}} \left\{ \cos\left(\frac{2\pi}{3}\right) - \cos\left(\frac{\pi + 2\phi}{3/2}\right) \right\}^{-1} \\ &\quad \times \left\{ \cos\left(\frac{2\pi}{3}\right) - \cos\left(\frac{4\pi}{3} - \frac{2A_0}{3}\right) \right\}^{-1} e^{i[2kr - \frac{\pi}{4} + 2k(a \sin\phi + b \cos\phi) \cos\beta/2]} \quad (A-31) \\ &= 0; \quad \beta_0/2 < \phi < \pi/2 - \beta_0/2 \\ &\quad \pi/2 - \beta_0/2 \leq \phi \leq \beta_0/2 \end{aligned}$$

Notice that the preceding application of unmodified geometrical diffraction theory leads to singular results when specular scattering occurs ( $\phi = 0$  and  $\pi/2$ ) and for the forward-scattering bistatic situation ( $\beta = \pi$ ).

#### A. 4 SCATTERING CENTER NOTATION

Applications of geometrical diffraction in subsections A. 2. and A. 3 have led to expressions for the field  $\mu$  scattered at the various edges on a cylinder. Here we interpret these field expressions in terms of radar cross sections  $\sigma_i$  and phases  $\rho_i$  assigned to scattering centers. Once each  $\mu_{\text{edge diff}}$  is calculated for every edge on the body, an expression for  $\mu_{\text{total}}$  can be represented as such:

$$\mu_{\text{TOTAL}} = \sum_{i=1}^N (\mu_{\text{edge diff}})_i \quad (\text{A-32})$$

where  $\mu_{\text{total}}$  represents the sum of all the rays diffracted in the direction of the body. According to geometrical diffraction theory, the total radar cross section of a target is given by:

$$\sigma(\phi, \theta) = \left| \frac{2\sqrt{\pi}r}{A} \mu_{\text{TOTAL}} \right|^2$$

where  $\mu_{\text{total}}$  represents the sum of all the rays diffracted in the direction of the receiver. In scattering center notation the amplitude and phase of the field reradiated from the  $i^{\text{th}}$  scattering center can be written as

$$\sqrt{\sigma_i} e^{i(k2r + \rho_i)} = \frac{2\sqrt{\pi}r}{A} (\mu_{\text{edge diff}})_i \quad (\text{A-33})$$

where  $\sigma_i$  = amplitude of reradiated field from  $i^{\text{th}}$  scattering center

$\rho_i$  = relative phase of reradiated field from  $i^{\text{th}}$  scattering center

$r$  = distance to radar from geometrical center of the target

$A$  = amplitude of incident plane wave

$S$  = distance from the edge of the target to the receiver

Putting Equation A-10 in Equation A-30 and substituting the result into Equation A-33 gives

$$\sqrt{\sigma_i} e^{i(2kr + \rho_i)} = \frac{2\sqrt{\pi}r}{A} \left[ \pm 0 \frac{\sqrt{\rho_d}}{\delta} A e^{i(\beta + \psi)} \right] \quad (\text{A-34})$$

where  $r \approx s$ . Thus

$$\sqrt{\sigma_i} = 2\sqrt{\pi} \left[ \pm 0 \sqrt{\rho_d} \right]$$

after discarding the phase terms contained in  $D$  and  $\sqrt{\rho_d}$ . Then according to scattering center notation, one obtains

$$\sigma(\phi, \beta) = \left| \sum_{i=1}^N \sqrt{\sigma_i} e^{i\rho_i} \right|^2 \cdot |e^{i2kr}|^2$$

and since the last term is equal to 1 the scattering center expression for the total radar cross section becomes

$$\sigma(\phi, \beta) = \left| \sum_{i=1}^N \sqrt{\sigma_i} e^{i\rho_i} \right|^2 \quad (\text{A-35})$$

where  $\phi$  and  $\beta$  are respectively the aspect and bistatic angles. Thus the  $2kr$  phase term is not important in determining the total radar cross section, it is the relative phase of each scattering center that is important. The  $2kr$  phase term is only important when it is desired to determine the absolute phase ( $2kr + \rho_i$ ) of the  $i^{\text{th}}$  scattering center. Notice also that, in scattering center notation, the phase  $\rho$  of the signal reradiated from the target is given by

$$\rho = \tan^{-1} \left\{ \frac{\sum_{i=1}^N \sqrt{\sigma_i} \sin \rho_i}{\sum_{i=1}^N \sqrt{\sigma_i} \cos \rho_i} \right\} \quad (\text{A-36})$$

Equations (A-33), (A-35), and (A-36) are relations necessary in the transformation of expressions of geometrical diffraction theory to corresponding formulas discussed in Section 4 of this report.

## A.5 SCATTERING BY CYLINDER AT AND NEAR SPECULAR ASPECTS

### A.5.1 Background

It is a characteristic of applications of unmodified geometrical diffraction theory that singularities arise in formulas at aspects which produce specular scattering. These undesired singularities may arise in the diffraction coefficient, in the divergence factor, or in both quantities used in describing reradiation from scattering centers. In the case of the cylinder, modification of theory at and near axial and broadside aspects is required to obtain a description of reradiation phenomena continuous in aspect angle. Keller<sup>14</sup> has proposed modification of his theory by means of a caustic correction. In brief, multiplication of unmodified formulas by the caustic correction factor removes undesired singularities in the case of an axially symmetric edge. While his method has obvious application in the case of axial incidence on the cylinder, we note two drawbacks. First, the predicted scattering dependence will be of the form  $J_0(x)$ , whereas the actual functional dependence is known to be  $\frac{J_1(x)}{x}$ . Second, his modification allows prediction of scattering at but not near the axial aspect. For these reasons, a search for an alternate modification technique was initiated. It was found that, in cases where the two scattering centers which contribute to the specular return exhibit symmetrical geometry and identical dimensions, small angle approximations allow cancellation of singularities. Then expressions for specular scattering derived from geometrical diffraction theory in the manner noted are in essential agreement with well known physical optics results.

We now illustrate the method in the case of a cylinder target. First, the small angle approximation is shown to be applicable for aspects at and near broadside incidence. Then the same approximation is employed as an alternative to the caustic correction for aspects at and near axial incidence.

### A.5.2 Cylinders Scattering At and Near Broadside Aspects

As illustrated in Figure A-3, subsection A.2.2, scattering centers  $S_1$  and  $S_2$  should describe the specular return  $\sqrt{\sigma_b} e^{i\phi_b}$  from a

cylinder viewed at and near the broadside aspect ( $\phi = \frac{\pi}{2}$ ). That is

$$\sqrt{\sigma_b} e^{j\rho_b} = \sqrt{\sigma_1} e^{j\rho_1} + \sqrt{\sigma_2} e^{j\rho_2} \quad (\text{A-37})$$

For convenience in discussion, we present expressions for the contributions from these two scattering centers below (see Equations (A-28), (A-29), and (A-35).

$$\begin{aligned} \sqrt{\sigma_1} e^{j\rho_1} = & \frac{2}{3} \sin\left(\frac{2\pi}{3}\right) \sqrt{\frac{a}{k \cos \beta_{1/2} \sin \phi}} \left[ \left\{ \cos\left(\frac{2\pi}{3}\right) - \cos\left(\frac{\pi + 2\phi}{3/2}\right) \right\}^{-1} \right. \\ & \left. \tau \left\{ \cos\left(\frac{2\pi}{3}\right) - \cos\left(\frac{2\beta_2}{3}\right) \right\}^{-1} \right] e^{j\frac{\pi}{4} - j2(k \cos \beta_{1/2})[a \sin \phi + h \cos \phi]} \quad (\text{A-38}) \end{aligned}$$

$$\begin{aligned} \sqrt{\sigma_2} e^{j\rho_2} = & \frac{2}{3} \sin\left(\frac{2\pi}{3}\right) \sqrt{\frac{a}{k \cos \beta_{1/2} \sin \phi}} \left[ \left\{ \cos\left(\frac{2\pi}{3}\right) - \cos\left(\frac{4\phi}{3}\right) \right\}^{-1} \right. \\ & \left. \tau \left\{ \cos\left(\frac{2\pi}{3}\right) - \cos\left(\frac{2\beta_2}{3}\right) \right\}^{-1} \right] e^{j\frac{\pi}{4} - j2(k \cos \beta_{1/2})[a \sin \phi + h \cos \phi]} \quad (\text{A-39}) \end{aligned}$$

where the angular restrictions on Equation (A-29) have been deleted since we limit present discussion to aspects near broadside. Observe the presence of singularities in the polarization-independent components of the diffraction coefficient assigned in Equations (A-38) and (A-39) when  $\phi = \frac{\pi}{2}$ . In order to remove these undesired singularities, we introduce the aspect notation

$\phi = \frac{\pi}{2} - \Delta$ , where  $\Delta$  is a small angle. Allowing  $\cos \frac{4\Delta}{3} \rightarrow 1$ ,  $\sin \frac{4\Delta}{3} \rightarrow \frac{4\Delta}{3}$ , the following simplification obtains

$$\left\{ \cos\left(\frac{2\pi}{3}\right) - \cos\left(\frac{\pi + 2\phi}{3/2}\right) \right\}^{-1} \longrightarrow \frac{1}{\frac{4\Delta}{3} \sin\left(\frac{2\pi}{3}\right)} \quad (\text{A-40})$$

$$\left\{ \cos\left(\frac{2\pi}{3}\right) - \cos\left(\frac{4\phi}{3}\right) \right\}^{-1} \longrightarrow -\frac{1}{\frac{4\Delta}{3} \sin\left(\frac{2\pi}{3}\right)} \quad (\text{A-41})$$

We now consider only the polarization independent component of Equation (A-37), and denote this contribution by  $(\sqrt{\sigma_b} e^{j\beta_b})_{poli}$ . Substituting Equation (A-40) into Equation (A-38) and Equation (A-41) into Equation (A-39), we have

$$(\sqrt{\sigma_b} e^{j\beta_b})_{poli} = -\sqrt{\frac{a}{k \cos \theta_2 \sin \phi}} e^{j\frac{\pi}{4} - j2k \cos \theta_2 a \sin \phi} \left[ \frac{e^{+j2k \cos \theta_2 \Delta} - e^{-j2k \cos \theta_2 \Delta}}{2\Delta} \right] \quad (A-42)$$

The bracket in Equation (A-42) is of the form  $\sin x/x$ , and this simplification is made to obtain

$$(\sqrt{\sigma_b} e^{j\beta_b})_{poli} = -2h \sqrt{ka \cos \theta_2} e^{-j2k \cos \theta_2 a \sin \phi + j\frac{\pi}{4}} \frac{\sin(2k \cos \theta_2 h \Delta)}{(2k \cos \theta_2 h \Delta)} \quad (A-43)$$

Equation (A-43) is well behaved at and near broadside aspects. Evaluated for  $\phi = \frac{\pi}{2}$  ( $\Delta = 0$ ), it gives

$$\sigma(\phi = \frac{\pi}{2}) = ka (2h)^2 \cos \theta_2 \quad (A-44)$$

For  $\beta = 0$ , Equation (A-44) agrees with the well known physical optics result for broadside scattering by a cylinder.<sup>19</sup>

The modification to geometrical diffraction theory in this instance involves substitution of Equation (A-43) in lieu of the polarization-independent contributions from scattering centers  $S_1$  and  $S_2$ . Both the polarization-dependent contributions from centers  $S_1$  and  $S_2$  and the total contribution from center  $S_3$  remain unaltered. A smooth transition between scattering computations based upon unmodified and modified theory is realized at a cross over aspect  $\phi_{cb}$  given by

$$2kh \cos \phi_{cb} = 2.25 \quad (A-45)$$

For  $\phi < \phi_{cb}$  we use the conventional scattering center formulation. For  $\phi > \phi_{cb}$  we employ the modification indicated in Equation (A-43).

### A.5.3 Cylinders Scattering At and Near Axial Aspects

According to Figure A-3 of subsection A.2.2, the combined contribution from scattering centers  $S_1$  and  $S_3$  should account for the specular observed at and near the axial aspect ( $\phi = 0$ ). Denoting the axial specular by the symbol  $\sqrt{\sigma_a} e^{j\beta_a}$ , we have

$$\sqrt{\sigma_a} e^{j\beta_a} = \sqrt{\sigma_1} e^{j\beta_1} + \sqrt{\sigma_3} e^{j\beta_3} \quad (\text{A-46})$$

where scattering center contributions are obtained from Equations (A-28), (A-30), and (A-35), and are presented below

$$\begin{aligned} \sqrt{\sigma_1} e^{j\beta_1} = & \frac{2}{3} \sin\left(\frac{2\pi}{3}\right) \sqrt{\frac{a}{k \cos \beta_{1/2} \sin \phi}} \left[ \left\{ \cos\left(\frac{2\pi}{3}\right) - \cos\left(\frac{\pi+2\phi}{3/2}\right) \right\}^{-1} \right. \\ & \left. \mp \left\{ \cos\left(\frac{2\pi}{3}\right) - \cos\left(\frac{2\beta_a}{3}\right) \right\}^{-1} \right] e^{j\frac{\pi}{4} - j2k \cos \beta_{1/2} [a \sin \phi + h \cos \phi]} \quad (\text{A-47}) \end{aligned}$$

$$\begin{aligned} \sqrt{\sigma_3} e^{j\beta_3} = & \frac{2}{3} \sin\left(\frac{2\pi}{3}\right) \sqrt{\frac{a}{k \cos \beta_{3/2} \sin \phi}} \left[ \left\{ \cos\left(\frac{2\pi}{3}\right) - \cos\left(\frac{\pi-2\phi}{3/2}\right) \right\}^{-1} \right. \\ & \left. \mp \left\{ \cos\left(\frac{2\pi}{3}\right) - \cos\left(\frac{2\beta_a}{3}\right) \right\}^{-1} \right] e^{-j\frac{\pi}{4} + j2k \cos \beta_{3/2} [a \sin \phi - h \cos \phi]} \quad (\text{A-48}) \end{aligned}$$

Examination of Equations (A-47) and (A-48) at the axial aspect ( $\phi = 0$ ) reveals the presence of singularities in the divergence factors ( $\frac{1}{\sin \phi}$ ) and the polarization-independent components of the diffraction coefficients

$$\left( \left\{ \cos\left(\frac{2\pi}{3}\right) - \cos\left(\frac{\pi+2\phi}{3/2}\right) \right\}^{-1}, \left\{ \cos\left(\frac{2\pi}{3}\right) - \cos\left(\frac{\pi-2\phi}{3/2}\right) \right\}^{-1} \right).$$



Modification of the theory is begun by treating these polarization-independent terms, again using the notation  $(\sqrt{\sigma_a} e^{i\phi_a})_{poli}$  for their contribution. Introducing small angle approximations, allow

$\cos \frac{2\phi}{3} \rightarrow 1$ ,  $\sin \frac{2\phi}{3} \rightarrow \frac{2\phi}{3}$  to obtain

$$\left\{ \cos\left(\frac{2\pi}{3}\right) - \cos\left(\frac{\pi + 2\phi}{3/2}\right) \right\}^{-1} \rightarrow \frac{1}{\frac{2\phi}{3} \sin\left(\frac{2\pi}{3}\right)} \quad (A-49)$$

$$\left\{ \cos\left(\frac{2\pi}{3}\right) - \cos\left(\frac{\pi - 2\phi}{3/2}\right) \right\}^{-1} \rightarrow -\frac{1}{\frac{2\phi}{3} \sin\left(\frac{2\pi}{3}\right)} \quad (A-50)$$

Equations (A-49) and (A-50) are substituted into Equations (A-47) and (A-48) and the following contribution is extracted.

$$\begin{aligned} (\sqrt{\sigma_a} e^{i\phi_a})_{poli} = & \frac{1}{2} \sqrt{\frac{a}{k \cos \beta/2}} \frac{1}{\phi} e^{-j2k \cos \beta/2 h \cos \phi} \times \\ & \left[ \frac{e^{-j2k \cos \beta/2 a \phi + j\pi/4} + j2k \cos \beta/2 a \phi - j\pi/4}{\sqrt{\phi} - e} \right] \end{aligned} \quad (A-51)$$

At this point we introduce\* the large argument approximation for the first order Bessel function

\*Some justification for this step is offered in the following discussion, which borrows freely from Keller.<sup>20</sup> In the region of axial incidence, an exact solution of the reduced wave equation is

$$\mu = J_N(x) \cos N\phi$$

This has the asymptotic expansion for  $k$  large

$$\mu \approx \frac{2 \cos N\phi}{\sqrt{2\pi x}} \cos \left[ x - (N + \frac{1}{2}) \frac{\pi}{2} \right]$$

We will show that the above expression has the same form as unmodified geometrical diffraction theory (provided  $N = 1$ ) and that both representations are singular for axial incidence. From this we infer that the well behaved parent function (of which the scattering center formulas are asymptotic expansions) is related to  $J_1(x)$ .

$$J_1(x) \approx \sqrt{\frac{2}{\pi x}} \cos(x - \frac{3\pi}{4}) \quad (\text{A-52})$$

and recast it to show that the bracketed term in Equation (A-50) is

$$\left[ \frac{e^{-j2k \cos \frac{\theta}{2} a \phi + j\frac{\pi}{4}} - e^{-j2k \cos \frac{\theta}{2} a \phi - j\frac{\pi}{4}}}{j\phi} \right] = e^{-j\frac{\pi}{4}} \sqrt{4\pi k \cos \frac{\theta}{2} a} J_1(2k \cos \frac{\theta}{2} a \phi) \quad (\text{A-53})$$

Finally, substituting Equation (A-53) into Equation (A-51), we have as our result

$$(\sqrt{\sigma_a} e^{j\rho_a})_{\text{pol}} = 2\sqrt{\pi} k a^2 \cos \frac{\theta}{2} \frac{J_1(2k \cos \frac{\theta}{2} a \phi)}{(2k \cos \frac{\theta}{2} a \phi)} e^{-j\frac{\pi}{4} - j2k \cos \frac{\theta}{2} a \cos \phi} \quad (\text{A-54})$$

Equation (A-54) agrees with the physical optics result for specular scattering by a disc.<sup>19</sup>

Equation (A-54) is well behaved at the axial aspect and predicts a radar cross section

$$\sigma(\phi = \frac{\pi}{2}) = \frac{4\pi^2 a^4}{\lambda^2} \cos^2 \frac{\theta}{2} \quad (\text{A-55})$$

The monostatic form of Equation (A-55) agrees with the well known physical optics result. Thus, we will use Equation (A-54) to replace polarization-independent components of contributions from centers  $S_1$  and  $S_2$  at and near axial aspects.

Although the critical portion of the analysis is completed, there still exist potential singularities in the polarization-dependent component of  $\sqrt{\sigma_a} e^{j\rho_a}$ , and in the total contribution from scattering center  $S_2$ . In all cases the trouble lies with the  $1/\sin \phi$  dependence of the divergence factor.

Our modification in these instances consists of placing an arbitrary\* upper limit on the singularity, i.e.,

$$\frac{1}{\sin \phi} \leq ka \cos \beta/2 \quad (\text{A-56})$$

The details of this criterion are not presented since the particular value of the upper limit is not crucial provided that 1)  $1/\sin \phi < ka \cos \beta/2$  prior to the cross over aspect, and 2) the polarization dependent components of  $\sqrt{\sigma_1}$ ,  $\sqrt{\sigma_2}$  and  $\sqrt{\sigma_3}$  being included to insure smooth transition do not noticeably alter the specular return given by Equation (A-54).

The modification to geometrical diffraction theory at and near axial aspects involves substitution of Equation (A-54) in lieu of the polarization-independent contributions from scattering centers  $S_1$  and  $S_3$ . In addition, the factor  $1/\sin \phi$  in the divergence factor of all remaining terms is given the upper limit  $ka \cos \beta/2$ . A smooth transition between scattering computations based upon unmodified and modified theory is observed at the cross over aspect  $\phi_{ca}$  given by

$$2ka \sin \phi_{ca} = 2.44 \quad (\text{A-57})$$

For  $\phi \leq \phi_{ca}$  we use modifications outlined above. For  $\phi > \phi_{ca}$  we employ the conventional scattering center formulation.

---

\*The limit is not completely arbitrary. It was obtained in the following manner:

1. determine the contribution from the rear of the cylinder at axial incidence using small angle approximations on  $\sqrt{\sigma_2} e^{j\beta/2} + \sqrt{\sigma_4} e^{j\beta/2}$ . The result has dependence upon  $J_0$ .
2. expand  $J_0$  and compare with unmodified geometrical diffraction theory.
3. comparison in 2. indicates that the divergence factor should not exceed  $a$ , from which  $1/\sin \phi \leq ka \cos \beta/2$

## A. 5. 4

Remarks

The analysis reported in this appendix was directed toward extension of the excellent capabilities of unmodified geometrical diffraction theory in predicting scattering by large cylinders at nonspecular aspects. Although modification of the theory proved straightforward at and near broadside aspects, certain heuristic arguments were found necessary at axial aspects. For this reason, engineering considerations such as the limit on the divergence factor found their way into the analysis. They need not have. Later analyses based upon a Green's function approach have since validated results obtained using small angle approximations (see Appendix C). In particular, if one keeps his head, the small angle approximation approach offers a short cut. For example, further examination of small angle results shows that the polarization dependent contribution from centers  $S_1$  and  $S_2$  at and near axial incidence can be related to either  $J_0(x)$  or  $J_2(x)$ . Realizing that this contribution disappears at the axial aspect, one should choose  $J_2(x)$  dependence. Fortunately, the strong specular from the face of the cylinder completely overrides the polarization dependence left in our expressions.

## Appendix B

### SCATTERING BY A FRUSTUM

#### B.1 INTRODUCTION

A frustum is a doubly truncated cone. It is convenient to obtain expressions for the complex contributions from the scattering centers on a frustum by reexamining the detailed analysis of the cylinder presented in Appendix A. Indeed, it is only required that the geometrical differences between a frustum and a cylinder be observed in order to generate the required formulation by inspection. Modification of geometrical diffraction theory for axial aspects may also be effected in the same manner employed in the cylinder investigation. However, the use of small angle approximations does not produce cancellation of singularities when incidence is at and near the broadside aspect. Here we report results of analyses based upon physical optics and an alternate scheme of curve-fitting.

One purpose of this appendix is to illustrate the manner in which the detailed analyses of Appendix A may be generalized for other targets of interest to this program. Although we show the procedure for a frustum, similar considerations lie behind formulations which are simply presented for the frustum-cylinder and the cylinder-flare.

#### B.2 SCATTERING AT NONSPECULAR ASPECTS

Figure B-1 shows the bistatic radar-target relationship. Two axially symmetric edges located at the extremities of the frustum give rise to four geometric discontinuities in the azimuth (x-y) plane; these discontinuities, labelled  $S_1$ ,  $S_2$ ,  $S_3$  and  $S_4$  constitute the four scattering centers on the target. The fundamental difference between the geometry of a frustum and a cylinder is that the former target requires two radii of curvature to describe shape. We denote the smaller radius of the frustum by  $a_1$ , and the larger radius by  $a_2$ . Further, there are now two values of the wedge parameter  $\pi$ , where  $\pi$  is equal to  $\gamma_k/\pi$ , and  $\gamma_k$  is the exterior wedge angle. If the

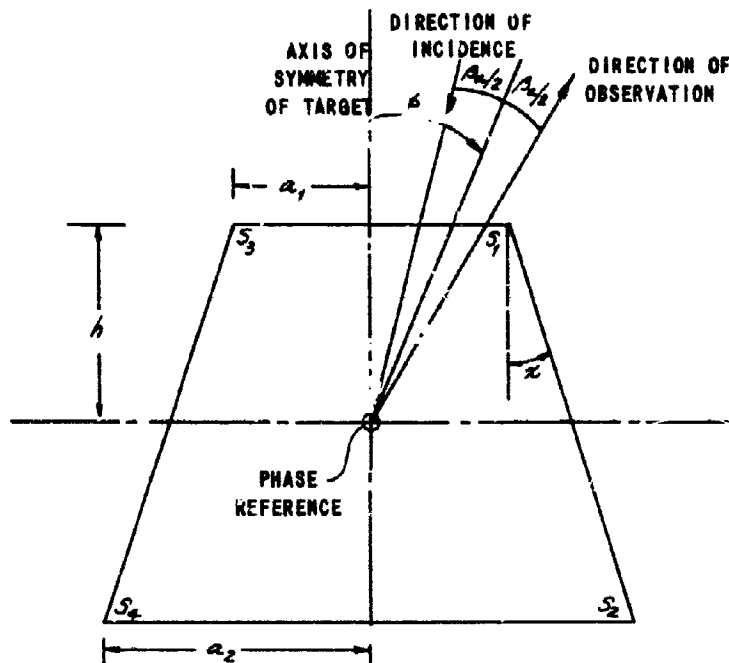


Figure B-1 SCATTERING CENTERS ON FRUSTUM

half angle of the frustum is  $\alpha$  ( $\alpha = \tan^{-1} \left( \frac{a_2 - a_1}{2h} \right)$ ) where  $2h$  is the height of the frustum, then the following definitions of the parameter  $n$  apply:

$n_1 = 3/2 - \alpha/\pi$  at the narrow end of the target;  $n_2 = 3/2 + \alpha/\pi$  at the broad end. By inserting the appropriate values of  $a$  and  $k$  into Equation A-28 through A-31 of Appendix A, we obtain the field relations

$$\mu_1 = \frac{A \sin(\pi/n_1)}{2\sqrt{\pi k r} n_1} \sqrt{\frac{a_1 \csc \phi}{\cos \beta/2}} \left[ \left\{ \cos\left(\frac{\pi}{n_1}\right) - \cos\left(\frac{\pi + 2\phi}{n_1}\right) \right\}^{-1} \right. \\ \left. \mp \left\{ \cos\left(\frac{\pi}{n_1}\right) - \cos\left(\frac{\beta}{n_1}\right) \right\}^{-1} \right] \times \\ e^{i[2kr + \pi/4 - 2k(a_1 \sin \phi + h \cos \phi) \cos \beta/2]} \quad (B-1)$$

$$\mu_2 = \frac{A \sin(\pi/n_2)}{2\sqrt{\pi k r} n_2} \sqrt{\frac{a_2 \csc \phi}{\cos \beta/2}} \left[ \cos\left(\frac{\pi}{n_2}\right) - \cos\left(\frac{2\pi - 2\phi}{n_2}\right) \right]^{-1} \\ \times \left[ \cos\left(\frac{\pi}{n_2}\right) - \cos\left(\frac{\beta}{n_2}\right) \right]^{-1} e^{i[2kr + \pi/4 - 2k(a_2 \sin \phi - h \cos \phi) \cos \beta/2]} \quad (\text{B-2})$$

$$\phi > -\pi + \beta/2$$

$$= 0; \quad \phi \leq -\pi + \beta/2$$

$$\mu_3 = \frac{A \sin(\pi/n_1)}{2\sqrt{\pi k r} n_1} \sqrt{\frac{a_1 \csc \phi}{\cos \beta/2}} \left[ \cos\left(\frac{\pi}{n_1}\right) - \cos\left(\frac{\pi - 2\phi}{n_1}\right) \right]^{-1} \\ \times \left[ \cos\left(\frac{\pi}{n_1}\right) - \cos\left(\frac{\beta}{n_1}\right) \right]^{-1} e^{i[2kr - \pi/4 + 2k(a_1 \sin \phi - h \cos \phi) \cos \beta/2]} \quad (\text{B-3})$$

$$\phi < \pi/2 - \beta/2$$

$$= 0; \quad \phi \geq \pi/2 - \beta/2$$

$$\mu_4 = \frac{A \sin(\pi/n_2)}{2\sqrt{\pi k r} n_2} \sqrt{\frac{a_2 \csc \phi}{k \cos \beta/2}} \left[ \cos\left(\frac{\pi}{n_2}\right) - \cos\left(\frac{3\pi + 2\phi}{n_2}\right) \right]^{-1} \\ \times \left[ \cos\left(\frac{\pi}{n_2}\right) - \cos\left(\frac{\beta}{n_2}\right) \right]^{-1} e^{i[2kr - \pi/4 + 2k(a_2 \sin \phi + h \cos \phi) \cos \beta/2]} \\ = 0; \quad \pi/2 + \beta/2 \geq \phi \geq \pi - \beta/2 \quad (\text{B-4})$$

$$= \frac{A \sin(\pi/n_2)}{2\sqrt{\pi k r} n_2} \sqrt{\frac{a_2 \csc \phi}{k \cos \beta/2}} \left[ \cos\left(\frac{\pi}{n_2}\right) - \cos\left(\frac{-\pi + 2\phi}{n_2}\right) \right]^{-1} \\ \times \left[ \cos\left(\frac{\pi}{n_2}\right) - \cos\left(\frac{\beta}{n_2}\right) \right]^{-1} e^{i[2kr - \pi/4 + 2k(a_2 \sin \phi + h \cos \phi) \cos \beta/2]} \\ \phi > \pi/2 + \beta/2$$

Scattering center amplitudes  $\sqrt{\sigma_i}$  and phases  $\rho_i$  follow from Equations B-1 through B-4 above. They are presented as Equations 26 through 34 in subsection 4.2.1 of this report.

### B.3 SCATTERING AT AND NEAR AXIAL ASPECTS

According to Figure B-1, the combined contributions from scattering centers  $S_1$  and  $S_3$  should account for the specular observed at and near the nose-on axial aspect ( $\phi = 0$ ). Denoting the axial specular by the symbol  $\sqrt{\sigma_a} e^{j\rho_a}$ , we have

$$\sqrt{\sigma_a} e^{j\rho_a} = \sqrt{\sigma_1} e^{j\rho_1} + \sqrt{\sigma_3} e^{j\rho_3} \quad (\text{B-5})$$

where scattering center contributions are obtained from Equations B-1, B-3, and A-35 are presented below.

$$\begin{aligned} \sqrt{\sigma_1} e^{j\rho_1} = & \frac{\sin(\pi/n_1)}{n_1} \sqrt{\frac{a_1 \csc \phi}{k \cos \beta/2}} \left[ \left\{ \cos\left(\frac{\pi}{n_1}\right) - \cos\left(\frac{\pi + 2\phi}{n_1}\right) \right\}^{-1} \right. \\ & \left. \mp \left\{ \cos\left(\frac{\pi}{n_1}\right) - \cos\left(\frac{\beta_a}{n_1}\right) \right\}^{-1} \right] \times \\ & e^{j\pi/4 - j2k(a_1 \sin \phi + h \cos \phi) \cos \beta/2} \end{aligned} \quad (\text{B-6})$$

$$\begin{aligned} \sqrt{\sigma_3} e^{j\rho_3} = & \frac{\sin(\pi/n_1)}{n_1} \sqrt{\frac{a_1 \csc \phi}{k \cos \beta/2}} \left[ \left\{ \cos\left(\frac{\pi}{n_1}\right) - \cos\left(\frac{\pi - 2\phi}{n_1}\right) \right\}^{-1} \right. \\ & \left. \mp \left\{ \cos\left(\frac{\pi}{n_1}\right) - \cos\left(\frac{\beta_a}{n_1}\right) \right\}^{-1} \right] \times \\ & e^{-j\pi/4 + j2k(a_1 \sin \phi - h \cos \phi) \cos \beta/2} \end{aligned} \quad (\text{B-7})$$



Examination of Equations B-6 and B-7 at the nose-on axial aspect ( $\phi = 0$ ) reveals singularities in the divergence factor and in the polarization-independent component of the diffraction coefficient. Modification of theory is effected by introducing small angle approximations in the manner of subsection A.5.3 of Appendix A. Allowing  $\cos \frac{2\phi}{n_1} \rightarrow 1$ ,  $\sin \frac{2\phi}{n_1} \rightarrow \frac{2\phi}{n_1}$  we have

$$\left\{ \cos\left(\frac{\pi}{n_1}\right) - \cos\left(\frac{\pi+2\phi}{n_1}\right) \right\}^{-1} \rightarrow \frac{1}{\frac{2\phi}{n_1} \sin\left(\frac{\pi}{n_1}\right)} \quad (\text{B-8})$$

$$\left\{ \cos\left(\frac{\pi}{n_1}\right) - \cos\left(\frac{\pi-2\phi}{n_1}\right) \right\}^{-1} \rightarrow -\frac{1}{\frac{2\phi}{n_1} \sin\left(\frac{\pi}{n_1}\right)} \quad (\text{B-9})$$

Substituting Equations B-8 and B-9 into Equations B-6 and B-7, respectively, we recognize the large argument approximation for a first order Bessel function (see subsection A.5.3 of Appendix A). Then the polarization-independent term in Equation B-5 becomes

$$\left( \sqrt{\sigma_a} e^{j\beta_a} \right)_{\text{poli}} = 2\sqrt{\pi} k a_1^2 \cos \beta/2 \frac{J_1(2ka_1 \cos \beta/2 \sin \phi)}{(2ka_1 \cos \beta/2 \sin \phi)} \times e^{-j\pi/2 - j2kh \cos \beta/2 \cos \phi} \quad (\text{B-10})$$

All other contributions are well behaved when we apply the constraint  $\csc \phi \leq ka_1 \cos \beta/2$ . We employ Equation B-10 for  $0 \leq \phi \leq \phi_{ca}$ , and assume that  $\phi_{ca}$  is the same cross-over aspect angle as that determined in the cylinder study: i.e.,  $2ka_1 \sin \phi_{ca} = 2.44$ .

From Figure B-1, the combined contributions from scattering centers  $S_2$  and  $S_4$  should describe the specular observed at and near the tail-on axial aspect ( $\phi = \pi$ ). These contributions are defined by the field Equations B-2 and B-4, and the conversion relation given by Equation A-35 of Appendix A. The results are

$$\sqrt{\sigma_2} e^{j\beta_2} = \frac{\sin(\pi/n_2)}{n_2} \sqrt{\frac{a_2 \csc \phi}{k \cos \beta/2}} \left[ \left\{ \cos\left(\frac{\pi}{n_2}\right) - \cos\left(\frac{3\pi - 2\phi}{n_2}\right) \right\}^{-1} \right. \\ \left. \mp \left\{ \cos\left(\frac{\pi}{n_2}\right) - \cos\left(\frac{\beta_2}{n_2}\right) \right\} \right] \times \\ e^{j\pi/4 - jzk(a_2 \sin \phi - h \cos \phi) \cos \beta/2} \quad (\text{B-11})$$

$$\sqrt{\sigma_4} e^{j\beta_4} = \frac{\sin(\pi/n_2)}{n_2} \sqrt{\frac{a_2 \csc \phi}{k \cos \beta/2}} \left[ \left\{ \cos\left(\frac{\pi}{n_2}\right) - \cos\left(\frac{-\pi + 2\phi}{n_2}\right) \right\}^{-1} \right. \\ \left. \mp \left\{ \cos\left(\frac{\pi}{n_2}\right) - \cos\left(\frac{\beta_2}{n_2}\right) \right\} \right] \times \\ e^{-j\pi/4 + jzk(a_2 \sin \phi + h \cos \phi) \cos \beta/2} \quad (\text{B-12})$$

Applying small angle approximations (  $\cos \frac{2\phi}{n_2} \rightarrow 1$  ,  $\sin \frac{2\phi}{n_2} \rightarrow \frac{2\phi}{n_2}$  ) in the polarization-independent terms in Equation B-11 and B-12, we note the relations

$$\left\{ \cos\left(\frac{\pi}{n_2}\right) - \cos\left(\frac{3\pi - 2\phi}{n_2}\right) \right\}^{-1} \rightarrow \frac{1}{\frac{2\phi}{n_2} \sin \frac{\pi}{n_2}} \quad (\text{B-13})$$

$$\left\{ \cos\left(\frac{\pi}{n_2}\right) - \cos\left(\frac{-\pi + 2\phi}{n_2}\right) \right\}^{-1} \rightarrow -\frac{1}{\frac{2\phi}{n_2} \sin \frac{\pi}{n_2}} \quad (\text{B-14})$$

where Equations B-13 and B-14 correspond with similar results obtained for aspects near the nose-on value (see Equations B-8 and B-9). The polarization-independent terms in Equations B-11 and B-12 reduce to

$$\begin{aligned}
 (\sqrt{\sigma_a} e^{j\rho_a})_{\text{poli}} &= 2\sqrt{\pi} k a_z^2 \cos \beta/2 \frac{J_1(2ka_z \cos \beta/2 \sin \phi)}{(2ka_z \cos \beta/2 \sin \phi)} \times \\
 &\quad e^{-j\pi/2 + j2kh \cos \beta/2 \cos \phi} \quad (B-15)
 \end{aligned}$$

with Equation B-15 employed in the aspect region  $\pi - \phi_{ca} \leq \phi \leq \pi$  where  $2ka_z \sin \phi_{ca} = 2.44$ . Again we introduce the constraint  $\csc \phi \leq ka_z \cos \beta/2$  to remove all remaining singularities.

#### B.4 SCATTERING AT AND NEAR THE BROADSIDE ASPECT

At and near the broadside aspect ( $\phi = \pi/2 - \chi$ ), scattering centers  $S_1$  and  $S_2$  contribute to the specular return. All scattering center contributions are well behaved except the polarization-independent terms in expressions for  $\sqrt{\sigma_1} e^{j\rho_1}$  and  $\sqrt{\sigma_2} e^{j\rho_2}$ . From Equations B-6 and B-10 we have

$$\begin{aligned}
 (\sqrt{\sigma_1} e^{j\rho_1} + \sqrt{\sigma_2} e^{j\rho_2})_{\text{poli}} &= \sqrt{\frac{\csc \phi}{k \cos \beta/2}} e^{j\pi/4} \left[ \frac{\sin(\pi/n_1)}{n_1} \sqrt{a_1} \left\{ \cos\left(\frac{\pi}{n_1}\right) \right. \right. \\
 &\quad \left. \left. - \cos\left(\frac{\pi+2\phi}{n_1}\right) \right\}^{-1} e^{-j2k(a_1 \sin \phi + h \cos \phi) \cos \beta/2} \right. \\
 &\quad \left. + \frac{\sin(\pi/n_2)}{n_2} \sqrt{a_2} \left\{ \cos\left(\frac{\pi}{n_2}\right) - \cos\left(\frac{3\pi-2\phi}{n_2}\right) \right\}^{-1} \times \right. \\
 &\quad \left. e^{+j2k(a_1 \sin \phi - h \cos \phi) \cos \beta/2} \right] \quad (B-16)
 \end{aligned}$$

Introducing the relation  $\phi = \pi/2 - \alpha - \Delta$ , where  $\Delta$  is small, small angle approximations give

$$\left( \sqrt{a_1} e^{j\beta_1} + \sqrt{a_2} e^{j\beta_2} \right)_{\rho, \phi} = \frac{j k \Delta \cos \theta_2 \left[ (a_1 \cos \alpha + a_2 \sin \alpha) - \Delta \left( \frac{a_1 + a_2}{2} \right) \sin \alpha \right]}{2 \sqrt{k \cos(\alpha + \Delta)}} \times$$

$$\left\{ \frac{\sqrt{a_2} e^{j k \Delta \cos \theta_2 \left( \frac{a_2 - a_1}{\sin \alpha} \right)} - \sqrt{a_1} e^{-j k \Delta \cos \theta_2 \left( \frac{a_2 - a_1}{\sin \alpha} \right)}}{\Delta} \right\} \quad (\text{B-17})$$

Notice that singularities in Equation B-17 do not combine, since  $a_2 \neq a_1$ . Thus, the small angle approximation technique appears to fail when scattering centers have different dimensions.

We have noticed that Equation B-17 agrees with the corresponding physical optics result. (To see this expand the stationary phase expression given by Equation 4.3.9 of Reference 21, for aspects near broadside). This suggests that a smooth transition between geometrical diffraction theory and physical optics may be achieved in the angular region under investigation. Then physical optics may be employed to accurately predict the specular lobe.

A physical optics results may be obtained under the following assumption: areal elements of the frustum are considered to contribute specularly for  $\Delta$  small, and the phase between elements is taken into account.\* Then we have

$$\sigma_{po}(\phi = \pi/2 - \alpha - \Delta) = k (\sin \phi + \tan \alpha \cos \phi) \times |M|^2 \quad (\text{B-18})$$

\* This approximation procedure was suggested by M. E. Bechtel, and he obtained results given by Equations B-18 and B-19.

where

$$\begin{aligned}
 M = & \left\{ \frac{2}{3 \sin \chi} (a_2^{3/2} - a_1^{3/2}) \right. \\
 & - \frac{4k^2 \sin^2 \Delta}{\sin} \left[ \frac{a_2^{7/2} - a_1^{7/2}}{7} - \frac{2}{5} a_1 (a_2^{5/2} - a_1^{5/2}) + \frac{1}{3} a_1^2 (a_2^{3/2} - a_1^{3/2}) \right] \\
 & + \frac{4}{3} \frac{k^4 \sin^4 \Delta}{\sin^3 \chi} \left[ \frac{a_2^{11/2} - a_1^{11/2}}{11} - \frac{4}{9} a_1 (a_2^{9/2} - a_1^{9/2}) \right. \\
 & \left. \left. + \frac{6}{7} a_1^2 (a_2^{7/2} - a_1^{7/2}) - \frac{4}{5} a_1^3 (a_2^{5/2} - a_1^{5/2}) + \frac{a_1^4}{3} (a_2^{3/2} - a_1^{3/2}) \right] \right\} \quad (B-19) \\
 & + j \left\{ \frac{4k \sin \Delta}{\sin^2 \chi} \left[ \frac{a_2^{5/2} - a_1^{5/2}}{5} - \frac{a_1}{3} (a_2^{3/2} - a_1^{3/2}) \right] - \frac{8k^3 \sin^3 \Delta}{3 \sin^4 \chi} \times \right. \\
 & \left. \left[ \frac{a_2^{9/2} - a_1^{9/2}}{9} - \frac{3a_1}{7} (a_2^{7/2} - a_1^{7/2}) + \frac{3}{5} a_1^2 (a_2^{5/2} - a_1^{5/2}) - \frac{1}{3} a_1^3 (a_2^{3/2} - a_1^{3/2}) \right] \right\}
 \end{aligned}$$

It was found that the above approximation to the quantity  $M$  allowed a smooth transition between the physical optic and geometric diffraction theory results; i. e., less than 0.2 dB discontinuity in predicted values of radar cross section at the cross-over aspects. While Equation B-19 does not present computational problems, the physical optics result is too lengthy compared with simple formulations based upon geometrical diffraction theory.

It was decided to terminate the investigation of the broadside specular at this point, with the hope that the parent function associated with Equation B-17 may eventually be recognized. In the meanwhile, a curve-fitting routine has been incorporated in the computer program. Figure B-2 shows the behavior of unmodified geometrical diffraction theory in the vicinity of the broadside aspect. Because the theory fails gracefully at the broadside value ( $\phi = \pi/2 - \chi$ ), it is feasible to fit a smooth curve which bridges the valid geometrical-diffraction-theory estimates, and which passes through the specular value predicted by physical optics.

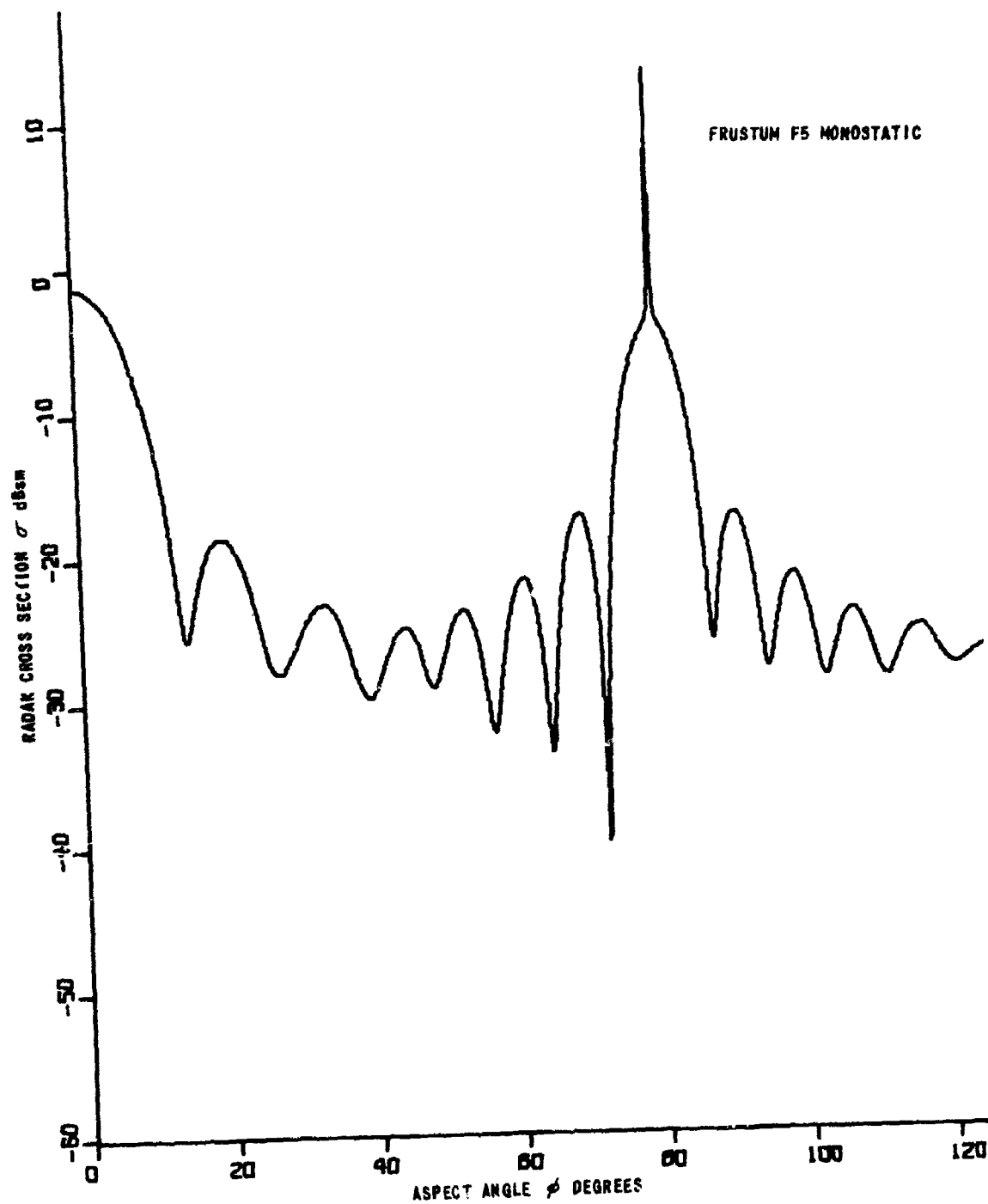


Figure B-2 BROADSIDE SPECULAR: UNMODIFIED GEOMETRICAL DIFFRACTION THEORY

A curve fitting technique, Subroutine SPLN46\* was incorporated into the computer programs for the frustum, frustum-cylinder, and the cylinder-flare. This subroutine utilizes as input the four values of computed cross section on either side of the specular point and the cross section at the specular point computed by use of the physical optics approximation. A parabolic curve is then fitted through these nine points with the specular aspect as the symmetry axis of the curve.

In actual operation, the printed output of the computer programs is that computed via unmodified theory. The curve obtained by use of SPLN46 is used to produce values for the plotting routine only.

\*SPLN46 is part of the computer library at CAL. A description of the routine is contained in CAL internal memo No. DDL-2AL, "Spline Interpolation" 17 July 1968, by D. D. Larson.

## Appendix C

### SCATTERING BY A CONE

In this appendix we present results of preliminary analyses of scattering by a finite, right-circular cone. We start with a review of Keller's<sup>14</sup> analysis of the two scattering centers located at the base of the cone. He presents formulas for radar cross section when the cone is viewed at the nose-on axial aspect, the tail-on axial aspect, and at aspects intermediate angles which exclude the broadside aspect. Both Keller<sup>15</sup> and Bechtel<sup>16</sup> have evaluated geometrical diffraction theory by comparing predictions with measurement data. In summary, the theory fails near axial aspects, and at and near the broadside aspect. Modifications to geometrical diffraction theory are sought in these three aspect regions.

First we modify the theory for application at and near tail-on aspect. Then we generate expressions which apply when incidence is at and near the axial aspect. Then an approximation for scattering by the cone tip is introduced as a preliminary step in the eventual generation of a specular lobe when incidence is broadside to the cone. Finally, results of short pulse measurements are discussed.

#### C.1. SUMMARY OF PREVIOUS ANALYSES

The utility of geometrical diffraction theory for predicting high-frequency scattering by a finite, right-circular cone has been examined by Keller<sup>14,15</sup> and by Bechtel.<sup>16</sup> Figure C-1 illustrates the backscattering problem; a pointed cone having base radius  $a$  and half angle  $\alpha$  is illuminated by an incident plane wave at an angle  $\phi$  to the axis of symmetry of the target. Keller noted that small wavelength scattering from the tip is negligible compared with contributions arising at the two scattering centers (labelled  $S_1$  and  $S_2$  in Figure C-1) located at the base of the cone. He obtained the following expressions for the fields singly-diffracted at these two centers.\*

---

\*Equations C-1 and C-2 agree with Keller's result (Equation 70 of Reference 14) if we allow for differences in notation, a correction of magnitude  $1/\sqrt{2}$  noted by Bechtel,<sup>16</sup> and the transition from the acoustical to the electromagnetic problem discussed in Appendix A.



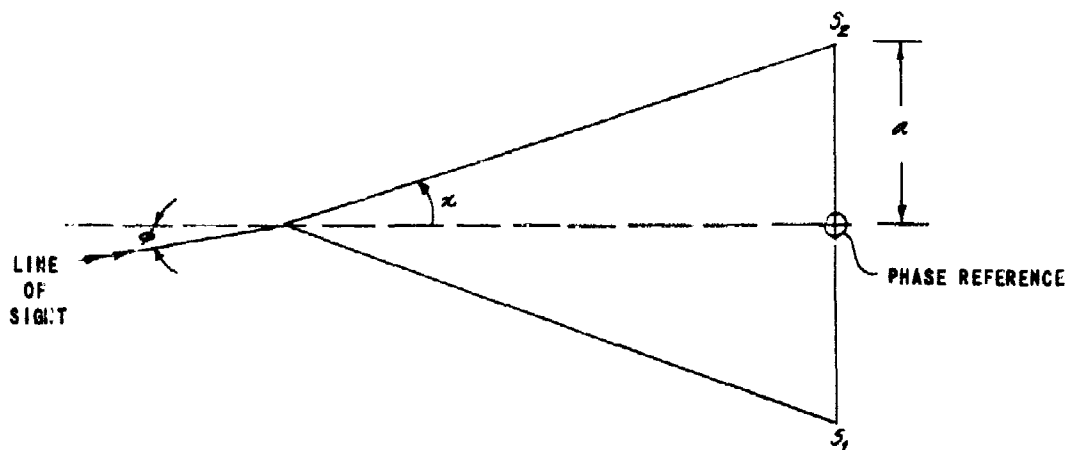


Figure C-1 LONGITUDINAL SECTION OF A POINTED,  
RIGHT-CIRCULAR CONE

$$\mu_{e_1} = \frac{\sin \frac{\pi}{n}}{2\pi r} \sqrt{\frac{a}{\pi k \sin \phi}} A e^{ikr} \left[ \cos \frac{\pi}{n} - \cos \frac{3\pi - 2\phi}{n} \right]^{-1}$$

$$\times \left[ \cos \frac{\pi}{n} - 1 \right]^{-1} e^{i(kr + \frac{\pi}{4} - 2ka \sin \phi)} \quad (C-1)$$

$$\mu_{e_2} = \frac{\sin \frac{\pi}{n}}{2\pi r} \sqrt{\frac{a}{\pi k \sin \phi}} A e^{jkr} \left[ \left\{ \cos \frac{\pi}{n} - \cos \frac{3\pi + 2\phi}{n} \right\}^{-1} \right. \\ \left. \mp \left\{ \cos \frac{\pi}{n} - 1 \right\}^{-1} \right] e^{j(kr - \frac{\pi}{4} + 2ka \sin \phi)}$$

$$0 \leq \phi \leq \pi$$

$$= 0; \pi < \phi < \frac{\pi}{2}$$

(C-2)

$$= \frac{\sin \frac{\pi}{n}}{2\pi r} \sqrt{\frac{a}{\pi k \sin \phi}} A e^{jkr} \left[ \left\{ \cos \frac{\pi}{n} - \cos \frac{\pi - 2\phi}{n} \right\}^{-1} \right. \\ \left. \mp \left\{ \cos \frac{\pi}{n} - 1 \right\}^{-1} \right] e^{j(kr - \frac{\pi}{4} + 2ka \sin \phi)}$$

$$\pi/2 \leq \phi \leq \pi$$

where

$\mu_{e_1}$  is the field singly diffracted at  $S_1$

$\mu_{e_2}$  is the field singly diffracted at  $S_2$

$A e^{jkr}$  represents the incident plane wave

$n = \frac{3}{2} + \frac{\pi}{\pi}$  where  $\pi$  is the half angle of the cone

$k = \frac{2\pi}{\lambda}$  the wave number

$r$  is the separation between the radar and the phase reference indicated in Figure C-1

and the choice of signs in Equations C-1 and C-2 relates to polarization dependence: use the upper signs for vertical polarization ( $E$  vectors associated with incident and scattered fields lie perpendicular to the plane containing Figure C-1); use the lower signs for horizontal polarization ( $E$  vectors lie in the plane of Figure C-1). The angular restriction on Equation C-2 is a consequence of the single-diffraction analysis; individual centers contribute to the total scattered field only when they are directly illuminated by the transmitter and observed by the receiver.

Notice that Equations C-1 and C-2 contain singularities in the divergence factor when incidence is axial ( $\phi = 0, \pi$ ). Keller removed these singularities by introducing a caustic correction factor. This multiplicative correction factor contains the reciprocal of these singularities and a Bessel function of zero order. By further invoking a theorem relating scalar solutions at the axial aspect to achieve suppression of the polarization-dependent contribution, he obtained the results (see Equations 22 and 23 of Reference 14).

$$\sigma(0) = \frac{4\pi a^2 \sin^2 \frac{\pi}{n}}{\pi^2} (\cos \frac{\pi}{n} - \cos \frac{3\pi}{n})^2 \quad (C-3)$$

$$\sigma(\pi) = \pi k^2 a^4 \quad (C-4)$$

Also, if the cone is viewed along a radar line of sight normal to the generator of the cone, i.e., if  $\phi = \frac{\pi}{2} - \alpha$ , then the geometrical-diffraction-theory Equation B-1 fails and another method must be used. In this case, a convenient, and quite accurate, formula can be obtained by means of an asymptotic expansion of the conventional physical optics expression; this formula, valid only when  $\phi = \frac{\pi}{2} - \alpha$ , is

$$\sigma(\frac{\pi}{2} - \alpha) = \frac{8}{9} \pi \frac{a^3}{\lambda} \left[ \sin^2 \alpha \cos \alpha \right]^{-1} \quad (C-5)$$

Equation C-5 above is Equation 3 of Reference 16.

When incidence is axial ( $\phi = 0$ ), Keller and Bechtel have shown that radar cross section predictions based upon Equation C-3 are accurate for cones having large  $ka$ . For the broadside case ( $\phi = \frac{\pi}{2} - \alpha$ ), Equation C-5 gives a good estimate of the specular peak since it is based upon physical optics. For axial illumination of the base ( $\phi = \pi$ ), Equation C-4 is valid and agrees with the corresponding physical optics result. Bechtel has evaluated the ability of geometrical diffraction theory (Equations B-1 and B-2) in predicting the principal polarization radar cross sections of cones at intermediate aspect angles. Based upon gross comparison of theory with

available measurement data,\* he reported good agreement for large cones ( $ka \geq 8$ ) except where the target is observed within about 30 degrees of nose-on with vertical polarization. In this aspect region he noted that large errors occur for some as yet unknown reason. For smaller cones ( $ka$  around 3), the computed radar cross section is generally predicted within 5 dB, but the form of the pattern is not predicted very accurately.

In the following subsections we present results of analyses directed toward extension of theoretical capability in the angular regions near specular aspects.

## C.2 SCATTERING AT AND NEAR AXIAL ASPECTS

Direct extension of Keller's approach (i.e., the caustic correction factor) for near-axial aspects does not appear to be straightforward; the scalar theorem mentioned above is limited to interpretation at axial aspects only. In this subsection we show that the small angle approximation technique introduced in Appendix A is applicable. Although the method is easy to apply, the treatment of near nose-on aspects involves certain heuristic arguments which may be objectionable. For this reason, a more satisfying approach based upon a geometrical-diffraction-theory interpretation of the Green's function is applied in this aspect region to obtain the same result.

### C.2.1 At and Near Tail-On Aspects

At and near tail-on aspects we apply the small angle approximation technique in the same fashion detailed in subsection A.5.3 of Appendix A: Only the critical steps are presented below. Modification of geometrical-diffraction theory is begun by treating the polarization-independent terms in Equations C-1 and C-2. Introducing the angular convention  $\phi = \pi - \Delta$ , where  $\Delta$  is small, and allowing  $\cos \frac{2\Delta}{n} \rightarrow 1$ ,  $\sin \frac{2\Delta}{n} \rightarrow \frac{2\Delta}{n}$ , we have

---

\* These measurement data were reported by Keys and Primich and had a stated accuracy of  $\pm 2$  dB.

$$\left\{ \cos \frac{\pi}{n} - \cos \frac{3\pi - 2\phi}{n} \right\}^{-1} \longrightarrow - \frac{1}{\frac{2\Delta}{n} \sin \frac{\pi}{n}} \quad (C-6)$$

$$\left\{ \cos \frac{\pi}{n} - \cos \frac{\pi - 2\phi}{n} \right\}^{-1} \longrightarrow + \frac{1}{\frac{2\Delta}{n} \sin \frac{\pi}{n}} \quad (C-7)$$

Employing the large argument approximation for the first order Bessel function, and expressing the polarization-independent contribution from centers  $S_1$  and  $S_2$  as radar cross section, we have

$$(\sqrt{\sigma_R} e^{j\rho_R})_{poli} = 2\sqrt{\pi} k a^2 \frac{J_1(2ka\Delta)}{(2ka\Delta)} e^{-j\pi/2} \quad (C-8)$$

Comparing the specular contribution from the base of the cone with that from the end of the cylinder (Equation A-54), we see complete agreement. This is due to the absence of dependence of specular scattering upon the wedge angle. The polarization-dependent terms in Equations C-1 and C-2 retain dependence upon the wedge parameter  $n$ . They are made well behaved by invoking the constraint introduced as Equation A-57 of Appendix A.

## C.2.2 At and Near Nose-On Aspects

### C.2.2.1 Small Angle Approximation

We now consider the return from the base of the cone in the limited aspect interval where centers  $S_1$  and  $S_2$  contribute, i.e.,  $0 \leq \phi \leq \kappa$ . For narrow-angle cones,  $\kappa$  is small (say less than 15 degrees) so that the aspect angle  $\phi$  is small in the region of investigation. Let us examine the polarization-independent terms in Equations C-1 and C-2 when  $\phi \approx 0$ . Allowing  $\cos \frac{2\phi}{n} \rightarrow 1$ ,  $\sin \frac{2\phi}{n} \rightarrow \frac{2\phi}{n}$ . The following relations obtain

$$\left\{ \cos \frac{\pi}{n} - \cos \frac{3\pi - 2\phi}{n} \right\}^{-1} \longrightarrow \left\{ \cos \frac{\pi}{n} - \cos \frac{3\pi}{n} \right\}^{-1} \left( 1 + \frac{\frac{2\phi}{n} \sin \frac{3\pi}{n}}{\cos \frac{\pi}{n} - \cos \frac{3\pi}{n}} \right) \quad (C-9)$$

$$\left\{ \cos \frac{\pi}{n} - \cos \frac{3\pi + 2\phi}{n} \right\}^{-1} \rightarrow \left\{ \cos \frac{\pi}{n} - \cos \frac{3\pi}{n} \right\}^{-1} \left( 1 - \frac{\frac{2\phi}{n} \sin \frac{3\pi}{n}}{\cos \frac{\pi}{n} - \cos \frac{3\pi}{n}} \right) \quad (C-10)$$

Substituting approximations C-9 and C-10 into Equations C-1 and C-2, respectively, and rearranging, the combined result is

$$\begin{aligned} \mu_{\theta_1} + \mu_{\theta_2} = & \frac{\sin \frac{\pi}{n} a}{\pi r} A e^{i2kr} \left[ \left\{ \cos \frac{\pi}{n} - \cos \frac{3\pi}{n} \right\}^{-1} C_1 \right. \\ & \left. - i \frac{\frac{2\phi}{n} \sin \frac{3\pi}{n}}{\left( \cos \frac{\pi}{n} - \cos \frac{3\pi}{n} \right)^2} C_2 + \left\{ \cos \frac{\pi}{n} - 1 \right\}^{-1} C_3 \right] \end{aligned} \quad (C-11)$$

where

$$\begin{aligned} C_1 = & \sqrt{\frac{2}{2\pi ka \sin \phi}} \left[ \frac{e^{i(2ka \sin \phi - \pi/4)} + e^{-i(2ka \sin \phi - \pi/4)}}{2} \right] \\ = & C_3 \end{aligned} \quad (C-12)$$

$$C_2 = \sqrt{\frac{2}{2\pi ka \sin \phi}} \left[ \frac{e^{i(2ka \sin \phi - \pi/4)} - e^{-i(2ka \sin \phi - \pi/4)}}{2i} \right] \quad (C-13)$$

But  $C_1$  can be recognized as the large argument expansion of the Bessel functions  $J_{2n}(2ka \sin \phi)$ , where  $n = 0, 1, 2, \dots$ . Similarly  $C_2$  is the large argument expansion of  $J_{1+2n}(2ka \sin \phi)$  if we neglect signs. Consider first the polarization-independent terms in Equation C-11. We expect a large return from the ring discontinuity for axial incidence ( $\phi = 0$ ). Since this cannot arise due to the factor associated with  $C_2$ , we assign  $C_1 = J_0(2ka \sin \phi)$ . We arbitrarily choose  $C_2$  to have the lowest allowable order indicated above, i.e.,  $C_2 = J_1(2ka \sin \phi)$ . Finally, we examine the polarization-dependent terms in Equation C-11. In the light of known scattering behavior, we know that this term must vanish at axial incidence and we assign  $C_3 = J_2(2ka \sin \phi)$ .

Then Equation C-11 becomes

$$\begin{aligned} \mu_{e_1} + \mu_{e_2} = & \frac{\sin \frac{\pi}{n}}{\pi r} a A e^{i2kr} \left[ \left\{ \cos \frac{\pi}{n} - \cos \frac{3\pi}{n} \right\}^{-1} J_0(2ka \sin \phi) \right. \\ & \left. - i \frac{\frac{2\phi}{n} \sin \frac{3\pi}{n}}{\left( \cos \frac{\pi}{n} - \cos \frac{3\pi}{n} \right)^2} J_1(2ka \sin \phi) \pm \left\{ \cos \frac{\pi}{n} - 1 \right\}^{-1} J_2(2ka \sin \phi) \right] \end{aligned} \quad (C-14)$$

From Equation C-14 the backscattering radar cross section  $\sigma(\phi)$  is given by

$$\begin{aligned} \sigma(\phi) = & 4\pi r^2 \left| \frac{\mu_{e_1} + \mu_{e_2}}{A} \right|^2 \\ = & \frac{4\pi a^2 \sin \frac{2\pi}{n}}{n^2} \left| \left\{ \cos \frac{\pi}{n} - \cos \frac{3\pi}{n} \right\}^{-1} J_0(2ka \sin \phi) \right. \\ & \left. - i \frac{\frac{2\phi}{n} \sin \frac{3\pi}{n}}{\left( \cos \frac{\pi}{n} - \cos \frac{3\pi}{n} \right)^2} J_1(2ka \sin \phi) \pm \left\{ \cos \frac{\pi}{n} - 1 \right\}^{-1} J_2(2ka \sin \phi) \right|^2 \end{aligned} \quad (C-15)$$

where it is understood that Equation C-15 applies in the limited aspect interval  $0 \leq \phi \leq \pi$ . At the axial aspect ( $\phi = 0$ ) agrees with Keller's result (see Equation C-3). Because the small angle method involves certain arbitrary choices in the assigning of Bessel functions, we now rederive Equation C-15 using a more rigorous technique.

#### C.2.2.2 Green's Function Approach

Let us reconsider the problem of diffraction at the base of a flat-backed cone in the aspect region  $0 \leq \phi \leq \pi$ . For the aspect interval chosen for study, the entire ring discontinuity at the cone base is directly illuminated. Indeed, at the axial aspect ( $\phi = 0$ ), each point on the ring contributes to the backscattered field. It is only as aspect angle increases that this uniform distribution of scattering tends towards localization at the two scattering centers  $S_1$  and  $S_2$  depicted in Figure C-1. One can express

the same idea by introducing Green's theorem to represent the field scattered by the ring discontinuity in the integral form<sup>12,21</sup>

$$u^s = \frac{1}{\lambda r} \int u_i e^{ik\rho} f(\phi, \theta') dA \quad (C-16)$$

where  $u^s$  is the scattered field in the three-dimensional problem,  $u_i$  is the incident plane wave,  $\rho$  is the distance along the propagation direction,  $A$  is the area of projection of the part of the ring to one side of a plane of constant phase, and  $f(\phi, \theta')$  is a function which represents the scattering properties of the edge. Since Equation C-16 is the general description of the scattering phenomenon, it is clear that scattering center formulations (such as Equations C-1 and C-2) arise from stationary phase evaluation of the integral under the assumption  $2ka \sin \phi \gg 1$ . Our present problem concerns evaluation of the same integral under the small angle assumption  $\phi \approx 0$ . Either evaluation of Equation C-16 requires knowledge of the function  $f(\phi, \theta')$ . The Green's function approach becomes practical when it is shown that geometrical diffraction theory can be used to estimate the unknown function, i. e.,

$$f(\phi, \theta') = e^{-i\frac{\pi}{4}} \sqrt{\lambda} D(\phi, \theta') \quad (C-17)$$

where  $D(\phi, \theta')$  is the general form of the diffraction coefficient used in three-dimensional problems. The coefficient  $D(\phi, \theta')$  is derived as a function of aspect angle  $\phi$  and position on the rotationally symmetric edge in Appendix D. The result is substituted into Equation C-17 to obtain

$$f(\phi, \theta') = \frac{\sin \frac{\pi}{4}}{nk} \frac{1}{\sqrt{1 - \sin^2 \phi \sin^2 \theta}} \left[ \left\{ \cos \frac{\pi}{n} - \cos \frac{3\pi - 2 \tan^{-1} [\cos \theta \tan \phi]}{n} \right\}^{-1} \right. \\ \left. \mp \left\{ \cos \frac{\pi}{n} - 1 \right\}^{-1} \cos 2\theta \right] \quad (C-18)$$



The remaining parameters in the Green's integral are evaluated below

$$\begin{aligned} u_i &= A e^{ik\rho} \\ \rho &= r - ka \sin \phi \cos(\theta) \\ dA &= a d\theta \end{aligned} \quad (C-19)$$

Substituting Equations C-18 and C-19 into Equation C-16, we have

$$\begin{aligned} u^s &= \frac{a A e^{i2kr}}{2\pi r} \frac{\sin \frac{\pi}{n}}{n} \int_{\theta=0}^{\theta=2\pi-\theta} \frac{1}{\sqrt{1 - \sin^2 \phi \sin^2(\theta - \theta')}} \times \\ &\quad \left[ \cos \frac{\pi}{n} - \cos \frac{3\pi - 2 \tan^{-1} [\cos(\theta - \theta') \tan \phi]}{n} \right]^{-1} \\ &\quad \left[ \cos \frac{\pi}{n} - 1 \right]^{-1} \cos 2(\theta - \theta') \left[ e^{-i2ka \sin \phi \cos(\theta - \theta')} d\theta' \right] \end{aligned} \quad (C-20)$$

If one evaluates Equation C-20 by stationary phase, the scattering center contributions given by Equations C-1 and C-2 are obtained. This serves as a check on our result above. We now wish to derive an approximate representation for  $u^s$  assuming  $\phi \approx 0$ . Allowing  $\sqrt{1 - \sin^2 \phi \sin^2(\theta - \theta')} \rightarrow 1$  we write Equation C-20 in the form

$$u^s = \frac{a A e^{i2kr}}{\pi r} \frac{\sin \frac{\pi}{n}}{n} [I_1 + I_2] \quad (C-21)$$

where

$$\begin{aligned} I_1 &= \int_{\theta=0}^{\theta=2\pi-\theta} \left[ \cos \frac{\pi}{n} - \cos \frac{3\pi - 2 \tan^{-1} [\cos(\theta - \theta') \tan \phi]}{n} \right]^{-1} \times \\ &\quad e^{-i2ka \sin \phi \cos(\theta - \theta')} d\theta' \end{aligned} \quad (C-22)$$

$$I_2 = \left\{ \cos \frac{\pi}{n} - 1 \right\}^{-1} \int_{\theta=0}^{\theta=\pi-\theta} \cos 2(\theta-\theta') e^{-i2ka \sin \phi \cos(\theta-\theta')} d\theta' \quad (C-23)$$

Evaluation of the integral  $I_2$  is straightforward and gives the result

$$I_2 = -\pi \left\{ \cos \frac{\pi}{n} - 1 \right\}^{-1} J_2(2ka \sin \phi) \quad (C-24)$$

The integral  $I_1$  is evaluated following expansion of the integrand for  $\phi$  small, i. e.,

$$\cos \frac{3\pi - 2 \tan^{-1} [\cos(\theta-\theta') \tan \phi]}{n} \rightarrow \cos \frac{3\pi}{n} - \frac{2}{n} \cos(\theta-\theta') \tan \phi \sin \frac{3\pi}{n} \quad (C-25)$$

so that

$$\begin{aligned} \left\{ \cos \frac{\pi}{n} - \cos \frac{3\pi - 2 \tan^{-1} [\cos(\theta-\theta') \tan \phi]}{n} \right\}^{-1} &\rightarrow \left\{ \cos \frac{\pi}{n} - \cos \frac{3\pi}{n} \right\}^{-1} \times \\ \left\{ 1 - \frac{\frac{2}{n} \sin \frac{3\pi}{n} \cos(\theta-\theta') \tan \phi}{\left( \cos \frac{\pi}{n} - \cos \frac{3\pi}{n} \right)} \right\}^{-1} &\approx \left\{ \cos \frac{\pi}{n} - \cos \frac{3\pi}{n} \right\}^{-1} \times \\ \left[ 1 + \frac{\frac{2}{n} \sin \frac{3\pi}{n} \cos(\theta-\theta') \tan \phi}{\left( \cos \frac{\pi}{n} - \cos \frac{3\pi}{n} \right)} \right] & \end{aligned} \quad (C-26)$$

Substituting Equation C-26 into Equation C-22, we express  $I_1$  as

$$\begin{aligned} I_1 &= \left\{ \cos \frac{\pi}{n} - \cos \frac{3\pi}{n} \right\}^{-1} \int_{\theta=0}^{\theta=\pi-\theta} e^{-i2ka \sin \phi \cos(\theta-\theta')} d\theta' \\ &+ \frac{\frac{2}{n} \sin \frac{3\pi}{n} \tan \phi}{\left( \cos \frac{\pi}{n} - \cos \frac{3\pi}{n} \right)^2} \int_{\theta=0}^{\theta=\pi-\theta} \cos(\theta-\theta') e^{-i2ka \sin \phi \cos(\theta-\theta')} d\theta' \end{aligned} \quad (C-27)$$

The first integral on the right hand side of Equation C-27 gives

$$\pi \left\{ \cos \frac{\pi}{n} - \cos \frac{3\pi}{n} \right\}^{-1} J_0(2ka \sin \phi) \quad (C-28)$$

The second integral gives

$$-i \frac{\frac{2\pi}{n} \sin \frac{3\pi}{n} \tan \phi}{\left(\cos \frac{\pi}{n} - \cos \frac{3\pi}{n}\right)^2} J_1(2ka \sin \phi) \quad (C-29)$$

The derivation of the Green's integral result is completed when we collect Equations C-24, C-28, and C-29 and substitute into Equation C-21.

$$\begin{aligned} u^s = & \frac{a A e^{i k r}}{r} \frac{\sin \frac{\pi}{n}}{n} \left[ \left\{ \cos \frac{\pi}{n} - \cos \frac{3\pi}{n} \right\}^{-1} J_0(2ka \sin \phi) \right. \\ & - i \frac{\frac{2\pi}{n} \sin \frac{3\pi}{n} \tan \phi}{\left(\cos \frac{\pi}{n} - \cos \frac{3\pi}{n}\right)^2} J_1(2ka \sin \phi) \\ & \left. \pm \left\{ \cos \frac{\pi}{n} - 1 \right\}^{-1} J_2(2ka \sin \phi) \right] \end{aligned} \quad (C-30)$$

Again the expression for radar cross section is  $\sigma(\phi) = 4\pi r^2 \left| \frac{u}{A} \right|^2$  so that

$$\begin{aligned} \sigma(\phi) = & \frac{4\pi a^2 \sin^2 \frac{\pi}{n}}{n^2} \left| \left\{ \cos \frac{\pi}{n} - \cos \frac{3\pi}{n} \right\}^{-1} J_0(2ka \sin \phi) \right. \\ & - i \frac{\frac{2\pi}{n} \sin \frac{3\pi}{n} \tan \phi}{\left(\cos \frac{\pi}{n} - \cos \frac{3\pi}{n}\right)^2} J_1(2ka \sin \phi) \pm \left\{ \cos \frac{\pi}{n} - 1 \right\}^{-1} J_2(2ka \sin \phi) \left. \right|^2 \end{aligned} \quad (C-31)$$

In summary, Equation C-31 is the result of evaluation of the Green's integral for scattering from the ring discontinuity at the base of a cone. It is valid for  $\phi$  at and near the axial aspect. The result agrees with that obtained using the small angle approximation method on scattering center contributions (compare Equations C-15 and C-31).

Predictions based upon the ring formulation have been compared with measurement data taken on a pointed cone. Principal polarization radar cross sections were obtained at 6.00 GHz for a cone with base radius 3.16 inches and height 11.783 inches (which results in a cone half angle  $\alpha \approx 15$  degrees). Figure C-2 and C-3 compare theory and measurement

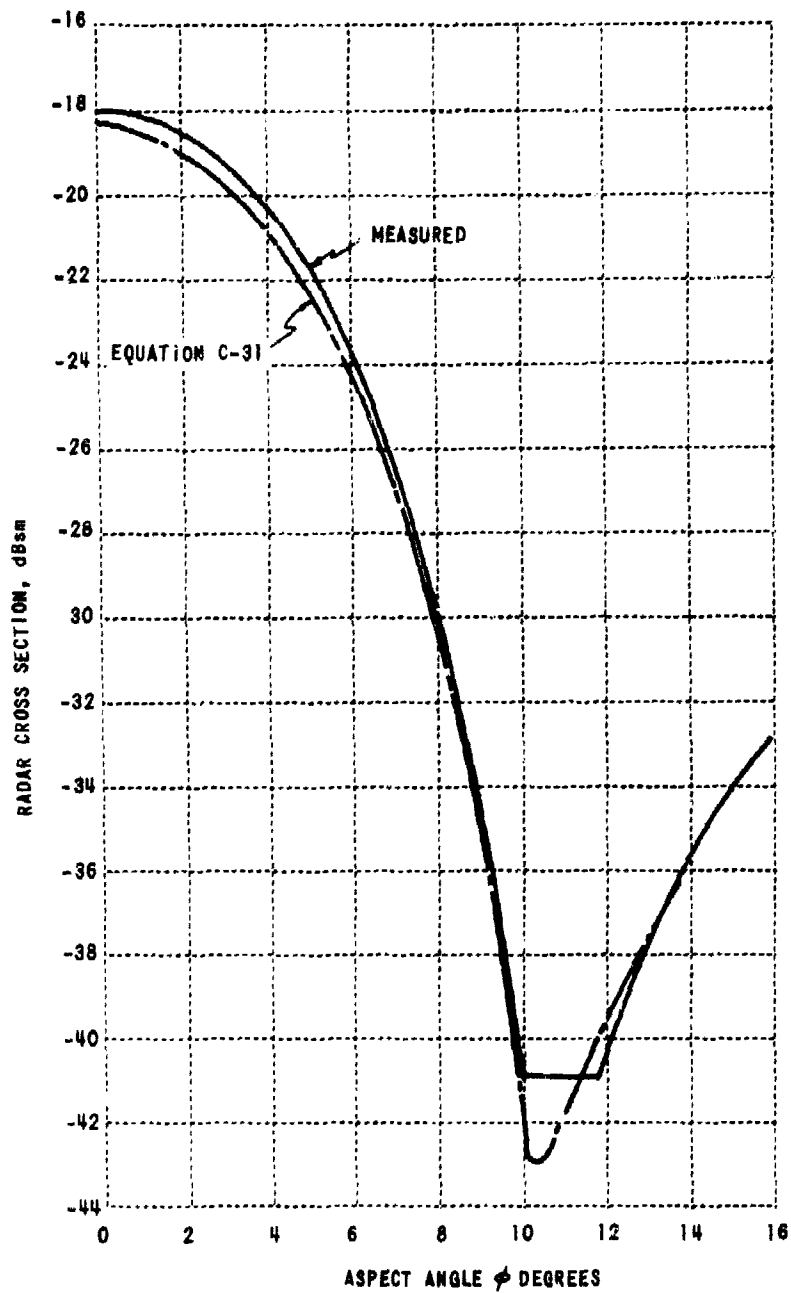


Figure C-2 RADAR CROSS SECTION OF POINTED CONE,  
VERTICAL POLARIZATION

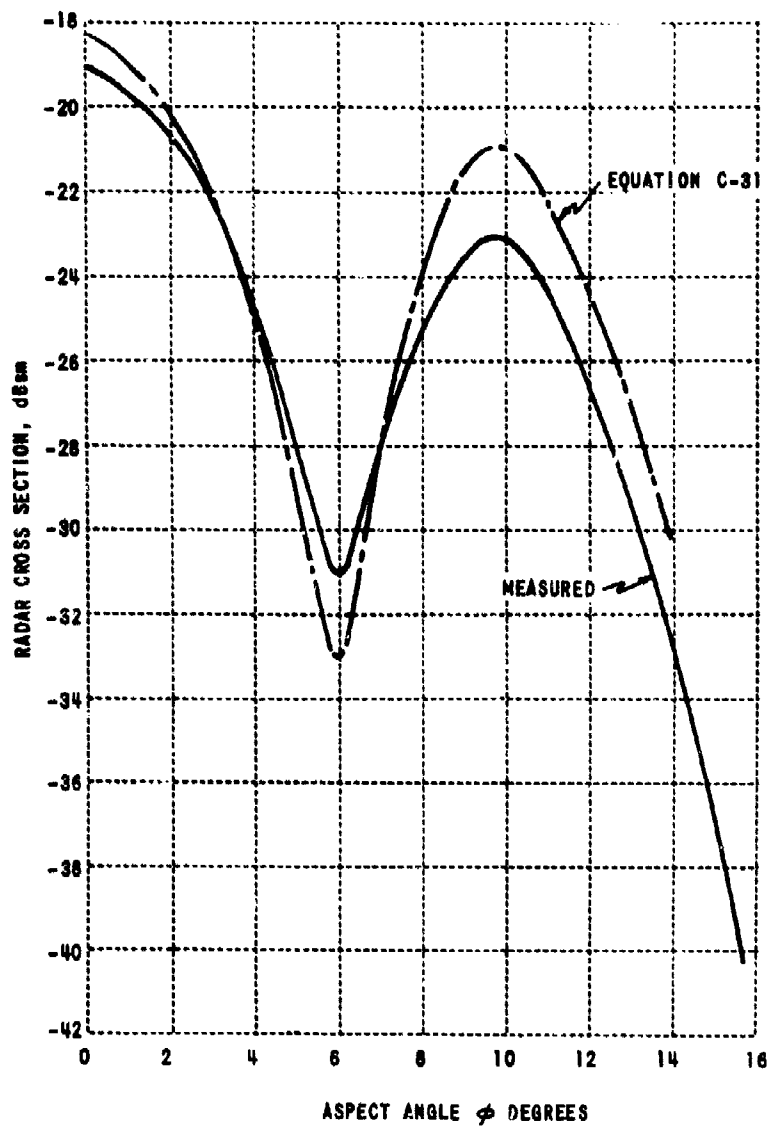


Figure C-3 RADAR CROSS SECTION OF POINTED CONE,  
HORIZONTAL POLARIZATION

in the limited aspect interval  $0 \leq \phi \leq \chi$ . It is seen that agreement between amplitudes is good, and that the measured polarization dependence is accurately predicted by modified geometrical diffraction theory.

### C.3 SCATTERING AT AND NEAR THE BROADSIDE ASPECT

When incidence is at and near the broadside aspect ( $\phi = \pi/2 - \chi$ ), the total return from the cone arises at scattering center  $S$ , according to our model (see Figure C-1). Thus, the predicted radar cross section is cusp-like due to the lone singularity contained in the diffraction coefficient of Equation C-1. What we now seek is a method of producing a specular lobe instead of the cusp. We wish to accomplish this within the context of geometrical diffraction theory; i.e., retaining Equation C-1 in the modified formulation. One possibility is to assign a contribution to the cone-tip. While the aspect-dependent diffraction coefficient for a tip is presently unknown, certain desired characteristics of the assigned contribution are evident. First, the contribution should agree with the physical optics solution for scattering at axial incidence on a semi-infinite cone, which is exact. Second, the contribution should have aspect dependence such that a singularity arises at the broadside aspect. Then there exists a possibility of generating a specular lobe which fails gracefully as in the case of broadside incidence on a frustum. If this behavior is realized, a curve can be fit through the invalid portion of the aspect registry as before.

One way of assigning a contribution to the scattering center formed by the tip of a cone is to consider the related two-dimensional wedge. The desired aspect dependence is contained in the resulting three-dimensional solution

$$\sqrt{\sigma_0} e^{j\beta_0} = \frac{\sin \pi/n_0}{4k\sqrt{2\pi} n_0} \left\{ \cos \frac{\pi}{n_0} - \cos \frac{2(\pi - \chi - \phi)}{n_0} \right\}^{-1} \quad (C-32)$$

where  $\sqrt{\sigma_0} e^{j\rho_0}$  represents an approximation to the contribution from scattering center  $S_0$  formed by the cone tip, and  $\pi_0 = 2 - 2z/r$ . Deletion of polarization-dependent terms is in keeping with the generality of the present discussion. From Equations C-1 and C-32, we have, for aspects near broadside

$$\sigma(\phi \approx \pi/2 - \alpha) = \left| \sqrt{\sigma_0} e^{j\rho_0} + \sqrt{\sigma_1} e^{j\rho_1} \right|^2$$

#### C.4 DIAGNOSTIC MEASUREMENTS TAKEN ON A CONE

Preliminary analyses of scattering by a cone were performed in the aspect interval  $\alpha \leq \phi \leq \pi/2$ . In this aspect region poor correspondence is obtained between predicted and measured values of radar cross section: for vertical polarization, the theoretical estimate is uniformly low; for horizontal polarization it is uniformly high. It was recognized at the outset that cone theory would require upgrading in this aspect region, and a diagnostic program involving short pulse measurements was initiated. In this subsection we discuss results based upon reduction of these short pulse data.

##### C.4.1 Scope of Experiment

Figure C-4 depicts the sphere-tipped cone employed in the diagnostic investigation of scattering by a finite cone. The aspects and polarization at which C-band (5.9 GHz) short pulse data were obtained are contained in Table C-1; these data include all aspect angle ranges where GD/FW personnel observed a secondary scattering phenomenon. Notice that Table C-1 presents two independent sets of data according to attenuation: The -20 dB attenuation data are useful for gross reduction of data; the 0 dB attenuation data provide detailed information concerning secondary scattering phenomena.

In a short pulse investigation, the experimental observables are the radar cross section  $\sigma_i$  and phase  $\rho_i$  associated with each scattering center on the target. Whereas a direct measure of  $\sigma_i$  is obtained, the estimate

Table C-1 C-band Short Pulse Data

|               | 0dB<br>Attenuation |       | -20 dB<br>Attenuation |       |
|---------------|--------------------|-------|-----------------------|-------|
|               | H                  | V     | H                     | V     |
| AZIMUTH ANGLE | 359.2              | 359.4 | 359.4                 | 359.0 |
|               | 0.2                | 0.4   | 0.4                   | 360.0 |
|               | 1.2                | 1.4   | 1.4                   | 1.1   |
|               | 2.3                | 2.5   | 2.4                   | 2.2   |
|               | 3.3                | 3.5   | 3.3                   | 3.3   |
|               | 4.4                | 4.5   | 4.4                   | 4.4   |
|               | 36.2               | 36.5  | 36.8                  | 36.7  |
|               | 37.2               | 37.5  | 37.8                  | 37.7  |
|               | 37.9               | 38.6  | 38.8                  | 38.8  |
|               | 38.9               | 39.6  | 39.8                  | 39.9  |
|               | 39.9               | 40.7  | 40.7                  | 40.9  |
|               | 40.9               | 41.7  | 41.7                  | 41.9  |
|               |                    | 42.8  | 46.6                  | 47.3  |
|               |                    | 43.8  | 47.6                  | 48.3  |
|               | 49.1               | 50.1  | 48.6                  | 49.5  |
|               | 50.1               | 51.1  | 49.6                  | 50.6  |
|               | 51.2               | 52.2  | 50.6                  | 51.7  |
|               | 52.2               | 53.3  | 51.5                  | 52.7  |
|               | 53.2               | 54.3  | 52.5                  | 53.8  |
|               | 54.3               | 55.4  | 53.5                  | 54.9  |
|               |                    |       | 54.5                  |       |
|               |                    |       | 55.5                  |       |
|               | 55.3               | 56.4  | 56.3                  | 56.0  |
|               | 56.3               | 57.5  | 57.4                  | 57.1  |
|               | 57.4               |       | 179.0                 | 179.5 |
|               | 58.4               |       | 180.0                 | 180.6 |
|               |                    |       | 181.8                 | 181.7 |
|               |                    |       | 182.8                 | 182.8 |
|               |                    |       | 188.6                 | 188.0 |
|               |                    |       | 189.4                 | 189.1 |



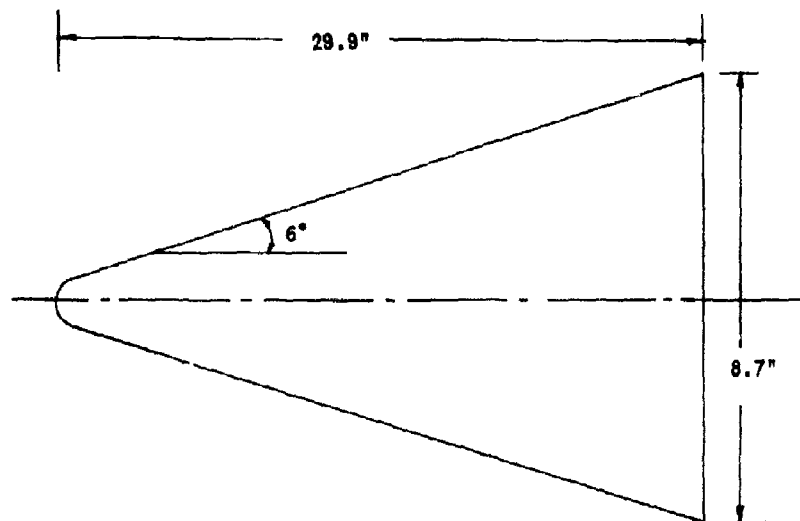


Figure C-4 SHORT PULSE TARGET

of  $\rho_i$  is contained in the time history of the short pulse return. It is common to reduce the short pulse return to obtain the radial depth of each center. Figure C-5 shows the location of the three known scattering centers on a sphere-tipped cone. Scattering center  $S_0$  gives rise to the specular return from the spherical segment of the target, and centers  $S_1$  and  $S_2$  are the usual contributions associated with the return from the base of a flat-backed cone. Consider the form of the short pulse response from this target when contributions from centers  $S_0$ ,  $S_1$  and  $S_2$  are dominant and resolvable. The time history begins with a return of magnitude  $\sigma_0$  arising from the sphere tip. At a time  $t_1$  seconds later, a return of magnitude  $\sigma_1$  is observed, where  $t_1 = \frac{1}{c} \times 2kR_{01}$ ,  $c$  is the velocity of light and  $R_{01}$  is the radial depth between  $S_0$  and  $S_1$  (see Figure C-5). Finally, a third contribution having magnitude  $\sigma_2$  will be seen a time  $t_2$  after the time history begins, where  $t_2 = \frac{1}{c} \times 2kR_{02}$ . If any additional contributions are apparent in the time history, we associate them with scattering phenomena which are neglected in the present description.

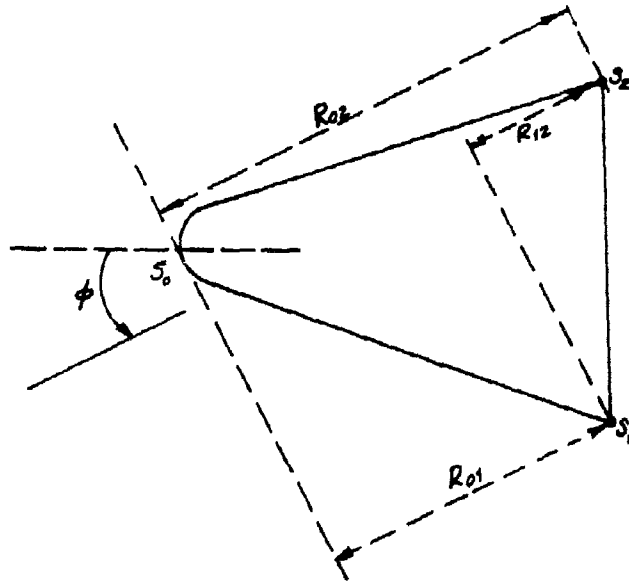


Figure C-5 SPHERE-TIPPED CONE USED FOR SHORT PULSE MEASUREMENTS

The aspect region of interest in this study involves use of data measured in the interval  $37.2 \leq \phi \leq 58.4$  degrees. The single diffraction model predicts strong returns from centers  $S_0$  and  $S_1$ , with no contribution from center  $S_2$  due to shadowing. Processing of the largest return in the -20 dB attenuation data measured with horizontal polarization provided experimental results for center  $S_1$ . Figure C-6a compares theory and measurement for the radial depth  $2R_{01}$ ; good agreement is observed over a wide region of aspects. Figure C-6b shows that theoretical and experimental radar cross sections of center  $S_1$  correspond to within 3 dB. The agreement observed in Figure C-6a and C-6b confirmed the validity of measurement data, and a search of corresponding 0 dB attenuation data for new scattering phenomena was initiated. While new and significant contributions were observed at isolated aspects, these effects persisted over extremely short aspect intervals (several degrees). In summary, the search for secondary scattering phenomena was unsuccessful; no systematic return was observed in the short pulse data. The single well-defined return was again associated with center  $S_1$ . Figure C-6c shows the resultant

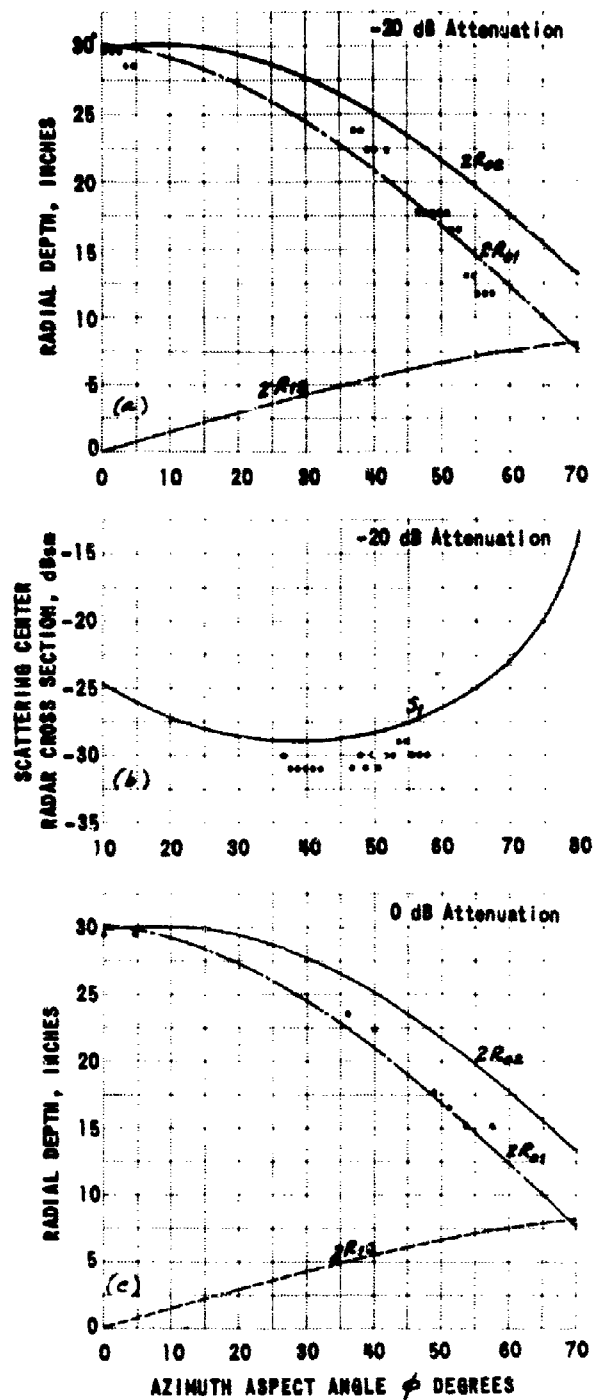


Figure C-6 LOCATION AND MAGNITUDE OF MAJOR SCATTERING CENTER ON CONE  
 . . . . SHORT PULSE DATA      ——— GEOMETRICAL DIFFRACTION THEORY

estimates of radial depth  $2R_o$  ; related values of measured cross section were unavailable due to saturation of the return from  $S$ , when no attenuation is employed.

## Appendix D

### GENERAL EDGE DIFFRACTION COEFFICIENT

Here we derive the general form for the edge diffraction coefficient  $D(\phi, \theta)$  to be used in a Green's function evaluation of the field scattered at the ring discontinuity formed by the base of a flat-backed cone. First we introduce the expression for the diffraction coefficient given by Keller. Then the base of the cone is considered to consist locally of infinite wedges and we obtain  $D(\phi, \theta)$  as a function of position on the cone base. Finally, the polarization reference is translated from the source to the edge to obtain the general expression for  $D(\phi, \theta)$ .

#### D.1 DIFFRACTION COEFFICIENT FOR TWO-DIMENSIONAL WEDGE

To determine the diffraction coefficient for an edge, the expression for  $D$  applied to a two-dimensional (infinite) wedge is taken from Equation A-4 of Appendix A.

$$D = \frac{e^{i\frac{\pi}{4}} \sin \frac{\pi}{4}}{n \sin \beta_k \sqrt{2\pi k}} \left[ \left\{ \cos \frac{\pi}{n} - \cos \frac{\theta_k - \alpha_k}{n} \right\}^{-1} \mp \left\{ \cos \frac{\pi}{n} - \cos \frac{\pi + \theta_k + \alpha_k}{n} \right\}^{-1} \right] \quad (D-1)$$

where

$\alpha_k$  is the angle of incidence

$\theta_k$  is the angle of diffraction

$n = \gamma_k / \pi$  ( $\gamma_k$  being the exterior wedge angle)

$\beta_k$  is the angle between the incident ray and the positive tangent to the wedge

$k$  is  $\frac{2\pi}{\lambda}$  where  $\lambda$  is the wavelength.

and the angles  $\alpha_k$  and  $\theta_k$  introduced in Equation D-1 are defined by Keller as described in subsection A.2.2 of Appendix A.

Figure D-1 illustrates the coordinate convention employed in describing diffraction at the edge of a two-dimensional wedge having interior angle  $\frac{\pi}{2} - \alpha$ . An x-y-z coordinate system has been chosen such that the x-axis is coincident with the edge of the wedge, the z-axis is perpendicular to the rear face of the wedge, and the y-z plane is normal to the edge at the point of diffraction. The angle between the incident ray and the positive tangent to the edge is denoted by  $\beta_k$ . The angle between the projection of the direction of incidence in the plane normal to the edge at the point of diffraction (y-z or azimuth plane), and the normal to the wedge (negative x-axis) is denoted by  $\theta_k$ . From Figure D-1 we note the following relations

$$\begin{aligned}\theta_k &= \pi - \phi_k \\ \beta_0 &= \frac{\pi}{2} - \beta_k\end{aligned}\tag{D-2}$$

According to the law of edge diffraction, the family of rays diffracted at the edge lie on the surface of a cone with apex located at the point of diffraction (coordinate origin), and with half-cone angle  $\beta_k$ . One member of this family of diffracted rays is illustrated in Figure D-1.

In order to proceed, we must modify the law of edge diffraction. We assume that the diffracted ray which scatters in the direction  $\alpha_k = \theta_k$  contributes to the monostatic return despite the presence of the finite bistatic angle  $2\beta_0$ . This assumption is necessary to overcome the following discrepancy in the law of edge diffraction: as aspect angle increases from the axial value, the contribution from the ring discontinuity changes discontinuously from equal contribution from each point on the ring to two isolated contributions from the scattering centers. Substituting Equation D-2 into Equation D-1 and observing the above assumption, we have

$$D = \frac{e^{i\frac{\pi}{4}} \sin \frac{\pi}{n}}{n \cos \beta_0 \sqrt{2\pi k}} \left[ \left\{ \cos \frac{\pi}{n} - \cos \frac{3\pi - 2\phi_k}{n} \right\}^{-1} \mp \left\{ \cos \frac{\pi}{n} - 1 \right\}^{-1} \right]\tag{D-3}$$

where Equation D-3 has been modified for application to the electromagnetic case.

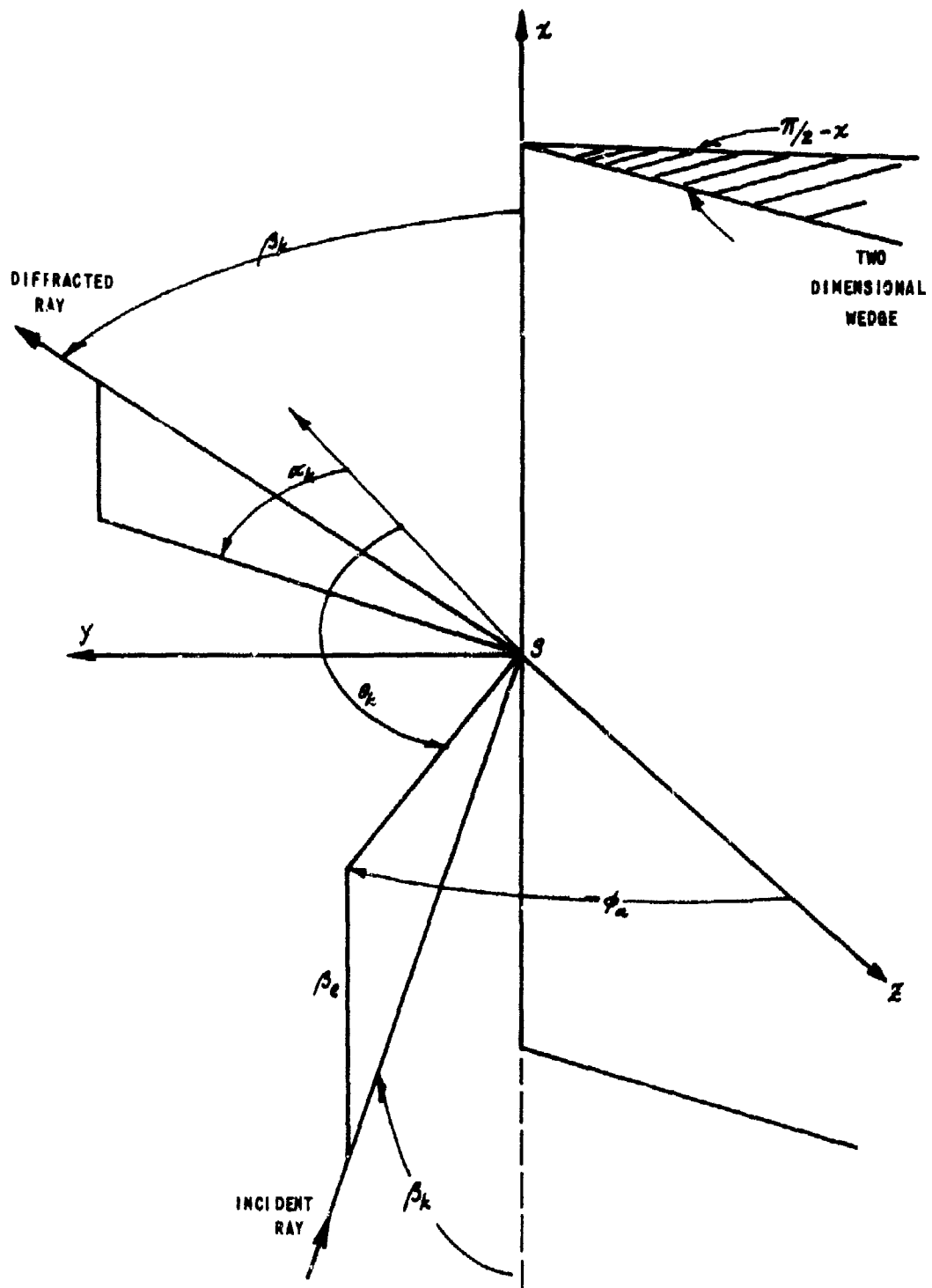


Figure D-1 DIFFRACTION AT THE EDGE OF A TWO-DIMENSIONAL WEDGE

## D.2 DIFFRACTION COEFFICIENT FOR RING DISCONTINUITY AT BASE OF CONE

We next consider diffraction at each point  $P$  on the ring discontinuity to arise due to an infinitesimal segment of an infinite wedge tangent to the cone base at that point. The geometry is illustrated in Figure D-2. Any point on the ring is defined by the angular parameter  $\theta$  : as  $\theta$  swings through the angular interval  $0 \leq \theta \leq 2\pi$ , the corresponding points on the edge develop the ring discontinuity in the x-y plane. We wish to determine the parameters  $\phi_a$  and  $\beta_e$  of Equation D-3 in terms of the generator  $\theta$ . We do this by relating Figures D-1 and D-2 in the manner shown in Figure D-3.

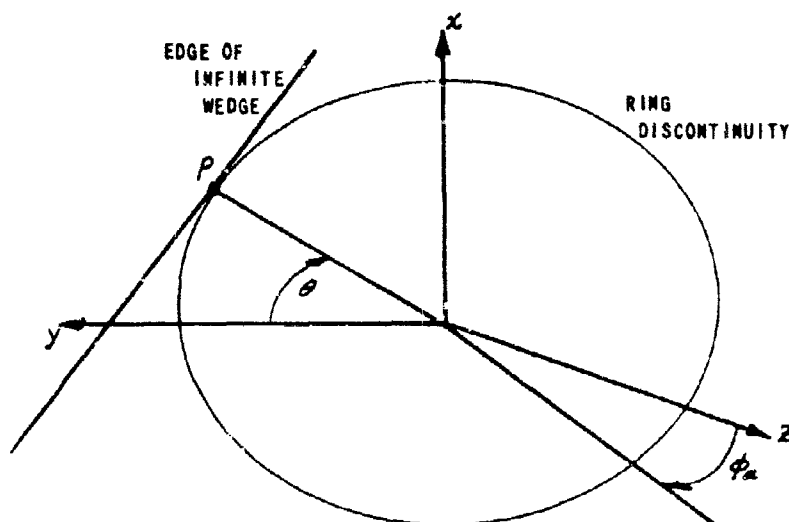


Figure D-2 LOCAL INTERPRETATION OF RING DISCONTINUITY IN TERMS  
OF INFINITE WEDGE

Here the edge of the wedge is visualized coincident with the x-axis as shown in Figure D-3. For any point  $P$  lying on the ring discontinuity, the aspect angle  $\phi$  will appear to traverse the arc  $AD$ , where the line  $PD$  makes an angle  $\theta$  with the y-axis.



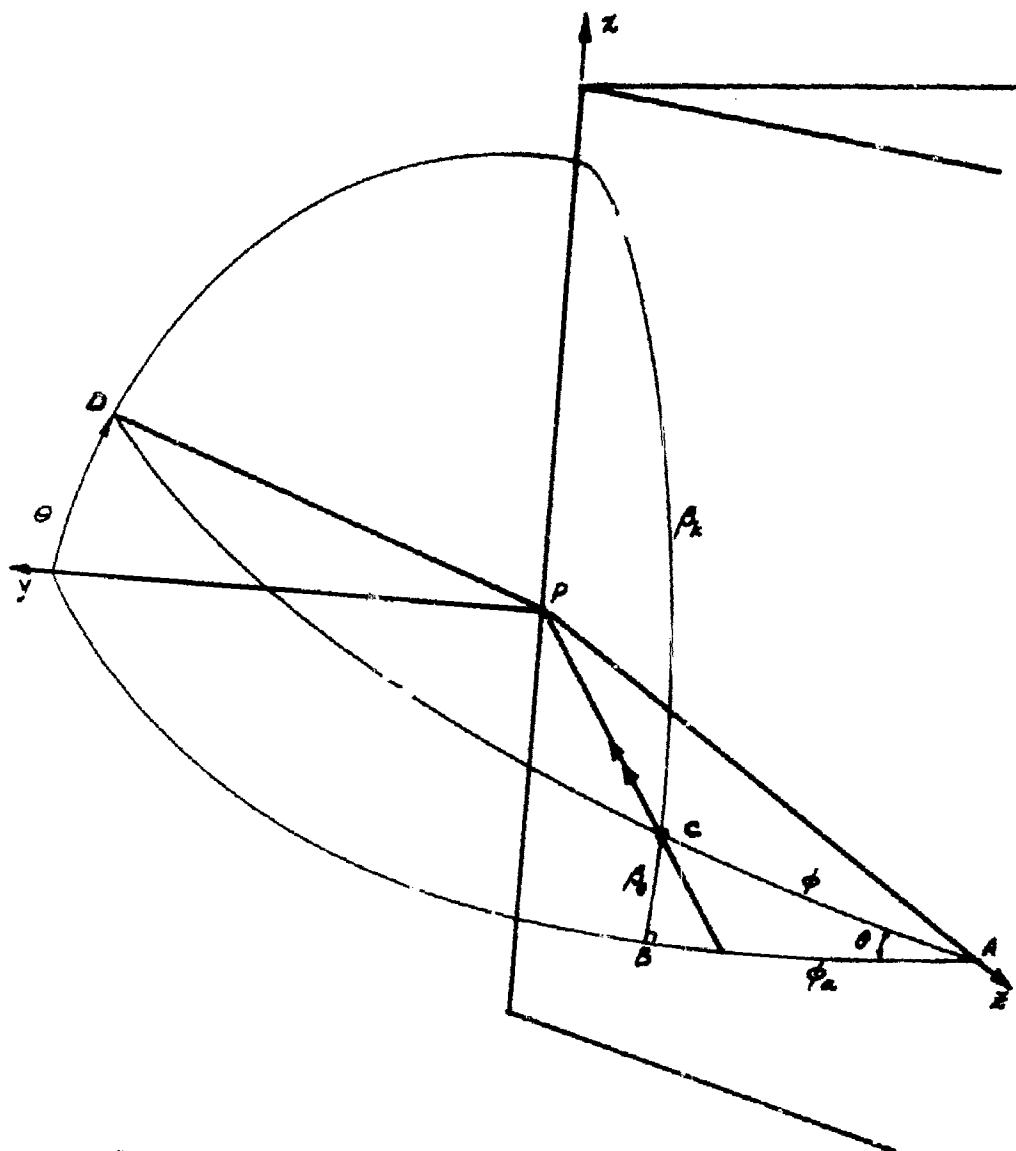


Figure D-3 ANGULAR RELATIONS AS A FUNCTION OF POSITION ON THE RING DISCONTINUITY

For a particular aspect coincident with the line  $CP$ , it is seen that the spherical triangle  $ABC$  in Figure D-3 relates the four parameters of interest:  $\phi$ ,  $\theta$ ,  $\beta_e$ , and  $\phi_e$ . The angle  $CBA$  is a right angle, so that

$$\begin{aligned}\phi_e &= \tan^{-1} \{ \cos \theta \tan \phi \} \\ \sin \beta_e &= \sin \theta \sin \phi\end{aligned}\quad (D-4)$$

Substituting the relations above into Equation D-3, we have

$$D(\phi, \theta) = \frac{e^{i\frac{\pi}{4}} \sin \frac{\pi}{n}}{n\sqrt{2\pi k} \sqrt{1 - \sin^2 \theta \sin^2 \phi}} \left[ \left\{ \cos \frac{\pi}{n} - \cos \frac{3\pi - 2\tan^{-1} \{ \cos \theta \tan \phi \}}{n} \right\}^{-1} \right. \\ \left. + \left\{ \cos \frac{\pi}{n} - 1 \right\}^{-1} \right] \quad (D-5)$$

Notice that Equation D-5 exhibits polarization dependence referred to the plane containing the arc  $AD$ . We now must transfer this polarization dependence to the  $y$ - $z$  or azimuth plane. This operation is simplified by the fact that, for an edge with circular symmetry, the polarization transformation is independent of aspect angle  $\phi$ . We choose the case of axial incidence in Figure D-4 to illustrate the transformation of the polarization conventions. In Figure D-4, the polarization reference for Equation D-5 is denoted by the orthogonal unit vectors  $\hat{t}_v$  and  $\hat{t}_h$ , where the subscripts refer to vertical and horizontal polarization cases, respectively. The second set of vectors ( $\hat{t}_z$ ,  $\hat{t}_y$ ) shown at an orientation  $\theta$  to the first set

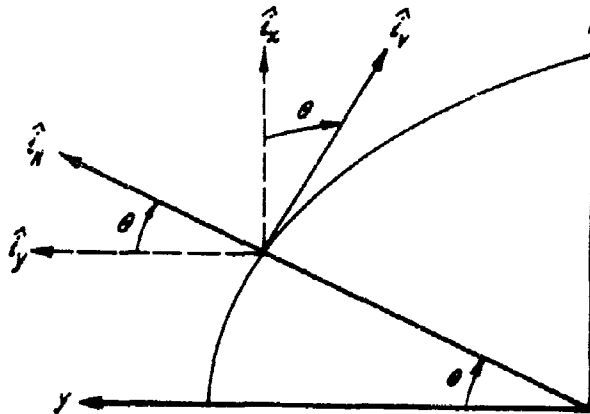


Figure D-4 POLARIZATION TRANSFORMATION

illustrate the polarization convention for the radar. Let us represent Equation D-5 by the short-hand notation

$$\begin{aligned} D_v(\phi, \theta) &= P_{oli} - P_{old} \\ D_h(\phi, \theta) &= P_{oli} + P_{old} \end{aligned} \quad (D-6)$$

where  $D_v(\phi, \theta)$  [ $D_h(\phi, \theta)$ ] denote the vertical (horizontal) polarization expressions for the diffraction coefficient, and  $P_{oli}$  ( $P_{old}$ ) stand for the polarization-independent (-dependent) components, respectively. The field  $u^s$  scattering in the  $\hat{i}_x, \hat{i}_y$  frame is proportional to

$$u^s \propto (\hat{i}_v \cdot E_{inc}) \hat{i}_v [D_v(\phi, \theta)] + (\hat{i}_h \cdot E_{inc}) \hat{i}_h [D_h(\phi, \theta)] \quad (D-7)$$

To obtain the desired principal polarization solutions to Equation D-7, we set the incident field  $E_{inc}$  equal to  $\hat{i}_x$  and  $\hat{i}_y$ . From Figure D-4, the following relations obtain

$$\begin{aligned} \hat{i}_v \cdot \hat{i}_x &= \cos \theta & \hat{i}_v \cdot \hat{i}_y &= -\sin \theta \\ \hat{i}_h \cdot \hat{i}_x &= \sin \theta & \hat{i}_h \cdot \hat{i}_y &= \cos \theta \\ \hat{i}_v &= \hat{i}_x \cos \theta - \hat{i}_y \sin \theta \end{aligned} \quad (D-8)$$

Substituting the above relations into Equation D-7 and introducing the notation defined in Equation D-6 we find that

$$\begin{aligned} u_v^s &\propto (P_{oli} - \cos 2\theta P_{old}) \\ u_h^s &\propto (P_{oli} + \cos 2\theta P_{old}) \end{aligned} \quad (D-9)$$

From the results of Equation D-9, we now write the general diffraction coefficient given by Equation D-5 in the proper polarization reference.

$$D(\phi, \theta) = \frac{e^{i\frac{\pi}{2}} \sin \frac{\pi}{2}}{n\sqrt{2\pi k} \sqrt{1 - \sin^2 \theta \sin^2 \phi}} \left\{ \cos \frac{\pi}{n} - \cos \frac{3\pi - 2 \tan^{-1} [\cos \theta \tan \phi]}{n} \right\}^{-1} \times \left\{ \cos \frac{\pi}{n} - 1 \right\} \cos 2\theta \quad (D-10)$$

Equation D-10 is used in the definition of the scattering function  $f(\phi, \theta)$ ,  
Equation C-17 of Appendix C.

UNCLASSIFIED  
Security Classification

| DOCUMENT CONTROL DATA - R & D   |  |  |
|---|--|--|
| (Security classification of title, body of abstract and indexing annotation must be entered when the overall report is classified)  |  |  |
| 1. ORIGINATING ACTIVITY (Corporate author)<br>General Dynamics, Fort Worth Division<br>P.O. Box 748<br>Fort Worth, Texas 76101  |  | 2a. REPORT SECURITY CLASSIFICATION<br>Unclassified   |
|   |  | 2b. GROUP<br>N/A   |
| 3. REPORT TITLE<br>Investigation of Scattering Principles, Volume III - Analytical Investigation  |  |  |
| 4. DESCRIPTIVE NOTES (Type of report and inclusive dates)<br>Final  |  |  |
| 5. AUTHOR(S) (First name, middle initial, last name)<br>R. A. Ross - Cornell Aeronautical Laboratory, Inc (Subcontractor)   |  |  |
| 6. REPORT DATE<br>May 1969  | 7a. TOTAL NO. OF PAGES<br>259  | 7b. NO. OF REFS<br>24  |
| 8a. CONTRACT OR GRANT NO.<br>F30602-67-C-0074   | 9a. ORIGINATOR'S REPORT NUMBER(S)<br>FZE-793   |  |
| 8b. PROJECT NO.<br>6512   | 9b. OTHER REPORT NO(S) (Any other numbers that may be assigned this report)<br>RADC-TR-68-340, Vol III |  |
| 8c. Task No:<br>651207  |  |  |
| 10. DISTRIBUTION STATEMENT<br>This document is subject to special export controls and each transmittal to foreign governments, foreign nationals or representatives thereto may be made only with prior approval of RADC (EMASS), GAFB, NY 13440.   |  |  |
| 11. SUPPLEMENTARY NOTES<br>Project Engineer:<br>John C. Cleary<br>AC 315 330 2118   |  | 12. SPONSORING MILITARY ACTIVITY<br>Rome Air Development Center (EMASS)<br>Griffiss Air Force Base, New York 13440 |
| 13. ABSTRACT<br>The objective of this effort was to establish and apply the mechanics of radar scattering from complex objects in terms of actual measurement data and the resulting empirically derived mathematical relationships. Volume I contains a summary of each task as well as detailed documentation on the experimental and superposition investigations. Volume II contains the radar range measurement data used in the experimental portion of the effort. Volume III contains the results of the analytical investigation, which uses geometric diffraction theory to predict radar cross section and scattering phase. Volume IV contains the potential military applications and results of the inverse scattering investigation. |  |  |

DD FORM 1 NOV 65 1473

UNCLASSIFIED  
Security Classification

UNCLASSIFIED  
Security Classification

| 14<br>KEY WORDS   | LINK A |    | LINK B |    | LINK C |    |
|---|--------|----|--------|----|--------|----|
|   | ROLE   | WT | ROLE   | WT | ROLE   | WT |
| Scattering Matrix Measurements<br>Radar Range<br>Radar Target<br>Long Pulse<br>Short Pulse<br>Statistical Analysis<br>Statistical Signature Analysis<br>Equivalence Class |        |    |        |    |        |    |

UNCLASSIFIED  
Security Classification

APLO—Distribution APP NY 15 Jul 74-127